TU Delft

Delft University of Technology

Document Version
Final published version

Citation (APA)
Conboy, J. P. (2026). *A Tale of Cytoskeletal Teamwork*. [Dissertation (TU Delft), Delft University of Technology]. https://doi.org/10.4233/uuid:cd32f72c-4e94-4dd7-a1bd-6d31eadede68

Important note
To cite this publication, please use the final published version (if applicable).
Please check the document version above.

Copyright
In case the licence states “Dutch Copyright Act (Article 25fa)”, this publication was made available Green Open Access via the TU Delft Institutional Repository pursuant to Dutch Copyright Act (Article 25fa, the Taverne amendment). This provision does not affect copyright ownership.
Unless copyright is transferred by contract or statute, it remains with the copyright holder.

Sharing and reuse
Other than for strictly personal use, it is not permitted to download, forward or distribute the text or part of it, without the consent of the author(s) and/or copyright holder(s), unless the work is under an open content license such as Creative Commons.

Takedown policy
Please contact us and provide details if you believe this document breaches copyrights.
We will remove access to the work immediately and investigate your claim.

This work is downloaded from Delft University of Technology.

A Tale of Cytoskeletal Teamwork



James P. Conboy

A TALE OF CYTOSKELETAL TEAMWORK

A TALE OF CYTOSKELETAL TEAMWORK

Dissertation

for the purpose of obtaining the degree of doctor
at Delft University of Technology
by the authority of the Rector Magnificus,
prof. dr. ir. T.H.J.J. H. Bijl,
chair of the Board for Doctorates
to be defended publicly on
Monday the 23rd of February at 15:00 o'clock.

by

James Peter CONBOY

This dissertation has been approved by the promotors.

Composition of the doctoral committee:

Rector Magnificus,	chairperson
Prof. dr. G. H. Koenderink,	Technische Universiteit Delft, promotor
Dr. P. E. Boukany,	Technische Universiteit Delft, promotor
Independent members:	
Prof. dr. C. Joo	Technische Universiteit Delft
Prof. dr. A. S. Akhmanova,	Universiteit Utrecht
Prof. dr. T. Betz,	Georg-August-Universität Göttingen (Germany)
Prof. dr. C. P. Broedersz,	Vrije Universiteit Amsterdam
Prof. dr. G. T. Charras,	University College London (United Kingdom)
Prof. dr. S. J. Picken,	Technische Universiteit Delft, reserve member

ISBN 978-94-6518-240-7

An electronic version of this dissertation is available at
http://repository.tudelft.nl/.

SUMMARY

At the core of all living organisms are cells, the basic building blocks of life. To survive and function, they must endure mechanical stresses while still performing essential processes such as division and migration. In our own bodies, cells are continually stretched and compressed as we breathe, our hearts beat, and as forces are applied to and by muscles and joints with every step we take. To withstand these forces while maintaining their function, cells rely on the cytoskeleton, a dynamic network composed of three distinct types of protein filaments: actin, microtubules and intermediate filaments. When the cytoskeleton is disrupted by genetic defects, cells can no longer withstand mechanical stress effectively, which can result in various diseases and developmental disorders. For example, mutations in intermediate filaments are linked with conditions such as muscular dystrophies and certain skin disorders, where cells are unable to cope with mechanical strain. Seemingly paradoxically, the cytoskeleton provides cells with elastic mechanical strength, while its ability to actively remodel gives rise to behaviours commonly seen in liquids, such as flowing and deforming over time, enabling essential processes like spreading, migration and division. These properties arise from the complex interplay between cytoskeletal filaments, molecular motors, and cross-linking proteins, which together enable cells to finely tune their mechanical responses. This combination of elastic solidity and liquid-like flow is known as viscoelasticity, a property that allows cells to change shape, adapt to their mechanical environment, and perform dynamic functions. Understanding how cells regulate their viscoelastic properties is key to revealing how they maintain their integrity under stress while remaining flexible enough to grow, move, and divide. In this light, we can think of the cell as a cabinet of mechanical curiosities, where the cytoskeleton, motors, and cross-links interact in finely tuned ways to generate this remarkable mechanical versatility.

Traditionally, scientists studying cytoskeletal mechanics have focused on the individual contributions of a single cytoskeletal system, such as actin, microtubules, or intermediate filaments, to overall cell mechanics. However, there is growing evidence and increasing interest in the idea that the components of the cytoskeleton do not act in isolation, but instead work together to determine the overall mechanical properties of the cell. In the work presented in this thesis, we focus primarily on the relative contributions of actin and vimentin (a particular type of intermediate filament protein) to cell mechanics, beginning with their individual contributions, and gradually building complexity to explore how crosslinking between the two networks allows them to cooperate and synergistically shape the mechanical properties of cells. Through this approach, we uncover that not only do actin and vimentin contribute individually and cooperatively to cell mechanics, but also that the way a cell is deformed, whether by compression or shear, profoundly influences how these cytoskeletal networks respond, emphasising that different modes of mechanical stress can lead to distinct cellular behaviours.

This thesis starts with an introduction to the important concepts and the cytoskeletal

protagonists in **Chapter 1**. We outline the mechanical properties of the three cytoskeletal filament systems and review how they team up to make cells mechanically strong.

After having set the scene, in **Chapter 2** we explore how two key components of the cytoskeleton of mesenchymal cells, actin and vimentin, help these cells respond to being compressed. To do this, we used a custom single-cell rheometer that allows us to compress single cells with well-defined amplitude and rate and precisely measure their mechanical properties. We studied cells from normal mice and from mice that lack vimentin, and also used drugs to alter how actin behaves inside the cells. Our experiments show that vimentin, which has often been overlooked, is just as important as actin in helping cells maintain their mechanical properties and resist compressive deformation. Meanwhile, actin plays a larger part in how cells absorb and release energy when under stress. We also resurrected a protocol from the 1970s to remove the nuclei of our cells, and found that the stiffening of cells under compression mainly comes from the actin and vimentin networks, not the nucleus. These findings provide first insights into how different parts of the cytoskeleton work together to shape how cells behave mechanically, helping them cope with forces both from their surroundings and from within.

Building on the clues we discovered in Chapter 2 about how different parts of the cytoskeleton complement each other, in **Chapter 3** we focused on how actin and vimentin interact. To understand how this interaction is controlled and how it affects the cell's mechanical properties, we studied a protein called plectin. Plectin is a crosslinking protein that helps physically connect the different parts of the cytoskeleton inside mammalian cells. It is abundant in many types of tissue, especially tissues that experience high mechanical stress, such as skin. Accordingly, genetic defects in plectin can lead to severe diseases such as skin blistering conditions. While plectin is known to help maintain the strength of cells and tissues, its role in how cells behave under different types of mechanical stress is not well understood. In this chapter, we used the same single-cell compression rheometer from Chapter 2 to study how plectin affects the way fibroblasts respond to both small and large deformations. By comparing normal fibroblasts with fibroblasts that lack plectin, we found that cells without plectin were almost twice as soft. Over longer timescales, these plectin-deficient cells relaxed mechanical stress more quickly, which we linked to a much faster turnover of actin, based on experiments using fluorescence recovery after photobleaching. We also found that these cells relaxed stress more quickly at short times, which we link to changes in the rate of fluid flow through the cytoskeleton. Using confocal imaging, we saw that the vimentin network in these cells changed from a fine, interconnected web in normal cells to thick bundles when plectin was missing. Overall, these results show that plectin plays an important role in organising the cytoskeleton and in controlling how fibroblasts respond to mechanical stress, emphasising how important the integration of different cytoskeletal systems is for the mechanical properties of cells.

After showing how important plectin is for linking the actin and vimentin networks in Chapter 3, in **Chapter 4** we looked more closely at the different roles plectin plays in the mechanics of cells. Plectin not only connects parts of the cytoskeleton together, but also helps attach the vimentin network to other structures inside the cell, including the nucleus. Because of these two functions, it is difficult to figure out exactly which role affects the cell's mechanics and structure the most. To explore this, we used a specially

designed crosslinker in cells that lacked plectin. This engineered crosslinker could join actin and vimentin, like plectin does, but could not anchor them to other parts of the cell. Using various mechanical tests, including the same cell compression method from earlier chapters, we found that this synthetic crosslinker was able to completely restore the mechanical strength of the cells without plectin. This showed that the linking function of plectin is what mainly helps maintain the cell's viscoelastic properties. However, without plectin's anchoring role, the shape of the nucleus was disrupted and the cells produced less traction force. These results show that plectin has specialised roles besides its crosslinking function, which allow cells to manage mechanical forces both in the cytoskeleton and in connection with the nucleus.

In **Chapter 5**, we returned to studying the actin and vimentin networks, this time focusing on how cells respond to shear forces rather than compression. While most studies in cell mechanics focus on compressive stress, cells in the body are also frequently exposed to shear, such as when tissues slide against each other or when cells migrate through tissues. How the cytoskeleton responds to these different types of forces is still not fully understood. To investigate this, we adapted our single-cell measurement tool to apply shear stress. Using mouse fibroblasts from both normal and vimentin-deficient cells, along with drugs that affect actin, we studied how each network contributes to the cell's mechanical response. We found that cells soften when sheared, mainly due to actin, while vimentin helps stiffen the cell at larger shear strains. This shear-softening was strikingly different from the compression-stiffening seen in earlier chapters. We suggest this difference arises because cytoskeletal filaments are stretched more when the cell is sheared as compared to when it is compressed. Large tensile strains can lead to breakage of actin filaments or their connections, whilst vimentin, being more resilient stays intact. These findings show how cytoskeletal elements act together like a composite material, with their response depending on the type and direction of mechanical stress. They furthermore again highlight how the cell's strength and flexibility arise from the interplay between its distinct structural networks.

In **Chapter 6**, we move away from focusing on specific parts of the cytoskeleton and instead look at how we measure the mechanical properties of cells. One common technique for this is atomic force microscopy (AFM), which allows scientists to probe how soft materials, like cells, respond to nanoscale forces. Although AFM has provided valuable insights into cell stiffness, researchers often notice that the measured stiffness values tend to follow a log-normal distribution, meaning most values are low, with a few much higher ones. Until now, it has been unclear whether this pattern reflects real biological differences or something about the way the measurements are analysed. In this chapter, we show that the shape of this distribution is not necessarily an inherent mechanical property of cells, but rather is a result of how the data are processed. These findings emphasise the need for careful and consistent analysis methods when studying cell mechanics. By showing that some of the variability in AFM data comes from analysis choices rather than from inherent differences among the cells themselves, this work helps improve the accuracy and reliability of mechanical measurements.

Finally, in **Chapter 7**, we reflect on the key findings of this thesis and discuss how our results help to connect studies in whole cells with research using simplified systems outside the cell. We focus on how these approaches together can help answer important

questions about how the cytoskeleton and its interactions provide cells with mechanical strength. We end by sharing our thoughts on the future direction of research in cell mechanics.

SAMENVATTING

Elk levend organisme bestaat uit cellen, de fundamentele bouwstenen van het leven. Om te overleven en te functioneren, moeten cellen mechanische spanningen doorstaan terwijl ze toch essentiële processen blijven uitvoeren, zoals celdeling en migratie. Terwijl ons hart klopt, we ademen en ons bewegen worden cellen voortdurend uitgerekt en samengedrukt. Cellen kunnen deze krachten weerstaan dankzij het cytoskelet, een dynamisch netwerk dat uit drie soorten eiwitvezels bestaat: actine, microtubuli en intermediaire filamenten. Wanneer het cytoskelet verstoord is door genetische defecten, kunnen cellen mechanische stress minder goed weerstaan, wat tot verschillende ziekten en ontwikkelingsstoornissen kan leiden. Mutaties in intermediaire filamenten zijn bijvoorbeeld gekoppeld aan aandoeningen zoals spierdystrofieën en bepaalde huidaandoeningen.

Enerzijds voorziet het cytoskelet cellen van elastische stevigheid, anderzijds zorgt actieve hermodellering van het cytoskelet voor gedrag dat op dat van vloeistoffen lijkt. Cellen stromen en vervormen in de loop van de tijd, waardoor essentiële processen zoals verspreiding, migratie en deling mogelijk worden. Deze eigenschappen komen voort uit een complex samenspel tussen de cytoskeletvezels, moleculaire motoren en crosslinkereiwitten. De combinatie van elastische stevigheid en vloeistofachtige stroming noemen we viscoelasticiteit, en deze eigenschap geeft cellen het vermogen om van vorm te veranderen, zich aan hun mechanische omgeving aan te passen en zich te bewegen. Om te begrijpen hoe cellen onder mechanische spanning hun integriteit behouden en tegelijkertijd flexibel genoeg blijven om te groeien, bewegen en zich te delen, is het essentieel om te weten hoe cellen hun viscoelastische eigenschappen reguleren. In dit licht kunnen we de cel beschouwen als een mechanisch rariteitenkabinet, waarin het cytoskelet, de motoren en de crosslinkers op fijn afgestemde manieren samenwerken en voor een opmerkelijke mechanische veelzijdigheid zorgen.

Traditioneel hebben wetenschappers die cytoskeletmechanica bestuderen zich gericht op de individuele mechanische bijdragen van een enkel cytoskeletsysteem, zoals actine, microtubuli of intermediaire filamenten. Er is echter groeiend bewijs voor en een toenemend interesse in het idee dat de componenten van het cytoskelet niet geïsoleerd werken, maar dat hun samenwerking de mechanische eigenschappen van de cel bepaalt. In deze scriptie richten we ons voornamelijk op de relatieve bijdragen aan de celmechanica van vimentine, een intermediair filament-eiwit, en actine. We beginnen met hun individuele bijdragen en beschouwen daarna hoe koppelingen tussen de individuele netwerken ervoor zorgen dat de netwerken samenwerken en synergetisch de mechanische eigenschappen van de cel bepalen. We ontdekken niet alleen dat actine en vimentine individueel en in samenwerking aan de celmechanica bijdragen, maar ook dat de manier waarop de cel vervormd wordt uitmaakt. Compressie en schuifspanning leiden tot verschillende reacties van de cytoskelet-netwerken, en we concluderen dat verschillende manieren van mechanische spanning tot verschillend celgedrag kunnen

leiden.

Deze scriptie begint met een introductie van belangrijke concepten en de protagonisten in het cytoskelet in **hoofdstuk 1**. We schetsen de mechanische eigenschappen van de drie cytoskelet-netwerken en bekijken hoe ze samenwerken om cellen mechanisch sterk te maken.

In **hoofdstuk 2** onderzoeken we hoe twee belangrijke componenten van het cytoskelet van mesenchymale cellen, actine en vimentine, tot de celrespons op compressieve spanning bijdragen. Hiervoor hebben we een aangepaste cell-rheometer gebruikt die ons in staat stelt om enkele cellen met een precies gedefinieerde amplitude en snelheid te comprimeren en hun mechanische respons nauwkeurig te meten. We bestudeerden cellen afkomstig van normale muizen en muizen die geen vimentine aanmaken, en gebruikten farmaca om het gedrag van actine in de cellen te veranderen. Onze experimenten laten zien dat vimentine, dat zelden is onderzocht, even belangrijk is als actine bij het behouden van de celmechanische eigenschappen en de weerstand tegen compressieve vervorming. Tegelijkertijd is actine belangrijker bij het absorberen en vrijgeven van energie wanneer de cel onder mechanische spanning staat. We hebben ook een protocol uit de jaren 1970 weer tot leven gebracht, waarmee celkernen uit de cel kunnen worden gehaald. We zagen dat de verstijving van cellen onder compressie vooral van de actine- en vimentine-netwerken komt, en niet van de celkern. Deze bevindingen bieden een eerste inzicht in hoe verschillende delen van het cytoskelet het mechanische gedrag van cellen vormgeven en hen helpen om te gaan met krachten uit hun omgeving en van binnenuit.

Voortbouwend op de inzichten uit hoofdstuk 2 over hoe verschillende delen van het cytoskelet elkaar aanvullen, richtten we ons in **hoofdstuk 3** op de interacties tussen actine en vimentine. Om te begrijpen hoe deze interacties worden gecontroleerd en de mechanische eigenschappen van de cel beïnvloeden, bestudeerden we het eiwit plectine. Plectine is een crosslinker-eiwit dat verschillende delen van het cytoskelet in zoogdiercellen fysiek met elkaar verbindt. Het is veeltallig aanwezig in vele weefseltypen, vooral in weefsels die veel mechanische spanning ondervinden, zoals de huid. Daarom kunnen genetische defecten in plectine leiden tot ernstige ziekten met blaarvorming op de huid. Hoewel bekend is dat plectine cellen en weefsels sterker maakt, is de precieze rol van plectine in de reactie van cellen op verschillende soorten mechanische spanning niet goed begrepen. In dit hoofdstuk gebruikten we de cell-rheometer uit hoofdstuk 2 om te bestuderen hoe plectine de manier beïnvloedt waarop fibroblasten reageren op zowel kleine als grote compressieve vervormingen. Door normale fibroblasten te vergelijken met fibroblasten zonder plectine, ontdekten we dat cellen zonder plectine bijna twee keer zo zacht waren. Over langere tijdschalen relaxeerden deze cellen zonder plectine sneller, wat we in verband brachten met een veel snellere turnover van actine, gebaseerd op experimenten met *fluorescence recovery after photobleaching*. Ook op korte tijdschalen relaxeerden de cellen sneller, door veranderingen in de snelheid waarmee vloeistof door het cytoskelet stroomt. Middels confocale microscopie zagen we dat het vimentinenetwerk van een fijn, onderling verbonden netwerk in normale cellen veranderde in dikke bundels wanneer plectine ontbrak. Samenvattend laten deze resultaten zien dat plectine een belangrijke rol speelt bij het organiseren van het cytoskelet en bij de reactie van fibroblasten op mechanische stress. Zij benadrukken hoe belangrijk de

integratie van verschillende cytoskeletsystemen is voor de mechanische eigenschappen van cellen.

Nadat we in hoofdstuk 3 hebben laten zien hoe belangrijk plectine is voor het verbinden van het actine- en vimentinenetwerk, keken we in **hoofdstuk 4** nader naar de verschillende rollen die plectine speelt in de mechanica van cellen. Plectine verbindt niet alleen delen van het cytoskelet met elkaar, maar helpt ook het vimentinenetwerk te hechten aan andere structuren in de cel, waaronder de celkern. Vanwege deze twee functies is het moeilijk om erachter te komen welke rol het meest van invloed is op de mechanica en structuur van de cel. Om dit te onderzoeken gebruikten we een speciaal ontworpen crosslinker in cellen zonder plectine. Deze synthetische crosslinker kan actine en vimentine verbinden, zoals plectine doet, maar kan ze niet verankeren aan andere delen van de cel. Met behulp van verschillende mechanische testen, waaronder dezelfde celcompressiemethode uit eerdere hoofdstukken, ontdekten we dat deze crosslinker in staat was om de mechanische sterkte van de cellen zonder plectine volledig te herstellen. Dit toonde aan dat vornamelijk de verbindende functie van plectine helpt om de visco-elastische eigenschappen van de cel te behouden. Zonder de verankerende rol van plectine werd de vorm van de celkern echter verstoord en produceerden de cellen minder trekkracht. Deze resultaten laten zien dat plectine naast zijn verankeringsfunctie gespecialiseerde rollen heeft die cellen in staat stellen om mechanische krachten te beheersen, zowel in het cytoskelet als in verbinding met de celkern.

In **hoofdstuk 5** zijn we teruggekeerd naar de actine- en vimentinenetwerken en richtten we ons op hoe cellen reageren op schuifkrachten. Hoewel de meeste studies naar celmechanica zich richten op compressie, worden cellen in het lichaam vaak blootgesteld aan schuifkrachten, zoals wanneer weefsels tegen elkaar wrijven of wanneer cellen door weefsels migreren. Hoe het cytoskelet reageert op deze verschillende soorten krachten is nog niet volledig begrepen. Om dit te kunnen onderzoeken door schuifspanningen op cellen te leggen hebben we onze cel-rheometer aangepast. Met behulp van normale muizenfibroblasten, cellen zonder vimentine en farmaca die actine beïnvloeden, bestudeerden we hoe elk netwerk bijdraagt aan de mechanische respons van de cel. We ontdekten dat cellen zachter worden bij opgelegde schuifspanning, voornamelijk door actine, terwijl vimentine helpt de cel te verstijven bij grotere schuifspanningen. Deze schuif-verzachting verschilde opvallenderwijs van de compressie-versteviging die we in eerdere hoofdstukken zagen. We denken dat dit verschil ontstaat doordat cytoskeletfilamenten meer worden uitgerekt wanneer de cel wordt afgeschoven dan wanneer deze wordt samengedrukt. Grote trekspanningen kunnen leiden tot de breuk van actinefilamenten of hun verbindingen, terwijl vimentine veerkrachtiger is en intact blijft. Deze bevindingen laten zien hoe cytoskeletale elementen samenwerken als een composietmateriaal, waarbij hun respons afhangt van het type en de richting van de mechanische spanning. Bovendien laten ze opnieuw zien hoe de sterkte en flexibiliteit van de cel voortkomen uit de wisselwerkingen tussen de verschillende structurele netwerken.

In **hoofdstuk 6** richtten we ons niet meer op specifieke delen van het cytoskelet, maar onderzochten we een meetmethode die we op cellen toepassen. De atomaire krachtmicroscopie (AFM) is een veelgebruikte techniek waarmee wetenschappers kunnen onderzoeken hoe zachte materialen, zoals cellen, reageren op krachten op de nanoschaal. Hoewel AFM waardevolle inzichten heeft opgeleverd in de stijfheid van cellen, merken

onderzoekers op dat de gemeten stijfheidswaarden vaak een log-normale verdeling volgen, wat betekent dat de meeste waarden laag zijn, met een paar veel hogere waarden. Tot nu toe was het onduidelijk of dit patroon echte biologische verschillen weerspiegelt of te maken heeft met de manier waarop de metingen worden geanalyseerd. In dit hoofdstuk laten we zien dat de vorm van de verdeling niet noodzakelijkerwijs een inherente mechanische eigenschap van cellen is, maar eerder een gevolg is van de manier waarop de gegevens worden verwerkt. In het bijzonder vonden we dat wanneer krachtcurven worden geanalyseerd met behulp van een vastgelegde maximale kracht, wat een gangbare praktijk is, dit de resultaten vertekent. Deze bevindingen benadrukken de noodzaak van zorgvuldige en consistente analysemethoden bij het bestuderen van celmechanica. Door aan te tonen dat een deel van de variabiliteit in AFM-metingen komt door keuzes in de analyse in plaats van door inherente verschillen tussen de cellen zelf, dragen wij met dit werk bij aan de verbetering van de nauwkeurigheid en betrouwbaarheid van mechanische metingen.

Tot slot reflecteren we in **hoofdstuk 7** op de belangrijkste bevindingen van dit proefschrift en bespreken we hoe onze resultaten helpen om celstudies te verbinden met onderzoek waarbij vereenvoudigde systemen buiten de cel worden gebruikt. We bekijken hoe deze benaderingen kunnen helpen bij het beantwoorden van belangrijke vragen over hoe het cytoskelet en zijn interacties cellen voorzien van mechanische sterkte. We eindigen met onze gedachten over de toekomstige richting van het onderzoek naar celmechanica.

CONTENTS

Summary **7**

Samenvatting **14**

1 Introduction **19**
1.1 The cell . . . 20
1.2 The cytoskeleton . . . 21
1.2.1 Actin filaments . . . 21
1.2.2 Microtubules . . . 22
1.2.3 Intermediate filaments . . . 22
1.3 The cytoskeleton and the mechanics of cells . . . 22
1.3.1 Live-cell studies . . . 23
1.3.2 Cell-free studies . . . 25
1.4 The cytoskeleton and cell contractility . . . 27
1.4.1 Live-cell studies . . . 28
1.4.2 Cell-free studies . . . 29
1.5 Outline of this thesis . . . 30
1.6 Acknowledgements . . . 32

2 Actin and vimentin jointly control cell viscoelasticity and compression stiffening **33**
2.1 Introduction . . . 34
2.2 Results . . . 35
2.2.1 Frequency-dependent rheology of single mouse embryonic fibroblasts . . . 35
2.2.2 Actin and vimentin both contribute to bulk cell viscoelasticity . . . 37
2.2.3 Strain ramp experiments to characterize the nonlinear elasticity of MEF cells . . . 39
2.2.4 Actin and vimentin both contribute to the compression-stiffening of cells . . . 41
2.2.5 The cytoskeleton, not the nucleus, causes compression stiffening . . . 43
2.3 Discussion . . . 44
2.4 Conclusions . . . 47
2.5 Acknowledgements . . . 48
2.6 Materials and Methods . . . 48
2.6.1 Cell culture . . . 48
2.6.2 Fabrication of wedged force cantilevers . . . 49
2.6.3 Single cell rheology experiments . . . 49
2.6.4 Dynamic mechanical analysis measurements . . . 50

2.6.5 Strain-controlled compressive ramps . . . 51
2.6.6 Live cell imaging with confocal microscopy . . . 51
2.6.7 Removal of nuclei from cells . . . 52
2.6.8 Statistics and code availability . . . 52
2.7 Supplementary information . . . 53
2.7.1 Supplementary figures . . . 53
2.7.2 Supplementary methods . . . 61

3 Plectin affects cell viscoelasticity at small and large deformations 63
3.1 Introduction . . . 64
3.2 Results . . . 66
3.2.1 Plectin influences actin and vimentin organization in fibroblasts . . . 66
3.2.2 Small amplitude oscillatory compression shows that plectin stiffens cells . . . 67
3.2.3 Plectin affects poroelastic and viscoelastic stress relaxation . . . 69
3.2.4 Plectin knockout does not impact fibroblast strain-stiffening . . . 74
3.2.5 Repeated compression softens wild type cells more than plectin knockout cells . . . 75
3.3 Discussion . . . 77
3.4 Conclusion . . . 81
3.5 Acknowledgement . . . 82
3.6 Materials and methods . . . 82
3.6.1 Cell culture and sample preparation for compression experiments . . . 82
3.6.2 Single-cell compression experiments . . . 83
3.6.3 Analysis of single-cell compression data . . . 84
3.6.4 Confocal microscopy experiments . . . 86
3.6.5 Analysis of confocal microscopy data . . . 86
3.6.6 FRAP measurements of cytoplasmic viscosity and actin network turnover . . . 87
3.6.7 Analysis of FRAP measurements . . . 87
3.6.8 Western blotting . . . 88
3.6.9 Statistics . . . 88
3.7 Supplementary information . . . 89
3.7.1 Supplementary figures . . . 89
3.7.2 Supplementary tables . . . 99
3.7.3 Supplementary methods . . . 100
3.7.4 Supplementary results . . . 101

4 Untangling the cytoskeletal crosslinking and anchoring functions of plectin in cells 103
4.1 Introduction . . . 104
4.2 Results . . . 105
4.2.1 ACTIF crosslinking mediates colocalization of actin and vimentin filaments in fibroblasts. . . . 105
4.2.2 ACTIF-mediated cytoskeletal crosslinking rescues cell stiffness . . . 107
4.2.3 ACTIF crosslinking does not rescue traction force generation . . . 110

4.2.4 Plectin-mediated nuclear anchoring is needed to restore wild type nuclear morphology . . . 112
4.2.5 Plectin speeds up 2D cell migration . . . 114
4.3 Discussion . . . 116
4.4 Conclusion . . . 118
4.5 Acknowledgements . . . 118
4.6 Materials and methods . . . 119
4.6.1 Cell culture. . . . 119
4.6.2 Cell transfection . . . 119
4.6.3 Atomic force microscopy (AFM) . . . 119
4.6.4 Single cell compression experiments and data analysis . . . 120
4.6.5 Lysosome tracking experiments . . . 120
4.6.6 Traction force microscopy (TFM) . . . 122
4.6.7 Immunofluorescence imaging . . . 123
4.6.8 Analysis of vimentin distribution . . . 123
4.6.9 Single cell migration tracking . . . 124
4.7 Supplementary information . . . 125
4.7.1 Supplementary methods . . . 125
4.7.2 Supplementary figures . . . 126
4.7.3 Supplementary tables . . . 133

5 Actin and vimentin exhibit complementary mechanical responses in single cells under shear 135
5.1 Introduction . . . 136
5.2 Results . . . 137
5.2.1 Single-cell shear rheology measurements . . . 137
5.2.2 Actin shear-softens while vimentin shear-stiffens . . . 139
5.2.3 Repeated shearing softens cells . . . 141
5.2.4 Rate dependence of the nonlinear shear response of single cells . . . 143
5.3 Discussion . . . 143
5.4 Conclusion . . . 147
5.5 Acknowledgements . . . 147
5.6 Materials and methods . . . 148
5.6.1 Cell culture. . . . 148
5.6.2 Single-cell rheometer plate manufacture . . . 148
5.6.3 Single cell shear rheology . . . 148
5.6.4 Imaging of cells confined between the rheometer plates . . . 150
5.6.5 Data processing . . . 150
5.6.6 Statistics . . . 150
5.7 Supplementary information . . . 151
5.7.1 Supplementary figures . . . 151
5.7.2 Supplementary tables . . . 157
5.7.3 Supplementary methods . . . 159

6 Beyond bell curves: The origin of non-Gaussian distributions in atomic force microscopy elasticity measurements **161**
6.1 Introduction . . . 162
6.2 Results . . . 163
6.2.1 Measuring elasticity using atomic force microscopy . . . 163
6.2.2 The elastic moduli of polyacrylamide hydrogels display a skewed distribution . . . 164
6.2.3 The elastic modulus distribution of single mammalian cells . . . 167
6.2.4 The elastic modulus distribution of a cell population . . . 169
6.2.5 Deviations from the Hertz model lead to a skewed distribution of Young's moduli. . . . 170
6.3 Discussion . . . 172
6.4 Conclusion . . . 173
6.5 Acknowledgements . . . 173
6.6 Materials and methods . . . 173
6.6.1 Atomic force microscopy. . . . 173
6.6.2 Data and statistical analysis . . . 174
6.6.3 Polyacrylamide gel preparation . . . 174
6.6.4 Cell culture. . . . 175
6.6.5 Monte Carlo force-curve simulations . . . 176
6.6.6 Skewness and kurtosis calculation . . . 176
6.7 Supplementary information . . . 177
6.7.1 Theory . . . 177

7 Outlook **179**
7.1 Where are we now? . . . 180
7.2 Bridging cell and cell-free studies . . . 180
7.3 The future is 3D . . . 186
7.4 Acknowledgements . . . 187

References **189**

1

INTRODUCTION

Living cells are the fundamental units of life. They possess the remarkable ability to combine mechanical strength with the flexibility to change shape during essential processes such as cell division and migration. This seemingly paradoxical behaviour is made possible by the cytoskeleton, a dynamic network composed of three distinct types of protein filaments: actin, microtubules and intermediate filaments. These filaments were traditionally regarded as separate systems with distinct cellular roles. However, recent research suggests they are closely interconnected, working together through physical interactions and coordinated biological regulation. This chapter introduces the mechanical functions of the cytoskeleton in mammalian cells and explores how the interplay between its components contributes to cellular strength and adaptability. It also lays out the motivation and aim of the thesis and ends with an outline of the chapters that follow.

This chapter is partly based on the review paper *How cytoskeletal crosstalk makes cells move: Bridging cell-free and cell studies.* published in Biophysics Reviews (2024). The review paper was jointly written by **J. P. Conboy**, I. Istúriz Petitjean, A. van der Net and G. H. Koenderink.

1.1. THE CELL

In October 1676, Antonie van Leeuwenhoek of Delft wrote a letter to the Royal Society of London [1]. In his remarkable letter, van Leeuwenhoek observed that ordinary water contained countless tiny living organisms far smaller than anything previously imagined, a discovery that was met with scepticism [2]. He called these organisms 'animalcules', a term he used to describe their microscopic size and motile behaviour. No one else had seen such things, and van Leeuwenhoek, a self-taught lens grinder with no formal scientific training, provided little beyond his own testimony and the use of his unusual microscopes. Yet his descriptions were so detailed, and his discovery so sensational, that the members of the Royal Society could not set them aside without further inquiry. With the assistance of the physicist Robert Hooke, a prominent member of the Society and a pioneer of microscopy whose *Micrographia* had, nearly a decade earlier, revealed the intricate structure of objects visible to the naked eye, efforts were undertaken to verify Van Leeuwenhoek's claims. It was Hooke who had first coined the term 'cell', describing the box-like compartments he observed in slices of cork [3], and it was he who, after several attempts, succeeded in confirming the presence of the minuscule, motile organisms Van Leeuwenhoek had described. Through his meticulous observations, Van Leeuwenhoek became the first person to witness what is now recognised to be single-celled organisms, revealing a hidden living world that had never before been seen by human eyes.

More than three hundred years later, those of us working in Delft[1] have a far more comprehensive understanding of living cells and the building blocks that comprise them. Among the many perspectives that have deepened this understanding, studying cells through a soft matter physicist's lens is particularly fascinating[2]. Soft matter is a class of materials whose mechanical properties depend on the time, amplitude and type of deformation. In this context, cells can be seen as an intriguing form of soft matter since also their mechanical response depends sensitively on both the timescale and magnitude of deformation, enabling them to endure large and repeated stresses, and actively reshape themselves. This complex mechanical behaviour is central to many essential cellular processes, from cell migration and division to the ability to sense and adapt to changes in their physical (micro)environment. Such behaviours are evident when cells squeeze through narrow tissue spaces during migration, divide under mechanical constraints, or remodel their internal architecture in response to external forces.

Understanding how cells generate and withstand forces in these contexts calls for precise experimental tools capable of applying and detecting forces at the nanoscale, while capturing the dynamic behaviour of living matter. Rather than treating cells as uniform materials, these approaches aim to dissect how different components contribute to their mechanical properties and responses. To probe cell mechanics across different length and force scales, researchers have developed a wide range of techniques, including optical tweezers [4, 5], atomic force microscopy [6], magnetic twisting cytometry [7], and particle-tracking microrheology [8, 9, 10] to assess local mechanical properties, as

[1] And elsewhere

[2] This may be a somewhat biased viewpoint

well as single-cell stretching and compression assays using either adhesive [11, 12] or non-adhesive [13] parallel plates to explore larger, physiologically relevant deformations. What unites these diverse experimental approaches is the consistent finding that the cytoskeleton, an intracellular biopolymer network, plays a central role in determining the rich mechanical behaviour of cells. In this thesis, we develop and use precise single-cell measurements to investigate how the properties of the cytoskeleton give rise to, and govern, the mechanical behaviour of the cell as a whole. Viewed through the lens of soft matter physics, this approach allows us to explore how the mechanical response of cells emerges from the cytoskeleton, depending not only on its composition but also on the timescale, scale and type of deformation applied. This mechanical response is inherently viscoelastic and often highly nonlinear, reflecting the complex interplay between passive structural elements and active force-generating processes within the cytoskeleton. In the following section, we review the composition of the cytoskeleton and discuss how its constituent biopolymers contribute to the mechanical properties of cells.

1.2. THE CYTOSKELETON

Cellular responses to mechanical deformation rely on the structural and mechanical properties of the cytoskeleton, a network of dynamic biopolymers that self-assemble from small protein building blocks. There are three main cytoskeletal biopolymers: actin filaments, microtubules, and intermediate filaments (Figure 1.1A). These filaments differ markedly in their architecture, stiffness, and turnover rates. In addition, septins have recently been identified as a fourth cytoskeletal component, although their role in cell mechanics is still obscure [14]. Cells exhibit viscoelastic and nonlinear elastic behaviour, as the three cytoskeletal filaments have different stiffnesses and are interconnected by a multitude of transient crosslinking proteins, each with its own characteristic turnover dynamics. Collectively, crosslinker unbinding and cytoskeletal (de)polymerisation give rise to dissipative mechanical responses that evolve over a range of timescales.

1.2.1. ACTIN FILAMENTS

Actin filaments are double helices with a diameter of ~ 7 nm, made of two strands of globular monomers [15]. The filaments are semiflexible since their thermal persistence length $l_p = \kappa / k_B T$ (where κ is the bending rigidity and $k_B T$ thermal energy) is ~ 10μm, of the same order as the filament contour length [16]. Actin filaments have an intrinsic structural polarity with a "barbed end" and a "pointed end". Polymerization-linked ATP hydrolysis causes treadmilling, where the filaments grow at the barbed end and disassemble from the pointed end [17]. Filaments reconstituted from purified actin turn over slowly (one subunit every 3–4 s), but actin turnover in the cell is catalyzed by actin-binding proteins. Typical actin network turnover times are of order seconds in the leading edge of motile cells [18] to minutes in the actin cortex [19]. Together with myosin motor proteins, actin filaments form networks and bundles that generate contractile forces [20].

1.2.2. MICROTUBULES

Microtubules form hollow tubes of 13 protofilaments that are much wider (~ 25 nm)[21] and hence substantially stiffer (l_p ~ 1 mm)[22] than actin filaments. Like actin filaments, microtubules have an intrinsic structural polarity with distinct plus and minus ends. GTP hydrolysis results in dynamic instability, characterized by alternating phases of microtubule growth and shrinkage [23]. In the cell, this process is tightly regulated by accessory proteins that bind at the microtubule tips or lattice.

1.2.3. INTERMEDIATE FILAMENTS

Intermediate filaments are homo-/heteropolymers made of rod-shaped proteins that are encoded by more than 70 genes in humans [24]. Intermediate filament proteins are expressed in a cell-type-specific manner. Mesenchymal cells for instance express vimentin, whereas epithelial cells express keratins. The intermediate filament proteins share a common secondary structure consisting of an alpha-helical rod domain flanked by intrinsically disordered head and tail domains. Intermediate filaments are somewhat thicker (~ 10 nm) [25] than actin filaments, but they are nevertheless much more flexible (l_p ~ 0.5 - 2 μm, depending on intermediate filament composition and ionic strength [26, 27, 28, 29, 30]) because of their hierarchical rope-like structure. Intermediate filaments are much more stable than actin filaments and microtubules, with slow subunit exchange along their length and annealing and fragmentation on hour time scales in reconstituted systems [31, 32] and in cells [33, 34].

1.3. THE CYTOSKELETON AND THE MECHANICS OF CELLS

Having introduced the individual properties of actin filaments, microtubules, and intermediate filaments, we now review the foundation for what is known about how each of these cytoskeletal networks contributes to cellular mechanics, and how their crosstalk further shapes the mechanical behaviour of cells. We begin by reviewing what is known about the mechanics of mammalian cells, which are the primary focus of this thesis. We also review insights from *in vitro* reconstitution experiments, which provide a complementary perspective by isolating specific cellular components and allowing precise control over experimental conditions. While caution is needed in extrapolating from cell-free systems to the cellular environment, since cytoskeletal interactions or mechanical effects observed in reconstituted systems do not necessarily occur in the same way as in cells, these studies nonetheless provide valuable insight into the fundamental mechanisms that may underlie the more complex behaviour of living cells. Furthermore, my approach to measuring the mechanics of living cells was inspired by insights gained from *in vitro* reconstitution studies, which highlight the power of a reductionist approach in uncovering fundamental and universal physical principles.

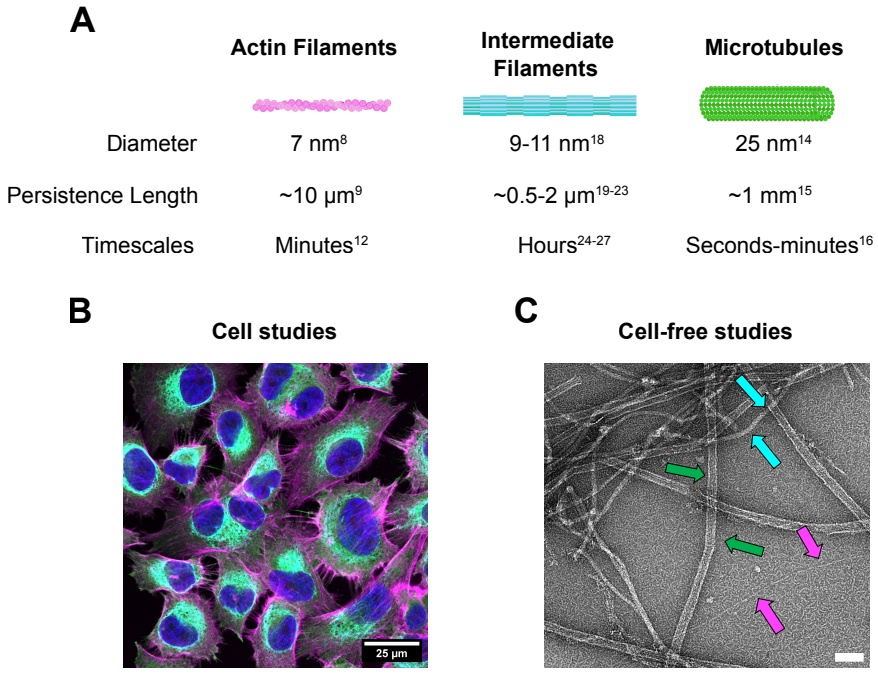

Figure 1.1: (a) Schematic of the three major cytoskeletal filament types and their distinctive physical properties. (b) Fluorescent confocal microscopy image of human melanoma (MV3) cells stained for α-tubulin (green), F-actin (magenta), and vimentin (cyan). The cell nuclei are shown in blue. (c) An electron microscopy image of an *in vitro* reconstituted three-component cytoskeletal network showing F-actin (magenta arrows), microtubules (green arrows) and vimentin (cyan arrows). Filaments were pre-polymerized separately at 1 μM. Actin and microtubules were polymerized in MRB0 buffer (80 mM PIPES pH 6.8, 1 mM EGTA and 4 mM $MgCl_2$) with 50 mM KCl, 1 mM DTT and 0.5 mM ATP, while vimentin was polymerized in V-buffer (40 mM PIPES pH 7, 1 mM EGTA and 4 mM $MgCl_2$, 100 mM KCl, 1 mM DTT). The filaments were combined in MRB80 buffer (with 50 mM KCl, 1 mM DTT and 0.5 mM ATP). Scale bar 100 nm.

1.3.1. LIVE-CELL STUDIES

Cells in the body experience a complex combination of tensile, compressive and shear deformations of varying amplitude and rate. The effect of these mechanical parameters on cell deformability has been extensively characterised using quantitative biophysical techniques. To study the viscoelastic properties of cells without the impact of cell adhesion, cells can be detached from their substrate and measured in suspension by micropipette aspiration [35], optical stretching [36], parallel-plate rheometers [37], or high-throughput microfluidic methods [38]. Whole-cell measurements of adherent cells can be done by monolayer rheology or stretching [39, 40, 41] or by single-cell atomic force microscopy [42, 43]. Localized measurements to resolve the mechanics of specific subcellular regions can be done by magnetic twisting cytometry [44], atomic force microscopy [45], optical or magnetic tweezers [46, 47], or particle tracking microrheology [48].

The actin cytoskeleton is often considered the main determinant of cell mechanics. Drug-induced depolymerization of actin filaments indeed significantly softens cells both under non-adherent and adherent conditions [49, 50]. An important contribution of the actin cytoskeleton to cell stiffness comes from contractile forces generated by actin-myosin stress fibers [51] and by the actin cortex [52]. Intermediate filaments form dense networks that are mainly perinuclear, so they contribute little to cortical stiffness but strongly affect the cytoplasmic shear modulus [53] and the resistance of cells to compression [43]. For leukocytes and tumor cells performing 3D migration, the intermediate filament cytoskeleton is a major determinant of cell deformability. Intermediate filament protein deletion or network disruption causes significant cell softening while at the same time enhancing cell migration [54, 55, 56, 57]. Microtubules generally do not contribute much to cell stiffness, with drugs that interfere with microtubule polymerization having minor effects on cell mechanics [58]. Recently, though, microtubules were shown to exhibit interesting mechano-responsive properties. Cytoskeletal compression induced by cyclic cell stretching or by confined migration was shown to stabilize deformed microtubules by triggering recruitment of the microtubule-binding protein CLASP2 [59]. When cells are transferred from rigid 2D substrates to softer 3D hydrogels, the mechanical contribution of microtubules becomes more important because actin stress fibers become less prominent. In cells migrating through collagen gels, microtubules for instance play a crucial role in mechanical support of cellular protrusions [60].

It remains an open question how the interactions between the three cytoskeletal biopolymers influence the mechanics of the composite cytoskeleton. Theoretical models predict that composite networks composed of interpenetrating networks of a rigid and a flexible polymer are substantially stiffer than expected from the sum of the moduli of the separate networks [61]. Rigid fiber networks by themselves are expected to be soft at low deformation because they deform in a non-affine manner, where the elasticity is governed by fiber bending [62]. The presence of a background network of flexible polymer suppresses these non-affine bending deformations [61]. Unfortunately this prediction is difficult to directly test in live-cell experiments because it is very challenging to specifically remove one cytoskeletal network without also affecting the others. Microtubule depolymerization is for instance well-known to activate actomyosin contraction by the release of the microtubule-associated guanine nucleotide exchange factor GEF-H1 [63]. At large strains, there is some evidence of mechanical synergy between the cytoskeletal networks. Epithelial cell layers are able to undergo extreme stretching under constant tension ('active superelasticity') by strain-softening of the actin cortex followed by re-stiffening thanks to the keratin intermediate filament network [64]. Physical crosslinking between actin and keratin is essential for the maintenance of epithelial stability [65]. The ability of flexible polymers to suppress bending deformations of rigid polymers has the interesting consequence that the rigid polymers are reinforced against compressive loads [66]. Under compressive loading, rigid polymers exhibit an Euler buckling instability at a critical compression force $f_c \sim 10\kappa/L^2$, where L is the polymer length. For microtubules, the critical compression force is only of order 1 pN [67]. In the cell, however, microtubules can bear 100-fold larger compression forces because the surrounding actin and intermediate filament

cytoskeleton constrains microtubule buckling [68, 69]. This is consistent with the so-called tensegrity model, which states that cellular shape stability is achieved via a balance between actin filaments and intermediate filaments loaded under tension, and microtubules and thick actin bundles under compression [70].

1.3.2. CELL-FREE STUDIES

Live-cell mechanical measurements can be difficult to interpret in quantitative terms because they are sensitive to the amplitude, type and rate of deformation, geometry of the mechanical probe, the probed location in the cell, and the cell's extracellular environment [71]. Cell-free studies provide a useful complement because they permit quantitative measurements of the mechanical properties of isolated cytoskeletal components, both at the single filament and at the network level.

At the single filament level, cytoskeletal biopolymers have been bent, stretched, compressed, and twisted using optical and magnetic tweezers [72, 73, 74, 75], atomic force microscopy [76, 77], and microfluidic devices [78]. Actin filaments and microtubules have a high bending and stretching rigidity, but they break at rather low tensile strains ($\sim$ 150% strains) [79, 80]. Moreover, actin filaments become more fragile under torsion [79] and microtubules soften upon repeated bending [78]. This fragility is likely related to the fact that actin filaments and microtubules are made of globular subunits. By contrast, intermediate filaments are made of fibrous subunits held together by extensive lateral interactions. Intermediate filaments easily stretch and bend due to their open structure and they can withstand tensile strains of more than 200% before rupture [76]. Similar to a car's safety belt, intermediate filaments are soft under small and slow deformations but stiff under large and fast deformations [72]. Recent evidence suggests that different intermediate filament proteins respond differently to tensile loads. When subjected to stretch-relax cycles, keratin filaments elongate with every cycle but keep the same stiffness, whereas vimentin filaments soften with every cycle but always return to the same initial length [81]. It appears that vimentin stretches by monomer unfolding [82], whereas keratin filaments stretch by viscous sliding of subunits [81]. It will be interesting to see what further diversity may be generated by co-polymerization of different intermediate filament proteins and by post-translational modifications.

On the network level, mechanical properties of cytoskeletal filaments are most conveniently probed by either bulk rheology or microrheology. In bulk rheology, cytoskeletal networks are sheared between the two parallel plates of a rheometer, providing a readout of the macroscopic viscoelastic response [83]. Microrheology instead probes the localized viscoelastic response of a material by tracking the motion of embedded probe particles, either in response to thermal fluctuations (passive microrheology [84]) or to a force applied by optical or magnetic tweezers (active microrheology [85]). The mechanical response of cytoskeletal networks is determined by an interplay of the stiffness of the filaments and their interactions.

Actin filaments and microtubules form entangled networks that easily fluidize under shear due to filament disentanglement [86, 87, 88]. Filament crosslinking via crosslinker proteins prevents this fluidization and causes the networks to strain-stiffen. This strain-stiffening response is only moderate for microtubules because of their high rigidity and

because shearing causes force-induced unbinding of crosslinks [86, 85]. Actin networks exhibit more pronounced strain-stiffening because their elasticity is affected by the entropic elastic response of the filaments to tensile loading [89]. Tensile loading reduces the conformational entropy of actin filaments, pulling out bending fluctuations, causing entropic strain-stiffening [90]. Increased crosslink densities shift the onset of strain-stiffening to smaller shear strains because less excess length is stored in bending fluctuations when the crosslinks are more closely spaced [89]. Some crosslinker proteins (most notably filamin) are so large that their compliance directly contributes to the network response. Crosslinker extensibility increases the rupture strain by postponing the point where the actin filaments experience tensile loading [91, 92]. Bundling of actin filaments, which is common at high concentrations of crosslinker proteins, suppresses entropic elasticity. Bundled actin networks still strain-stiffen [89], but by an enthalpic mechanism that involves a transition from soft bending modes at low strains to rigid stretching modes at high strain [93, 94]. Under compression, actin and microtubule networks soften due to filament buckling [43]. For branched actin networks, compressive softening has been shown to be reversible, likely because the buckled filaments are prevented from collapsing by their connections with the network [95].

The mechanical properties of intermediate filament networks differ in various respects from those of actin and microtubule networks. First, intermediate filaments form strain-stiffening networks even in absence of any crosslinker proteins, as demonstrated for vimentin, neurofilaments, desmin, and keratin [96, 97]. The filaments spontaneously form crosslinks mediated by electrostatic interactions between their disordered C- terminal tails. Upon tail truncation, the networks no longer strain-stiffen [98, 99, 100]. The effective crosslink density depends on the concentration of divalent cations such Mg^{2+}, Ca^{2+} or Zn^{2+} [98, 97, 101, 102] and is sensitive to the buffer ionic strength and pH [103]. For keratins, there are additional hydrophobic interactions between the central rod domains that stiffen the networks [28]. Second, intermediate filament networks have much larger rupture strains than actin and microtubule networks as a consequence of the larger single-filament extensibility. This is reflected in the dependence of the elastic modulus K on the applied shear stress σ. While actin networks only exhibit an entropic strain-stiffening regime where K increases as $\sigma^{\frac{3}{2}}$, intermediate filament networks exhibit an additional enthalpic regime where K increases more weakly, reflecting strain-induced filament alignment [96]. After yielding, intermediate filament networks can even recover their initial shear modulus, likely by the re-establishment of tail-tail crosslinks [104, 99].

Recently there has been increasing attention for the mechanical properties of cytoskeletal composites. Reconstitution of composite networks requires careful tuning of the buffer conditions since the different cytoskeletal polymers are traditionally reconstituted in their own optimized buffer conditions. Intermediate filaments are especially sensitive to solution pH and ionic concentrations, forming filaments of different widths and protein mass-per-length ratios depending on the buffer [105]. Until now nearly all studies of composite networks have focused on two-component composites of cytoskeletal filaments co-polymerized in the absence of crosslinkers. At small strains, co-entangled composites (specifically combinations of actin/vimentin [106], actin/keratin [107, 108], actin/microtubules [109], and vimentin/microtubules [110]) have generally

been shown to exhibit a simple additive viscoelastic response. However, there is evidence for direct interactions of vimentin filaments with actin filaments [111] as well as microtubules [112], which could potentially influence the network rheology. These interactions could potentially lead to cell-type specific cytoskeletal crosstalk, since they are mediated by the C-terminal tail of intermediate filaments that shows large length and sequence variations between different intermediate filament proteins. It was furthermore shown that vimentin can impose steric constraints that hamper actin network formation and thus cause network weakening [113]. At large strains, there is evidence of synergistic enhancement of the mechanical properties in certain cytoskeletal composites. For actin/keratin composites, the strong strain-stiffening response of the keratin network was found to dominate the high-strain response of the composites [108]. For actin/microtubule composites, microtubules were shown to promote strain-stiffening of the actin networks, even at low density [114, 115]. This effect was explained by the ability of rigid microtubules to suppress nonaffine bending fluctuations of actin filaments. It will be interesting to explore how these synergies are modified in the presence of crosslinkers. Recent work showed that when actin filaments and microtubules are crosslinked to each other by biotin-streptavidin, the composite is more elastic than when both filaments are independently crosslinked [116].

To the best of our knowledge, there has so far been only one study of three-component networks combining actin, vimentin and microtubules [117]. It was shown by microrheology that the linear elastic modulus of the composite is dominated by actin, with little contribution from either microtubules or vimentin. Yet vimentin was shown to significantly extend the elastic regime to longer timescales. The authors proposed that the vimentin network fills in the pore spaces of the actin network and slows stress relaxation by constraining actin reptation [118]. More work is needed to systematically study cytoskeletal composites and to explore the impact of crosslinking with cytolinker proteins such as plectin. Due to their high molecular weight these proteins are difficult to purify. To circumvent this problem, one can engineer proteins that contain only the cytoskeletal binding domains separated by a spacer [119]. Using this approach, the Biological Soft Matter group recently found that crosslinking with a plectin-mimetic crosslinker causes synergistic stiffening of actin-vimentin composites [120].

1.4. THE CYTOSKELETON AND CELL CONTRACTILITY

While the previous section focused on how the cytoskeleton enables cells to deform in response to external forces, we now turn to the ability of cells to generate forces internally. This contractile behaviour, driven largely by the actomyosin cytoskeleton, plays a central role in shaping cell mechanics and underpins many essential processes, including migration, division, and morphogenesis. In this section, we review the physical basis of cell contractility in mammalian cells and highlight how insights from *in vitro* reconstitution have helped identify the minimal requirements for active force generation.

1.4.1. LIVE-CELL STUDIES

The actin cytoskeleton is the engine behind cell contractility, which is most commonly studied in the context of single-cell migration, where contractile forces are critical for driving movement and shape changes [121]. Depending on the extracellular environment, cells can switch between different mechanisms that use actin-based forces in different ways[122]. Fibroblasts and other adherent cells perform *mesenchymal migration*, which relies on integrin-based adhesion to the extracellular matrix (ECM). The process occurs via a four-step cycle. First, actin polymerization pushes against the membrane at the leading edge, producing lamellipodia in cells migrating on flat rigid surfaces or pseudopodia in cells migrating in 3D extracellular matrices. Next, the cell generates integrin-based adhesions with the substrate that connect to the contractile machinery of acto-myosin stress fibres. Through a combination of pulling from the front and squeezing from the rear, the cell body moves forward. Finally, old adhesions are detached from the substrate or dissolved at the trailing edge [123]. The contractile forces involved in cell migration have been measured through the traction forces exerted on the substrate. This is usually done by adhering cells to a hydrogel substrate with known mechanical properties, such as polyacrylamide. By measuring the displacements of fluorescent tracer particles incorporated in the gel with fluorescence microscopy, one can computationally infer the traction forces using continuum mechanics models [124]. Adherent cells that experience strong confinement utilize a *nuclear piston* mechanism where actin-myosin contraction in front of the nucleus pulls the nucleus forward. Since the nucleus divides the cell in forward and rearward compartments, it acts as a piston that pressurizes the forward compartment and drives forward a cylindrical lobopodial protrusion [125]. Weakly adherent cells such as leukocytes and physically confined fibroblasts and cancer cells perform *amoeboid migration*, characterized by spherical membrane blebs at the leading edge (reviewed in [126]). Blebs are created by myosin-driven contraction of the actin cortex underneath the cell membrane, which builds up hydrostatic pressure in the cytoplasm. Local rupture of the actin cortex or its attachment to the membrane causes local membrane delamination, pushing forward a membrane bleb. Over time the actin cortex regrows under the bleb membrane and myosin contraction drives bleb retraction. Confinement can also induce other migration modes that require little substrate adhesion. Cells can move via friction generated by actin flows within the cortex generated by myosin contraction and actin turnover [127], and some tumour cells can still migrate by using active transport of water from the front to the back of the cell to propel themselves forward (*osmotic engine* model [128]).

While not being components of the contractile machinery, both microtubules and intermediate filaments are important for regulating cell contraction. Microtubules negatively regulate the assembly and contractility of actin stress fibers by sequestering GEF-H1, an activator of the small GTPase Rho, in an autoinhibited state [129]. Microtubule depolymerization by nocodazole releases active GEF-H1, leading to a global increase of contractility as measured by traction force microscopy [130]. During both mesenchymal and amoeboid migration, microtubule depolymerization and consequent GEF-H1 is tightly regulated so that actin contractility can be precisely timed and localized in a mechanosensitive manner [131, 132, 133]. Besides biochemical regulation, it is likely that mechanical synergy is also involved in microtubule-based control of actin contrac-

tility, since microtubules are able to absorb some of the forces from the contractile actin cytoskeleton [70].

Intermediate filaments likewise regulate actin-based cell contraction by a combination of mechanical synergy and biochemical signaling. In cells migrating on flat surfaces, vimentin has been reported to inhibit stress fiber assembly and contractility through down-regulating GEF-H1 and RhoA [134]. Nevertheless, traction force measurements have shown that vimentin-null cells are less contractile than their wild-type counterparts [118]. Taken together with the observation that vimentin filaments orient traction stresses along the front-rear axis, this suggests a mechanical synergy where vimentin helps build up and transmit larger contractile forces [135]. Recently it was shown by structured illumination microscopy and electron microscopy that vimentin filaments are closely associated with actin stress fibers, forming meshworks that wrap around stress fibers or co-align with them [118, 136]. Physical coupling between the two systems is dependent on the cytolinker protein plectin [137]. Interestingly, it was recently shown that plectin binds vimentin in response to acto-myosin pulling forces [138]. The mechanism for this mechanosensitivity is unknown but could involve catch bonding[139]. Plectin-mediated coupling of actin and vimentin was recently shown to be essential for cells migrating via the nuclear piston mechanism [138]. The vimentin network helps transmit acto-myosin pulling forces to the nucleus, thus enhancing the pressure in the front of the nucleus. It is not yet known whether intermediate filaments also influence cell migration modes driven by contractile activity of the actin cortex, but recent observations that vimentin and F-actin are associated within the cell cortex suggest this is likely [118].

1.4.2. CELL-FREE STUDIES

There is an extensive body of work using cell-free reconstitution to elucidate the mechanisms by which myosin II motor proteins contract actin networks (reviewed in [140]). The contraction mechanism has been found to depend on the actin network connectivity, which is controlled by filament length and by crosslinking. Well-connected networks of long filaments contract because myosins generate compressive stress that causes the actin filaments to buckle and break [141]. By contrast, when the filaments are short, myosins contract the network by polarity sorting, transporting and clustering actin filament plus ends to form polar actin asters [142]. In both cases, the length scale of contraction is set by the network connectivity. Global network contraction requires the actin network to be crosslinked above a critical percolation threshold [143]. However, excessive crosslinking will prevent contraction by making the network too rigid [144]. As described above, several cell migration mechanisms rely on myosin-driven contraction of the actin cortex. Recently several groups have been able to reconstitute biomimetic actin cortices by co-encapsulating actin and myosin inside cell-sized lipid vesicles. For weak actin-membrane attachment, the network detaches from the membrane upon contraction [145]. In case of stronger attachment, myosin contraction can cause membrane blebbing [146]. Cortical flows that are important for driving amoeboid migration require not only myosin activity, but also network remodelling through actin depolymerization [147]. Under particular conditions, crosslinked actin-myosin cortical networks in emulsion droplets have been observed to exhibit cortical flows [148], likely because

myosin can promote actin turnover [149]. Cell extracts, which contain additional proteins to promote actin turnover, also exhibit cortical flows when encapsulated in emulsion droplets [150, 151, 152]. When these droplets are confined, the myosin-driven cortical flows can propel the droplets forward due to friction with the channel walls, mimicking amoeboid migration of nonadhesive cells [153].

So far only few studies have looked at the effect of intermediate filaments or microtubules on contraction of actin-myosin networks. The addition of a vimentin network that interpenetrates an actin network has been shown to promote myosin-driven contraction by increasing the network connectivity [117]. Similarly, also the addition of microtubules has been shown to promote uniform macroscopic myosin-driven contraction [154].

1.5. OUTLINE OF THIS THESIS

Having reviewed the current understanding of how cytoskeletal components and their interactions give rise to cellular mechanics, we now turn to the central questions addressed in this thesis. By combining experimental approaches with a physics perspective, we seek to dissect how these fundamental building blocks contribute to the mechanical integrity of living cells. The aim of this thesis was to determine how each component of the cytoskeleton contributes to cell mechanics, and how they team up through their interactions to make cells strong. In this thesis, we build up complexity by first examining the individual contributions of actin and vimentin to cell mechanics, then exploring the crosslinking between them, before zooming back out to investigate how the cytoskeletal networks respond to different modes of deformation, specifically compression versus shear.

In **Chapter 2**, we investigate the distinct mechanical roles of actin and vimentin in cellular responses to uniaxial compression using a custom-designed single-cell rheometer. Using mouse embryonic fibroblasts (MEFs) derived from both wild type (WT) and vimentin knockout (vim -/-) mice, along with chemical treatments to modulate actin polymerisation and contractility, we dissect the contributions of each cytoskeletal component. Small amplitude oscillatory tests and strain ramp experiments reveal that vimentin, until recently overlooked in studies of cellular mechanics, contributes as significantly as actin to maintaining cell stiffness and resisting compressive stress. In contrast, actin plays a more prominent role in regulating energy dissipation. Finally, by comparing intact and enucleated cells, we demonstrate that compression stiffening originates primarily from the actin and vimentin cytoskeleton, while the nucleus appears to play a minimal role. The findings from this chapter provided initial hints into how cytoskeletal networks work together to define the viscoelastic and nonlinear mechanical behaviour of cells, offering a foundation for understanding how cells resist both external and internal mechanical forces.

Following up on the hints of cytoskeletal crosstalk identified in Chapter 2, we then turned our attention in **Chapter 3** to the interplay between actin and vimentin. To investigate how this interaction is coordinated and mechanically integrated, we focused on plectin, a large cytolinker protein of the plakin family that physically connects dif-

ferent cytoskeletal systems within mammalian cells. It is ubiquitously expressed across tissues, and its dysfunction has been implicated in a range of diseases, including skin blistering disorders. While plectin is known to contribute to the mechanical integrity of cells and tissues, how it modulates cellular mechanics across different frequencies and amplitudes of deformation remains poorly understood. In this chapter, we used the same quantitative single-cell compression apparatus used in Chapter 2 to assess the role of plectin in the viscoelastic behaviour of fibroblasts across both small and large deformations. By comparing wild type and plectin knockout fibroblasts, we found that loss of plectin results in cells that are nearly twice as soft, although their strain-stiffening response remains largely unchanged. At long timescales, viscoelastic stress relaxation was faster in plectin-deficient cells, which we traced to a threefold increase in actin turnover, as measured by fluorescence recovery after photobleaching. We also observed faster poroelastic relaxation at short times, consistent with a sparser cytoskeletal network. Confocal imaging revealed a marked architectural shift in the vimentin network, from a fine, interconnected meshwork in wild type cells to prominent bundles in plectin knockout cells. Together, the findings from this chapter demonstrate that plectin is a key regulator of cytoskeletal organisation and viscoelastic response in fibroblasts, highlighting the importance of cytoskeletal integration in shaping the mechanical versatility of cells.

Having established the mechanical importance of plectin in integrating the actin and vimentin networks, in **Chapter 4** we further dissected its distinct mechanical roles. Plectin not only crosslinks cytoskeletal components, but also anchors the vimentin network to intracellular structures, including the nucleus. This dual functionality makes it challenging to disentangle its specific contributions to cellular mechanics and architecture. To address this, we introduced an engineered actin–vimentin crosslinker in plectin-deficient cells that mimics the structural coupling function of plectin, but lacks its anchoring capability. Using several mechanical assays including whole-cell compression as in Chapters 2 and 3, we found that this synthetic crosslinker was sufficient to fully restore the mechanical properties of plectin-deficient cells, indicating that the crosslinking role of plectin is key for maintaining viscoelastic integrity. However, the anchoring function proved essential for preserving nuclear morphology and sustaining traction force generation. The results from this chapter underscore the functional modularity of plectin and highlight how its distinct interactions enable cells to coordinate mechanical responses across the cytoskeleton and nucleus.

In **Chapter 5**, we return our focus to the actin and vimentin cytoskeletal networks, this time examining how cells respond to shear forces rather than compression. While much of cellular mechanics research has centred on compressive deformation, cells within tissues are routinely exposed to a variety of mechanical environments, including shear stress. It remains unclear how cytoskeletal networks, which are highly anisotropic and dynamic, respond to different modes of deformation. To address this, we modified the single-cell shear rheometer used in the previous chapters to investigate the nonlinear viscoelastic response of cells under simple shear. Using mouse embryonic fibroblasts (MEFs) derived from wild type (WT) and vimentin knockout (vim -/-) mice, in combination with pharmacological inhibition of actin polymerisation, we disentangled the contributions of actin and vimentin to shear mechanics. Strain ramp tests re-

vealed that cells exhibit a pronounced shear-softening behaviour primarily governed by the actin network. In contrast, vimentin shear-stiffened and dominated cell stiffness at large shear strains. The shear-softening response of the cells stood in stark contrast to the compression-stiffening observed in earlier chapters. To reconcile this difference, we considered the nature of internal filament strains under different loading modes: at equivalent macroscopic strain levels, cytoskeletal filaments are subject to greater tensile deformation under shear than under compression. We propose that the large tensile strains experienced under shear lead to cell softening by inducing rupture of crosslinks or actin filaments, while the more resilient vimentin network remains intact, facilitating mechanical recovery. The findings from this chapter deepen our understanding of how cytoskeletal components behave as a composite material under varying mechanical loads, and underscore the importance of loading direction in determining cellular mechanical response. They also reinforce the idea that the mechanical resilience of cells arises from the interplay between structurally and mechanically distinct cytoskeletal elements.

In **Chapter 6**, we shift focus from the role of specific cytoskeletal components to the broader methodological considerations involved in measuring cellular mechanics. Atomic force microscopy (AFM) is a widely used technique for probing the local mechanical properties of soft materials, including mammalian cells. While AFM has yielded rich insights into cell elasticity, a recurring observation is that elasticity values often appear to follow a log-normal distribution. However, the origin of this apparent non-normality has remained unresolved. In this chapter, we demonstrate that the shape of the observed distribution does not necessarily arise from intrinsic biological variability, but rather from the method used to analyse force–indentation curves. These findings highlight the importance of methodological rigour in interpreting mechanical measurements and call for greater care in the choice of analysis parameters. By clarifying the origins of commonly reported variability, this work contributes to a more accurate and reproducible understanding of cellular mechanical properties.

Finally, in **Chapter 7** we present an outlook where we summarise the main findings of this thesis and offer our perspective on bridging insights from cell-based studies and *in vitro* reconstitution work to address the open questions surrounding how the cytoskeleton and cytoskeletal crosstalk contribute to cellular mechanical strength. We conclude by offering an opinion on the future of cell mechanics studies.

1.6. ACKNOWLEDGEMENTS

We gratefully acknowledge funding from the VICI project *How cytoskeletal teamwork makes cells strong* (project number VI.C.182.004) and from the OCENW.GROOT.20t9.O22 project *The Active Matter Physics of Collective Metastasis*, both financed by the Dutch Research Council (NWO).

2

ACTIN AND VIMENTIN JOINTLY CONTROL CELL VISCOELASTICITY AND COMPRESSION STIFFENING

The mechanical properties of cells are governed by the cytoskeleton, a dynamic network of actin filaments, intermediate filaments, and microtubules. Understanding the individual and collective mechanical contributions of these three different cytoskeletal elements is essential to elucidate how cells maintain mechanical integrity during deformation. Here we use a custom single-cell rheometer to identify the distinct contributions of actin and vimentin to the viscoelastic and nonlinear elastic response of cells to uniaxial compression. We used mouse embryonic fibroblasts (MEFs) isolated from wild type (WT) and vimentin knockout (vim -/-) mice in combination with chemical treatments to manipulate actin polymerization and contractility. We show through small amplitude oscillatory measurements and strain ramp tests that vimentin, often overlooked in cellular mechanics, plays a role comparable to actin in maintaining cell stiffness and resisting large compressive forces. However, actin appears to be more important than vimentin in determining cellular energy dissipation. Finally we show by comparing wild type and enucleated cells that compression stiffening originates from the actin and vimentin cytoskeleton, while the nucleus appears to play little role in this. Our findings provide insight into how cytoskeletal networks collectively determine the mechanical properties of cells, providing a basis to understand the role of the cytoskeleton in the ability of cells to resist external as well as internal forces.

This chapter is published in *Molecular Biology of the Cell.* The paper was co-authored by **J .P. Conboy** M. G Lettinga, P. E. Boukany, F. C. MacKintosh and G. H. Koenderink.

2.1. INTRODUCTION

In multicellular organisms, cells are continuously exposed to different physical stresses. In some tissues and organs, cells are constantly subject to stretching (e.g. the heart, lungs and skin), while in others they are subject to compression (e.g. joints and the spine) [155]. Cells can also actively generate forces to deform themselves, for instance during migration, which exposes cells to a complex combination of shear, tensile and compressive forces [156]. Furthermore, cells are able to stress-stiffen in response to mechanical stimuli [12]. In mammalian cells, the building blocks responsible for generating and responding to mechanical stress are the nucleus [157] and the cytoskeleton, a biopolymer scaffold comprised of three distinct components: actin, microtubules and intermediate filaments [158].

In animal cells, filamentous actin is primarily located in the cell cortex, a dense meshwork that lines the plasma membrane, and in stress fibers, linear arrays of actin filaments that span the length of a cell [159]. In conjunction with myosin motor proteins, both the actin cortex and actin stress fibers are capable of generating contractile forces, termed cellular prestress, which has been shown to modulate cell stiffness [20]. Intermediate filaments are a large family of proteins expressed in a tissue-specific manner. The two most extensively researched intermediate filaments are keratin, which is found in non-motile epithelial cells, and vimentin, which is present in motile mesenchymal cells [160]. In mesenchymal cells, such as fibroblasts, vimentin intermediate filaments organize into a cage-like structure that envelops the nucleus and radiates outward towards the cell membrane [161]. Vimentin has been likened to a 'cellular safety belt' that protects cells against large mechanical strains [162]. Microtubules also form a cell-spanning network [163], but due to their limited abundance in the cell and their prevalence mainly as isolated filaments, they do not significantly contribute to whole-cell stiffness [37].

Understanding the relative contributions of actin and vimentin to cell rheology, as well as the potential mechanical synergy between these cytoskeletal networks, has long been a challenging question. Although actin and vimentin are widely recognized as key players in determining the cell's mechanical response to external stress, precisely how each network contributes to cell elasticity and energy dissipation remains unclear. Previous studies have demonstrated that both actin [164] and vimentin [53] are integral to the material properties of cells, but their specific roles and interplay in these mechanical behaviors are yet to be fully understood.

Probing a cell's mechanics at the nanometer to the micrometer scale has been performed via a plethora of techniques including optical tweezers [4, 5], atomic force microscopy [6], magnetic twisting cytometry [7] and particle tracking microrheology [8, 9, 10]. However, these localized techniques probe either mainly actin or mainly intermediate filaments, rather than their combined response. For example, mechanical measurements obtained from magnetic twisting cytometry are dominated by actin rather than vimentin because deformations are applied to the cell membrane, where the actin cortex provides the primary mechanical resistance [165, 53]. Generally, due to the highly heterogeneous intracellular environment, it is difficult to extrapolate these microrheological results to a whole-cell mechanical response. Furthermore these local measure-

ment techniques are often limited to small nanometer scale deformations, whereas cells in the body can experience rather large deformations. For instance, lung tissue cells are subjected to large cyclical forces from breathing. To access the large deformation regime, single-cell stretching and compression assays have previously been developed, where cells are either suspended between adhesive [11, 12] or non-adhesive [13] parallel plates. However, these studies for the most part ignored the role of intermediate filaments in the cell's mechanical response to large strain deformations. Intriguing recent work indicates that intermediate filaments provide a major contribution to the mechanical response of cells under large compressive strains [166]. This is consistent with observations from cell-free reconstitution experiments, which have shown that networks of intermediate filaments can carry much larger strains and exhibit more pronounced strain-stiffening than actin networks [167, 99].

Here, we dissect the contributions of the actin and vimentin cytoskeletal networks to the nonlinear mechanical behavior of single fibroblasts by means of uniaxial compression rheology experiments on single fibroblasts confined between two nonadhesive parallel plates, a deliberate design choice to isolate the intrinsic contributions of the cytoskeleton independent of adhesion-mediated effects. To quantify the relative contributions of the two cytoskeletal networks, we used mouse embryonic fibroblasts isolated from wild type (WT) and vimentin knockout (vim -/-) mice in combination with drugs to influence actin polymerization (cytochalasin D) and contractility (blebbistatin). We show through small amplitude oscillatory measurements that the actin and vimentin networks equally contribute to total cell stiffness. However, actin plays a larger role than vimentin in determining cellular energy dissipation. Furthermore, we show that the strain-stiffening behaviour of cells arises from the actin and vimentin cytoskeleton rather than from the nucleus.

2.2. RESULTS

2.2.1. FREQUENCY-DEPENDENT RHEOLOGY OF SINGLE MOUSE EMBRYONIC FIBROBLASTS

To quantify the macroscopic viscoelastic properties of single cells, we established a single cell rheometer assay for dynamic mechanical analysis on cells suspended between two parallel surfaces (Figure 2.1 A, top). Using an optical fiber with a wedge, we apply an oscillatory compressive strain of defined amplitude and frequency and measure the concomitant stress, which is used to calculate the frequency-dependent complex *apparent* Young's modulus, $E^*(f)$ (Figure 2.1 A, bottom). In these measurements, we separate the mechanical response into an elastic modulus, describing how much energy the cell can store and release when deformed, and a viscous modulus, describing how much energy is lost or dissipated during deformation. See Supplementary Figure S2.6 for details on inferring the energy dissipated per cycle of oscillation from frequency-sweep experiments. We first validated the setup by benchmarking the system with polyacrylamide (PAA) microgels, which we used as a cell-sized proxy with well-characterized rheological properties [168] (Figure 2.1 B, top). Our experiments showed that the elastic (storage) modulus,

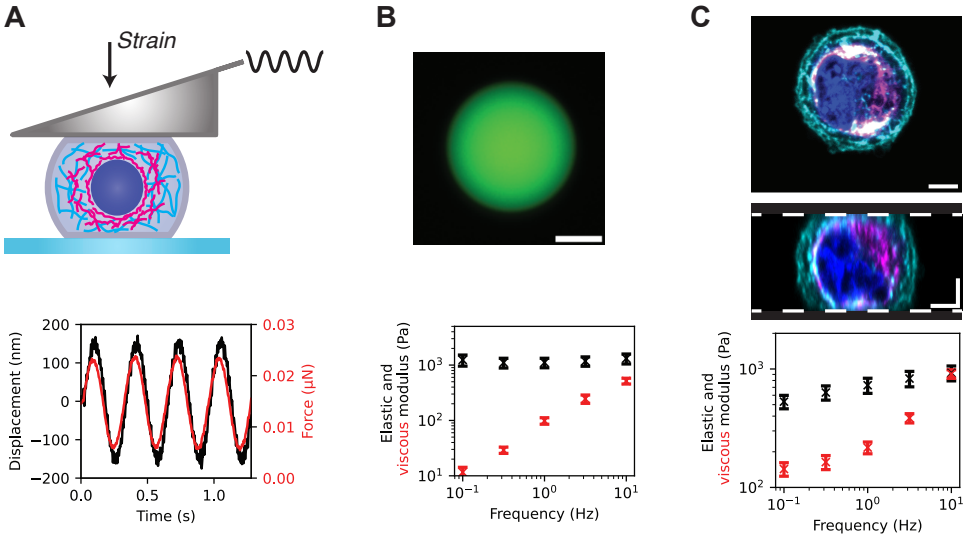

Figure 2.1: Oscillatory compression measurements of the linear viscoelastic properties of mouse embryonic fibroblasts (MEFs). (A) Top: schematic of a single MEF cell sandwiched between a glass coverslip and wedged flexible cantilever. We focus on the mechanical contributions of the actin cytoskeleton (cyan), vimentin cytoskeleton (magenta), and nucleus (dark blue). Bottom: representative measurement at an oscillation frequency of 0.32 Hz, showing the applied displacement of the cantilever (black; left y-axis) and observed force (red; right y-axis) as a function of time. (B) Top: epifluorescence image of a spherical polyacrylamide microgel used as a cell-sized analogue for benchmarking the setup. Scale bar: 20 m. Bottom: Frequency-dependent elastic and viscous moduli (black and red symbols, respectively) of polyacrylamide microgels (average for N=8). (C) Single confocal slice through the equator (top) and orthogonal projection through the centre (middle) of a live MEF cell confined between two coverslips (indicated by white dashed lines) obtained by confocal fluorescence imaging. SiR-labeled actin (cyan) is largely located at the cortex while vimentin-GFP (magenta) forms a cage around the nucleus (dark blue). Bottom: frequency-dependent elastic and viscous moduli (black and red symbols, respectively) of MEF cells (average for N=16). Scale bars: 5μm.

E', of the microgels was constant between 0.1-10 Hz, and the viscous (loss) modulus, E'', increased with the frequency of the applied strain (Figure 2.1 B, bottom), consistent with the predominantly elastic behavior of PAA as measured with bulk rheometry and atomic force microscopy [168].

We next performed similar measurements on mouse embryonic fibroblasts (MEFs). In contrast to the microgels, the cells behaved as viscoelastic solids with a power law dependence of E' on frequency (Figure 2.1 C). At the highest frequency of 10 Hz, E' and E'' crossed, indicating that the cell transitioned to a viscoelastic liquid response. This type of power law dependence is a well-established phenomenological behavior of mammalian cells [169].

2.2.2. ACTIN AND VIMENTIN BOTH CONTRIBUTE TO BULK CELL VISCOELASTICITY

To understand the contributions of actin and vimentin to cell mechanics, we first used confocal microscopy to examine the organization of the two networks in the wild type (WT) MEF cells. As shown in Figure 2.1C, the cells are quasi-spherical with a radially uniform distribution of actin and vimentin. We therefore performed live cell imaging on WT, WT cells drugged with cytochalasin D, and vim -/- cells to characterize the organization of the cytoskeleton (Fig. 2.2 A). Filamentous actin is largely located at the cell periphery lining the plasma membrane as expected, but also extends to the interior of the cell. By contrast, vimentin is located in between actin and the nucleus. However, the radial profiles of actin and vimentin signals show that there is also a significant overlapping region where both actin and vimentin are localized. To analyze this for many cells, we generated average radial profiles, rescaling each cell to correct for differences in cell size (Fig. 2.2 B). We observed that the average profiles resembled those of individual cells.

Next, to isolate the individual contributions of actin and vimentin to the mechanical response of the MEF cells, we set up experiments where we removed either F-actin or vimentin. To remove F-actin, we treated the WT cells with cytochalasin D [170]. As shown in the averaged confocal images and radial intensity profiles in Figure 2.2 (middle row), there is a remaining filamentous actin signal after cytochalasin D treatment, but this signal is diffuse and less strongly located at the cortex than in WT cells. We do not observe any striking change in the localization of the vimentin network upon cytochalasin D treatment. To remove the contribution of vimentin, we turned to vim -/- MEFs that are genetically depleted of vimentin [171]. As shown in the images and radial intensity profiles in Figure 2.2 (bottom row), the cells are indeed completely devoid of vimentin while the actin network appears somewhat more confined close to the membrane compared with WT cells.

To quantify the relative contributions of actin and vimentin to single cell viscoelasticity, we compared compression measurements on the wild type cells, cytochalasin D treated cells, and the vim -/- cells. As shown in Fig. 2.3A, the viscoelastic moduli significantly decreased both upon drug-induced depolymerization of actin and upon knocking out vimentin. In order to make a quantitative comparison, we chose to model the complex modulus with the structural damping law, a well-known phenomenological model of cell rheology [172, 173, 174]. To separate out the contribution of the cytoplasm, we included an additive Newtonian viscous damping term:

$$E^*(f) = E_0 c(\alpha)(1 + i\eta(\alpha))(f/f_0)^\alpha + i\mu f. \tag{2.1}$$

Here, E_0 is a scaling factor for the elastic and viscous moduli at a frequency scale factor f_0 (which we arbitrarily set to 1 Hz), $c(\alpha)$ is $\Gamma(1-\alpha)\cos(\pi\alpha/2)$ where Γ denotes the gamma function, $\eta = \tan(\pi\alpha/2)$ is the structural damping coefficient, α is the power law exponent and μ is the Newtonian viscous term. The great advantage of this model is its ability to reduce the frequency-dependent measurements to three parameters (E_0, α and μ), which provide a mechanical fingerprint to allow comparisons between different conditions. Importantly, the structural damping law provides a self-consistent fit

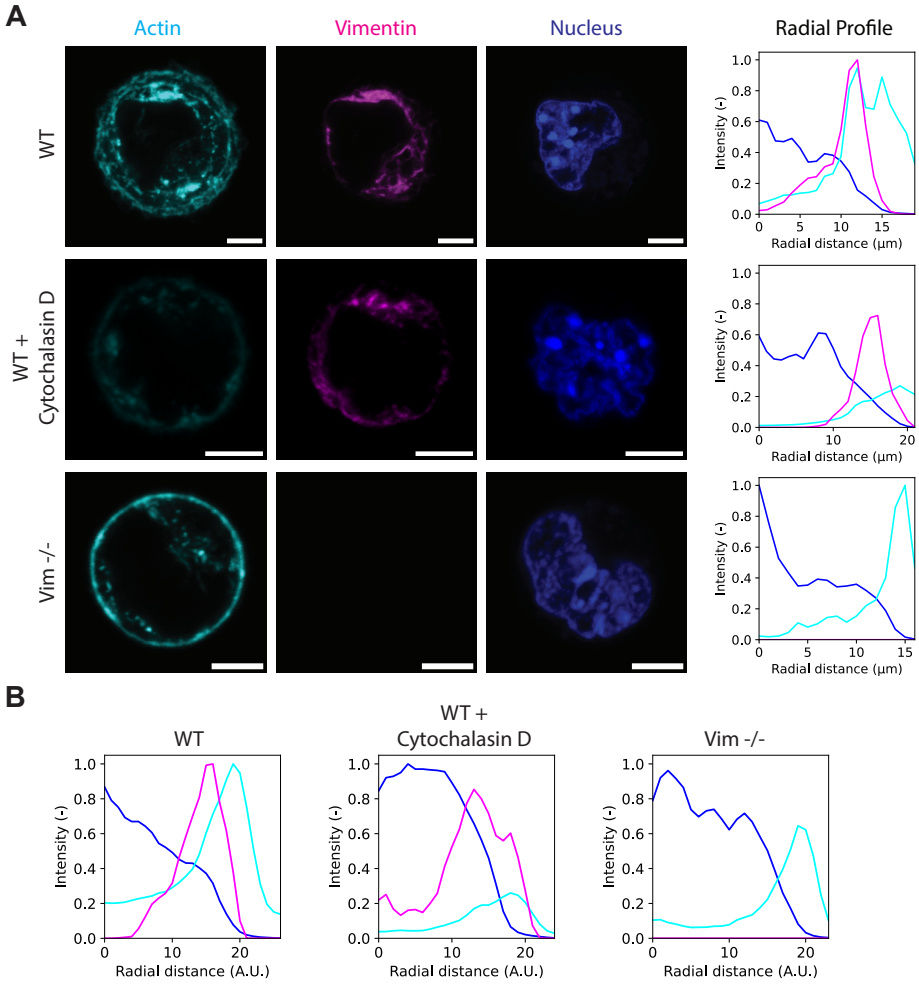

Figure 2.2: (A) Representative confocal images of WT cells (top), WT cells drugged with cytochalasin D (middle), and vim -/- cells (bottom). For all conditions, filamentous actin (cyan) is located largely at the cell periphery and vimentin (magenta) is located closer to the center of the cell and surrounds the nucleus (dark blue). Average radial profiles of the fluorescent signals (right) were calculated by taking normalized intensities around concentric circles from the center of the image. The radial distance is set to zero at the cell center. We observe a significant overlapping region between actin and vimentin. Scale bars 10μm. (B) Average actin (magenta), vimentin (cyan) and nuclear (dark blue) radial profiles in WT MEF cells (left), WT cells drugged with cytochalasin D (middle), and vim -/- cells (right), averaged over multiple cells (N=12 cells for each condition). As we rescale cells to compensate for different cell sizes, scale bar not applicable (see Methods for details). Averaged profiles resembled those of individual cells.

of E' and E'' to the real and imaginary parts of the complex modulus (lines in Figure 2.3A). This choice is consistent with a fractional rheological framework inspired by recent work [174], which can be thought of as a springpot in parallel with a Newtonian dashpot, where the springpot (set by E_0 and α) captures cytoskeletal viscoelasticity and the dashpot (μ) represents cytoplasmic solvent damping (Figure 2.3 A inset), thereby linking the phenomenological fit to an intuitive mechanical picture.

We find that the scaling factor E_0 decreases from 505 ± 70 Pa for wild type cells to $E_0 = 130 \pm 30$ Pa for cells drugged with cytochalasin D and $E_0 = 196 \pm 30$ Pa for vimentin -/- cells (see Fig. 2.3B left). This finding demonstrates that both actin and vimentin contribute to the bulk elasticity of the cell. Interestingly, if one were to model the E_0 value for WT cells as the sum of two independent elastic contributions from the actin and vimentin cytoskeletal networks by adding the E_0 values we measured for the cytochalasin-D treated cells and the vimentin -/- cells, one obtains a value (326 Pa) that is significantly less than the value measured for wild type cells. This suggests a mechanical crosstalk between the two networks. At the same time, the power law exponent α increased from $\alpha = 0.112 \pm 0.005$ for wild type cells to $\alpha = 0.30 \pm 0.06$ for actin-depolymerized cells. However, for vimentin -/- cells, we observed no significant change in α value (0.20 ± 0.04) as compared to wild type cells (see Fig. 2.3B middle). The measured exponents reveal viscoelastic behavior, being in between the limits of an ideal solid ($\alpha = 0$) and an ideal fluid ($\alpha = 1$). Depolymerization of actin causes the cells to become more fluid-like, indicating that actin is more important than vimentin in controlling energy dissipation. Finally, the Newtonian viscous damping term μ remained invariant for all cell perturbations (Fig. 2.3B right). In an attempt to further probe the interplay between the two networks, we depolymerized actin in vimentin -/- cells but found that these cells were too soft to permit reliable oscillatory measurements. To verify previous findings that microtubules contribute minimally to cell stiffness under compression [37], we treated cells with nocodazole to depolymerize microtubules and observed no measurable change in the value of E_0 (Supplementary Figure S2.7). This supports earlier conclusions and justifies our focus on actin and vimentin as the dominant contributors to the cell's mechanical response in our experiments.

2.2.3. STRAIN RAMP EXPERIMENTS TO CHARACTERIZE THE NONLINEAR ELASTICITY OF MEF CELLS

Next, we sought to determine whether the stiffness of the cells changes with increasing compression. We applied a uniaxial compression where we steadily increased the strain from zero to ~50% at a fixed deformation rate of 1 μm/s (Figure 2.4A). We selected this rate to minimize potential viscous effects and ensure that the cell's mechanical response remained primarily elastic. We limited the compressive strain to 50% because we observed that cells could tolerate repeated straining up to this point without any visible damage or changes in mechanics (Supplementary Video 1). By contrast, cells often forms blebs indicative of loss of viability at strains when we compressed them beyond this point (see Supplementary Video 2).

We first benchmarked the assay by compressing the same microgel beads also used for benchmarking the oscillatory measurements. We found that the stress increased lin-

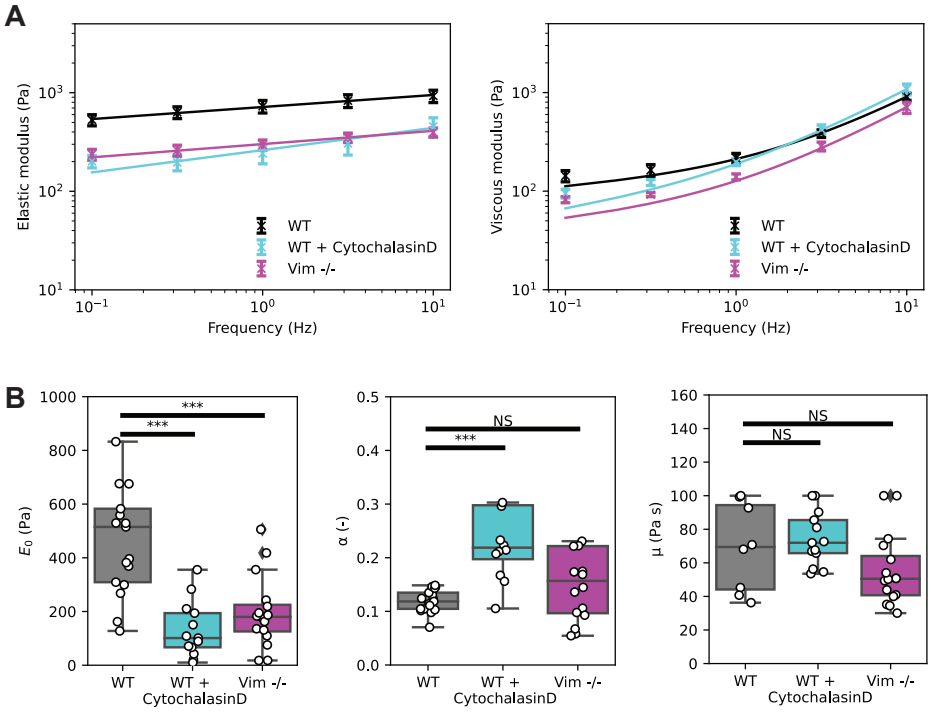

Figure 2.3: (A) Elastic (left) and viscous (right) linear moduli (symbols), measured for oscillation frequencies between 0.1Hz and 10Hz, with fits (solid lines) to the structural damping model (represented by the springpot and dashpot schematic shown in the insets and described by Eq. 3.4). (B) The prefactor E_0 from the viscoelastic fit shows a significant decrease, both after drug-induced depolymerization of actin and upon knocking out vimentin, as compared to wild type cells. (E) The power law exponent α increases only upon actin depolymerization. (F) Neither actin depolymerization nor vimentin knockout changes the Newtonian viscous damping term μ. **P<0.01, ***P<0.001. NS, not significant.

early with strain (green curve in Figure 2.4B), equivalent to the linear elastic response of polyacrylamide as measured in bulk rheometry [175]. In stark contrast, the cells showed a marked strain-stiffening response (black curve in Figure 2.4B). To characterize this response, we calculated the nonlinear stiffness K of the cells to compressive loading in a way similar to what has been done for shear stress in reconstituted networks, as a derivative of the stress with respect to strain, rather than the ratio of stress to strain in the case of the linear modulus [89, 169]. Specifically, $K = \frac{\partial}{\partial \epsilon}\sigma_e$, where ϵ is the compressive strain and σ_e is the resulting compressive stress measured in Figure 2.4B. From this procedure, we found that wild type MEF cells exhibited a linear regime for compressive strains below ~10%, followed by nonlinear stiffening (Figure 2.4C). This finding shows that cells compression-stiffen under uniaxial load, consistent with prior reports [176].

2.2.4. ACTIN AND VIMENTIN BOTH CONTRIBUTE TO THE COMPRESSION-STIFFENING OF CELLS

To test the contribution of the actin cytoskeletal network to the nonlinear stiffening behaviour of the cells, we then performed strain ramp measurements on wild type cells drugged with cytochalasin D. Actin depolymerization resulted in a marked softening of the cells over the entire strain range compared to wild type cells, but the cells continued to exhibit strain-stiffening behaviour (cyan curve in Figure 2.4C). The linear modulus dropped from 747 ± 80 to 230 ± 30 Pa, the onset strain for strain-stiffening did not change significantly, and the onset stress was reduced (Figure 2.4D). When we performed the same experiment on vimentin knockout cells, we again observed a lower linear elastic modulus (234 ± 40 Pa) compared to wild type cells, invariant onset strain and a lower onset stress (magenta curve in Figure 2.4C, summary in Figure 2.4D). Our findings indicate that actin and vimentin both contribute to the strain-stiffening behavior of MEF cells. To test whether strain-stiffening is preserved when both networks are removed, we measured the response of vimentin knockout cells drugged with cytochalasin D to strain ramps. Strikingly, we observed a complete loss of strain stiffening behaviour in addition to a strong drop of the elastic modulus (red curve in Figure 2.4C). We note that, despite this drastic treatment to the cytoskeleton, cell viability was not impacted (Figure S2.8). Therefore, we conclude that both the actin and vimentin networks are responsible for the compression stiffening of the cells.

It is known that the stiffness of mammalian cells is strongly influenced by the level of internal contractile stress σ_p (also known as prestress) generated by nonmuscle myosin-2 motor activity [169]. It has also been shown that motor-generated stress and externally applied stress σ_e play similar roles in the stiffening of reconstituted actomyosin networks [177], as has also been shown in simulations of model fiber networks [178]. It has further been suggested that the nonlinear increase in the modulus is proportional to the sum of internal and external stress $\sigma_p + \sigma_e$. According to this phenomenological model, the nonlinear stiffness would increase linearly with applied stress. To investigate the dependence of cell stiffness (in Fig. 2.4C) on applied stress, we rescale K by the linear value (i.e., in the limit of small stress and strain) and plot this by the ratio of the stress to its value at the onset of stiffening. This rescaling allows us to test if cells with different cytoskeletal perturbations follow the same mechanical relationship between stiffness and

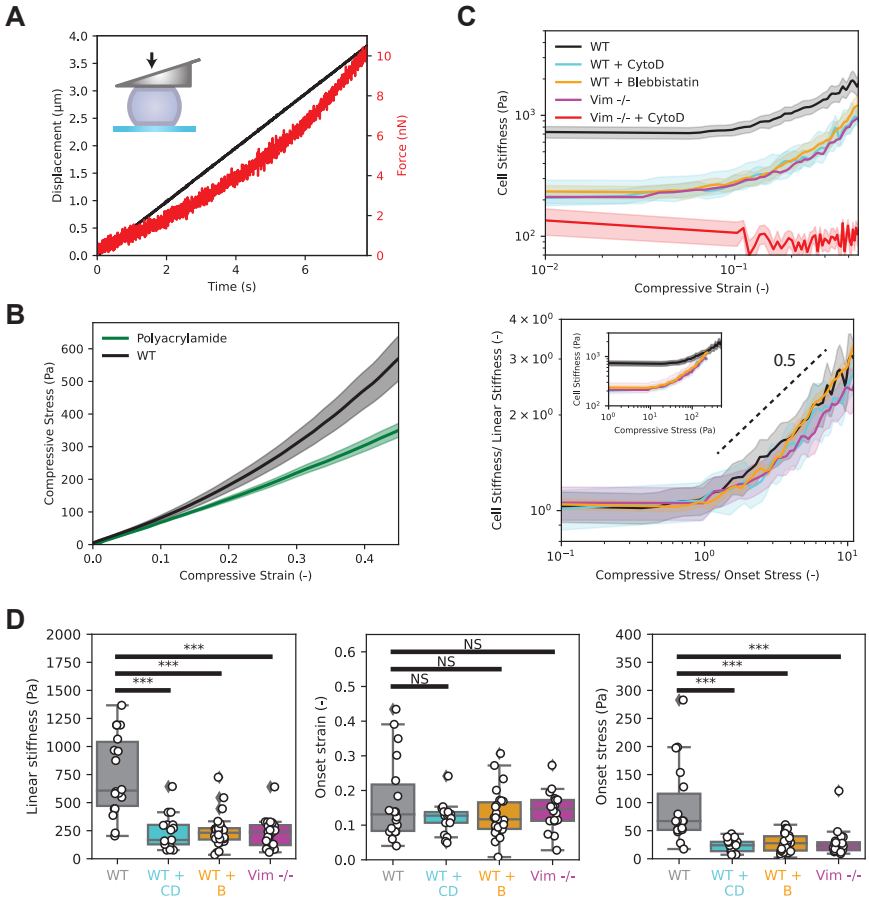

Figure 2.4: Strain ramp experiments to characterize the nonlinear response of MEFs to large compressions. (A) Representative strain ramp measurement showing the applied displacement of the cantilever (black, left y-axis) and observed force (red, right y-axis). (B) Applied strain versus measured stress for wild type cells (N=18) and polyacrylamide microgels (N=8). Cells strain-stiffen whereas polyacrylamide gels show a linear response. Shaded areas around the curves show the standard error. (C) Top: Cell stiffness versus strain, obtained by taking the numerical derivative of the stress-strain curves from panel B. Wild type cells (untreated (N=18) or treated with either blebbistatin (N=26) or cytochalasin D (N = 17) and vimentin KO (N=20) cells strain-stiffen. Vimentin KO cells treated with cytochalasin D (N=14) are significantly softer and no longer strain-stiffen. Bottom: Normalizing the stress by the onset stress for stiffening and the cell stiffness by the linear stiffness, respectively, collapses the curves onto a single master curve. The dashed line indicates power-law stiffening with an exponent of 0.5. Inset shows the same data without rescaling. (D) Left: All drug and genetic perturbations lead to a significant decrease in the linear stiffness of the cells. Middle: The onset strain for strain-stiffening is invariant. Right: all drug and genetic perturbations lead to an earlier onset stress for strain-stiffening. Shaded areas around each line show the standard error on the mean. ***P<0.001. NS, not significant. All statistical comparisons not shown were not significant.

applied stress. Importantly, this rescaling procedure is found to result in a good collapse of all data to a single master curve that characterizes both wild type cells and cells with different drug or genetic manipulations. The observation that all curves collapse onto a single master curve indicates that the mechanism cells use to stiffen under compression is universal, regardless of the specific cytoskeletal components involved.

In the stiffening response to stress, we observe an apparent power-law stiffening exponent of ~ 0.5 (Figure 2.4C bottom). While this differs from the linear dependence suggested in prior work, we note that such an exponent has been predicted theoretically for fibrous networks [179, 178, 180] and seen experimentally for other biopolymer networks [181]. The onset stress is reduced for both actin-depleted and vimentin knock out cells (Figure 2.4D). Indeed, assuming a given onset tension per filament, the removal of network filaments is expected to lead to both a reduction in the linear modulus and in the onset stress. In the case of actin, depletion can also reduce the prestress σ_p. In order to identify the role of prestress, we also treated wild type cells with blebbistatin, which inhibits myosin-2. As shown in Fig. 2.4 (yellow curve), the blebbistatin-treated cells showed an identical strain-stiffening response to cells treated with cytochalasin D (cyan curve), indicating that myosin-generated prestress dominates the mechanical contribution of actin. Thus, the higher onset stress of wild type cells can be accounted for by their higher contractile prestress σ_p.

2.2.5. THE CYTOSKELETON, NOT THE NUCLEUS, CAUSES COMPRESSION STIFFENING

From the imaging experiments, we observed that the nucleus occupied a large volume fraction (~60%) of our cells (Figure 2.2). While the nucleus has long been regarded as the stiffest component of the cell [182], recent studies suggest that it may actually be softer than the cell as a whole [183, 184, 185]. Therefore, we sought to distinguish the response of the cytoskeleton from any stiffening or softening effects that could be caused by compression of the nucleus. To this end, we removed the nucleus from wild type MEF cells by centrifuging cells plated on coverslips following a well-established procedure [186].

As shown in Figure 2.5A, the resulting enucleated cells (also known as cytoplasts) retain an actin and vimentin cytoskeleton with similar architecture to that of WT cells. When we performed strain ramps on the enucleated cells, we found that they still strain-stiffened, although they were softer than the intact cells (Figure 2.5B). The stress-stiffening curves of intact and enucleated cells collapsed onto a single master curve upon normalizing the stress and modulus axes (Figure 2.5B inset), showing that the stiffening is controlled by the cytoskeleton. We performed the same enucleation procedure on vimentin-null cells and found that, although these enucleated cells were softer than the intact vimentin-null cells, they still exhibited strain stiffening. We conclude that the cells stiffen under macroscopic compression due to the nonlinear response of the cytoskeleton rather than as a consequence of the nucleus.

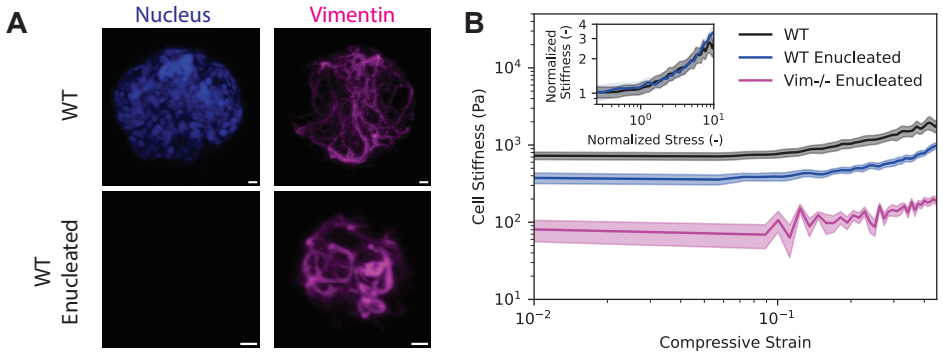

Figure 2.5: Strain ramp experiments on intact and enucleated wild type cells. (A) Maximum projection confocal images of the nucleus and vimentin in single wild type (top) and enucleated wild type (bottom) cells. Enucleated cells no longer have a nucleus but vimentin still is able to form a network. (B) Wild-type (N=18), enucleated wild-type (N=15), and enucleated vim-/- cells (N=18) all strain-stiffen, with the same onset strain for stiffening, but enucleated cells are softer. Inset: The stress-stiffening curves collapse onto a single master curve upon normalization by the linear stiffness (labelled as the normalized stiffness in the figure inset) and by the onset stress for stress-stiffening (labelled as the normalized stress in the inset). Shaded areas around the curves show the standard error on the mean.

2.3. DISCUSSION

In this study, our aim was to quantify the viscoelastic properties and nonlinear elasticity of single mouse embryonic fibroblasts (MEFs) and to dissect the contributions of the actin and vimentin cytoskeletal networks. Using a custom single-cell rheometer, we measured the linear viscoelastic properties through small amplitude oscillatory compression, where we controlled the applied strain and measured the concomitant stress. Using polyacrylamide (PAA) microgels, we validated the rheometer setup, showing expected elastic and viscous responses consistent with bulk measurements and linear elastic behavior. Our oscillatory measurements revealed that single fibroblasts behave as viscoelastic solids, with a frequency-dependent elastic modulus, E', that increases with frequency following a power-law, a characteristic feature of mammalian cells. Beyond small deformations, we applied large uniaxial strains to assess nonlinear cell elasticity. Although we impose purely uniaxial compression, the stress we record represents a convolution of the interior bulk response, the thin cortical shell and the enclosing plasma membrane, and any volume-conserving shear that arises under compression. In these measurements, we found that the cells exhibit pronounced strain-stiffening, with the differential elastic modulus increasing steeply beyond 10% compressive strain. Both small and large strain experiments highlighted the critical roles of actin and vimentin in cell mechanics. Depolymerizing actin or knocking out vimentin led to significant reductions in both the linear viscoelastic moduli and the nonlinear strain-stiffening response, underscoring that both networks contribute to the cell's resistance to deformation, especially under large mechanical loads.

Our mechanical fingerprinting allowed us to distinguish the contributions of actin

and vimentin to cell viscoelasticity. Our small amplitude oscillatory measurements show that the WT MEFs are 3-fold stiffer as compared to cells lacking actin (WT MEFs drugged with cytochalasin) or vimentin (Vim -/- MEFs). Although actin has traditionally been considered the dominant contributor to cell stiffness, we found that vimentin and actin make comparable contributions to the linear and nonlinear elasticity of suspended MEF cells. Our measured cell stiffness values (E_0) are about one order of magnitude lower than values reported for cells adhered to glass [187], but comparable to prior measurements on fibroblasts in suspension [188] (see Table 3.1). The discrepancy with adherent cells is likely due to the lack of visible actin stress fibers in suspended cells. In contrast, adherent MEF cells form pronounced stress fibers (see Supplementary Figure 2.9), which are known to contribute to stiffness in adhered cells [189]. In our study we make the deliberate choice to use MEFs in suspension, eliminating substrate adhesion and the associated contractile prestress. This reductionist philosophy allows us to probe a clean limiting case in which the intrinsic mechanics of the cytoskeletal networks can be isolated from the complex feedback of focal-adhesion signaling, stress-fiber formation, and cortex tension. Introducing adhesion and contractile stresses triggers actomyosin contractility and stress-fiber assembly, leading to actin network fluidization and dynamic remodeling that mask the cell interior's baseline viscoelastic behavior. This would be an interesting direction for future work. By studying non-adherent cells here, we capture the fundamental viscoelastic and strain-stiffening properties of actin and vimentin in a simple, well-defined limit. Previous studies showed that the measurement conditions also significantly affect cell stiffness. For instance, Fernández et al. [12] reported stiffness values of 15 kPa for 3T3 fibroblasts using microplate rheology, whereas Mendez et al. [187] measured smaller values of 3.5 kPa for wild type and 2.9 kPa for Vim -/- fibroblasts using atomic force microscopy. In both studies, the cells were adherent to a rigid substrate, which increases cell stiffness. Fibroblasts in suspension generally exhibit much lower stiffness. For example, Gerum et al. [188] reported 85 Pa for WT cells, decreasing to 75 Pa with cytochalasin D treatment, and even lower values (60 Pa without and 35 Pa with cytochalasin D) for Vim -/- cells. These values align with our findings, suggesting that suspended fibroblasts, regardless of cytoskeletal changes, are softer than adherent fibroblasts. Differences between our study and Gerum et al.'s could stem from variations in MEF cell lines and the use of different measurement methods. While we employed uniaxial compression, Gerum et al. used shear-based flow cytometry.

Interestingly we found that vimentin knockout altered the elastic component of the complex modulus but did not significantly change the power law scaling exponent α describing the frequency dependence. By contrast, actin depolymerization with cytochalasin D did change α. This observation indicates that actin plays a larger role than vimentin in controlling cellular energy dissipation. This is consistent with atomic force microscopy (AFM) experiments performed on bone-marrow-derived dendritic cells, where no significant difference was found in stress relaxation times between wild-type and vimentin knockout cells [190]. It is also consistent with bulk rheology measurements on reconstituted actin-vimentin composite networks, where vimentin was shown to be less dissipative than actin [120]. These findings also align with the known difference in stability of actin and vimentin networks in the cell. Actin networks are highly dynamic, with a typical turnover time on the order of minutes in case of stress fibers [191]

as well as the actin cortex [192]. By contrast, intermediate filament networks exhibit turnover times on the order of hours [33]. This picture is consistent with previous studies showing that vimentin intermediate filaments form a stretchable, hyperelastic network that enhances cytoplasmic resilience and toughness under mechanical stress [193]. Future experiments could directly probe how cytoskeletal turnover dynamics contribute to time-dependent cell mechanics, for example by tuning actin or vimentin turnover rates through targeted drug perturbations [194]. Consistent with this idea, studies in cells have shown that altering crosslinker dynamics can strongly modulate cytoskeletal turnover and mechanics [195, 196, 197, 198].

Our strain ramps combined with cytoskeleton perturbations and enucleation experiments point toward the cytoskeleton as the main component responsible for strain stiffening, with comparable contributions from actin and vimentin. Both purified actin and vimentin networks have indeed been shown to exhibit strain-stiffening as a consequence of the semiflexible polymer nature of the filaments. Recent evidence suggests that vimentin plays a dominant role in determining the stiffening behaviour of cells [166], but we observed that both actin and vimentin contribute to this stiffening behaviour. In the stiffening response to stress in Figure 2.4C bottom, we observe an apparent power-law stiffening exponent of ~ 0.5. Such an exponent has been predicted theoretically for networks [179, 178, 180] and seen experimentally for other biopolymer networks [181]. This behavior can be understood in simple terms as follows. If the stiffening is due to additional network elements becoming mechanically engaged only above a critical threshold strain ϵ_c, it is natural to expect that the stiffness K may increase approximately linearly in the excess strain $\epsilon - \epsilon_c$ above threshold. This would correspond to the stress contribution σ that would increase as $(\epsilon - \epsilon_c)^2$, leading to $K \sim \sigma^{1/2}$. While this behavior has previously been discussed in the context of shear strain and bulk expansion, it is important to note that cells are expected to maintain their volume under compression, which requires shear. Whether this mechanism is the origin of the approximate $K \sim \sigma^{1/2}$ scaling we observe is not yet clear. It may also be that a larger exponent closer to 1 may appear at higher stress. For cells under compression, however, the corresponding high strains may not be achievable without killing the cells.

Our compression experiments on enucleated cells show that the nucleus has a positive contribution to the elastic response of the cell to deformation. This is consistent with reports showing nuclei are stiffer than the surrounding cytoplasm [199]. However, our results show that the nucleus does not mediate the stress stiffening of single cells.

Table 2.1: Summary of previously measured stiffness values of mouse embryonic fibroblasts.

Reference	Cell Stiffness	Method
Fernández et al. [12]	15 kPa 3T3 and 3 kPa 3T3 + Latrunculin A	Microplate rheology†
Mendez et al. [187]*	3.5 kPa WT and 2.9 kPa Vim -/-	Atomic force microscopy†
Guo et al. [53]*	10 Pa WT and 5 Pa Vim -/-	Optical tweezers†
Gerum et al. [188]	85 Pa 3T3 and 75 Pa 3T3 + CytoD	Flow cytometry‡
	60 Pa Vim -/- and 35 Pa Vim -/- + CytoD	

*These are the same cells used in this study. †Cells in these studies were measured in an adherent state. ‡Cells in these studies were measured in an suspended state.

Previous attempts to explain the rheology of cells in suspension have utilized a shell model approach [13]. The shell model in cellular rheology assumes that mechanical behavior is primarily dominated by the cell cortex, with the bulk of the cell's mechanical response attributed to the elastic and viscous properties of this outer shell, rather than contributions from deeper cytoplasmic elements. However, our findings reveal that both vimentin and the nucleus significantly contribute to cell elasticity. Since these structural elements are located within the cell's interior, this suggests that the cortex alone does not fully account for cellular mechanical behavior, indicating a more complex interplay of intracellular components in determining cell mechanics.

Our strain ramp experiments demonstrate that both actin and vimentin are key mediators of prestress. Cells are able to generate contractile stresses through the interaction of actin filaments and myosin motors, which gives rise to cellular prestress [200]. The strain ramp experiments suggest that actin depolymerization reduces the cellular prestress, which makes sense since contractility requires an intact actin filament network to allow force transmission. Interestingly, vimentin knockout also appears to reduce the cellular prestress. The reason for this effect is less clear. Clues for this have emerged from growing evidence that vimentin is a key regulator of actin organization in the cell cortex [201] and in stress fibres [137]. Furthermore, previous traction force microscopy measurements have shown that wild type MEFs are ~46% more contractile than their vimentin knockout counterparts [202]. Although these measurements were performed on adherent cells spread on flat substrates, in contrast to our suspended cell setup, our finding that vimentin knockout reduces cellular prestress is nevertheless consistent with the observation of reduced traction force. A loss of contractile ability upon vimentin depletion may help explain why cells without vimentin exhibit slower migration speeds as compared to WT cells [190]. Our findings are particularly relevant for understanding the ability of cells to migrate through narrow extracellular spaces, which requires deformation of both the nucleus and the cytoskeleton [203]. Understanding how these internal components modulate cell mechanics could lead to more accurate models of cancer cell migration and help develop targeted therapies that alter intracellular structures to inhibit metastatic spread.

Strikingly, in all of our experiments we found that total cell stiffness cannot be solely attributed to the individual contributions of actin and vimentin, suggesting a mechanical synergy between these filaments. A possible candidate for this synergy is crosslinking, likely mediated by the cytolinker plectin that forms crosslinks between actin and vimentin filaments [204]. Crosslinkers generally increase the elastic modulus of cytoskeletal networks while reducing viscous dissipation [205]. Our recent rheology experiments of reconstituted crosslinked actin-vimentin networks, facilitated by a plectin-like cytolinker, revealed clear evidence of mechanical synergy between the filaments [120].

2.4. CONCLUSIONS

We demonstrated that actin and vimentin networks play complementary roles in determining the mechanical properties of mouse embryonic fibroblasts. Using a custom single-cell rheometer, we quantified the viscoelastic and nonlinear elasticity of sus-

pended cells, revealing significant strain-stiffening behavior. Both actin and vimentin contribute to cellular stiffness, with vimentin also influencing prestress and hyperelasticity. Our results highlight the mechanical synergy between these two cytoskeletal networks and provide insight into how cytoskeletal organization impacts cell mechanics. This study offers a deeper understanding of the mechanical behavior of fibroblasts and emphasizes the importance of both actin and vimentin in cellular function and response to mechanical forces.

2.5. ACKNOWLEDGEMENTS

We gratefully thank J. Eriksson (University of Turku) for generously supplying the cells used in this study and R. Rodriguez and T. Schmidt (Leiden University) for providing the hydrogel beads. We thank M. Mavrakis (Institut Fresnel) for donating the vimentin-GFP plasmid used for live cell imaging experiments. We thank D. de Roos (TU Delft) for manufacturing the centrifuge tube inserts used for cell enucleation and N. van Vliet for help with electroporation. G.H.K. gratefully acknowledges funding from the NWO Talent Programme which is financed by the Dutch Research Council (project number VI.C.182.004). P.E.B. gratefully acknowledges funding from the European Research Council (ERC) under the European Union's Horizon 2020 research and innovation program (grant agreement no. 819424). F.C.M. was supported in part by the National Science Foundation Division of Materials Research (Grant No. DMR-2224030) and the Center for Theoretical Biological Physics (Grant No. PHY-2019745)

2.6. MATERIALS AND METHODS

2.6.1. CELL CULTURE

Wild type (WT) and vimentin-null (Vim -/-) mouse embryonic fibroblast (MEF) cells, obtained from WT and Vim -/- embryos [206], were cultured in Dulbecco's modified Eagle's medium with glutamax (DMEM, 10565018 Gibco) supplemented with 10% fetal bovine serum (FBS, 10270106 Gibco) and 5% penicillin-streptomycin (Pen-Step, 15070063 Gibco). Cells were cultured in a humidified incubator maintained at 37°C and 5% CO_2, and subcultured when they reached approximately 80% confluency. Cells were subcultured twice per week and were tested for mycoplasma contamination every four months. The day prior to mechanical loading experiments, 10000 cells, counted with a Countess cell counter (Thermo Fisher Scientific), were seeded in 6 plastic cell culture well plates (83.3920.005 Sarstedt) in standard cell culture medium. On the day of experiments, cells were detached with Trypsin-EDTA (0.25%) (25200056 Thermo Fisher Scientific) and resuspended in CO_2-independent medium (18045088 Gibco) supplemented with 10% fetal bovine serum. For actin depolymerization experiments, CO_2-independent medium was supplemented with Cytochalasin D (C8273 Sigma) at a concentration of 1 μM, chosen based on previous reports [188]. For myosin inhibiting experiments, CO_2-independent medium was supplemented with blebbistatin (203391 Sigma)

at a concentration of 20 μM, also based on literature reports [207]. Cells were incubated in drug-supplemented medium for at least 15 minutes before experiments.

2.6.2. FABRICATION OF WEDGED FORCE CANTILEVERS

Tipless microcantilevers with a nominal spring constant of 0.018 N/m (Optics11 Life) were modified to correct for a 3° cantilever tilt [208] and thus facilitate uniaxial compression. We first prepared coverslips, functionalized to prevent cell adhesion. 18 mm glass coverslips were cleaned by sonicating them in 2-Propanol (34863 Sigma) for 5 minutes and were then air-dried. The cleaned coverslips were next submerged in a solution of 10% v/v SurfaSil (TS-42800 Thermo Fisher Scientific) in chloroform for 10 seconds. The coated coverslips were then air dried overnight on parafilm-coated 10cm petri dishes. We checked the efficacy of the Surfasil coating by placing a small drop of UV NOA81 curing polymer adhesive (NOA81 Norland) on the coverslip followed by curing using a UV (395 nm) LED (11504255 Leica) at a distance of approximately 5 cm. If the drop could be moved with a pipette tip without any difficulty, the coverslip could be used for cantilever fabrication. Next a small amount of NOA81 polymer adhesive was deposited on the microcantilever using the tip of a needle under a stereoscopic microscope. The cantilever was pressed against a coated coverslip to create a flat surface and the polymer adhesive was cured using the UV LED at a distance of approximately 5 cm for two hours. The resulting wedged cantilever was carefully removed from the coverslip by first gently tapping the microscope stage to promote detachment and then gradually moving the cantilever up in steps of 2 μm. Cantilevers were calibrated by acquiring a force-distance curve on a stiff surface (glass), according to the manufacturer's instructions. This was performed before and after wedge manufacture to ensure no change in spring constant. After fabrication, the cantilever was cleaned with 2-Propanol, rinsed with MilliQ water and carefully dried with a Kimtech tissue.

2.6.3. SINGLE CELL RHEOLOGY EXPERIMENTS

The uniaxial compression setup consisted of an optical fiber-based nanoindenter (Optics11 Life) mounted on a Leica Thunder Imager widefield microscope equipped with a 200 mW solid state LED5 light source (Leica) and a monochrome sCMOS camera (Leica). For imaging, we used a 10x dry objective (HC PL APO 0.45NA, Leica). At the beginning of every measurement session, cantilevers were calibrated using the stiff-surface contact method, performed according to the manufacturer's instructions. To prevent adhesion between cells and the culture dish, dishes were first cleaned with isopropanol, exposed to deep UV via a ProCleaner UV ozone cleaner (Bioforce Nanosciences), incubated for 1 hour in 0.1 mg/mL PLL-g-PEG solution (SuSoS), and finally washed with MilliQ water and allowed to air dry. The dishes were used within one week of PLL-g-PEG coating. For uniaxial compression of cells on PEG-coated dishes, we used the indentation mode of the Piuma control software (Optics11 Life), which allowed us to control the strain rate at which we deformed the sample. During measurements, the elapsed time, piezo displacement, and measured force were recorded at a time resolution of 1000 Hz. To address concerns that keeping our fibroblasts in suspension would affect cell viability, we measured the live-to-dead ratio of the cells and found no decrease over a period of 2

hours (the maximum length of an experiment) (Supplementary Figure2.10). We calculated the contact area between the cell and the plates from epifluorescence microscopy images of the cytoplasm labeled with CellTracker orange (Fisher Scientific), where we thresholded each image using Otsu's method in the Python library scikit image [209] and counted the number of pixels in the thresholded image. The applied stress was thus calculated as the measured force divided by the contact area. We calculated the uniaxial strain strain by approximating each cell as a sphere, and dividing the length of compression by the cell diameter. All measurements were made at 37°C, maintained by a microscope stage heater (Tokai Hit). For our polyacrylamide (PAA) benchmarking experiments, microgels with radii between 5 and 50 μm [210], were immersed in MilliQ water for measurement. We selected beads with a diameter approximately equal to that of our cells (~18μm). We applied the exact same experimental protocols to our PAA microgels as for cells to test our setup. After each experimental session, the cantilever was cleaned with 2-Propanol, rinsed with MilliQ water and carefully dried with a Kimtech tissue to remove organic waste.

2.6.4. DYNAMIC MECHANICAL ANALYSIS MEASUREMENTS

To measure the viscoelastic response of cells in the small deformation regime, we sinusoidally compressed them with the wedged microcantilever. First, the microcantilever was lowered towards the cell's top surface, until the cell was compressed by 1 μm, corresponding to an approximate 5 % strain determined from the average cell size. After a waiting time of 20 seconds to allow for initial viscoelastic relaxation, cells were subjected to 200 nm oscillations (the minimum amplitude to obtain an acceptable signal-to-noise ratio) at 5 frequencies logarithmically spaced between 0.1 Hz and 1 Hz. From the applied strain and measured stress as a function of frequency, f, the complex viscoelastic modulus, $E^*(f)$, was calculated as

$$E^*(f) = \frac{\bar{\sigma}(f)}{\bar{\epsilon}(f)}, \tag{2.2}$$

where $\bar{\sigma}$ and $\bar{\epsilon}$ are the Fourier transforms of the time-dependent stress and strain, respectively. This equation tells us the frequency dependence of the cell mechanical response. We applied Equation 2.2 at each measured oscillation frequency by taking the fast Fourier transform (FFT) of the signal in Python, using the FFT function in Python's numpy library. $E^*(f)$ data were decomposed into real (in phase) and imaginary (out of phase) parts, $E^*(f) = E'(f) + iE''(f)$, where $E'(f)$ and $E''(f)$ are the compressive storage and loss moduli, respectively. $E'(f)$ corresponds to the elastic modulus of the cell (i.e., the energy stored per cycle of oscillation), whereas $E''(f)$ corresponds to the viscous component (i.e., the energy dissipated per cycle of oscillation). We further decomposed Equation 3.4, the structural damping model, into real and imaginary parts:

$$E'(f) = E_0 c(\alpha) \cos\left(\frac{\pi\alpha}{2}\right)\left(\frac{f}{f_0}\right)^{\alpha} \tag{2.3}$$

$$E''(f) = E_0 c(\alpha) \sin\left(\frac{\pi\alpha}{2}\right)\left(\frac{f}{f_0}\right)^{\alpha} + \mu f. \tag{2.4}$$

Using the curve fit function from Python's SciPy [211] library, we simultaneously fit Equations 3.11 and 3.12 to our elastic and viscous moduli, which yielded shared parameters for E_0, α and μ.

2.6.5. STRAIN-CONTROLLED COMPRESSIVE RAMPS

The same wedged microcantilever as used for dynamic oscillatory measurements was lowered towards a cell's top surface in steps of 1 µm until cantilever deflection was detected, indicating contact with the cell. We then allowed the cell to relax for 30 seconds before beginning the strain ramp measurement. We chose to start the measurement from this contact position as we often noticed a small amount of slip upon initial contact with the cantilever. The cantilever was then gradually lowered, controlling the speed of cell compression at 2 µm/s unless specified otherwise (for rate dependence, see Supplementary Figure 2.11), until a strain of approximately 40% was reached. We checked by concurrent imaging that the cell reversibly changed shape (Supplementary Video 1). Above strains of 50%, we observed cell death in a large proportion of cases, as indicated by bleb formation visible in wide field microscopy (Supplementary Video 2). The cantilever was subsequently retracted at the same rate. The force acting on the cantilever was recorded during the entire loading-unloading cycle. To calculate cell stiffness, K, stress-strain data were numerically differentiated using the Python numpy library's gradient function [212]. To determine the onset stress for stress-stiffening, we performed a piecewise linear fit to the stress/stiffness curve for each individual cell, where we fitted a horizontal line and a linear equation of the form $y = mx + c$ with the Python scipy library, optimizing the onset point by maximizing the combined R^2 values of both fits.

2.6.6. LIVE CELL IMAGING WITH CONFOCAL MICROSCOPY

Confocal microscopy to determine the localization and arrangement of the actin and vimentin cytoskeletal networks and the nucleus in cells was performed on a Leica Stellaris 8 LSCM utilising a 63x glycerol immersion objective (HC PL APO, WD 0.3 mm, NA 1.2), equipped with a white light laser operated at 488 nm (vimentin imaging) and 640 nm (actin imaging) and with a 405 nm diode laser (nucleus imaging). Detection was performed with the HyDS1 detector (440–480 nm, nucleus imaging), the HyDS2 detector (504-590 nm, vimentin imaging) and the HyDX3 detector (658-809 nm, actin imaging) operated in counting mode. To label vimentin, four days prior to imaging experiments, cells were transfected with vimentin-GFP [213] using the Neon Transfection System (Thermo Fisher Scientific) with a single pulse width of 30 ms and a pulse voltage of 1350 V, according to the manufacturer's instructions. We found that cells required four days to express vimentin at stable levels. For actin labeling, on the day of experiments, cell culture medium was replaced with fresh medium containing SiR actin (Tebu Bio, SC001) (1:1000) along with the pump inhibitor verampamil (Tebu Bio, SC001, part of SiR actin kit) (1:1000). Cells were incubated with the staining solution for 1 hour, before replacement with fresh medium, containing Hoechst 33342 (Thermo Fisher Scientific, H3570) (1:10,000) to label the nucleus. To mimic the conditions of our cell rheology experiments, cells were trapped between two coverslips coated with PLL-g-PEG, kept apart with 10 µm silica particles (Sigma, 904368) (see Supplementary Figure2.12 for

schematic). 3D confocal z-stacks were acquired with 256 x 256 pixel xy-slices separated by 0.33 μm at a scan speed of 400 Hz. The orthogonal projection tool in FIJI [214] was used to generate side projections of cells. To generate 'average cells', a maximum projection was generated from a 2 μm section centered at the cell equator. Multiple-channel stacks (containing projections of the actin, vimentin and the nucleus) were aligned using HyperStackReg plugin [215], which registered cells on top of each other, correcting for differences in cell size. In FIJI, we then made average intensity projections to generate an average cell. Finally, the radial profile plot tool in FIJI was used to calculate the normalized intensities around concentric circles from the center of the image. Images were collected from at least 2 independent experiments for each condition.

2.6.7. REMOVAL OF NUCLEI FROM CELLS

We developed a protocol for enucleating the cells following a well-established protocol [186]. Cells were seeded on 22 mm diameter plastic coverslips and grown to 90% confluency in standard culture medium. Next, the cells were treated with cytochalasin D at a concentration of 1 μM to promote cell membrane flexibility and facilitate enucleation under centrifugation. After exposure to cytochalasin D for 30 minutes, the cells were placed in centrifuge tubes (344058 Beckman Coulter), on top of custom-made Teflon inserts (for schematics, see Supplementary Figure 2.13) facing downwards and centrifuged at 1000×g for 1 hour to remove the nuclei. Enucleated cells were transferred to fresh culture dishes and maintained in the same culture conditions to observe post-enucleation viability and behavior. Although we observed some enucleated cells survived up to 3 days post-enucleation, cells were used in experiments within 24 hours. Enucleation efficiency was checked by Hoechst staining before and after the procedure.

2.6.8. STATISTICS AND CODE AVAILABILITY

All mechanical experiments shown were repeated on at least three different days and imaging experiments were repeated twice. P-values shown to determine statistical significance were calculated using the unpaired Student's t-test. Measured values in the main text are stated as the mean ± the standard error on the mean. Computer codes described in the Methods section are available on request.

2.7. SUPPLEMENTARY INFORMATION

2.7.1. SUPPLEMENTARY FIGURES

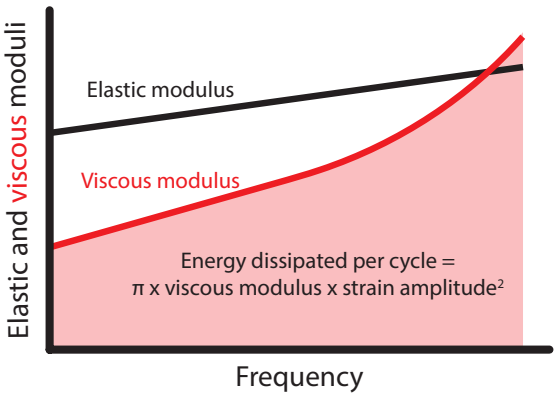

Figure 2.6: Schematic illustration of energy dissipation in cytoskeletal networks as inferred from frequency sweep experiments. The cartoon qualitatively depicts how different cytoskeletal compositions—wild-type, vimentin-null, and actin-disrupted (CytoD-treated)—influence the mechanical response of cells, particularly their ability to dissipate energy under oscillatory deformation. The energy dissipated per cycle of oscillation at a given frequency is given by π × the viscous modulus × the strain amplitude squared. For further details see reference [**?**].

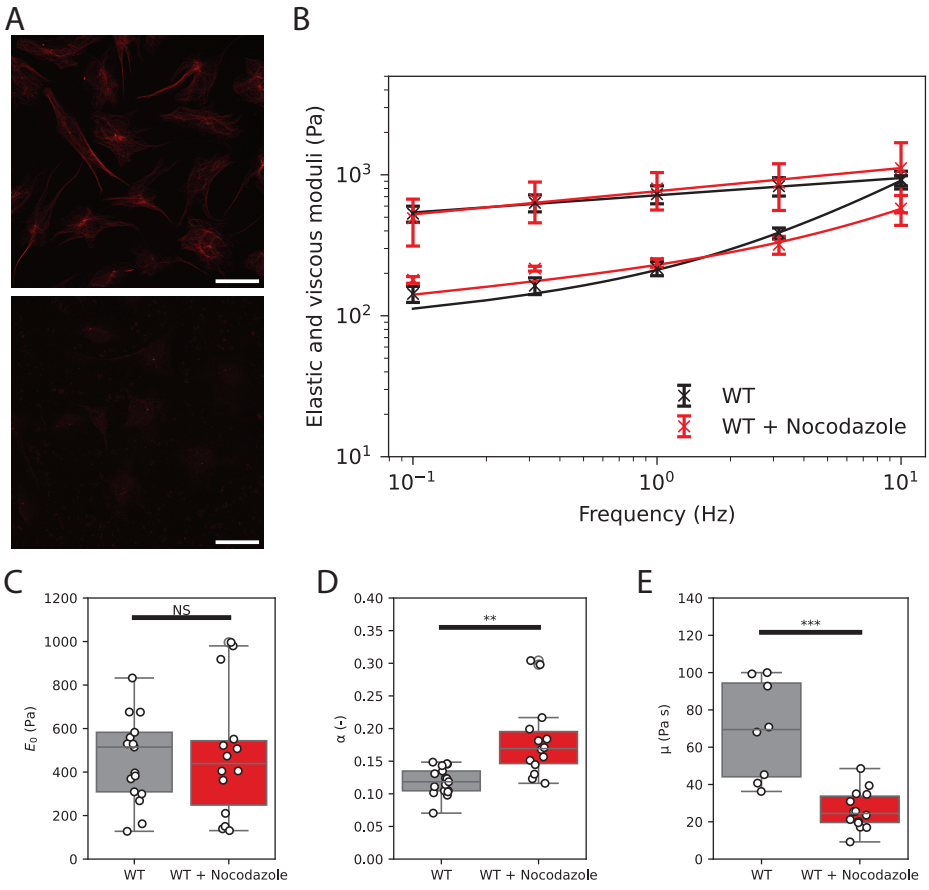

Figure 2.7: Microtubule depolymerization does not affect cell elasticity in the in the linear elastic regime. (A) Live-cell imaging of microtubules in MEFs labeled with SPY-650-tubulin before (top) and after (bottom) treatment with 5 µM nocodazole for 1 hour. The marked reduction in fluorescence intensity confirms effective microtubule depolymerization. Scale bars are 20 µm. (B) Frequency-dependent elastic (black symbols) and viscous (red symbols) moduli measured in wild-type cells with and without nocodazole treatment. Solid lines represent fits to the structural damping model. (C) Fit parameters from the model: the scaling prefactor E_0 shows no significant change following nocodazole treatment, indicating that microtubules do not contribute measurably to bulk cell elasticity. The power-law exponent α increases, while the Newtonian damping term μ decreases indicating reduced viscous drag as a result of loss of microtubules. $^{**}P < 0.01$, $^{***}P < 0.001$; NS, not significant.

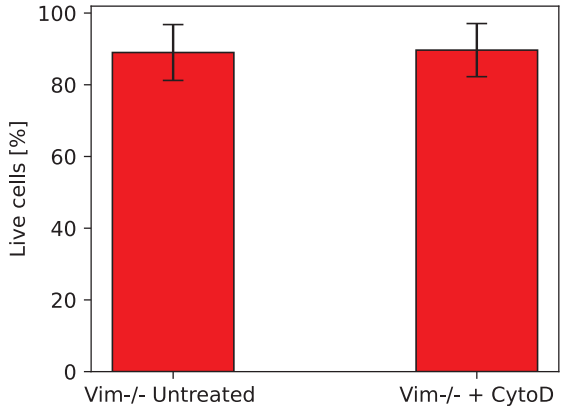

Figure 2.8: Live/dead comparison to test cell viability for vim -/- cells treated with cytochalasin D to depolymerize actin. Wild type mouse embryonic fibroblasts were stained with trypan blue to determine cell viability. Cell viability does not decrease after treatment with cytochalasin D. N=3. Error bars show the standard deviation.

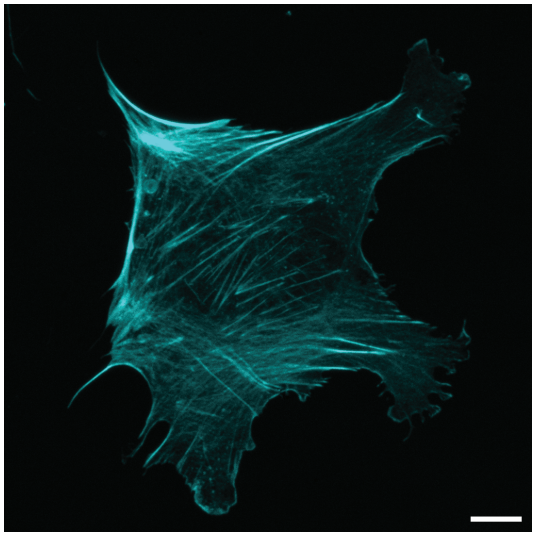

Figure 2.9: Representative maximum projection image (from a confocal z-stack with 32 slices separated by 0.33 µm) of a wild type mouse embryonic fibroblast adhered to fibronectin-coated glass and stained with Alexa-phalloidin to label F-actin. Adherent cells display pronounced stress fibres, in contrast to suspended cells (see images in main text). Scale bar 10 µm.

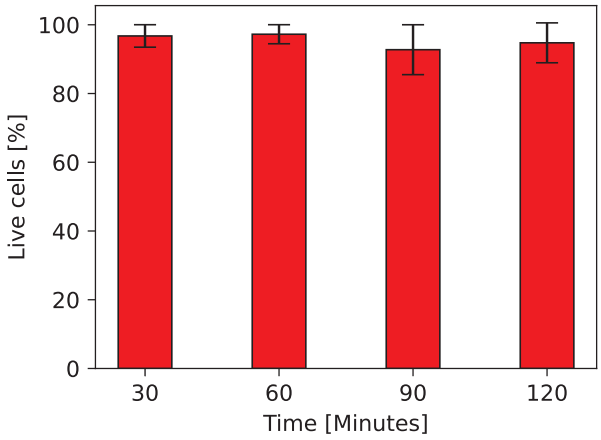

Figure 2.10: Live/dead comparison to test cell viability for the duration of a cell compression experiment. Wild type mouse embryonic fibroblasts were stained with trypan blue to determine cell viability. Cells were counted every 30 minutes up to 120 minutes (the maximum time cells were kept on the setup). Cell viability does not decrease during the course of an experiment. N=4. Error bars show the standard deviation.

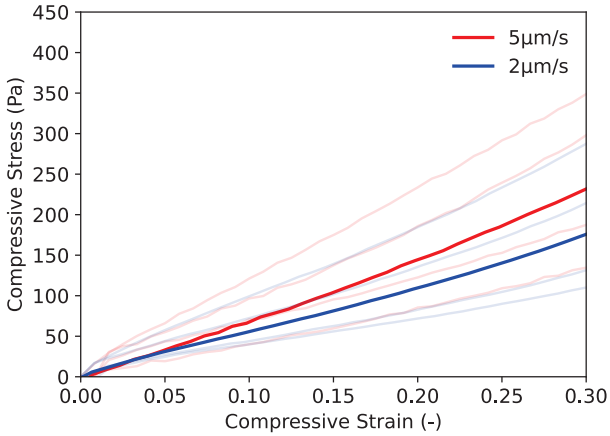

Figure 2.11: Experiments to determine the rate dependence of strain ramp tests. Compressing cells at a faster rate results in an apparently stiffer cell, consistent with general viscoelastic material properties. Wild type MEF cells were used for this experiment. Solid lines represent the average of all measurements and semi-transparent lines are the individual curves. N = 4 for both compression rates.

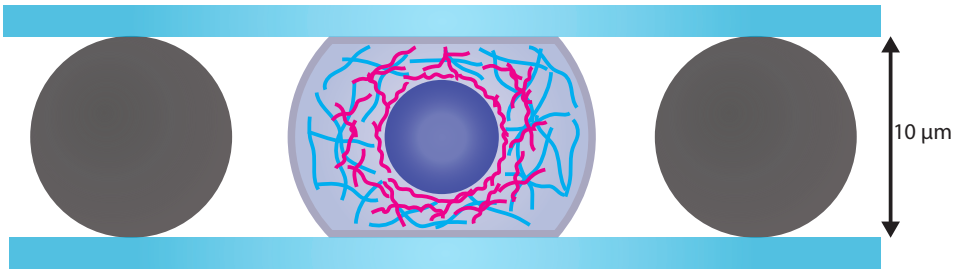

Figure 2.12: Schematic of the sample chamber used to acquire confocal images of single fibroblasts between two parallel glass coverslips to mimic the compression experiment conditions. Coverslips were coated with PLL-g-PEG to prevent cell adhesion, as in the compression experiments. Cells were trapped between coverslips separated by 10 µm beads.

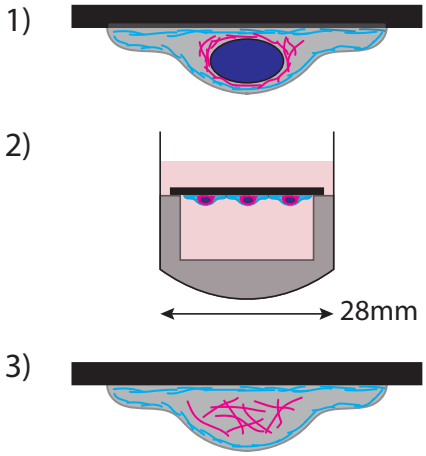

Figure 2.13: Schematic of the apparatus used to enucleate cells. 1) Cells are grown on fibronectin-coated plastic coverslips. 2) Cells are gently centrifuged faced down in a centrifuge tube with a teflon insert. 3) Enucleated cells remain adhered to the coverslip.

2.7.2. SUPPLEMENTARY METHODS

ACTIN STAINING FOR ADHERENT CELLS

35mm glass bottom coverlips (Ibidi, 81158) were incubated with 20 µg/mL bovine fibronectin (Thermo Fisher Scientific, 33010018) for 1 hour at room temperature. Cells were subsequently seeded into dishes and allowed to adhere overnight. The next day, cells were fixed with 4% paraformaldehyde (PFA) (Thermo Fisher Scientific, J19943.K2) in phosphate-buffered saline (PBS) for 15 minutes at room temperature. Fixed cells were washed three times with PBS and then permeabilized using 0.1% Triton X-100 (Sigma, X100-5ML) in PBS for 10 minutes. After an additional three washes with PBS, cells were incubated with Alexa Fluor® 568-phalloidin (Thermo Fisher Scientific, A12380) diluted (1:1000) in PBS containing 1% bovine serum albumin (BSA) (Thermo Fisher Scientific, 15260037) for 30 minutes at room temperature, protected from light. Cells were then washed three times with PBS and subsequently imaged using the Leica Stellaris confocal microscope described in the main text.

LIVE CELL IMAGING AND DEPOLYMERIZATION OF MICROTUBULES

Confocal microscopy to to validate the efficacy of microtubule depolymerization by nocodazole was performed on a Leica Stellaris 8 LSCM utilising a 63x glycerol immersion objective (HC PL APO, WD 0.3 mm, NA 1.2), equipped with a white light laser operated at 640 nm. Detection was performed with the the HyDX3 detector (658-809 nm) operated in counting mode. 35mm glass bottom coverlips (Ibidi, 81158) were incubated with 20 µg/mL bovine fibronectin (Thermo Fisher Scientific, 33010018) for 1 hour at room temperature. Cells were subsequently seeded into dishes and allowed to adhere overnight. For microtubule labeling, on the day of experiments, cell culture medium was replaced with fresh medium containing SPY-650 Tubulin (Tebu Bio) (1:1000). Cells were incubated with the staining solution for 1 hour in the cell culture incubator. Confocal images were acquired with 256 x 256 pixel resolution at a scan speed of 400 Hz. For microtubule depolymerization, the staining solution was replaced with cell culture medium supplemented with nocodazole D (C8273 Sigma) at a concentration of 5 µM in DMSO (according to Ref. [12]) one hour prior to imaging.

LIVE/DEAD STAINING

For experiments showing cell viability throughout the length of an experiment (Fig S4), cells were harvested from the compression setup at 30-minute intervals. For experiments testing cell viability of vim -/- cells treated with cytochalsin D, cells were incubated in CO_2 -independent medium supplemented with 1 µM Cytochalasin D for 20 minutes. Cells were counted using a Countess Cell Counter (Thermo Fisher Scientific). For live/dead assessment, 10 µL of cell suspension was mixed with 10 µL of 0.4% trypan blue solution (Thermo Fisher Scientific, 15250061). Dead cells, which take up the trypan blue dye and appear dark or black under the microscope, were distinguished from live cells, which exclude the dye. The ratio of live-to-dead cells was recorded for each time point.

3

PLECTIN AFFECTS CELL VISCOELASTICITY AT SMALL AND LARGE DEFORMATIONS

Plectin is a giant protein of the plakin family that crosslinks the cytoskeleton of mammalian cells. It is expressed in virtually all tissues and its dysfunction is associated with various diseases such as skin blistering. There is evidence that plectin regulates the mechanical integrity of the cytoskeleton in diverse cell and tissue types. However, it is unknown how plectin modulates the mechanical response of cells depending on the frequency and amplitude of mechanical loading. Here we demonstrate the role of plectin in the viscoelastic properties of fibroblasts at small and large deformations by quantitative single-cell compression measurements. To identify the importance of plectin, we compared the mechanical properties of wild type ($Plec^{+/+}$) fibroblasts and plectin knockout ($Plec^{-/-}$) fibroblasts. We show that plectin knockout cells are nearly 2-fold softer than wild type cells, but their strain-stiffening behaviour is similar. Plectin deficiency also caused faster viscoelastic stress relaxation at long times. Fluorescence recovery after photobleaching experiments indicated that this was due to 3-fold faster actin turnover. Short-time poroelastic relaxation was also faster in $Plec^{-/-}$ cells as compared to $Plec^{+/+}$ cells, suggesting a more sparse cytoskeletal network. Confocal imaging indicated that this was due to a marked change in the architecture of the vimentin network, from a fine meshwork in wild type cells to a bundled network in the plectin knockout cells. Our findings therefore indicate that plectin is an important regulator of the organization and viscoelastic properties of the cytoskeleton in fibroblasts. Our findings emphasize that mechanical integration of the different cytoskeletal networks present in cells is important for regulating the versatile mechanical properties of cells.

This chapter is published in *Biophysical Journal*. The paper was co-authored by **J. P. Conboy**, M. G. Lettinga, N. van Vliet, L. Winter, G. Wiche, F. C. MacKintosh and G. H. Koenderink. **J. P. Conboy** and M. G. Lettinga made equal contributions.

3.1. INTRODUCTION

Cells possess an extraordinary capacity to preserve their structural integrity in physically stressful environments. In mammalian cells, the main structure governing mechanical protection is the cytoskeleton, a biopolymer network that extends throughout the cell's interior [216]. The cytoskeleton is composed of four distinct biopolymers: actin, microtubules, intermediate filaments and septins, each playing specific roles in different cellular functions [217]. The filaments differ in their mechanical and dynamical properties. With respect to mechanics, intermediate filaments and septins are the softest, with a persistence length of only ~1 μm [218, 219], while actin filaments and microtubules are stiffer, with persistence lengths of ~10 μm and several millimeters, respectively [220]. With respect to dynamics, actin filaments and microtubules have high polymerization and depolymerization rates, while intermediate filaments and septins form more stable polymers [217]. Each cytoskeletal filament is organized into higher-order structures such as networks or bundles by their own dedicated set of accessory proteins such as crosslinker proteins and polymerization factors [221, 222, 223, 224]. Cell-free reconstitution experiments and theoretical models have shown that crosslinker proteins sensitively control the elastic properties of cytoskeletal networks, including the elastic modulus, rupture strength, and ability to strain-stiffen [225]. In addition, the dynamic binding and unbinding of actin crosslinkers introduces time-dependent viscoelastic properties [226, 227, 228].

The mechanical functions of the different cytoskeletal filament systems have traditionally been studied separately. Recently, however, there has been growing appreciation for the importance of physical and biochemical coupling of the filaments in the ability of cells to resist, transmit and generate mechanical forces [217]. Spectraplakin proteins play a particularly important role in mechanical integration of the cytoskeleton by forming crosslinks between different filament types [229, 230]. Spektraplakins are large (>500 kDa) and evolutionarily conserved crosslinker proteins that are part of the spectrin superfamily. Plectin is a widely expressed member of this protein family that serves as a crosslinker between actin and intermediate filaments [231, 232]. Human plectin is encoded by a single gene located on chromosome 8 [233], but alternative splicing creates 12 different plectin isoforms expressed in different combinations in different cell and tissue types [234].

All plectin isoforms have a C-terminal intermediate filament-binding domain and an actin-binding domain (ABD) located close to their N termini. Moreover, they all share a spectrin repeat-containing plakin domain and a central alpha-helical rod domain that mediates plectin dimerization. By contrast, the N-terminal head domain is variable. This domain controls the cellular localization of each plectin isoform by docking to distinct interaction partners such as the nucleus (plectin isoform P1), junctional complexes like focal adhesions (isoform P1f), or microtubules (isoform P1c) [234]. As a consequence, plectins simultaneously crosslink intermediate filaments to actin filaments and connect these cytoskeletal networks to microtubules, the nucleus, and adhesion complexes [235]. Through its connector role, plectin is essential for a stable cytoarchitecture and mechanical integrity of epithelial and endothelial tissues

[236, 237, 65, 238]. Accordingly, plectin mutations result in multiple multisystemic diseases known as plectinopathies [239, 240, 241]. A well-known example is epidermolysis bullosa simplex (EBS-MD), a disease characterised by spontaneous skin blistering, impaired wound healing and muscular dystrophy [242]. At the cell level, dermal fibroblasts from EBS-MD patients exhibit an anomalous vimentin network architecture, with vimentin intermediate filaments organized in bundles instead of meshworks [242]. Plectin knockout in keratinocytes results in similar changes in the keratin cytoskeleton, from keratin meshworks to bundles [243].

In mesenchymal cells, plectin crosslinks vimentin to different actin structures, including the actin cortex of mitotic cells [244, 245], invadopodial actin networks of invading cancer cells [246], and actin stress fibres in adherent cells [247, 248]. One function of plectin-mediated crosslinking of actin and vimentin is to control the transmission of actin-myosin-based forces in cells, both in 2D-adherent conditions and in 3D matrices [248, 249]. Given this mechanical function, plectin-mediated crosslinking would also be expected to influence the stiffness of the cytoskeleton. In biochemically reconstituted actin-vimentin networks, plectin-mediated crosslinking indeed causes network stiffening [250]. Surprisingly, however, measurements of plectin's contribution to cellular elasticity are contradictory. In mouse skin fibroblasts probed with magnetic twisting cytometry, plectin was found to increase cell stiffness [249]. Similar behaviour was observed for myoblasts probed with magnetic tweezers [251]. However, this same study showed an opposite behaviour for keratinocytes, where plectin knockout made cells stiffer. Atomic force microscopy (AFM) on malignant epithelial cells showed a negligible affect of plectin knock-down on cell stiffness [252]. These discrepancies could point to cell-type-specific functions of plectin, caused, for instance, by different expression levels of the various plectin isoforms. Differences in the experimental assays could also contribute to the reported discrepancies. It is well-known that values of cell stiffness and viscosity vary substantially depending on the level of applied mechanical stress, the rate of deformation, the geometry of the measurement probe, the location probed in the cell, and the extracellular microenvironment [71]. Prior studies of the role of plectin in cell mechanics were based on local probing by AFM-based nanoindentation or magnetic tweezer manipulation of micron-sized beads attached to focal adhesions. This type of local probing has been shown to be more sensitive to cortical actin than to cytoplasmic intermediate filaments [165, 53]. Furthermore, these methods are limited to small deformations, whereas cells in the body tend to experience large deformations where nonlinear elastic properties become important.

Here we investigate the mechanical role of plectin in fibroblasts at small and large deformations by single-cell compression with our newly developed device that affords high precision in strain rate and amplitude [253]. To measure the whole-cell mechanical response, we confined the cells between two nonadhesive parallel plates, a deliberate design choice to isolate the intrinsic contributions of the cytoskeleton independent of adhesion-mediated effects, thus preventing any contractile active response of the cells to compression. To identify the role of plectin, we compare the linear viscoelastic properties of wild type versus plectin knockout cells in response to small amplitude oscillatory and step strains. We find that plectin has a significant impact on bulk cell stiffness and also influences the time-dependent poroelastic and viscoelastic behaviour of the

cells. Strain ramp experiments compressing the cells into the nonlinear elastic regime confirm that the plectin knockout cells are softer than wild type cells at small strains, but show similar strain-stiffening behavior. Finally, under cyclical straining, we observed that wild type cells are initially stiffer than plectin knockout cells, but attain a similar stiffness as plectin knockout cells upon repeated loading, suggesting that plectin shields the cytoskeleton from damage by providing transient crosslinks that dissociate under load.

3.2. RESULTS

3.2.1. PLECTIN INFLUENCES ACTIN AND VIMENTIN ORGANIZATION IN FIBROBLASTS

The aim of this study was to determine the contribution of plectin to the viscoelastic behaviour of fibroblasts at small and large deformations. To this end, we made a side-by-side comparison between immortalized mouse fibroblasts derived from transgenic plectin wild-type ($Plec^{+/+}$) and plectin-deficient ($Plec^{-/-}$) mice (for details see [254, 255, 256]). Western blot analysis confirmed that the $Plec^{-/-}$ cells lack plectin, while the expression levels of actin and vimentin are comparable to wild type cells (Figure 3.1C and Figure S5.6). To measure the whole-cell mechanical response, we confined the cells between two parallel plates that were made nonadhesive to prevent any active response of the cells to compression.

To characterize the impact of plectin knockout on the organization of the cytoskeleton in this geometry, we first imaged cells confined between two nonadhesive coverslips spaced apart by a distance of 10 μm (Figure 3.1A). This separation distance is smaller than the average cell size determined by imaging flow cytometry measurements (Figure S3.9), thus allowing us to image our cells in a compressed state. $Plec^{+/+}$ and $Plec^{-/-}$ cells had comparable diameters (22.4 ± 3.1 μm and 22.2 ± 3.1 μm, respectively, see Figure S3.9A) and nucleus sizes (8.3 ± 1.4 μm and 8.2 ± 1.4 μm, respectively, see Figure S3.9B). Side projections (Figure 3.1A) and top views (Figure 3.1B) reconstructed from confocal z-stacks showed that the cells are quasi-spherical with a radially rather uniform distribution of both actin and vimentin. Actin predominantly lines the plasma membrane at the cell periphery, but also extends into the cell interior (Figure 3.1D). By contrast, vimentin is primarily distributed between the actin-rich region and the nucleus (Figure 3.1D). Most strikingly, the vimentin network in the $Plec^{-/-}$ cells displays increased bundling compared to the finer vimentin meshwork in $Plec^{+/+}$ cells (second column in Figure 3.1D, compare top and bottom rows). This effect is strongly reminiscent of earlier observations of vimentin filament bundling in EBS-MD patient cells [242] and of keratin filament bundling in $Plec^{-/-}$ keratinocytes [257]. Furthermore, three-dimensional reconstructions of confocal z-stacks reveal that vimentin filaments in $Plec^{+/+}$ cells are positioned in close proximity to the nuclear envelope, forming a filamentous network that encases the nucleus (Figure 3.1E, left). This structure has been referred to as the vimentin nuclear cage [258] and has been shown to protect the nucleus from mechanical stress [203]. By contrast, the thicker vimentin bundles in $Plec^{-/-}$ cells no longer form

such a protective meshwork structure around the nucleus (Figure 3.1E, right).

To better compare the spatial distributions of actin and vimentin within the cell interior, we calculated radial distributions of the intensities. For individual cells, this showed a considerable overlap between the actin and vimentin localization (Figure 3.1D, right). To analyze this for many cells, we constructed 'average cells' by computing the average of maximum intensity projections from 2 µm thick confocal slices centered at the cell equator, adjusting for variations in cell size (Supplementary Figure 1). This analysis revealed similar nuclear distributions between $Plec^{+/+}$ and $Plec^{-/-}$ cells and confirmed a significant region of overlap between the actin and vimentin networks (Figure 3.1F). This observation suggests that the two networks interpenetrate. We observed subtle differences between $Plec^{+/+}$ and $Plec^{-/-}$ cells. The vimentin network on average extended to the cell periphery in $Plec^{-/-}$ cells but not in $Plec^{+/+}$ cells. The peak intensity for actin was close to the peak intensity for vimentin in $Plec^{+/+}$ cells but closer to the cell periphery in $Plec^{-/-}$ cells. We conclude that plectin has a significant impact on the organization of the actin and especially the vimentin cytoskeleton.

3.2.2. SMALL AMPLITUDE OSCILLATORY COMPRESSION SHOWS THAT PLECTIN STIFFENS CELLS

To investigate how plectin removal impacts the mechanical response of the cells to small deformations, we used a single-cell compression device equipped with a wedged flexible cantilever. We subjected the cells to an oscillatory compressive strain with a small amplitude (~1%) and stepwise increasing oscillation frequency from 0.1 Hz to 10 Hz (Figure 3.2A). From the resulting force on the cantilever, we calculated the real and imaginary parts of the frequency-dependent complex apparent Young's modulus, $E^*(f)$. The real part corresponds to the storage modulus $E'(f)$, which reflects the elastic component of the response (closed symbols in Figure 3.2B). The imaginary part corresponds to the loss modulus $E"(f)$, which reflects the viscous component of the response (open symbols in Figure 3.2B). Both moduli show a qualitatively similar dependence on frequency for the $Plec^{+/+}$ cells (blue) and $Plec^{-/-}$ cells (red). In both cases, E' is larger than E'', in particular at low frequencies, consistent with predominantly solid-like behaviour. Furthermore, the elastic moduli increase with a weak power law dependence on frequency, characteristic for mammalian cells [169]. At the highest frequency, the elastic and viscous moduli tend towards a crossover. In quantitative terms, however, we see a clear difference: The moduli of $Plec^{+/+}$ cells are greater than those of $Plec^{-/-}$ cells by a factor ~ 1.4, indicating that plectin stiffens the cells. Additionally, we observe a shift in the projected crossover frequency for the elastic and viscous moduli, from ~12 Hz in $Plec^{+/+}$ cells to ~16 Hz in $Plec^{-/-}$ cells, signifying that $Plec^{-/-}$ cells may maintain an elastic mechanical response over a broader frequency range.

For a more in-depth comparison of the $Plec^{+/+}$ and $Plec^{-/-}$ cells, we fitted the experimental data to phenomenological models that describe the rheology in terms of a small number of characteristic material parameters. We first attempted to describe the data in terms of the structural damping law, an established phenomenological model of cell rheology [172, 173]. This model (see Equation 3.4) has the benefit that it only has three material parameters, namely the scaling factor E_0, power law exponent α, and cytoplasmic

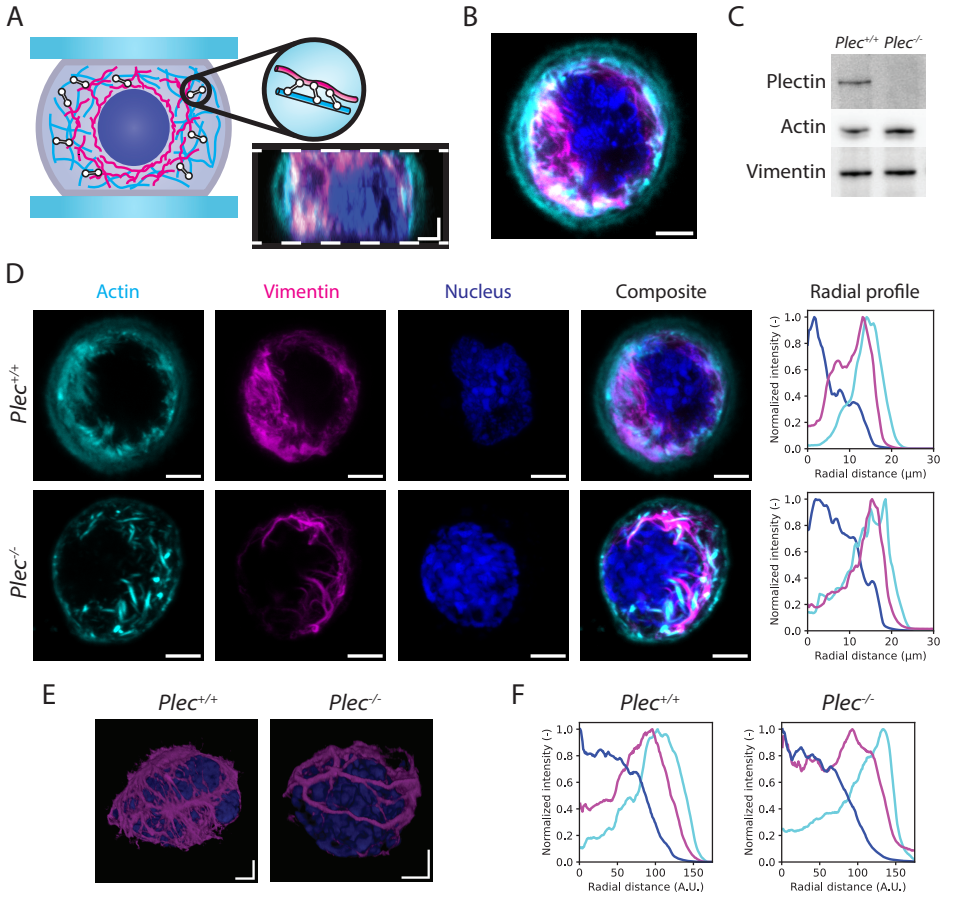

Figure 3.1: Plectin influences the organization of the actin and vimentin cytoskeleton in nonadherent fibroblasts. (A) The schematic shows how live fibroblasts were imaged while trapped between two nonadhesive surfaces. Plectin (white) forms crosslinks between actin filaments (cyan) and vimentin intermediate filaments (magenta). The image shows a side projection of a $Plec^{+/+}$ fibroblast. White dashed lines indicate the two confining surfaces. Scale bars are 3 μm. (B) Single confocal slice through the cell equator of a $Plec^{+/+}$ fibroblast. SiR-labeled actin (cyan) is concentrated at the cortex, while vimentin-GFP (magenta) surrounds the nucleus (dark blue). Scale bar 3 μm. (C) Immunoblot analysis of cell lysates from $Plec^{+/+}$ and $Plec^{-/-}$ cells using antibodies to plectin, actin and vimentin. (D) Representative images of $Plec^{+/+}$ and $Plec^{-/-}$ cells. Images are maximum intensity projections of 2 μm thick confocal sections at the cell equator. Actin is located largely at the cell periphery, while vimentin is located closer to the nucleus. Average radial profiles of the fluorescent signals (right) were calculated by taking normalized intensities around concentric circles from the center of the image. The radial distance is set to zero at the cell center. We observe a significant overlapping region between actin and vimentin. (E) 3D volume renderings of vimentin and the nucleus. In the $Plec^{+/+}$ cell, a cage-like vimentin structure surrounds the nucleus, whereas in the $Plec^{-/-}$ cell, vimentin forms bundles that no longer surround the nucleus on all sides. (F) We repeat the radial profile procedure shown in panel D by averaging the images of multiple cells (N=10 for both conditions) and computing the radial average. Average profiles resembled those of individual cells. Note that the scale of the 'average cell' images and line profile plots are in arbitrary units since the cells were rescaled to compensate for variations in cell size.

viscosity μ. We previously found that this model could capture the compressive modulus of mouse embryonic fibroblasts rather accurately [253]. However, we found that it strongly underestimated the viscous modulus of the fibroblasts studied in this work, particularly at low frequencies (Figure S3.11). Apparently, we need to include an additional viscous contribution that captures slow stress relaxation. Therefore, we developed a new fractional rheological model inspired by recent work [259, 260] that combines short-term power-law stress relaxation and long-term exponential stress relaxation. This model (see Equation 3.5) has five free parameters: the elastic modulus k representing the stiffness of the material, the dashpot viscosity η_1 capturing long-term viscous dissipation, the spring-pot parameter c_β describing the intermediate viscoelastic behaviour, the fractional exponent β characterising power-law scaling with frequency, and finally the Newtonian viscous term η_2 capturing the response of the cytoplasm. As shown in Figure 3.2B (solid lines), this model provides an accurate and self-consistent fit of E' and E''. The only fitting parameter that is significantly different between the *Plec*$^{+/+}$ and *Plec*$^{-/-}$ cells is the elastic modulus k, which decreases from $k = 232 \pm 20$ Pa in *Plec*$^{+/+}$ cells (N=36) to $k = 120 \pm 20$ Pa in *Plec*$^{-/-}$ cells (N=27) (Figure 3.2C). The two parameters characterizing the power-law scaling behavior, β and c_β, are comparable between *Plec*$^{+/+}$ and *Plec*$^{-/-}$ cells. Likewise, the dashpot viscosity η_1 and Newtonian damping term, η_2, were unchanged. We conclude that plectin only affects the elastic properties of the cytoskeleton at small deformations, within the frequency range probed here.

3.2.3. PLECTIN AFFECTS POROELASTIC AND VISCOELASTIC STRESS RELAXATION

The oscillatory compression measurements suggest that there is significant energy dissipation on time scales beyond 10 seconds, i.e., at frequencies below the measurement limit of 0.1 Hz. Since many organs and connective tissues experience deformations that persist for minutes [261, 262], we decided to measure the viscoelastic behaviour of the *Plec*$^{+/+}$ and *Plec*$^{-/-}$ cells on longer timescales via step strain experiments (Figure 3.1A top). We subjected cells to a rapid compression by a distance of 1 µm, corresponding to a small (~ 0.05) strain within the linear elastic regime. We then measured the stress relaxation dynamics whilst holding this displacement for 80 s (Figure 3.1A bottom). As shown in Figure 3.1B, both *Plec*$^{+/+}$ cells (blue solid line) and *Plec*$^{-/-}$ cells (red solid line) display marked stress relaxation over this time scale (for individual cell data see Figure S3.12). The stress is overall larger for the *Plec*$^{+/+}$ cells as compared to the *Plec*$^{-/-}$ cells, indicating that plectin depletion causes cell softening, consistent with the small amplitude oscillatory data. In a log-log representation, we can distinguish multiple relaxation regimes. At short times (< 0.1 s, indicated by a grey background in Figure 3.1B), we observe an exponential stress decay. Here, the mechanical response to compression is known to be dominated by the flow of cytosol through the porous elastic structure provided by organelles and the cytoskeleton [263] (see schematic inset of Figure 3.1B). Beyond 0.1 s, the stress relaxation response transitions to a power-law time dependence, reflecting a broad distribution of relaxation processes. In this regime we indeed expect power-law viscoelastic stress relaxation just like in the small amplitude oscillatory measurements. This is followed by exponential relaxation at long times.

To test how plectin changes the poroelastic and viscoelastic response of the cells, we fitted the stress relaxation data in the short and intermediate time regimes to corresponding theoretical model predictions. The short-time poroelastic response is expected to be single-exponential (Equation 3.8) with a characteristic poroelastic decay time τ_p, assuming that the cell can be approximated as a simple biphasic material consisting of a porous elastic meshwork with an elastic modulus, E_0, bathed in an interstitial fluid (cytosol) of viscosity μ. The data were well-described by this model (dashed lines in Figure 3.1B). From the fits, we found that plectin knockout significantly softens the cells, with an instantaneous elastic modulus (stiffness of the cell at t=0) of $E_0 = 230 \pm 30$ Pa for

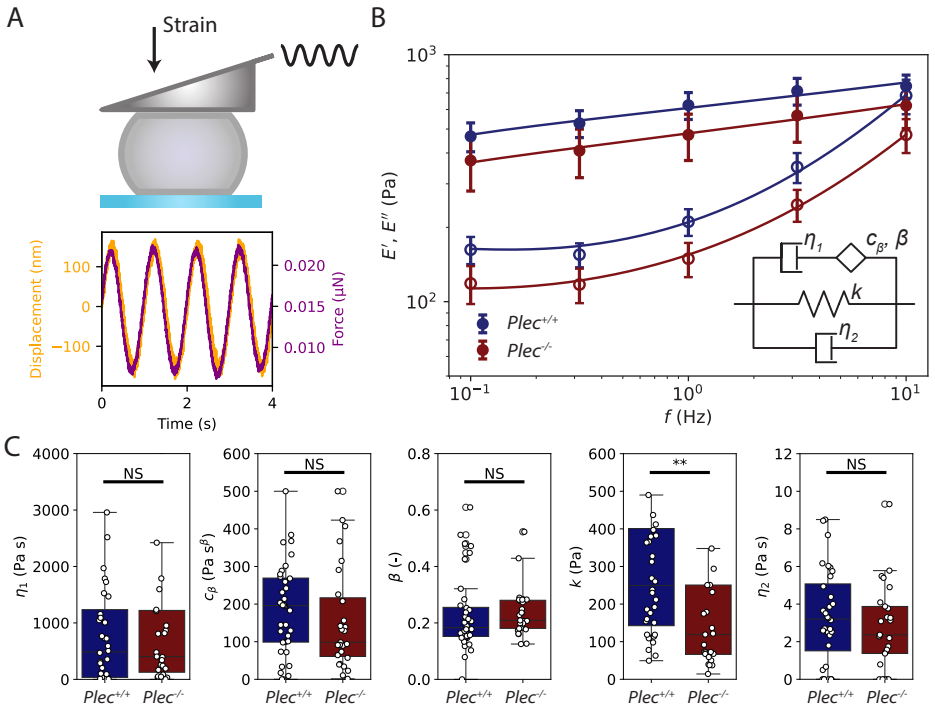

Figure 3.2: Small-strain oscillatory compression measurements on single fibroblasts reveal that $Plec^{+/+}$ cells are stiffer than $Plec^{-/-}$ cells. (A) Top: Illustration depicting a single cell positioned between a glass coverslip and the wedged cantilever. Bottom: Typical measurement for a $Plec^{+/+}$ cell at an oscillation frequency of 1 Hz, showing the cantilever's applied displacement (black; left y-axis) and the corresponding observed force (red; right y-axis) over time. (B) Storage (E') and loss (E'') linear compressive moduli (closed and open symbols, respectively), measured for oscillation frequencies between 0.1 Hz and 10 Hz for $Plec^{+/+}$ cells (N=36, blue) and $Plec^{-/-}$ cells (N=27, red). Fits on the average data (solid lines) to the fractional rheological model (inset) from Equation 3.5. (C) Material parameters determined from the fits of the fractional rheological model for each cell individually. The 5 fitting parameters are the dashpot viscosity η_1 capturing long-term viscous dissipation, the spring-pot parameter c_β describing the intermediate viscoelastic behaviour, the fractional exponent β characterising power-law scaling with frequency, the elastic modulus k representing the stiffness of the material, and the Newtonian viscous term η_2 capturing the response of the cytoplasm. Only the elastic parameter k changes upon plectin knockout, whereas all other parameters are unchanged. Asterisks indicates statistically significant differences (** denotes P<0.01), N.S. denotes non-significant differences.

Plec$^{-/-}$ cells compared to $E_0 = 360 \pm 30$ Pa for *Plec*$^{+/+}$ cells (Figure 3.1C left). Furthermore, poroelastic relaxation occurs more rapidly upon plectin knockout, with a poroelastic time scale of $\tau_p = 0.040 \pm 0.001$ s in *Plec*$^{-/-}$ cells as compared to $\tau_p = 0.030 \pm 0.001$ s in *Plec*$^{+/+}$ cells (Figure 3.1C middle).

The difference in poroelastic time scales suggests that the porosity of the cytoplasm might be higher in *Plec*$^{-/-}$ cells compared to *Plec*$^{+/+}$ cells. To test this idea, we first estimated the poroelastic diffusion constant D_p from the poroelastic time scales according to:

$$\tau_p \sim L^2/D_p \tag{3.1}$$

For simplicity, we assume that the elastic network of cytoskeleton and organelles is homogeneous across the distance between the cell membrane and nuclear envelope so we can define the characteristic length scale L as the distance between the cell membrane and the nuclear envelope. We can estimate this distance from the earlier mentioned flow cytometry measurements of the cell and nucleus sizes (Figure S3.9). *Plec*$^{+/+}$ and *Plec*$^{-/-}$ cells had varying sizes but both displayed a proportional increase of cell size with nucleus size (Figure S3.9E,F), resulting in a rather constant nucleus-to-cell diameter ratio of ~ 0.74 in both cases. We therefore assume a characteristic length scale of $L = 7.1\mu$m and thus estimate $D_p = (1500 \pm 100)\ \mu m^2/s$ for *Plec*$^{+/+}$ cells and $D_p = (2200 \pm 100)\ \mu m^2/s$ for *Plec*$^{-/-}$ cells (Figure 3.1C right). Note that if we assume fluid transport also occurs in the nucleus, so L equals the cell size, we still find a larger D_p in *Plec*$^{-/-}$ cells (see supplementary information for more details). The poroelastic diffusion constant D_p depends on the pore radius ξ of the cytoskeletal network, the cytosol viscosity μ, and the elastic modulus of the drained cytoskeletal network E according to [263]:

$$D_p \sim E\xi^2/\mu \tag{3.2}$$

To measure the unknown cytosol viscosity and test whether it changes upon plectin knockout, we performed fluorescence recovery after photobleaching (FRAP) on the cytoplasmic dye CellTracker Orange. We photobleached a small (1 μm) circular region and observed the recovery of the fluorescent signal (Figure 3.1D and Figure S3.13). By fitting the individual recovery curves to Equation 3.10, we recovered comparable recovery times for *Plec*$^{+/+}$ cells ($\tau_{FRAP} = 0.53 \pm 0.05$s) and *Plec*$^{-/-}$ cells (0.50 ± 0.06s), indicating comparable cytosol viscosities. We estimate a cytoplasmic viscosity $\mu \simeq 4$ Pa s for both *Plec*$^{+/+}$ and *Plec*$^{-/-}$ cells using the Stokes-Einstein relation for the diffusion of small molecules ($D = \frac{k_B T}{6\pi\mu R_h}$) [264], assuming a hydrodynamic radius $R_h \simeq 0.5$ nm [265] for the cytoplasmic dye. Encouragingly, this viscosity value is consistent with the cytoplasmic viscosity ($\eta_2 = 3.3 \pm 0.4$ Pa s) inferred by fitting the oscillatory compression data to the fractional rheological model (Figure 3.2C), lending support for this model. Plugging the poroelastic diffusion times from the step-strain data and the cytosol viscosity from the FRAP data into Equation 3.2, we calculate that the cytoskeletal meshwork of *Plec*$^{-/-}$ cells ($\xi = 7.2\mu$m) has larger pores than for *Plec*$^{+/+}$ cells ($\xi = 4.9\mu$m) by a factor of ~ 1.5. Interestingly, this is consistent with the observation that the plectin knockout cells have a more open, bundled vimentin cytoskeleton than wild type cells (Figure 3.1D) while having similar concentrations of vimentin and actin (Figure 3.1C).

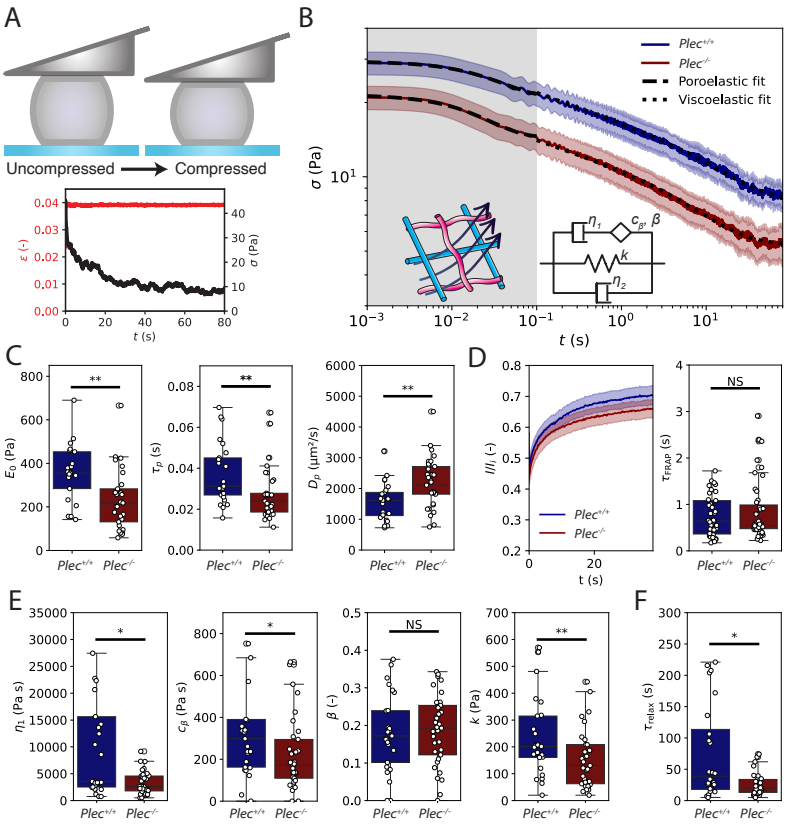

Figure 3.3: Small amplitude stress relaxation experiments for $Plec^{+/+}$ and $Plec^{-/-}$ cells. (A) Top: Schematic of the step-strain experiment (not to scale, the strain is only 0.05). Bottom: Typical measurement for a $Plec^{+/+}$ cell showing the cantilever displacement that is held constant (red; left y-axis), while the force (black; right y-axis) is measured over time. (B) Averaged stresses for $Plec^{+/+}$ cells (blue solid line, N = 25) and $Plec^{-/-}$ cells (red solid line, N = 33) over time in log-log representation. The shaded areas around the average relaxation curves represent the standard deviation. Stresses are higher for $Plec^{+/+}$ cells, indicating these cells are stiffer. At short time scales (from 0.001 s to 1 s, indicated by the grey background), the cells display exponential stress relaxation characteristic of a poroelastic material, where fluid flows through the cytoskeletal network (inset drawing). Fits to the poroelastic model (equation 3.8) are shown as dashed lines. At later times (from 0.1 s to 80 s, white background) the data are well-described by the same fractional rheological model (inset schematic) that also captures the oscillatory data, transformed to the time domain (fits shown as dotted lines; equation 3.9). (C) Elastic moduli E_0 (left) and poroelastic time scales τ_p (middle) determined from the poroelastic model fits for individual cells. The poroelastic diffusion coefficient D_p (right) calculated from τ_p data is faster for $Plec^{-/-}$ cells than for $Plec^{+/+}$ cells. (D) Comparison of cytoplasmic diffusion via fluorescence recovery after photobleaching (FRAP). Left: average FRAP recovery curves for $Plec^{+/+}$ and $Plec^{-/-}$ cells. The error band shows the standard error. Right: We measure no significant difference between the FRAP recovery times, τ_FRAP, of $Plec^{+/+}$ and $Plec^{-/-}$ cells. (E) Material parameters obtained from the fractional rheology fits, showing the dashpot viscosity η_1 describing long-term viscous dissipation, the spring-pot parameter c_β describing the intermediate viscoelastic behaviour, the fractional exponent β characterising power-law scaling with frequency, and the elastic modulus k representing cell stiffness. (F) Viscoelastic stress relaxation time scale τ_relax calculated from the data in panel E using Equation 3.3. Asterisks indicate statistically significant differences (* denotes P<0.05, ** P<0.01), N.S. denotes non-significant differences.

We next turned to the viscoelastic stress relaxation regime at intermediate times (0.1 s to 80 s), which should be describable by the same fractional rheological model used to model the oscillatory measurements (inset showing a schematic of the model in Figure 3.1B). To test this, we converted the model from the frequency domain (Equation 3.5) to the time domain (Equation 3.9) , enabling a direct comparison of the characteristic mechanical parameters. Note that the model involves 4 fit parameters in the time domain instead of 5 parameters in the frequency domain, since the 5th parameter, η_2, is reduced to a Dirac delta function after the Laplace transform. The fractional rheology model indeed fitted the force–relaxation curves well (dotted black lines in Figure 3.1B), returning similar conclusions as the oscillatory measurements. Again, we observed a significant decrease in the elastic modulus k, from $k = 250 \pm 30$ Pa for *Plec*$^{+/+}$ cells to $k = 170 \pm 30$ Pa in *Plec*$^{-/-}$ cells (Figure 3.1E) but an unchanged power-law scaling exponent β. However, contrary to the oscillatory measurements, the viscous modulus η_1 determined from the stress relaxation significantly decreased upon plectin knockout, from $\eta_1 = 8000 \pm 2000$ Pa for *Plec*$^{+/+}$ cells to $\eta_1 = 3700 \pm 500$ Pa for *Plec*$^{-/-}$ cells. The stress relaxation data are likely more accurate here because we could measure up to time scales of 80 s, much longer than in oscillatory measurements. We can calculate the viscoelastic relaxation time, τ_{relax}, that marks the transition from a power-law decay at intermediate times to an exponential relaxation regime at longer times inaccessible in the oscillatory measurements according to [260]:

$$\tau_{\text{relax}} = (\eta_1 / c_\beta)^{\frac{1}{1-\beta}} \tag{3.3}$$

This timescale indicates when the dashpot characterizing long-time scale relaxation processes (beyond ~ 10s) in the cytoskeleton begins to dominate stress relaxation [266]. We observed a statistically significant decrease in this time scale, from $\tau_{\text{relax}} = 75 \pm 15$ s for *Plec*$^{+/+}$ cells to $\tau_{\text{relax}} = 26 \pm 4$ s in *Plec*$^{-/-}$ cells, indicating faster stress relaxation upon plectin knockout (Figure 3.1F).

On long time scales, we expect that stress relaxation could occur due to unbinding of plectin and other cytoskeletal crosslinker proteins or by cytoskeletal turnover. Actin filaments turn over as a consequence of filament depolymerization, which is catalyzed by various actin-binding proteins. Actin network turnover times are typically reported to be on the order of seconds to minutes [18, 192], which could correspond to the time scale where we observe stress relaxation. The vimentin cytoskeleton is typically reported to turnover on much longer time scales on the order of hours, via subunit exchange along the filaments and fragmentation [267]. To determine the actin and vimentin turnover rates in our cells and test whether they are changed by plectin knockout, we performed fluorescence recovery after photobleaching (FRAP) experiments on cells tagged with GFP-actin (Figure 3.4A) and GFP-vimentin (Figure S3.15). As shown in Figure 3.4B, the GFP-actin signal averaged over many cells fully recovered within 60 s for both *Plec*$^{+/+}$ and *Plec*$^{-/-}$ cells (blue and red curves, respectively; see Figure S3.14 for individual curves). Strikingly, however, the actin turnover rate as quantified by the FRAP recovery time by fits to equation 3.10 was faster in *Plec*$^{-/-}$ cells by a factor of ~3 (Figure 3.4C). By contrast, FRAP experiments on GFP-vimentin transfected cells showed negligible recovery up to times of 80 s (corresponding to the time scale probed in the

step strain experiments) for both $Plec^{+/+}$ and $Plec^{-/-}$ cells (Figure S3.15). We therefore conclude that the faster viscoelastic stress relaxation rate in the plectin knockout cells at long times is likely due to faster actin turnover.

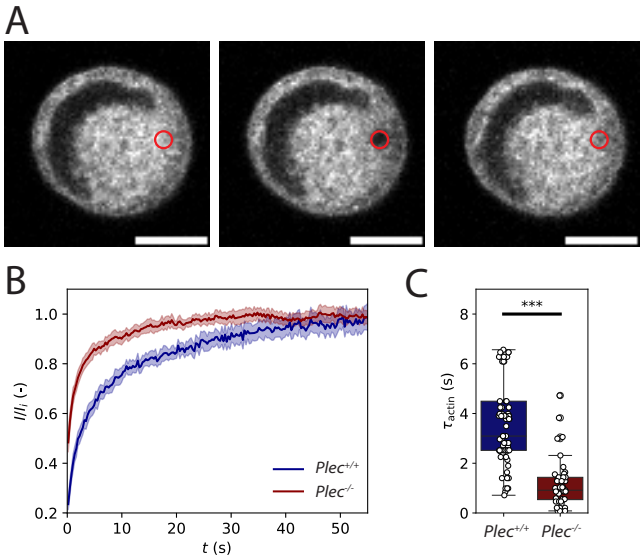

Figure 3.4: Comparison of actin turnover rates in $Plec^{+/+}$ and $Plec^{-/-}$ cells confined between two nonadhesive surfaces via fluorescence recovery after photobleaching (FRAP) experiments. (A) We bleach a small (1 µm) circular region (red open circle) in a region of the cell where we observe an actin network (tagged with GFP-actin) and monitor the fluorescence recovery over time. Note that the large dark region within the cell is occupied by the nucleus. Scale bar 10 µm. (B) Averaged FRAP recovery curves for GFP-actin-tagged $Plec^{+/+}$ cells (blue, N = 54) and $Plec^{-/-}$ cells (red, N = 35). In both conditions, the fluorescence fully recovers, but with a significantly higher rate in the $Plec^{-/-}$ cells. (C) FRAP recovery times τ_{actin} obtained by fitting to the individual recovery curves (shown in Supplementary Figure S3.14). We find average values of $\tau_{\text{actin}} = 3.6 \pm 0.4$s for $Plec^{+/+}$ cells and 1.4 ± 0.2 for $Plec^{-/-}$ cells, indicating ~3-fold faster actin turnover upon plectin knockout. *** indicates statistically significant differences (P<0.001).

3.2.4. PLECTIN KNOCKOUT DOES NOT IMPACT FIBROBLAST STRAIN-STIFFENING

To test the effect of plectin on the mechanical response of fibroblasts to large compressive deformations, we performed strain ramp experiments (Figure 3.5A). The cells were compressed gradually with a constant rate of 1 µm/s, which is slow enough to minimise stress from viscoelastic contributions [253]. Upon reaching the target deformation ($\epsilon \sim 0.4$), the cantilever was immediately retracted at the same rate. Figure 3.5B shows an example stress-strain cycle performed on a $Plec^{+/+}$ cell. The stress-strain curves during compression (indicated by the arrow up) and retraction (arrow down) do not overlap: for any given strain, the corresponding stress is lower during retraction than it is during compression. This hysteresis confirms the viscoelastic nature of the cells. We next

compared strain ramp experiments on $Plec^{+/+}$ cells (N = 13) and $Plec^{-/-}$ cells (N = 15) (see Figure S3.16 for individual stress-strain curves). The averaged data for the response upon compression reveal that $Plec^{-/-}$ cells are softer than $Plec^{+/+}$ cells: at any strain, the average resulting stress is lower for $Plec^{-/-}$ cells (red) than for $Plec^{+/+}$ cells (blue) (Figure 3.5C). However, the stress in both cases increases non-linearly with the applied strain. This type of compression-stiffening behavior under uniaxial load is consistent with earlier studies [176, 253].

To quantify this strain-stiffening behaviour, we defined the differential stiffness K as $K = \mathrm{d}\sigma/\mathrm{d}\epsilon$. The stiffness is constant ($K = K_0$) up to a certain onset strain ϵ^*, above which stiffening occurs (Figure 3.5D inset). Strikingly, the stiffness at large compressive stresses of 80 Pa is comparable for $Plec^{+/+}$ cells (blue) and $Plec^{-/-}$ cells (red). Also, normalizing the stiffness by $K = K_0$ and the stress by σ^* collapses the data onto a single master curve (Figure 3.5D). At large deformations, the stiffness approaches a power-law dependence on stress with best-fit values for the power law exponent being similar for $Plec^{+/+}$ cells (0.49±0.06) and $Plec^{-/-}$ cells (0.49±0.05). We note that the nonlinear regime covers less than a decade in stress, so these values should be taken as indicative only. The short dashed lines in Figure 3.5D show that the exponents lie somewhere between 0.5 and 1.

As shown in Figure 3.5E (left), the linear modulus K_0 is about 2-fold higher for the $Plec^{+/+}$ cells (440 ±70 Pa) as compared to the $Plec^{-/-}$ cells (220 ±40 Pa). This effect is consistent with the 1.7-fold difference found by small amplitude oscillatory and step strain measurements. The onset stress for stress-stiffening (σ^*) is also higher for $Plec^{+/+}$ cells (22±5Pa) as compared to $Plec^{-/-}$ cells (13±5Pa), consistent with their higher modulus (Figure 3.5E, right). The corresponding onset strains for strain-stiffening (ϵ^*) are therefore only slightly different between $Plec^{+/+}$ cells (0.063 ±0.008) versus $Plec^{-/-}$ cells (0.042 ± 0.004) (Figure 3.5E, middle).

3.2.5. REPEATED COMPRESSION SOFTENS WILD TYPE CELLS MORE THAN PLECTIN KNOCKOUT CELLS

In many organs, such as the heart, skin and lungs, cells are subject to repeated compression. To test whether plectin knockout changes the mechanical response of fibroblasts upon repeated loading, we applied five subsequent linear compression-decompression strain ramps with an amplitude of 5 µm and strain rate of 1 µm/s (Figure 3.6A). Figure 3.6B shows a typical example of the strain (yellow) and stress (purple) for a $Plec^{+/+}$ cell. In each subsequent cycle, we see that the stresses decrease for every given strain. To rule out the possibility that this softening was due to cell flattening, we performed widefield fluorescence imaging to monitor for possible changes in cell diameter or other morphological features. We found that the cell diameter returned to its original value after each cycle, indicating that no gross shape changes occurred with repeated compression (Figure S3.17). The cell contours remained smooth as long as the strain remained below 0.5, beyond which point cells often started to bleb as a sign of damage.

To quantify the degree of softening upon repeated loading-unloading cycles, we calculated the differential stiffness K for each cycle of deformation, following the same procedure as for the single cycle compressive ramps. For $Plec^{+/+}$ cells we found a substantial reduction in cell stiffness in the linear regime between the first and second cycle, with

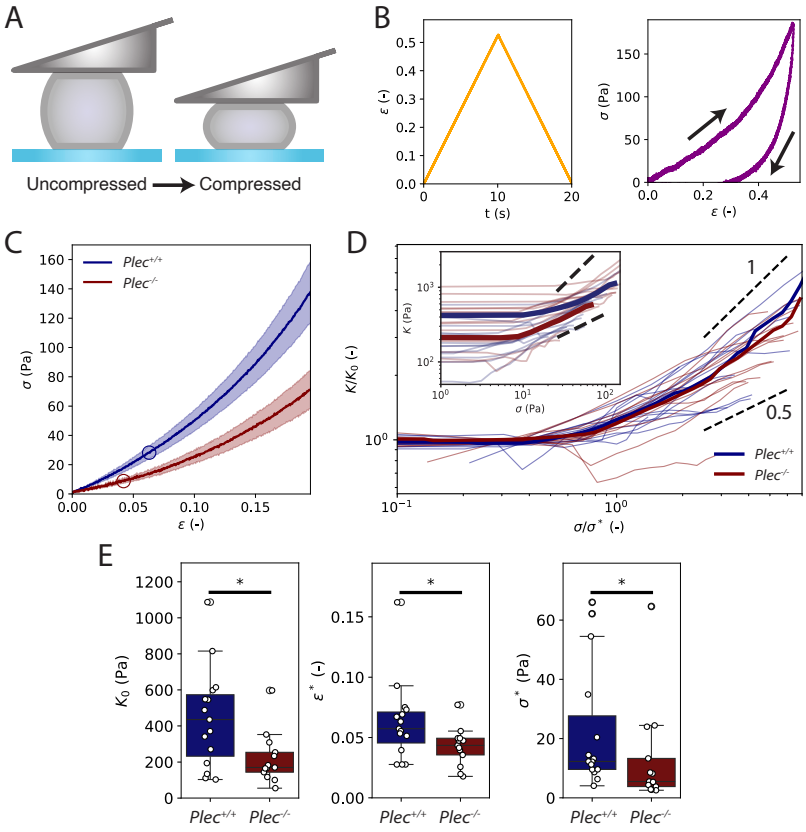

Figure 3.5: Strain ramp measurements of the nonlinear elastic response of $Plec^{+/+}$ and $Plec^{-/-}$ cells to large uniaxial compressions. (A) Schematic of the experiment where cells are compressed by gradually lowering the cantilever at a constant rate until a target strain of ~ 0.4, and then unloaded by raising the cantilever back to its original zero-strain position. (B) Representative strain ramp measurement of a single $Plec^{+/+}$ cell, showing the applied strain (left) and concomitant stress (right). The arrows show the order of loading and unloading. (C) Average stress-strain curves for $Plec^{+/+}$ (N=15) and $Plec^{-/-}$ (N=13) cells showing that $Plec^{-/-}$ cells are softer than $Plec^{+/+}$ cells but both cell types stress-stiffen. Shaded areas around the curves show the standard error. Circles indicate the onset of strain-stiffening. (D) Differential elastic modulus, K, for individual cells, obtained by taking the numerical derivative of the stress-strain curves from individual cells shown in Supplementary Figure 9. Inset shows the raw data, main plot shows the same data with σ normalized by the onset stress σ^* and K normalized by the linear modulus K_0. $Plec^{-/-}$ cells attain a similar stiffness as $Plec^{+/+}$ cells at large stress (inset) and normalization collapses the curves onto a single master curve. The short dashed lines indicate that the stress dependence falls between power-law dependences with an exponent between 0.5 and 1. (E) Comparison of the stress-stiffening behavior of $Plec^{+/+}$ cells and $Plec^{-/-}$ cells in terms of the linear modulus, K_0 (left), onset strain, ϵ^* (middle), and onset stress, σ^* (right). $Plec^{-/-}$ cells (red) are about two-fold softer than $Plec^{+/+}$ cells (blue) and, accordingly, display a smaller onset stress. * indicates statistically significant differences ($P > 0.05$).

a further gradual reduction as cells were subjected to additional cycles (Figure 3.6C). At high stress, the stress-strain curves converged. For $Plec^{-/-}$ cells we found qualitatively

similar behavior, but the reduction of the stiffness in the linear regime between the first and subsequent cycles was comparatively minor (Figure 3.6D). To better visualize this, we tracked the value of the linear modulus K_0 as a function of cycle number. For $Plec^{+/+}$ cells, K_0 was 400 ±70 Pa in the first cycle and only 120 ±30 Pa in the fifth cycle (Figure 3.6E). By contrast, $Plec^{-/-}$ cells displayed a comparable linear modulus throughout the cycles, with average K_0 values of 180 ±30 Pa for the first cycle and 160 ±40 Pa for the fifth cycle (Figure 3.6F). Interestingly, these stiffness values are comparable to the stiffness of $Plec^{+/+}$ cells after repeated compression, strongly suggesting that the plectin crosslinkers that contribute to the modulus initially are disrupted by large compressive deformations.

3.3. DISCUSSION

The aim of this study was to determine the contribution of plectin to the viscoelastic response of fibroblasts at small and large deformations using a custom single-cell rheometer. We first assessed the linear viscoelastic response using two complementary assays: small-amplitude oscillatory compressions and stress relaxation measurements. Both assays independently confirmed that fibroblasts behave as viscoelastic solids, displaying an elastic Young's modulus, $E'(f)$, that is larger than the loss modulus, $E"(f)$, with weak dependencies of the moduli on frequency. We next applied large uniaxial strains to investigate the nonlinear elasticity of the cells. Under these conditions, the cells showed pronounced strain-stiffening, with the differential elastic modulus rising sharply beyond ~ 4% compressive strain. Both the small and large amplitude experiments showed that plectin knockout makes the mouse embryonic fibroblasts about 2-fold softer. This finding is in line with previous measurements on mouse skin fibroblasts [249] and mouse myoblasts [251]. These studies used localized measurement methods in contrast to our whole-cell compression experiments, but also found $Plec^{-/-}$ cells to be softer than $Plec^{+/+}$ cells (see Table 3.1). However, other studies reported a modest 10% increase in stiffness upon plectin knockout in mouse keratinocytes [251] and no significant change in vulvar carcinoma cells [252]. These contradictory findings could stem from variations in cell lines and cell types used and/or from the different measurement techniques employed.

A more detailed interpretation of our data aided by available theoretical models showed intriguing effects of plectin on the time- and amplitude-dependent mechanical response of fibroblasts. First, the stress relaxation measurements revealed that plectin reduced the poroelastic time scale that characterizes stress relaxation via intracellular fluid flow at short times (< 1 s) after a rapid compression [263]. By also measuring the cytosolic viscosity by FRAP measurements on a small cytoplasmic dye, we found that this effect is caused by a larger pore size of the solid phase of the cytoplasm. The solid phase comprises the cytoskeleton, nucleus, and other organelles. Confocal imaging and flow cytometry showed that the wild type and plectin knockout cells had similar sizes and also similarly sized nuclei. However, the organization of the vimentin network was drastically different, with a dense meshwork in wild type cells versus a sparse network of bundles in plectin knockout cells. This bundling is expected to increase the pore size

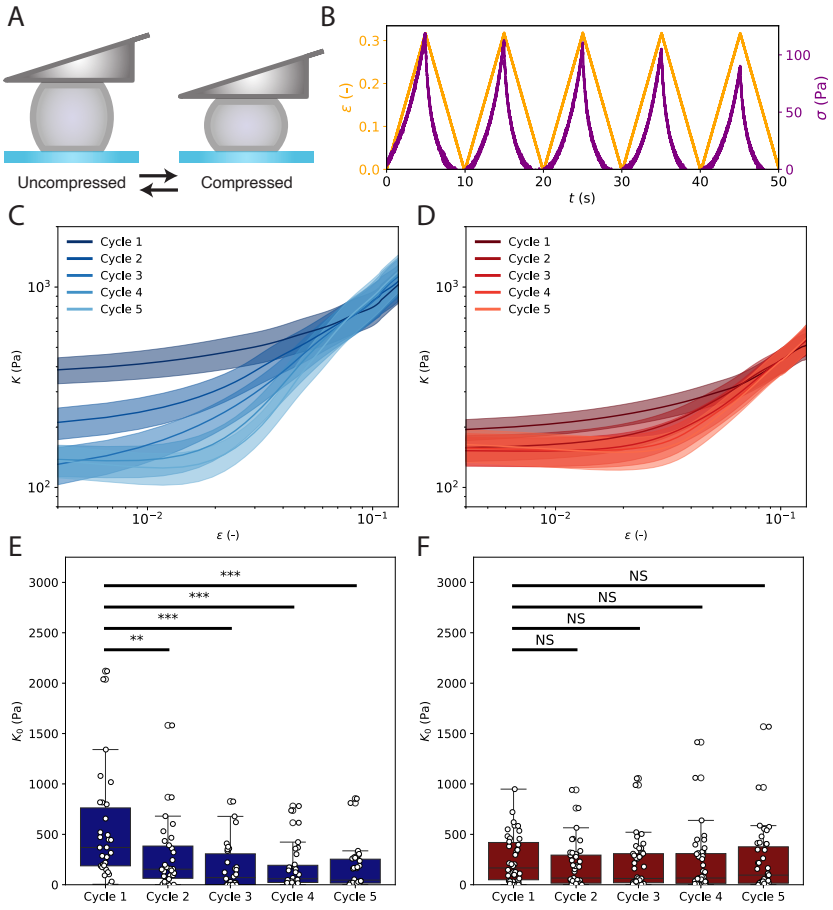

Figure 3.6: Mechanical response of $Plec^{+/+}$ and $Plec^{-/-}$ cells to repeated compressive loading-unloading cycles. (A) Schematic showing toggling between an uncompressed state (zero strain) and compressed state (strain ~ 0.4) by gradual lowering and raising of the cantilever. (B) Example measurement on a $Plec^{+/+}$ cell showing the applied strain (yellow, left y-axis) and measured stress (purple, right y-axis). For each subsequent cycle, the stress decreases. (C) Averaged dependence of the differential modulus K on applied strain for $Plec^{+/+}$ cells (N = 30). We observe a large reduction in K at small strain between the first and fifth cycle of compression, whereas the curves converge at high strain. (D) Average K/ϵ curves for $Plec^{-/-}$ cells (N = 42), showing little change in the modulus between cycles. Error bands in panels C and D represent the standard error. (E) Linear modulus K_0 as a function of cycle number for $Plec^{+/+}$ cells obtained from fitting data for individual cells (shown in Supplementary Figure 9). (F) K_0 as a function of cycle number for $Plec^{-/-}$ cells. Note that the $Plec^{+/+}$ cells show significant softening upon repeated loading (** denotes P<0.01, *** denotes P<0.001), while the $Plec^{-/-}$ cells do not soften appreciably (differences N.S.).

of the cytoskeletal matrix, which should indeed enhance the rate of poroelastic relaxation. Our data therefore suggest that plectin impacts poroelastic relaxation by regulating the organization of the vimentin cytoskeleton. This could be a consequence of its crosslinking role, both as a vimentin-vimentin and vimentin-actin crosslinker. In addi-

tion, anchoring of the vimentin network to focal adhesions and the nucleus by plectin could also help prevent vimentin filaments from collapsing into bundles.

A second finding from the stress relaxation experiments was that viscoelastic stress relaxation at times beyond the poroelastic regime obeys a fractional rheology model. According to this model, the cells display power law rheology for frequencies between 0.1 Hz and 10 Hz, characterized by a weak power law dependence of $E'(f)$ on f. Power law rheology signifies a broad distribution of characteristic time scales and is typical of mammalian cells [172]. On longer time scales, the model includes an additional stress relaxation mechanism characterized by an exponential dependence on time. The same fractional rheology model could also self-consistently capture the frequency dependence of both the elastic and viscous moduli measured through oscillatory measurements. This consistency suggests that this model, though phenomenological, provides an adequate description of the main mechanisms contributing to the cell's viscoelastic response. By fitting the data, we could compare the corresponding material parameters between $Plec^{+/+}$ and $Plec^{-/-}$ cells.

We found that removal of plectin altered the elastic component of the complex modulus, marked by a reduction in the elastic parameter k. It did not significantly change the power law scaling exponent β describing the frequency dependence at intermediate times. This result indicates that plectin's crosslinking function predominantly reinforces the elastic integrity of the cytoskeletal network, while the fundamental mechanisms governing energy dissipation at intermediate timescales remain intact. This is consistent with previous studies on reconstituted actin networks with cross-linkers [268], which demonstrated that increasing the cross-linker density markedly enhances the elastic stiffness while the frequency-dependent power-law scaling of the viscoelastic response remains largely unchanged. However, at longer timescales ($>\sim 10\,$s), we found faster stress relaxation for $Plec^{-/-}$ cells than for $Plec^{+/+}$ cells. At these long times, we expect stress relaxation to be tuned by the active turnover of the cytoskeletal filaments and/or rearrangements of the cytoskeleton via crosslinker exchange or myosin contractility [266]. Interestingly, FRAP experiments on actin-GFP transfected cells demonstrated that actin turnover was faster in plectin knockout cells and coincided with the time scale of stress relaxation in step strain experiments. Taken together, this suggests that plectin changes viscoelastic relaxation mainly by impacting actin turnover. Intriguingly, a similar increase in actin turnover has also been observed in vimentin knockout cells, where the absence of vimentin led to enhanced phosphorylation of GEF-H1 at Ser886, thereby elevating RhoA activity and promoting stress fiber assembly, which in turn accelerates actin dynamics [134]. However, we note that the environmental conditions in those experiments, where cells were adherent to flat substrates, are different from our experiments, where the cells were confined between nonadhesive plates. Consistent with these nonadherent conditions, confocal imaging did not reveal clear signs of stress fibers and only showed a fine actin meshwork. In future it will be interesting to investigate the dependence of actin turnover on plectin by comparing fibroblasts under different environmental conditions (2D versus 3D, adherent versus nonadherent).

Finally, our strain ramp experiments confirmed that plectin-deficient cells were softer than wild type cells at small deformations. However, at larger strains, both cell types showed stress-stiffening, characterized by a marked increase of the differential

Table 3.1: Summary of previously reported changes in the stiffness of single cells at small deformations upon plectin knockout for different cell model systems and with different measurement techniques.

Reference	Cell model	Measurement technique	Change in cell stiffness
Na et al. [249]	Mouse skin fibroblasts[*,a]	Magnetic twisting cytometry	*Plec*$^{-/-}$ cells ~30-60% softer
Bonakdar et al. [251]	Mouse myoblasts[*,b]	Magnetic tweezers microrheology	*Plec*$^{-/-}$ cells ~50% softer
	Mouse keratinocytes[*,b]	Magnetic tweezers microrheology	*Plec*$^{-/-}$ cells ~10% stiffer
Moch et al. [252]	Vulvar carcinoma cells[†,b]	Atomic force microscopy	No change

[*]Knockout model system
[†]Knockdown model system
[a]Primary cell system
[b]Cell model system

stiffness beyond a critical deformation. Notably, at large deformations, not previously accessed in other studies of the mechanical impact of plectin, plectin knockout cells reached a similar stiffness as wild type cells. The modulus-strain curves converged at high stress and showed a similar scaling with stress, suggesting that the mechanism of nonlinearity is the same. Actin and vimentin filaments are both semiflexible polymers. Theoretical models predict such semiflexible polymer networks to strain-stiffen due to the entropic cost of pulling out thermal bending fluctuations [180, 90]. For uniform dense networks, models predict an affine response with modulus increasing with stress as $\sigma^{3/2}$, consistent with experiments on reconstituted actin and intermediate filament networks [89, 96]. In our experiments the stiffening response tended to a weaker scaling, with an exponent between 0.5 and 1. This could potentially signify a nonaffine response. The comparable stress-stiffening response of wild type and plectin knockout cells revealed by the collapse of our data onto a master curve suggests that the processes underlying nonlinear elasticity remain largely unaffected by plectin's absence.

Strain ramps with repeated loading-unloading cycles revealed another interesting effect of plectin at large deformations. Wild type cells that had not yet been compressed had a higher linear modulus than plectin knockout cells, but after 1 or more additional cycles, the wild type cells became about as soft as plectin knockout cells. By contrast, the plectin knockout cells did not soften significantly during repeated loading. This finding suggests that plectin crosslinkers initially contribute to cell stiffness in wild type cells, but are disrupted by large compressive deformations. This suggests a model where plectin contributes an important mechanism of mechanical protection of the cytoskeleton (Figure 3.7). Upon uniaxial compression, due to its incompressible nature, the cell bulges at the edges, leading to stretching of the cytoskeleton (Figure 3.7A). In an unperturbed cell, actin and vimentin networks interpenetrate and are crosslinked by plectin (Figure 3.7B). With increasing deformations, stretching of the cytoskeleton first leads to the disruption of plectin crosslinking. We are not aware of any measurements of the plectin binding and unbinding rates to the cytoskeleton in cells. However, measurements on a biochemically reconstituted system showed that the PRD domains of plectin bind quite strongly to vimentin filaments, with a dissociation constant, k_d, of $0.5-0.9\times10^{-7}$M [269], while the actin-binding domain binds more weakly to actin filaments ($k_d = 3.2\times10^{-7}$M) [270]. Even if plectin could exhibit catch bond behavior like various actin-binding pro-

teins [228], at sufficiently large mechanical load we expect plectin bonds to dissociate. With further increasing compressive strain, most likely the actin network is disrupted first. The more mechanically resilient vimentin network can likely remain intact, as indicated by measurements on reconstituted networks and on cells showing that intermediate filaments can sustain large (> 200%) strains [271].

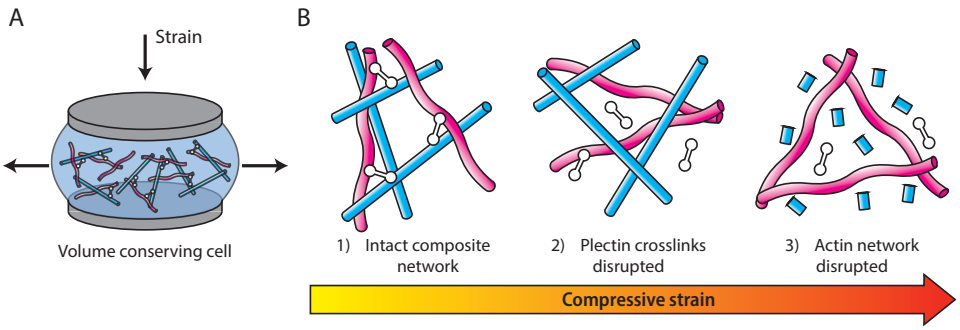

Figure 3.7: Proposed conceptual model for the impact of plectin on the strain-dependent mechanical response of single cells under compression. A) Upon uniaxial compression, due to its incompressible nature, the cell bulges at the edges leading to stretching of the cytoskeleton. (B) Starting with an intact composite actin-vimentin network crosslinked via plectin (left), stretching of the cytoskeleton first leads to the disruption of plectin crosslinking (middle). With further increasing compressive strain, the actin network is disrupted, leaving only the more mechanically resilient vimentin network intact (right).

Our results suggest that plectin contributes primarily to the elastic reinforcement of the cytoskeletal network at small deformations, while having minimal effect on the power-law rheology and stress-stiffening of fibroblasts. Crosslinking via plectin, mainly thought to be between actin and vimentin [234], makes a significant contribution to the rheology of fibroblasts. However, plectin's multifaceted roles complicate the interpretation of its mechanical contributions. In addition to crosslinking actin and intermediate filaments, plectin is known to interact with the linker of nucleoskeleton and cytoskeleton (LINC) complex [272, 273]—thereby linking the nucleus to the cytoskeleton—and to localize at focal adhesions where it contributes to adhesion dynamics and force transmission [249, 258]. Consequently, the observed reduction in stiffness upon plectin deficiency may result not only from the loss of its crosslinking activity but also from disrupted connections at the nuclear envelope and altered focal adhesion mechanics. Future studies employing domain-specific manipulations will be essential to disentangle these distinct functions and to clarify the relative contributions of plectin's various binding interactions to cellular mechanics.

3.4. CONCLUSION

In this study, we have shown that plectin knockout ($Plec^{-/-}$) fibroblasts are twice as soft as their wild type ($Plec^{+/+}$) counterparts at small and large deformations, but their strain-stiffening response to compression is similar. Applying a step strain led to poroelastic

stress relaxation at short times and a non-exponential response at long times with faster stress relaxation for $Plec^{-/-}$ cells as compared to $Plec^{+/+}$ cells. We hypothesize that this difference is due to a 3-fold difference in the kinetics of F-actin network turnover in the absence of plectin-mediated crosslinking to vimentin. When cells were subjected to repeated compression cycles, wild-type fibroblasts progressively softened to stiffness levels comparable to those of plectin knockout cells, indicating that plectin provides a first line of defense against large compressive loads. Confocal fluorescence images of the cells revealed an altered vimentin cytoskeletal network for $Plec^{-/-}$ cells, where vimentin intermediate filaments formed bundles, rather than the finer meshwork displayed in $Plec^{+/+}$ cells.

In conclusion, our findings reveal that plectin crosslinking significantly affects the cytoskeletal organization and viscoelastic properties of fibroblasts, at least partially through crosslinking of the actin and vimentin cytoskeletal networks. These findings provide a starting point towards understanding the role of mechanical integration of the different cytoskeletal networks in the cell interior and emphasize that these networks cannot be regarded as separate entities. Future work using engineered crosslinkers to selectively restore specific binding functions of plectin [234] could help disentangle its mechanical roles and reveal how distinct crosslinking interactions contribute to cytoskeletal mechanics.

3.5. ACKNOWLEDGEMENT

We thank M. Mavrakis (Institut Fresnel) for the vimentin-GFP plasmid used for live cell imaging experiments, C. Silva Martins (Institut Fresnel) for help with electroporation and G. Charras (University College London) for the actin-GFP plasmid used for FRAP measurements. We thank F. Ramirez Gomez for help with flow cytometry measurements and C. Sharma for helping with FRAP experiments. We thank A. Bonfanti for valuable help and advice regarding the RHEOS Julia package. G.H.K. gratefully acknowledges funding from the NWO Talent Programme, which is financed by the Dutch Research Council (project number VI.C.182.004). L.W. was funded by Austrian Science Fund (FWF) grants P31541-B27 (grant-DOI 10.55776/P31541) and I6049-B (grant-DOI 10.55776/I6049). F.C.M. was supported in part by the National Science Foundation Division of Materials Research (Grant No. DMR-2224030) and the Center for Theoretical Biological Physics (Grant No. PHY-2019745).

3.6. MATERIALS AND METHODS

3.6.1. CELL CULTURE AND SAMPLE PREPARATION FOR COMPRESSION EXPERIMENTS

All experiments were performed with immortalized mouse fibroblast cell lines derived from transgenic plectin wild-type ($Plec^{+/+}$) mice or plectin-deficient ($Plec^{-/-}$) mice in which the plectin gene had been targeted and inactivated by homologous recombina-

tion; consequently, *Plec*$^{-/-}$ fibroblasts used in this study were plectin-null, i.e. lacking all isoforms of plectin. Generation of transgenic mouse lines and isolation of immortalized cell lines have previously been described in detail (see [254, 255, 256]). Cells were cultured in Dulbecco's modified Eagle's medium with glutamax (DMEM, 10565018 Gibco) supplemented with 10% fetal bovine serum (FBS, 10270106 Gibco) and 5% penicillin-streptomycin (Pen-Strep antibiotic, 15070063 Gibco). Cells were maintained by subculturing twice a week and were screened for mycoplasma contamination every four months. Experiments were performed with cells up to passage number 20.

One day before experiments, cells were detached with 0.25% Trypsin-EDTA (25200056 Thermo Fisher Scientific) and counted using a Countess cell counter (Thermo Fisher Scientific). Next, 10,000 cells were transferred to plastic cell culture 6-well plates (83.3920.005 Sarstedt) containing culture medium. The cells were left to grow to ~70% confluence. On the day of the experiments, the cells were stained by replacing the medium with medium containing CellTracker Orange (10082742 Thermo Fisher Scientific, 1:1,000 dilution). After 30 min incubation, the medium was removed and the cells were detached from the plate by incubating with 200 µl Trypsin-EDTA (0.25%) for 3 minutes. The cells were then suspended in 4 mL CO_2-independent medium (18045088 Gibco), prewarmed to 37 °C. Next, the cells were seeded into 35 mm home-made dishes. Dishes were made by glueing 19 mm glass coverslips (12323138 Thermo Fisher Scientific) precleaned by sonication in 2-propanol (5 min) to Petri dishes (Sarstedt) with Norland Optical Adhesive glue. A drop of glue was placed in the dish, the coverslip was carefully placed on top to make sure the glue was evenly spread, and the glue was cured for 5 min using a UV ozone ProCleaner (Bioforce Nanosciences). The dishes were coated with Pluronic F-127 (P2443 Sigma) dissolved (1:100 w/v) in PBS (10010023 Gibco) for 15 min before the experiment.

3.6.2. SINGLE-CELL COMPRESSION EXPERIMENTS

Cell compression experiments were performed using a Chiaro Nanoindenter operated by the Piuma software (Optics11 Life) mounted on a Leica Thunder Imager wide field microscope. The cells were imaged *in situ* using a 200 mW solid state LED5 light source (Leica), a monochrome sCMOS camera (Leica), and a 10x dry objective (HC PL APO 0.45NA, Leica). We used custom-made wedged cantilevers prepared by modification of tipless cantilevers with a nominal spring constant of 0.018 N/m (Optics11 Life). To correct for the 3° tilt of the cantilevers [208], we fabricated a wedge using Norland optical adhesive (NOA81 Norland), as described in our previous work [253]. We calibrated the cantilevers before and after wedge manufacture by the stiff-surface contact method (as described by the manufacturer) to verify that the spring constant was unchanged.

In preparation for compression experiments, a cell dish containing 4 mL of prewarmed CO_2-independent medium was placed on the microscope stage. Before lowering the cantilever probe into the medium, we added a drop of medium onto the probe to prevent air bubbles. The probe was first calibrated by the stiff-surface contact method which involves pressing against the coverslip. Next, the cantilever was moved up and 200 µl of cell suspension was added to the dish. After allowing cells to sediment for 10 minutes, the cantilever was moved down to a distance of ~200 µm above the coverslip. We then positioned a single cell underneath the cantilever with help of the fluores-

cent signal of the CellTracker dye in the cytosol. We carefully lowered the cantilever until reaching contact with the cell, apparent from the optically detected cantilever deflection. In all experiments, we controlled the indentation (Indentation mode in the Piuma software), which allows precise control of the rate of deformation. During measurements, the elapsed time, piezo displacement, and cantilever deflection were recorded at a time resolution of 1000 Hz. We verified by live-dead staining that the cells remained viable over the entire duration (at most 120 min) of the experiments [253].

We used three different protocols to deform the cells. First, for small amplitude oscillatory measurements, we lowered the cantilever probe by 1 μm after finding the cell surface, corresponding to a compressive strain of ~ 0.05, which is well within the linear elastic regime. Next, a sinusoidal displacement with an amplitude of 200 nm was applied at five logarithmically spaced frequencies between 0.1 Hz and 10 Hz, corresponding to strain rates between 0.02 μm/s and 2 μm/s. Second, for stress relaxation measurement, we applied a small step strain by quickly compressing the cell by a distance of 1 μm (corresponding to a strain of ~ 0.05) at a large strain rate of 10 μm/s. We subsequently measured the time-dependent relaxation of the stress over a period of 80 s. Third, to capture the nonlinear response of the cells to high levels of compressive strain, we performed strain ramp measurements at a constant strain rate of 1 μm/s up to a maximal deformation of 8 μm, corresponding to a strain of ~ 0.4.

3.6.3. ANALYSIS OF SINGLE-CELL COMPRESSION DATA

All data analysis was performed using custom-written Python code available upon request. The load measured by the Nanoindenter was converted to compressive engineering stress based on the initial contact area between the cell and the cantilever. The contact area was determined from automated analysis of epifluorescence images of the cytosol by thresholding the images using Otsu's method in the Python library scikit-image [209] and multiplying the number of pixels by the pixel size in the thresholded image. The uniaxial strain was calculated by approximating cells as a sphere and dividing the amount of compression by the cell diameter. We note that the measurements and all analyses were previously benchmarked using cell-sized polyacrylamide microgel particles of known stiffness [253]. Curve fitting was done using the curve fit function from Python's SciPy library for oscillatory and strain ramp measurements [211] and the Julia RHEOS package [274] for stress relaxation experiments.

SMALL AMPLITUDE OSCILLATORY MEASUREMENTS

We calculated the complex viscoelastic modulus, $E^*(\omega) = FT(\sigma(t))/FT(\epsilon(t))$, at each oscillation frequency $\omega = 2\pi f$, from the Fourier transformed (FT) stress, $\sigma(\omega)$, and strain, $\epsilon(\omega)$. The Fourier transformations were performed using the fast Fourier transform (FFT) function in Python's numpy library. We separated the complex modulus, defined as $E^* = E' + iE''$, into its real and imaginary parts to obtain the compressive storage modulus, $E'(\omega)$, and loss modulus, $E''(\omega)$. $E'(\omega)$ corresponds to the elastic modulus of the cell (i.e., the energy stored per cycle of oscillation), whereas $E''(\omega)$ corresponds to the viscous component (i.e., the energy dissipated per cycle of oscillation).

To mechanically fingerprint our cells, we first tried to fit the frequency spectra to the simplest possible phenomenological model referred to as the structural damping

model [172, 173, 259] (for more details see Supplementary Methods). Briefly, this three parameter model is described by:

$$E^*(\omega) = E_0 c(\alpha)(1 + i\tan(\pi\alpha/2))(\omega/\omega_0)^\alpha + i\mu\omega, \tag{3.4}$$

where E_0 is a scaling factor for the elastic and viscous moduli at a frequency scale factor ω_0 (which we arbitrarily set to 1), $c(\alpha) = \Gamma(1-\alpha)\cos(\pi\alpha/2)$ with Γ the gamma function, α is the power law exponent and μ is the Newtonian viscous term. As this model failed to capture the rheology of our cells, we applied a fractional rheological model adapted from recent work of Bonfanti et al. [259, 260]:

$$E^*(\omega) = k\frac{\left[i\omega\frac{\eta_1}{k} + 1 + \left(i\omega\frac{c_\beta}{\eta_1}\right)^{1-\beta}\right]}{1 + \left(i\omega\frac{c_\beta}{\eta_1}\right)^{1-\beta}} + i\omega\eta_2 \tag{3.5}$$

This model has five fitting parameters: k is the elastic modulus representing the stiffness of the cell, η_1 is a dashpot viscosity capturing long-term viscous dissipation, c_β is a spring-pot parameter describing the intermediate viscoelastic behaviour, β is a fractional exponent that characterises power-law scaling with frequency, and η_2 is a Newtonian viscous term capturing the response of the cytoplasm. We further decomposed Equation 3.5 into real and imaginary parts:

$$E'(\omega) = k + \frac{\omega\eta_1\cos(\beta\frac{\pi}{2})}{(\omega\tau)^{-(1-\beta)} + 2\sin(\beta\frac{\pi}{2}) + (\omega\tau)^{1-\beta}}, \tag{3.6}$$

$$E''(\omega) = \frac{\omega\eta_1\left[1 + (\omega\tau)^{1-\beta}\sin(\beta\frac{\pi}{2})\right]}{1 + 2(\omega\tau)^{1-\beta}\sin(\beta\frac{\pi}{2}) + (\omega\tau)^{2(1-\beta)}} + \omega\eta_2, \tag{3.7}$$

For both models, we simultaneously fitted the measured storage and loss moduli to these equations to find a self-consistent description of the elastic and viscous response.

STEP STRAIN MEASUREMENTS

We found that stress relaxation after a step strain exhibited two distinct time regimes characterized by different functional forms. In the first regime, for times between 10^{-3}-10^{-1}s , we fitted the stress response to a poroelastic model, where stress decays exponentially with time [275]:

$$E(t) = E_0 e^{-t/\tau_p} + E_\infty. \tag{3.8}$$

Here, E_0 denotes the instantaneous modulus immediately after loading, E_∞ is the equilibrium modulus at long times, and τ_p is the poroelastic relaxation time. In the second regime (times between 0.1-80 s), where the cell behaves as a viscoelastic material, we fitted the same 5-parameter fractional rheological model as with the oscillatory measurements. To obtain the relaxation modulus $E(t)$, we calculated the Laplace transform of Equation 3.5, which yields

$$E(t) = c_\beta\, t^{-\beta}\, E_{1-\beta,1-\beta}\left(-\frac{c_\beta}{\eta_1}\, t^{1-\beta}\right) + k, \tag{3.9}$$

where $E_{a,b}(z)$ denotes the Mittag-Leffler function, a function that naturally appears in the solutions of fractional differential equations [71]. To obtain parameter fits, we fit Equation 3.9 to the stress relaxation data using the Julia RHEOS package [274].

STRAIN RAMP MEASUREMENTS

The differential cell stiffness K was calculated as the derivative of the stress versus strain curves using the Python np.gradient function [212]. The linear modulus K_0 and the onset strain (ϵ^*) and onset stress (σ^*) where stress-stiffening sets in were determined by performing a piecewise linear fit to the stress/stiffness curve for each individual cell. We fitted a horizontal line and a linear equation of the form $y = mx+c$ with the Python scipy library [211], optimizing the onset point by maximizing the combined R^2 values of both fits. The linear modulus was given by the y-intercept of the horizontal line. To rescale the stress/stiffness curves onto a single master curve, we rescaled K by K_0 and σ by σ^*.

3.6.4. CONFOCAL MICROSCOPY EXPERIMENTS

Confocal imaging of the cells was performed on a Leica Stellaris 8 LSCM microscope, using a 63x, NA 1.30 glycerol immersion objective, white light laser, and HyD S and HyD X detectors in counting mode. Four days prior to experiments, the vimentin cytoskeleton was labelled by transfecting the cells with a GFP-vimentin plasmid [213] using electroporation with the Invitrogen Neon transfection system (Thermo Fisher Scientfic) according to the manufacturer's instructions. A single pulse of 1350 V was applied for 30 ms. We found that cells required four days to express vimentin at stable levels. For actin labeling, on the day of experiments, cell culture medium was replaced with fresh medium containing SiR actin (Tebu Bio, SC001) (1:1000 from a 1 mM stock solution) along with the pump inhibitor verampamil (Tebu Bio, SC001, part of SiR actin kit) (1:1000 from a 1 mM stock solution). After a 1 hour incubation, the medium was replaced with fresh medium containing Hoechst 33342 (Thermo Fisher Scientific, H3570) (1:10,000) to label the nucleus. The dye incubation was done directly before imaging. To mimic the conditions of the single-cell compression experiments, cells were trapped between two coverslips coated with Pluronic F-127 (Sigma, P2443) spaced apart by 10 µm-sized silica particles (Sigma 904368). We acquired 3D confocal z-stacks of 256 x 256 pixel xy-slices separated by a z-distance of 0.33 µm at a scan speed of 400 Hz.

3.6.5. ANALYSIS OF CONFOCAL MICROSCOPY DATA

The orthogonal projection tool in FIJI [214] was used to generate side projections of cells. To generate 'average cells', a maximum intensity projection was generated from a 2 µm section centered at the cell equator. Multiple-channel stacks (containing projections of the actin, vimentin and the nucleus) were aligned using the HyperStackReg plugin [215], which registered cells on top of each other, correcting for differences in cell size. In FIJI, we then made average intensity projections to generate an average cell. Line profiles of the actin, vimentin and nucleus signals were determined both for single cells and 'average cells'. To this end, the radial profile plot tool in FIJI was used to calculate the normalized intensities around concentric circles from the center of the image. Images of at least twelve cells were collected from at least two independent experiments for each condition.

3.6.6. FRAP MEASUREMENTS OF CYTOPLASMIC VISCOSITY AND ACTIN NETWORK TURNOVER

Fluorescence recovery after photobleaching (FRAP) measurements were performed using the same Leica Stellaris 8 confocal microscope described above, operated in FRAP mode in the LASX software. To ensure effective photobleaching, we used the *zoom-in* and *background to zero* settings as well as the FRAP booster in the Leica LASX software. Cells were again trapped between two coverslips spaced apart by 10 µm-sized beads to mimic the geometry of the compression experiments. For determining cytoplasmic viscosity, the cells were stained with CellTracker Orange (10082742 Thermo Fisher Scientific, 1:1000 dilution in medium) on the day of the experiments. For determining actin turnover, the actin cytoskeleton was labelled by transfecting the cells with an actin-GFP plasmid [263] using electroporation with the Invitrogen Neon transfection system (Thermo Fisher Scientfic). A single pulse of 1350 V was applied for 30 ms.

For both CellTracker and actin FRAP experiments, we imaged a 128x128 pixel confocal xy-slice using the HyD S detector. First, two pre-bleach images were taken to determine the fluorescence intensity before bleaching. Both the CellTracker dye and the actin-GPF were photobleached within a circular region with a radius of 1 µm in the central xy-plane of the cell. This diameter was chosen to ensure that recovery is clearly visible in the images, while minimizing cell damage. To achieve efficient bleaching, we performed two exposures, each lasting 0.23 s, using four laser lines operated at 100% intensity (531 nm, 541 nm, 551 nm and 561 nm for CellTracker; 458 nm, 468 nm, 478 nm, 488 nm for actin-GFP). Following photobleaching, we recorded 200 post-bleach images every 0.23 s for both CellTracker and actin-GFP. For cytoplasm recovery measurements on $Plec^{+/+}$ cells, we performed 38 measurements in 11 different cells, and 36 measurements on 11 cells for $Plec^{-/-}$ cells. For actin turnover measurements, we performed 35 measurements in 15 different $Plec^{+/+}$ cells and 27 measurements in 14 different $Plec^{-/-}$ cells. Measurements were performed at varying locations distant from the nucleus and the cell membrane.

3.6.7. ANALYSIS OF FRAP MEASUREMENTS

To determine the fluorescence recovery times for CellTracker and actin-GFP after photobleaching, we analyzed the time-dependent intensity during recovery $I(t)$ in the bleached region throughout fluorescence recovery using a custom-written Python code. We computed the normalised intensity $I_n(t)$ by dividing $I(t)$ by the pre-bleach intensity I_i. We corrected for bleaching by the probe beam by also measuring the fluorescence over time in a reference region far away from the bleaching region. Assuming a two-dimensional circular ROI and a uniform laser disk profile, we determined the FRAP recovery time by fitting $I_n(t)$ to the following model [276]:

$$I_n = \exp\left(-\frac{2\tau}{t}\right)\left[\mathbf{I}_0\left(\frac{2\tau}{t}\right)+\mathbf{I}_1\left(\frac{2\tau}{t}\right)\right]+I_\infty, \tag{3.10}$$

where τ is the characteristic recovery time, $\mathbf{I}_0$, $\mathbf{I}_1$ are modified Bessel functions and $I_\infty < 1$ is the intensity asymptote due to an immobile fraction within the sample. For CellTracker, we can infer a diffusivity D from the relationship $\tau = r^2/(4D)$, with r being

the bleach radius [276]. It reacts with glutathione, which is most abundant in the cytoplasm, but is also present in subcellular organelles such as mitochondria [277]. We thus expect to see partial rather than total fluorescence recovery, i.e., $I_\infty > 0$. In the case of actin-GFP, we expect full fluorescence recovery [263].

3.6.8. WESTERN BLOTTING

Cells were seeded in 6 well culture plates (Thermo Fisher Scientific, NC0506188) containing 2 mL of culture medium and allowed to attach for 48 hours. Cells were scraped in phosphate-buffered saline (PBS) and lysed in equal volumes of 2x Laemmli buffer (4% sodium dodecyl sulfate (SDS), 20% glycerol, 120 mM Tris(hydroxymethyl)aminomethane (Tris) buffer with pH 6.8). Lysates were cleared of large DNA by passing through a 25G needle and then heated to 65°C for 10 minutes. Protein concentrations were measured with the Lowry protein assay [278]. Equal amounts of protein were size-separated by SDS-PAGE containing 2,2,2-Trichloroethanol (TCE). After running the gel, it was exposed to a 300 nm transilluminator (Bio-Rad Chemi-Doc Imaging System) for 5 minutes. The separated proteins were then transferred to a polyvinylidene fluoride (PVDF) membrane (Bio-Rad, 1704156) using the Bio-Rad Trans-Blot Turbo Transfer System, and imaged on the transilluminator to get a picture of the total protein. Membranes were blocked for 1 hour at room temperature by 5% BSA in PBS supplemented with 0.1% Tween-20, incubated overnight at 4°C with primary antibody (see Supplementary Table 2). Subsequently, membranes were washed 5 times with 0.1% Tween-20 in PBS and then incubated with horseradish peroxidase-conjugated secondary antibodies (see Supplementary Table 2) for 1 hour at room temperature. After adding Enhanced chemiluminescence (ECL) substrate (Thermo Fisher Scientific, 32106), blots were imaged with the Bio-Rad ChemiDoc Imaging System. The band intensities were quantified using FIJI [214].

3.6.9. STATISTICS

All mechanical experiments shown were repeated on at least 3 different days and imaging (including FRAP) experiments were repeated on 3 different days. Measured values in the main text are stated as the mean ± the standard error on the mean. For all mechanical measurements, P-values to quantify statistical significance were calculated using the Wilcoxon rank-sum test after assessing normality with the Shapiro-Wilk test, which confirmed that the data did not follow a Gaussian distribution. For FRAP measurements, P-values were calculated using the unpaired Student's t-test. Computer codes described in the Methods section are available on request.

3.7. SUPPLEMENTARY INFORMATION

3.7.1. SUPPLEMENTARY FIGURES

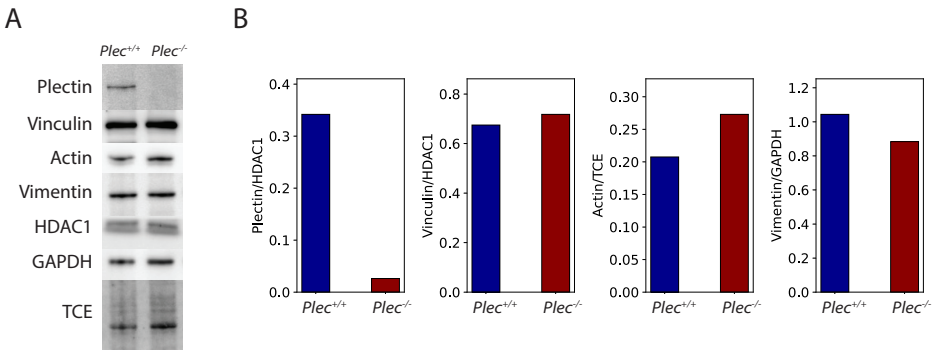

Figure 3.8: A) Protein expression levels of plectin, vinculin, actin and vimentin in Plectin+/+ and Plectin-/- mouse embryonic fibroblasts on cropped immunoblots. Depending on the protein of interest, HDAC1, GAPDH or TCE were used as a loading control. B) Quantification of the normalized band intensities as shown in panel A. Data shown for N=1 sample.

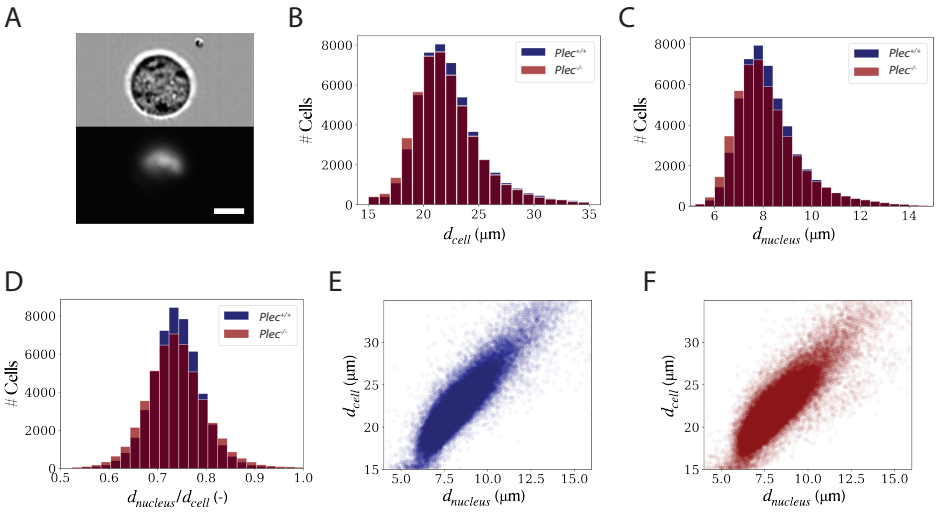

Figure 3.9: Cell and nucleus sizes measured by imaging flow cytometry for N = 50,220 $Plec^{+/+}$ cells and N = 48,711 $Plec^{-/-}$ cells. (A) Typical unprocessed bright field image of a cell (top) and corresponding epifluorescence image of its nucleus (bottom), which was stained with DRAQ5. Scale bar is 10 µm. (B) The mean cell diameters d_{cell} are 22.4 ± 3.1 µm for $Plec^{+/+}$ cells and 22.2 ± 3.1 µm for $Plec^{-/-}$ cells. (C) Nuclear diameters d_{nucleus} are 8.3 ± 1.4 µm for $Plec^{+/+}$ cells and 8.2 ± 1.4 µm for $Plec^{-/-}$ cells. (D) Nucleus-to-cell diameter ratio, $d_{\text{nucleus}}/d_{\text{cell}}$. On average, the ratio is the same for $Plec^{+/+}$ and $Plec^{-/-}$ cells (0.74 ± 0.06 and 0.74 ± 0.07, respectively). Values stated as mean ± standard deviation. (E)-(F) Each symbol represents the d_{cell} and d_{nucleus} of a single cell. Both $Plec^{+/+}$ cells (E) and $Plec^{-/-}$ (F) cells display a proportional increase in size with their nucleus size.

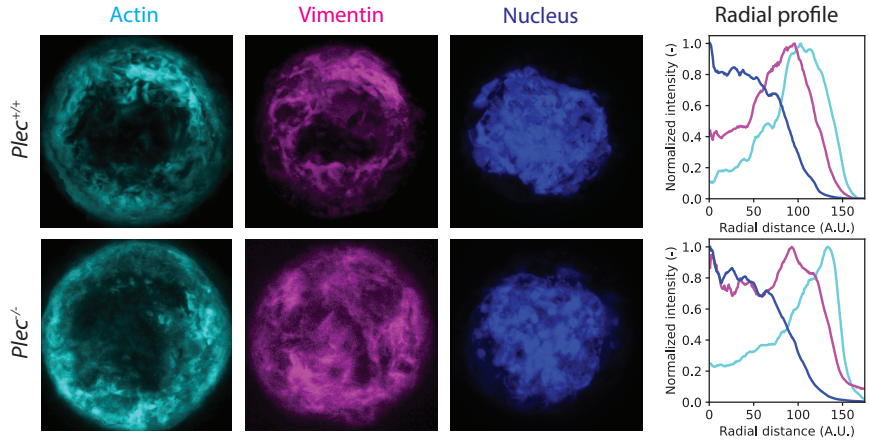

Figure 3.10: Actin, vimentin and nuclear organization in 'average' $Plec^{+/+}$ cells and $Plec^{-/-}$ cells. As we rescale cells to generate 'average' cells, scale bar not applicable. The images represent averages of a 2 µm thick confocal section at the cell equator for 10 $Plec^{+/+}$ and 10 $Plec^{-/-}$ cells. For both conditions, filamentous actin is located largely at the cell periphery, while vimentin is located closer to the center of the cell. Average radial profiles of the fluorescent signals (right) were calculated by taking normalized intensities around concentric circles from the center of the image, which show a significant overlapping region between actin and vimentin. The radial distance is set to zero at the cell center; the distance is in arbitrary units (see Methods for details).

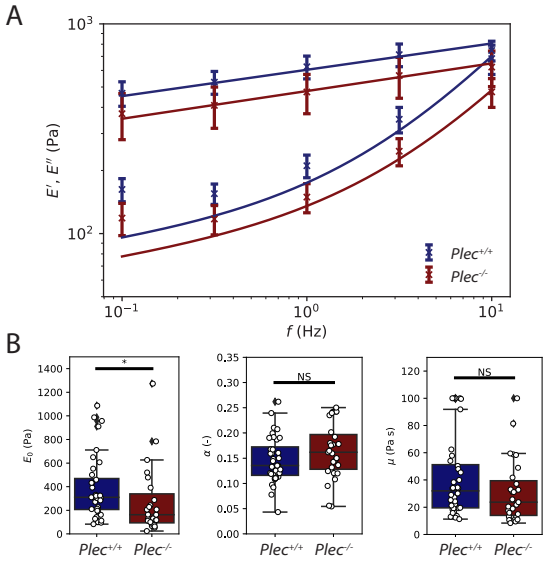

Figure 3.11: Small amplitude oscillatory strain measurements on single fibroblasts with fits to the structural damping model. (A) Storage (E') and loss (E'') linear compressive moduli (symbols), measured for oscillation frequencies between 0.1Hz and 10Hz for $Plec^{+/+}$ (N=36) and $Plec^{-/-}$ (N=27) cells. Fits of the average data (solid lines) to the structural damping model (equations 3.11 and 3.12). The model does a poor job of capturing the mechanical behaviour of these cells at low frequencies. (B) We fit the rheological model to the individual cells to obtain mechanical fingerprints, i.e., scaling factor E_0, power law exponent α and cytoplasmic viscosity μ. Asterisks indicate statistically significant differences (* denotes P < 0.05). N.S. denotes non-significant differences.

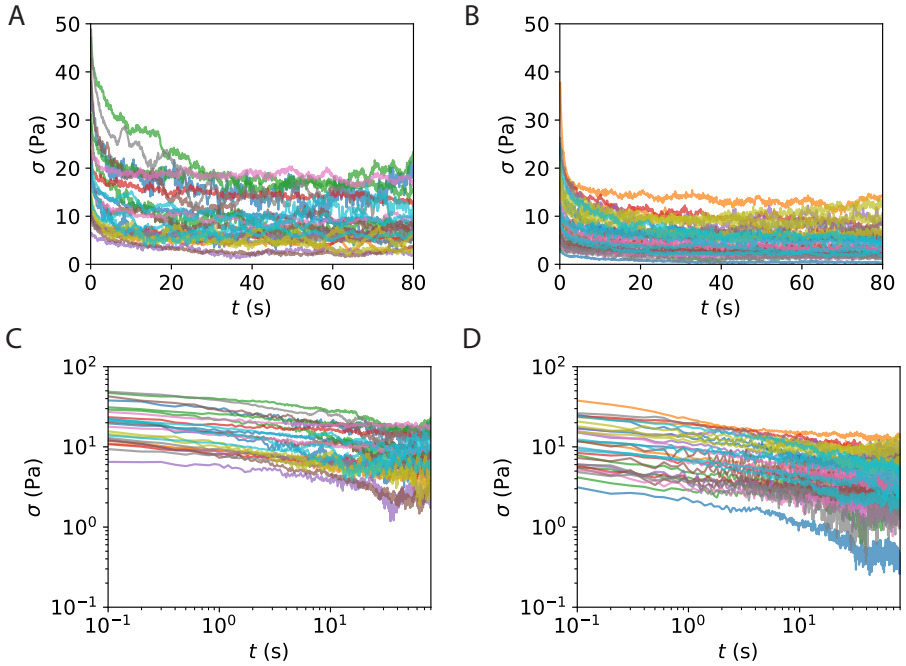

Figure 3.12: Individual stress relaxation measurements of the mechanical response of $Plec^{+/+}$ and $Plec^{-/-}$ cells to step strain compressions. We rapidly apply a compressive strain and hold it at a fixed value of 0.05. Subsequently, we monitor stress relaxation over 80 s. (A) Stress relaxation for all $Plec^{+/+}$ cells (N=25). (B) Stress relaxation for all $Plec^{-/-}$ cells (N=33). (C) We re-plot (A) on a log-log scale, as shown for averages in the main text. (D) We re-plot (B) on a log-log scale, as shown for averages in the main text.

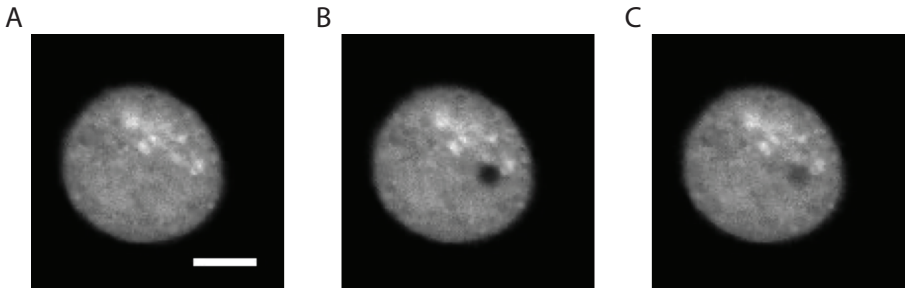

Figure 3.13: Fluorescence recovery after photobleaching (FRAP) on the cytoplasmic dye CellTracker Orange for a wild type fibroblast confined between two nonadhesive surfaces. The figure shows a representative example of (A) the pre-bleached cell, (B) the cell immediately after bleaching and (C) partial recovery of the fluorescence signal. Images are shown for a wild type cell. The FRAP experiment was performed in the mid-plane of the cell. Scale bar is 10 μm.

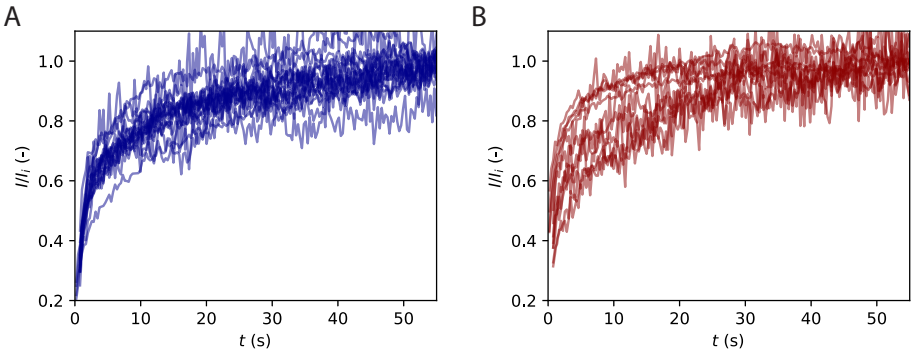

Figure 3.14: Individual fluorescence recovery curves for the comparison of actin turnover rates for $Plec^{+/+}$ cells (N=54) and $Plec^{-/-}$ cells (N=35) probed by fluorescence recovery after photobleaching (FRAP). (A) Individual normalized intensity curves for $Plec^{+/+}$ cells. (B) Individual curves for $Plec^{-/-}$ cells.

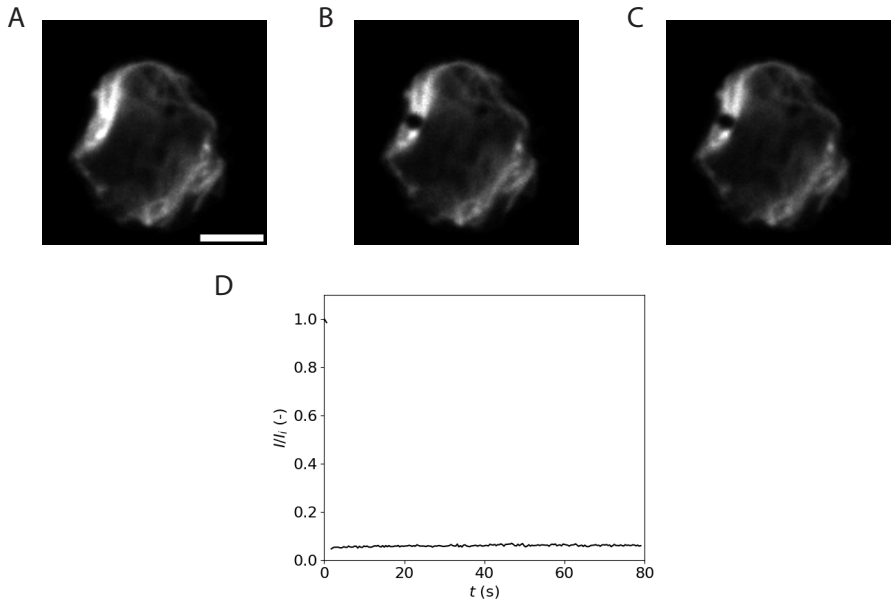

Figure 3.15: Fluorescence recovery after photobleaching (FRAP) experiments on vimentin-GFP tagged cells. Representative images of a FRAP experiment on a $Plec^{+/+}$ cell (A) before photobleaching, (B) immediately after bleaching, and (C) after 80 s of recovery. The FRAP experiment was performed in the mid-plane of the cell. Scale bar is 10 µm. (D) Representative recovery curve for the vimentin-GFP signal for a $Plec^{+/+}$ cell, showing negligible fluorescence recovery in 80 s (correspondin to the total duration of the stress relaxation experiments.

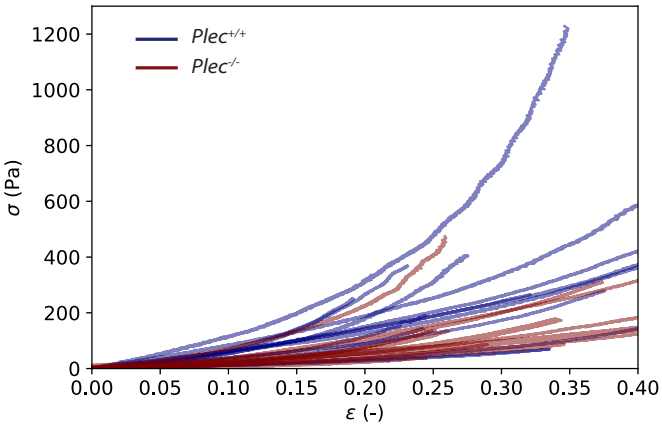

Figure 3.16: Individual strain ramp measurements of the nonlinear response of $Plec^{+/+}$ (blue, N=15) and $Plec^{-/-}$ (red, N=13) cells to large compressions, showing stress as a function of strain.

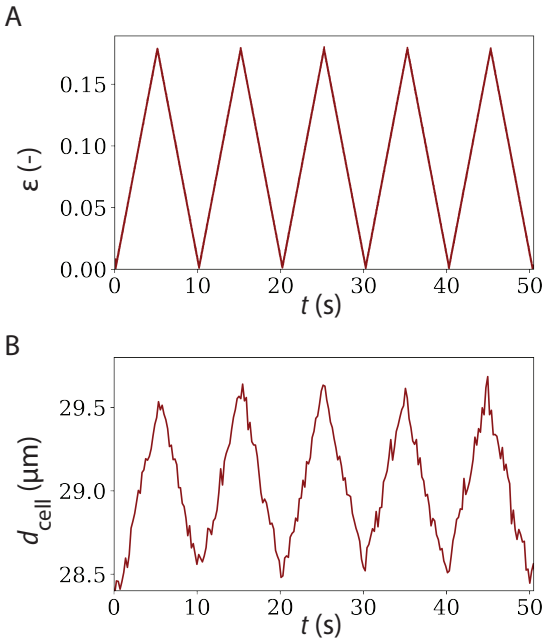

Figure 3.17: Representative cell diameter of a wild type fibroblast throughout 5 consecutive compressive loading-unloading cycles. (A) Strain profile during five consecutive strain cycles. (B) Measurement of the time-dependent changes in apparent cell diameter determined from the projected cell area observed by wide field epifluorescence imaging of CellTracker Orange. Changes in diameter are reversible.

3.7.2. SUPPLEMENTARY TABLES

Primary antibody	Dilution	Manufacturer	Catalog number
Rabbit anti-Plectin IgG	1:1000	Bioke	12254s
Rabbit anti-Vinculin IgG	1:500	Thermofisher	700062
Mouse anti-Actin IgG	1:500	Millipore	MAB1501 Clone C4
Mouse anti-Vimentin IgG1	1:2000	Abcam	AB8978
Rabbit anti-HDAC1 IgG	1:1000	ProteinTech	10197-1-AP
Rabbit anti-GAPDH IgG	1:5000	Cell signal/Bioke	2118s

Table 3.2: Primary antibodies used for western blot analysis of protein expression levels of $Plec^{+/+}$ and $Plec^{-/-}$ cells.

Secondary antibody	Dilution	Manufacturer	Catalog number
Rabbit anti-mouse IgG (HRP)	1:5000	Abcam	AB6728
Goat anti-rabbit IgG (HRP)	1:5000	Abcam	AB97051

Table 3.3: Secondary antibodies used for western blot analysis of protein expression levels of $Plec^{+/+}$ and $Plec^{-/-}$ cells.

3.7.3. SUPPLEMENTARY METHODS

FITTING THE STRUCTURAL DAMPING LAW TO OSCILLATORY STRAIN MEASUREMENTS

Before fitting the fractional viscoelastic model described in the main text, we first tried to capture the rheology of our cells using a simpler phenomenological model. This is a three parameter model referred to as the structural damping model [172, 173, 174], described in the main text as Equation 1. We take this equation and decompose it into its respective real and imaginary parts to yield the storage (E') and loss (E'') moduli which we fit to our data:

$$E'(f) = E_0 c(\alpha) \cos\left(\frac{\pi\alpha}{2}\right)\left(\frac{f}{f_0}\right)^{\alpha} \tag{3.11}$$

$$E''(f) = E_0 c(\alpha) \sin\left(\frac{\pi\alpha}{2}\right)\left(\frac{f}{f_0}\right)^{\alpha} + \mu f. \tag{3.12}$$

The three fitting parameters are the scaling factor E_0, power law exponent α, and cytoplasmic viscosity μ. Using the curve fit function from Python's SciPy library [211], we simultaneously fitted Equations 3.11 and 3.12 to the measured storage and loss moduli.

DETERMINATION OF CELL AND NUCLEUS SIZE BY IMAGING FLOW CYTOMETRY

An ImageStreamX Mark II Imaging Flow Cytometer with a 40x objective was used to measure the sizes of the cells and their nuclei. One day before cytometry experiments, cells were detached with Trypsin-EDTA (0.25%) (25200056 Thermo Fisher Scientific) and counted using a Countess cell counter (Thermo Fisher Scientific). Next, 100,000 cells were transferred to plastic cell culture 6-well plates (83.3920.005 Sarstedt) containing culture medium. On the day of experiments, cell nuclei were fluorescently stained with DRAQ5 (P5739873 ThermoFisher) by adding DRAQ5 from a 5 mM stock solution in DMSO to the culture medium (1:500), and leaving the cells to incubate for 30 min. The cells were imaged in bright field, while the DRAQ5-stained nuclei were imaged in fluorescence with a 642 nm laser. The flow rate was set to Low in the ImageStreamX software, with High sensitivity, amounting to a flow speed of 55 mm/s. Single cells were separated from debris and cell clusters by selecting only objects with a diameter between 10 µm and 35 µm, a nuclear area of 50-5000 µm^2, and a cellular aspect ratio of 0.7-1. A typical image taken with the ImageStream flow cytometer is shown in Figure S3.9A. From the projected areas of the cells and nuclei, the corresponding average diameters were calculated, assuming spherical shapes in an automated Python script.

MONITORING THE CELL DIAMETER DURING REPEATED RAMP EXPERIMENTS

For experiments measuring the cell diameter during repeated compression, we used 35 mm glass bottom dishes (81218-200 Ibidi), in combination with a 40x NA 1.10 water immersion objective. To determine the cell diameter, we recorded each cell at a frame rate of 5fps. To determine the cell area, we thresholded each frame using Otsu's method in the Python library scikit image [209] and multiplied the number of pixels by the pixel size in the thresholded image. To determine the cell diameter, we used the geometric relation between a circle diameter and area: $A = \pi(d_{\text{cell}}/2)^2$.

3.7.4. SUPPLEMENTARY RESULTS

FLOW CYTOMETRY

Complementing the images in the main text, we performed imaging flow cytometry measurements to determine cellular and nuclear sizes. The corresponding histograms are shown in Figure S3.9B-D. On average, *Plec*$^{-/-}$ cells have a diameter of 22.2 ± 3.1 µm, and are thus slightly smaller than *Plec*$^{+/+}$ cells with diameter 22.4 ± 3.1 µm. This diameter is calculated from the projected area a as $d_{\text{cell}} = 2\sqrt{a/\pi}$. In Figure S3.9B, we see that the diameters follow similar distributions, which appear to be log-normal distributions. Diameters range from 15 µm to 35 µm. The distributions for the nuclear sizes are shown in Figure S3.9C, where the diameter was again determined from the projected area. The resulting mean diameters d_{nucleus} are 8.3 ± 1.4 µm for *Plec*$^{+/+}$ cells and 8.2 ± 1.4 µm for *Plec*$^{-/-}$ cells. Dividing d_{nucleus} by d_{cell} for each cell yields the distribution shown in Figure 3.9D, with an average ratio of 0.74 ± 0.06 for *Plec*$^{+/+}$ cells and 0.74 ± 0.07 for *Plec*$^{-/-}$ cells. The ratios are thus comparable and both display a Gaussian distribution, with a slightly wider distribution for *Plec*$^{-/-}$ cells. This hints at a scaling between nucleus and cell size, which we confirmed by making scatter plots (Figure 3.9E-F).

ESTIMATION OF THE POROELASTIC DIFFUSION CONSTANT ASSUMING FLUID TRANSPORT THROUGH THE NUCLEUS

In the main text, we make an estimate of the poroelastic diffusion constant, where we assume that the relevant length scale of fluid transport in the cell (L) is that of the cell membrane to the nucleus. If we instead use the cell size as the relevant length scale (i.e., assuming fluid transport occurs through cytoplasm and nucleus), we estimate significantly larger values for D_{p} of (1700 ± 100) µm^2/s for *Plec*$^{+/+}$ cells and (3200 ± 200) µm^2/s for *Plec*$^{-/-}$ cells. Importantly, we still observe a larger poroelastic diffusion constant in *Plec*$^{-/-}$ cells.

4

UNTANGLING THE CYTOSKELETAL CROSSLINKING AND ANCHORING FUNCTIONS OF PLECTIN IN CELLS

Plectin is a large cytolinker protein within the plakin family, known for its role in integrating the cytoskeletal networks of mammalian cells. It is ubiquitously expressed across tissues, and its malfunction is implicated in a range of diseases, including skin blistering disorders. While previous studies suggested that plectin contributes to the viscoelastic and nonlinear mechanical behaviour of cells, it remains unclear whether this is primarily due to its actin-vimentin crosslinking activity or its more isoform-specific functions in anchoring vimentin filaments to different organelles. To disentangle these roles, we introduced a synthetic actin-vimentin crosslinker, ACTIF, into fibroblasts. Unlike plectin, ACTIF is designed solely to bridge actin and vimentin filaments without the capacity to anchor them to subcellular structures. We found that ACTIF fully restores the bulk mechanical properties of plectin-deficient fibroblasts, bringing them to levels comparable to wild-type cells. However, crosslinking alone was insufficient to rescue plectin's anchoring-dependent functions, such as traction force generation and regulation of nuclear morphology. These findings highlight that plectin's crosslinking and anchoring roles contribute independently to cellular mechanics. They underscore the joint importance of cytoskeletal filament connectivity and cellular anchoring of cytoskeletal elements for maintaining mechanical integrity and force transmission within cells.

This chapter is in preparation for publication. The paper is co-authored by **J. P. Conboy**, N. Vaes, J. Barrasa-Fano, L. Winter, H. van Oosterwyck, G. Wiche and G. H. Koenderink.

4.1. INTRODUCTION

The cytoskeleton performs essential roles within mammalian cells. It controls the cell's overall shape and its internal organization. At the same time it provides essential mechanical support, facilitates cell migration and division, enables cell-to-cell connections in tissues, and modulates intracellular signaling pathways. The cytoskeleton is a network of four different types of biopolymers: actin filaments (F-actin), microtubules (MTs), intermediate filaments (IFs) and septins. Each filamentous component exhibits distinct properties and hence contributes different functions [156]. From a mechanical perspective, intermediate filaments and septins are relatively compliant, with a persistence length of about 1 μm [218, 219], whereas actin filaments and microtubules are stiffer, with persistence lengths of about 10 μm and several millimeters, respectively [220]. Intermediate filaments and actin filaments are thought to contribute mainly to buffering tensile forces while microtubules can bear compressive forces [68]. Meanwhile septins have been been proposed to reinforce the actin cortex and actin stress fibers [279, 280]. All four cytoskeletal biopolymers are assembled into specialized higher-order structures like networks or bundles by dedicated accessory proteins such as crosslinkers and polymerization regulators [221, 222, 223] in conjunction with posttranslational modifications [281]. Cytoskeletal crosslinker proteins dynamically bind and unbind from the filaments, causing viscous dissipation that endows cells with viscoelastic properties [227, 282, 196]. By regulating force transmission across the cell membrane from the extracellular environment to the inside of the cell, the cytoskeleton also controls the shape of organelles such as the nucleus [283]. Actin networks exert forces that flatten, elongate, or otherwise deform the nucleus in fibroblasts [284, 285]. Vimentin intermediate filaments, on the other hand, form a structural cage that bolsters nuclear shape and stiffness, preventing nuclear damage in cells exposed to large deformations [286, 287]. The vimentin cage for instance prevents nuclear envelope rupture in cells migrating through narrow confining channels [286].

Traditionally, the four cytoskeletal biopolymers and their cellular functions have largely been studied separately. Yet, mounting evidence indicates that close coordination between them is crucial for numerous fundamental cellular processes such as cell migration [156] and mitosis [288, 201]. The networks are physically interconnected via crosslinking proteins that include members of the plakin family such as plectin [289]. Plectin is a large multidomain protein with a molecular weight exceeding 500 kDa. It primarily associates with intermediate filaments, but also interacts with actin filaments and microtubules [290, 291, 292, 138]. In mesenchymal cells, plectin connects vimentin with various actin structures. It links vimentin to the actin cortex in mitotic cells [244, 245], to invadopodial actin networks in invasive cancer cells [246], and to actin stress fibers in adherent cells [247, 248]. The actin-vimentin crosslinking function of plectin controls force transmission within the cytoskeleton and is therefore important for myosin-driven traction force generation by adherent cells [249] and for cell migration through three-dimensional environments [248].

In addition to serving as an actin-intermediate filament crosslinker, plectin exhibits isoform-specific anchoring functions that are pivotal for cellular integrity and func-

tion [291, 293]. For instance, the plectin isoform P1a specifically anchors the epithelial intermediate filament protein keratin to hemidesmosomes by binding to integrin 4. Notably, only full-length P1a, with its C-terminal IF-binding domain, supports proper hemidesmosomal recruitment of keratin filaments [294, 255, 295]. In skeletal muscle fibers, the plectin isoform P1f anchors desmin intermediate filaments to the subsarcolemmal protein network, ensuring costamere integrity and neuromuscular junction stability. P1f deficiency leads to myofibrillar misalignment and dispersal of acetylcholine receptor clusters [296, 297, 256]. Similarly, the plectin isoform P1b anchors vimentin intermediate filaments to mitochondria via its unique signal–anchor domain, which facilitates mitochondrial fusion [298, 299]. In neuronal and epithelial cells, plectin isoform P1c has been documented to bind directly to microtubules through its distinct N-terminal sequence, thereby modulating microtubule dynamics [300, 301]. Finally, P1d anchors desmin intermediate filaments to the Z-disc in myofibers, which is essential for maintaining sarcomeric organization [296, 302]. The interaction partners and targeting mechanisms for several other isoforms of plectin remain unknown [234].

Depletion of plectin has been demonstrated to modify the mechanical properties of various cell types, including fibroblasts, keratinocytes and myoblasts [249, 251, 198]. However, understanding the distinct contributions of plectin's crosslinking and anchoring functions to cell mechanics has been challenging. To untangle these two functions, we developed a synthetic actin-vimentin crosslinker termed 'ACTIF', engineered to crosslink actin and vimentin filaments like plectin, but without plectin's ability to anchor to specific cellular structures. Previously, through imaging and rheometry, we demonstrated that ACTIF, containing plectin's intermediate filament binding domain, can efficiently crosslink vimentin and actin filaments in reconstituted networks [250]. Here we 'reconstitute' actin-vimentin crosslinking in cells by expressing ACTIF in plectin knockout ($Plec^{-/-}$) fibroblasts. We demonstrate that ACTIF crosslinkers are able to fully rescue the bulk mechanical stiffness of wild type ($Plec^{+/+}$) cells. However, the crosslinking function alone is not able to rescue the more isoform-specific functions of plectin, such as traction force generation and regulation of nuclear shape. Thus, the distinct anchoring roles of plectin appear crucial for regulating specialised cellular functions beyond simple mechanical reinforcement.

4.2. RESULTS

4.2.1. ACTIF CROSSLINKING MEDIATES COLOCALIZATION OF ACTIN AND VIMENTIN FILAMENTS IN FIBROBLASTS

The aim of this study was to untangle the direct mechanical role of plectin as an actin-to-vimentin crosslinker from its indirect roles in anchoring vimentin to other cellular structures (Figure 4.1A). Full-length plectin is a giant multidomain crosslinker protein (Figure 4.1B top). Its isoform-specific N-terminal head domain (indicated by the star in the schematic) is followed by an actin-binding domain, an elongated plakin domain, a central rod domain that mediates plectin dimerization, and six plakin repeat domains, where the last two domains constitute the intermediate filament binding domain

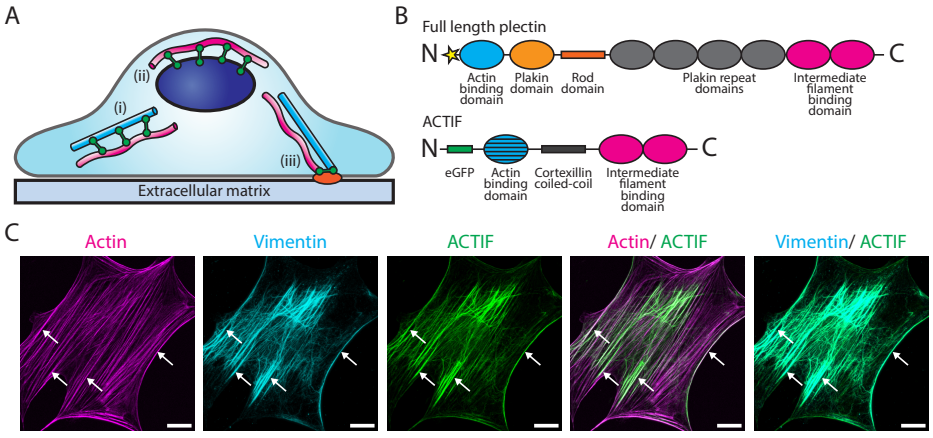

Figure 4.1: Actin-to-vimentin crosslinking via plectin in cells. (A) Plectin acts as (i) a crosslinker between the actin and vimentin cytoskeletal networks in cells but also as (ii) an anchoring protein that links the vimentin cytoskeleton to the nucleus and (iii) to the extracellular matrix via focal adhesions. (B) Domain structures of full length plectin (top) and our engineered actin-vimentin crosslinker (ACTIF) with the actin binding domain from the microtubule-actin crosslinker MACF and the intermediate filament binding domain from plectin (bottom), and a green fluorescent protein (eGFP) tag at the N-terminus. The star in the full length plectin schematic indicates the isoform-specificity of the N-terminal head domain. (C) Confocal immunofluorescence images of mouse fibroblasts on fibronectin-coated glass demonstrate that the ACTIF crosslinker (green, tagged with GFP) localizes to both actin (magenta, tagged with Alexa 568-phalloidin) and vimentin (cyan, tagged with rabbit anti-vimentin primary antibodies and anti-rabbit Alexa Fluor-647 secondary antibodies) structures, including regions where these filaments overlap (arrows indicate examples). Scale bars are 10 µm.

[303, 304, 305, 306]. The actin-binding domains and last plakin repeat domains are essential for plectin's crosslinker functions, while the N-terminal head domain is essential for plectin's anchoring functions. The head domain directs plectin to distinct subcellular structures within the cell in a cell-type-dependent manner, by specific recognition of distinct isoform-specific interaction partners [294].

To identify the contribution of plectin's crosslinking role to cell mechanics, we engineered a minimal crosslinker protein designed to model the crosslinking activity of plectin (Figure 4.1B bottom), which we call ACTIF. This engineered crosslinker is comprised of the F-actin binding domain of the actin-microtubule crosslinker MACF [307], a coiled-coil spacer domain that mediates dimerization, and the C-terminal intermediate filament binding domain of plectin [120]. We furthermore append an N-terminal GFP tag to facilitate fluorescence visualization of its cellular localization. ACTIF is designed to maintain the shared actin-vimentin crosslinking function of plectin while lacking the isoform-specific N-terminus imperative for anchoring to intracellular structures. We previously demonstrated via biochemical reconstitution experiments that ACTIF crosslinks actin and vimentin filaments into stable composite bundles and networks [120]. In this study, we transiently expressed ACTIF in immortalized mouse fibroblasts derived from transgenic plectin-deficient mice to understand the impact of actin-vimentin crosslinking on the mechanical behavior of cells. Specifically, we used an array of biophysical assays to make a side-by-side comparison between plectin wild-type cells ($Plec^{+/+}$), plectin-deficient cells ($Plec^{-/-}$), and $Plec^{-/-}$ cells expressing the ACTIF construct ($Plec^{-/-}$ ACTIF).

To test whether ACTIF can simultaneously co-localize with actin and vimentin in plectin-deficient cells, as expected in case it forms actin-vimentin crosslinks, we first performed confocal fluorescence imaging. As shown in Figure 4.1C, ACTIF indeed localized to both actin and vimentin structures, including regions where these filaments overlap. This suggests that ACTIF can take over plectin's crosslinking role, but with plectin's isoform-specific actin binding domain replaced by the actin binding domain of MACF.

4.2.2. ACTIF-MEDIATED CYTOSKELETAL CROSSLINKING RESCUES CELL STIFFNESS

Having shown that ACTIF associates with the actin and vimentin networks in ACTIF-expressing $Plec^{-/-}$ cells, we proceeded to investigate its impact on cell mechanics. We first performed nanoindentation on fibroblasts adhered to fibronectin-coated glass using atomic force microscopy (AFM). Using an AFM tip with a 1 μm radius spherical bead probe (Figure 4.2A inset), we measured force-distance curves during tip approach and retraction (black lines in Figure 4.2A). By fitting a viscoelastic material model to these data [308] that assumes that the cell follows power-law rheology [172] (red lines in Figure 4.2A), we were able to extract an apparent Young's modulus (E_0) and cell fluidity (β) for each cell. These two quantities allow us to directly compare the influence of crosslinking on the elastic and viscous components of the cells' linear (small-strain) mechanical response, respectively.

Plectin-deficient ($Plec^{-/-}$) cells were substantially softer than wild type cells ($Plec^{+/+}$), with an apparent Young's modulus of 2700 ± 100 Pa versus 4500 ± 300 Pa (Fig-

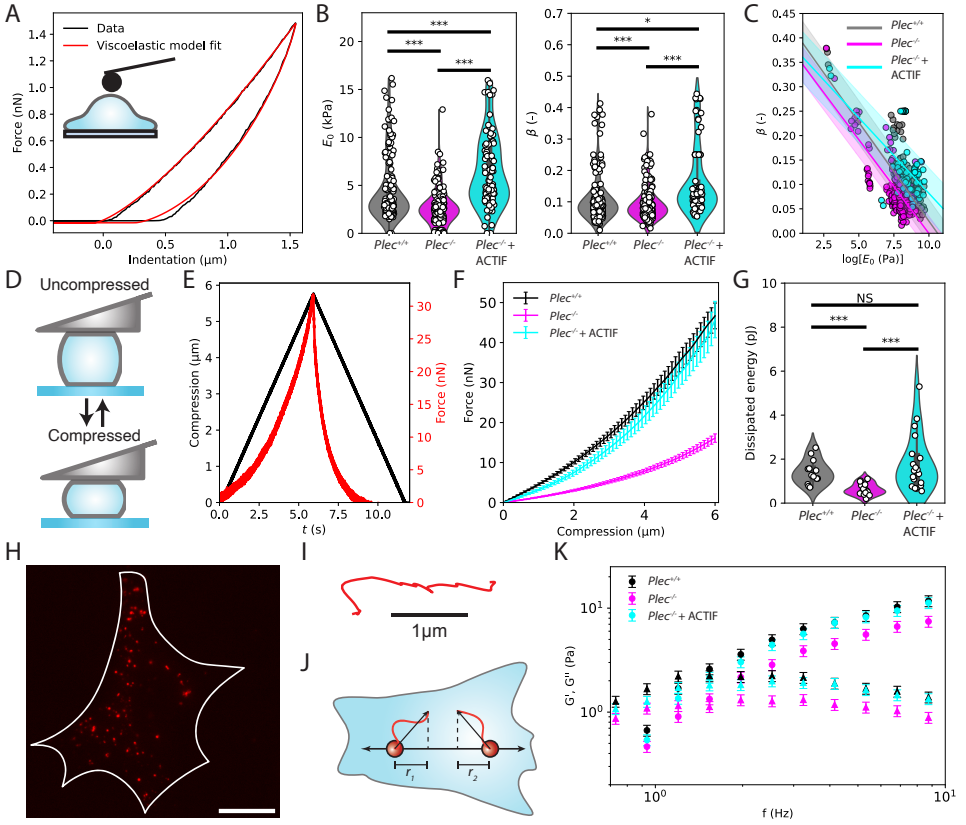

Figure 4.2: Introducing the engineered ACTIF crosslinker restores the stiffness of plectin-deficient cells back to that of wild type cells. (A) Representative indentation and retraction curves (black) measured by AFM nanoindentation of a $Plec^{+/+}$ cell. Red lines show fits to the viscoelastic model Equations 4.1 and 4.2. (B) Corresponding fitting parameters for $Plec^{+/+}$, $Plec^{-/-}$ and $Plec^{-/-}$ ACTIF cells: left panel shows the effective Young's modulus, E_0, right panel shows the fluidity β. Introducing ACTIF into $Plec^{-/-}$ cells increases cell stiffness and fluidity. (C) Correlation between the β and $\log[E_0]$ values from panel B. Each symbol indicates an individual cell. Solid lines show linear fits with the shaded error band representing the standard deviation of the fit. (D) Single fibroblasts were uniaxially compressed between two parallel, nonadhesive plates. (E) Representative compression measurement on a $Plec^{+/+}$ cell at a constant rate of 1 μm/s to a target deformation of 6 μm, followed by cantilever retraction at the same rate (black) and the measured force response (red). (F) Force-compression curves for $Plec^{+/+}$, $Plec^{-/-}$ and $Plec^{-/-}$ ACTIF cells. ACTIF stiffens $Plec^{-/-}$ cells to the same level as $Plec^{+/+}$ cells (for additional quantification, see supplementary Figure 4.7). (G) Energy dissipated in the loading-unloading cycles determined from the area under the force-compression curves. $Plec^{+/+}$ and $Plec^{-/-}$ cells expressing ACTIF both dissipate more energy than $Plec^{-/-}$ cells. (H) Particle tracking microrheology using lysosomes (fluorescently labeled with SiR-Lysosome) as fiducial markers. Image shows a single frame taken from a time lapse fluorescence movie. The white line circumscribing the cell shows the position of the cell edge. Scale bar is 20 μm. (I) Example trajectory of a single lysosome reveals a combination of diffusive motion and ballistic motion driven by active transport. (J) Two particle microrheology to extract the complex shear modulus of the cytoplasm. The motion of pairs of lyosomes along their mutual line of centres cancels out the contribution of active transport and hence allows us to use the generalized Stokes-Einstein relation to infer the shear modulus of the cytoplasm. (K) The resulting storage (G') and loss (G'') shear moduli. ACTIF restores the cytoplasmic rheology of $Plec^{-/-}$ cells back to the level of $Plec^{+/+}$ cells. * denotes P < 0.05, ** denotes P < 0.01, *** denotes P < 0.001, NS denotes no significance.

ure 4.2B left). When we expressed ACTIF in the $Plec^{-/-}$ cells, the Young's modulus increased to 6400 ± 400, exceeding the stiffness of $Plec^{+/+}$ cells (Figure 4.2B left). Under all three conditions, the cells behaved as viscoelastic materials, characterized by fluidity (β) values inbetween the limits of an ideal solid ($\beta = 0$) and an ideal liquid ($\beta = 1$). Surprisingly, cells expressing plectin ($Plec^{+/+}$) or ACTIF ($Plec^{-/-}$ ACTIF) were more fluid-like, with average β-values of 0.108 ± 0.006 and 0.16 ± 0.01, respectively, than $Plec^{-/-}$ cells, where $\beta = 0.0935 \pm 0.004$ (Figure 4.2B right). Given previous reports of an inverse relationship between stiffness and fluidity [172, 188], we then plotted β against $\log[E_0]$. For all three conditions, we observed a negative linear correlation between β and $\log[E_0]$ (Figure 4.2C), meaning that stiffer cells behaved in a more solid-like manner.

To test whether ACTIF crosslinking also affects the nonlinear mechanical response of cells to large deformations, we next subjected the cells to uniaxial compression using an indentation device with a wedged cantilever (Figure 4.2D left). The bottom surface and cantilever were coated with a nonadhesive layer to prevent integrin-dependent active responses of the cell to compression. We lowered the cantilever at a constant rate to apply a uniaxial compression until reaching a compressive strain of $\sim 40\%$ and then raised the cantilever back to test reversibility (black line in Figure 4.2D right). The resulting force signal revealed that the cells stiffened above a threshold compression and that compression was reversible (red line in Figure 4.2D right). A comparison of the loading curves showed that $Plec^{-/-}$ cells were softer than $Plec^{+/+}$ cells, with lower forces at any given compression level (magenta and black curves in Figure 4.2F, respectively). However, by expressing ACTIF in $Plec^{-/-}$ cells, the cells recovered the stiffness level of $Plec^{+/+}$ cells (cyan curve). By calculating the area between the loading and unloading parts of the compression cycle, we could also extract the energy lost during the compression measurement. We found that $Plec^{+/+}$ and ACTIF cells dissipated more energy than $Plec^{-/-}$ cells (Figure 4.2G), consistent with the fluidity measurements at smaller deformations obtained by AFM.

The AFM and compression experiments both show that ACTIF influences the mechanical response of cells to external deformations. This response is a combination of the cell membrane, nucleus and cytoskeleton-containing cytoplasm. To test whether ACTIF specifically influences the mechanics of the cytoplasm, we performed microrheology by tracking the movements of endogenous lysosomes tagged with SiR-Lysosome. Lysosomes were distributed throughout the cell (Figure 4.2H), thus providing convenient tracking of the cytoplasmic rheology. Single-particle trajectories showed phases of diffusive motion and ballistic transport, indicative of motor-driven active transport [309] (Figure 4.2I). Ensemble-averaged mean-squared displacements indeed confirmed that the lysosomes moved subdiffusively at short time scales and superdiffusively at longer time scales (Supplementary Figure 4.8). The rheological properties of the cytoplasm can in principle be inferred from the particle displacements using the generalised Stokes-Einstein relation [264]. However, this model assumes that motion is driven only by thermal fluctuations, whereas our data clearly show evidence for a contribution of active transport. To mitigate this effect, we used two-point microrheology [310]. The idea of this method is to cross-correlate the motions of pairs of lysosomes and compute the component along their mutual line of centres (Figure 4.2J). We then applied the generalised Stokes-Einstein relation to obtain the storage modulus $G'(\omega)$ and loss

modulus $G''(\omega)$, which correspond to the elastic and viscous components of the cytoplasm's shear rheology, respectively. For all three cell conditions, the viscous modulus exceeded the elastic modulus at low frequency, indicating that the cytoplasm is fluid on long timescales (Figure 4.2K). The crossover frequency where the cytoplasm transitions from liquid-like to solid-like behaviour (specifically, the frequency where $G'(\omega) = G''(\omega)$), was about 1.4 Hz for all three conditions (Supplementary Figure 4.9). The storage modulus of the cytoplasm of *Plec*$^{-/-}$1 cells (at 4 Hz) is softer than for *Plec*$^{+/+}$ cells by a factor of ~ 1.5 (see Supplementary Tables 1 and 2 for the other frequencies). However, expressing ACTIF in the *Plec*$^{-/-}$ cells brings G' back up to the level measured for *Plec*$^{+/+}$ cells (7.3 ± 0.7 Pa). Since ACTIF only has the crosslinker function of plectin and not its anchoring function, this observation suggests that the crosslinking function of plectin determines the cytoplasmic stiffness of cells. Likewise the loss modulus $G''(\omega)$ of the cytoplasm was also larger by a factor of ~ 1.4 for cells containing plectin (*Plec*$^{+/+}$) or ACTIF (*Plec*$^{-/-}$ cells rescued with ACTIF) as compared with *Plec*$^{-/-}$ cells. Apparently the greater viscous dissipation of these cells measured in AFM and whole-cell compression assays stems from crosslinker-dependent viscous dissipation in the cytoplasm.

4.2.3. ACTIF CROSSLINKING DOES NOT RESCUE TRACTION FORCE GENERATION

Our mechanical measurements suggest that the crosslinker function of plectin alone is enough to provide fibroblasts with normal viscoelastic properties. This raises the question whether the anchoring function of plectin has any mechanical effects. We reasoned that if plectin anchoring is important, this should show up in traction force generation, as plectin is known to associate with focal adhesions that anchor the cytoskeleton to the extracellular matrix [311]. To test this idea, we performed two-dimensional (2D) traction force microscopy (TFM) experiments. Cells were seeded on fibronectin-coated polyacrylamide gels with a Young's modulus of 4.5 kPa [312] embedded with 200 nm fluorescent beads that serve as fiducial markers (Figure 4.3A). We acquired two sets of Z-stack images per cell. The first set, captured 12 hours after seeding, represented the stressed state when cells had adhered to the gel and generated contractile forces that deformed its surface. The magnitude of these traction forces depends on the ability of the cytoskeleton to anchor to fibronectin extracellular matrix proteins on the gel surface. The second set, obtained 15 minutes after applying a droplet of 5% SDS to detach the cells, represented the relaxed state after the substrate returned to its original configuration. By measuring the bead displacements between these states and accounting for the gel's known mechanical properties, we were able to calculate cellular traction forces [313].

We found that *Plec*$^{+/+}$ cells generated larger bead displacements compared to *Plec*$^{-/-}$ cells, but also compared to ACTIF-expressing *Plec*$^{-/-}$ cells (Figure 4.3B). This implies that ACTIF is unable to rescue plectin's role in traction force generation. To quantify this effect, we measured the mean traction force, which was indeed significantly higher in *Plec*$^{+/+}$ cells (107 ± 3 Pa) than in *Plec*$^{-/-}$ (27 ± 1 Pa) and ACTIF-expressing *Plec*$^{-/-}$ cells (32 ± 3 Pa). Further analysis of the spatial organization of the traction force fields revealed that individual traction foci were larger in area in *Plec*$^{+/+}$ cells (170 ± 10 μm^2)

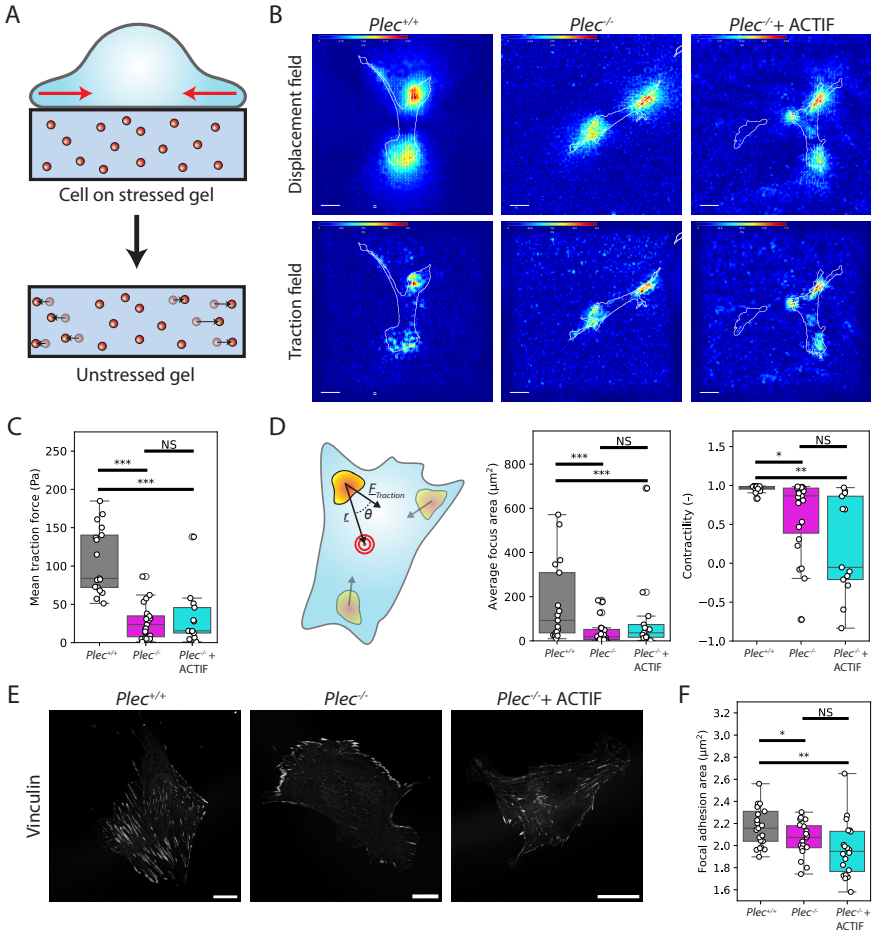

Figure 4.3: Actin-vimentin crosslinking does not rescue cellular traction force generation of plectin-deficient cells. (A) We seed fibroblasts on fibronectin-coated polyacrylamide gels (4.5 kPa) containing 200 nm diameter tracer particles (shown in red). Due to the traction forces exerted by the contractile cell (red arrows in the schematic), the gel is in a stressed state. Cell detachment with 5% SDS relieves the stress, causing bead displacements (shown by black arrows) from which we infer traction forces. (B) Top: Measured displacement fields for representative cells showing that particle displacements are greater for $Plec^{+/+}$ cells than for $Plec^{-/-}$ cells and $Plec^{-/-}$ ACTIF cells. Bottom: Corresponding traction force fields show that $Plec^{+/+}$ cells exert greater traction forces. Scale bars are 10 μm. (C) Mean total traction force per cell, calculated from the traction fields. $Plec^{+/+}$ cells exert significantly higher traction forces than $Plec^{-/-}$ or $Plec^{-/-}$ ACTIF cells. (D) Left graph: area of the traction foci (indicated by the orange islands in the schematic). Right graph: contractility, defined as the dot product between the traction force vector ($\underline{F}_{\text{Traction}}$ in the schematic) and the vector between the cell centroid and the origin of the traction force ($\underline{r}$ in the schematic). Note that the cells pull on the substrate towards their centroids. (E) Focal adhesions visualized by immunofluorescent confocal images of vinculin (white) in $Plec^{+/+}$, $Plec^{-/-}$ and $Plec^{-/-}$ ACTIF cells. (F) Average focal adhesion area per individual cell determined by automated image analysis of vinculin images. $Plec^{+/+}$ cells have significantly larger focal adhesion complexes than $Plec^{-/-}$ cells and $Plec^{-/-}$ ACTIF cells. * denotes P<0.05, ** denotes P<0.01, *** denotes P<0.001, NS denotes no significance.

than in *Plec*$^{-/-}$ (39 ± 2 μm^2) and ACTIF-expressing *Plec*$^{-/-}$ cells (102 ± 14 μm^2) (Figure 4.3D left). To ensure that these differences were not simply a consequence of variations in overall cell size, we compared cell areas across conditions and found no significant differences (Supplementary Figure 4.10). The traction forces were always predominantly directed toward the cell centroid. To quantify the efficiency of this inward pull, we defined contractility as the dot product between the traction force vector and the vector extending from the cell centroid to the force's point of origin (schematic in Figure 4.3D). To normalise the contractility, we converted the traction vectors and radial vectors to unit vectors and computed their dot product. This yielded nondimensional values ranging from 1 (indicating that the traction vector points directly towards the cell centroid) to -1 (indicating that the traction vector is directly antiparallel). Our measurements yielded contractility values of 0.957 ± 0.003 for *Plec*$^{+/+}$ cells, 0.62 ± 0.02 for *Plec*$^{-/-}$ cells, and 0.22 ± 0.05 for ACTIF-expressing *Plec*$^{-/-}$ cells (Figure 4.3D right), indicating that plectin makes wild type cells significantly more effective at directing traction forces inward toward the cell centroid.

To test whether the observed differences in traction force generation corresponded with changes in focal adhesion assembly, we performed immunofluorescence imaging of vinculin, a key marker of focal adhesion formation and maturation [314]. We indeed found that focal adhesions in *Plec*$^{+/+}$ cells were significantly larger than in *Plec*$^{-/-}$ cells as well as ACTIF-expressing *Plec*$^{-/-}$ cells (Figure 4.3F). Additionally, we found that *Plec*$^{+/+}$ cells had a significantly larger number of focal adhesions per cell compared to *Plec*$^{-/-}$ and ACTIF-expressing *Plec*$^{-/-}$ cells (Supplementary Figure 4.11). Altogether, our results show that, although ACTIF restores the viscoelastic properties of cells, it is not able to rescue traction force generation.

4.2.4. PLECTIN-MEDIATED NUCLEAR ANCHORING IS NEEDED TO RESTORE WILD TYPE NUCLEAR MORPHOLOGY

In addition to anchoring cells to the extracellular matrix, plectin is known to associate with the nuclear LINC complex via nesprin-3, allowing the formation of a protective vimentin 'cage' to reinforce the nucleus against compressive stress [272, 43]. Fibroblasts and keratinocytes in which plectin is knocked out as well as primary fibroblasts from EDS patients with low plectin expression levels have been shown to display perturbed nuclear morphologies [315, 273, 242]. We hypothesised that this function relies on plectin's anchoring role. If true, then ACTIF should be unable to rescue the perturbed nuclear morphology in plectin knockout cells. Confocal fluorescence images of cell nuclei labeled with Hoechst showed that *Plec*$^{-/-}$ cells indeed had strongly deformed nuclei, in contrast with the smooth ellipsoidal nuclei in wild type cells (Fig 4.4B). Consistent with recent observations in primary fibroblasts with low plectin expression levels [242], the nuclei of the *Plec*$^{-/-}$ cells were highly irregularly shaped, often adopting peanut shapes. They also exhibited frequent nuclear envelope herniations, also referred to as blebs. When ACTIF was expressed in the *Plec*$^{-/-}$ cells, the nuclei remained highly deformed, indicating that actin-vimentin crosslinking alone is indeed insufficient to rescue normal nuclear morphology. The nuclei were again irregularly shaped and often showed blebs. This finding indicates that nuclear shape protection relies on the anchor-

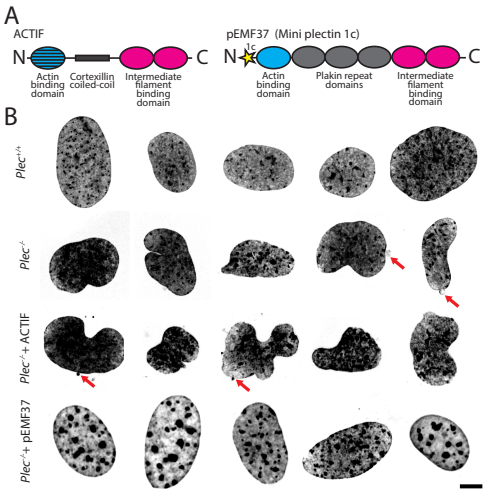

Figure 4.4: ACTIF does not rescue nuclear shape, but anchoring mediated by the N-terminus of plectin1c does restore a normal nuclear morphology. (A) Schematic showing the domain structures of the engineered ACTIF crosslinker (left) and a truncated variant of plectin isoform 1c referred to as pEMF37. (B) Maximum intensity projections of confocal z-stacks of fixed cell nuclei labelled with Hoechst in $Plec^{+/+}$, $Plec^{-/-}$, ACTIF-expressing $Plec^{-/-}$, and pEMF37-expressing $Plec^{-/-}$ cells. The spacing between z-slices was 0.33 µm and the z range was selected to encompass the whole nucleus for each cell. Red arrows show examples of nuclear herniations, also known as blebs (see Supplementary Figure 4.12 for quantification). Scale bars are 5 µm.

ing role of plectin rather than its crosslinking role. To test this idea, we transfected the $Plec^{-/-}$ cells with a truncated variant of plectin isoform 1c, referred to as pEMF37 (Figure 4.4A). pEMF37 contains exons 2α and 3α, characteristic of plectin isoform 1c, which has previously been shown to associate with the nuclear envelope [272]. Upon introduction of pEMF37 in $Plec^{-/-}$ cells, the nuclear morphologies were indeed restored to normal (Figure 4.4B bottom row), suggesting that this truncated plectin variant effectively compensates for the absence of full-length plectin with its ability to anchor vimentin to the nucleus.

Plectin's role in nuclear shape protection has been attributed to its ability to organize vimentin in a cage around the nucleus that protects the nucleus from forces exerted by the cytoskeleton [286]. To determine the contributions of plectin-crosslinking versus anchoring to the organization of vimentin, we quantified the distribution of vimentin in cells adhered to fibronectin-coated coverslips by confocal immunofluorescence imaging. As shown in Figure 4.5A, $Plec^{+/+}$ cells exhibited a fine network of interconnected vimentin filaments, whereas $Plec^{-/-}$ and ACTIF-expressing $Plec^{-/-}$ cells both displayed pronounced vimentin bundling. To characterize to what extent vimentin formed a perinuclear cage, we evaluated how the fluorescence intensity of vimentin varied with the lateral distance from the nucleus as well as the angle relative to the nucleus's centroid (Figure 4.5B). We found that within a 1 µm radius of the nucleus, the $Plec^{+/+}$ cells exhibited a uniform intensity profile (Figure 4.5C). In contrast, this intensity pattern was much less uniform in both the $Plec^{-/-}$ and the ACTIF-expressing $Plec^{-/-}$ cells. To quantify the distribution spread of the fluorescence around the nucleus, we calculated the

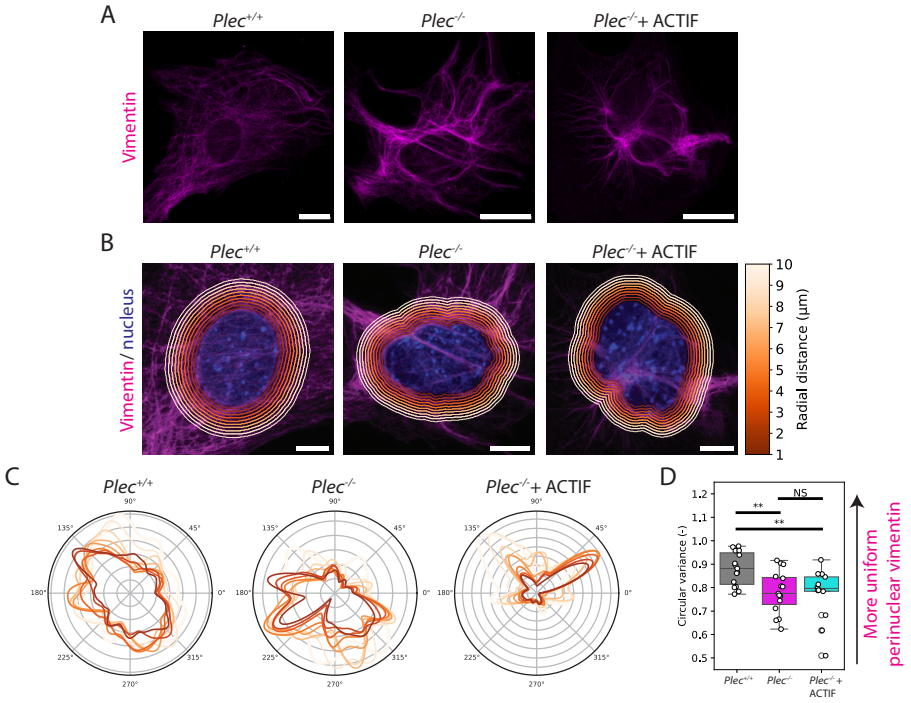

Figure 4.5: Vimentin distribution in $Plec^{+/+}$, $Plec^{-/-}$ and ACTIF-expressing $Plec^{-/-}$ cells adhered to fibronectin-coated glass. (A) Representative maximum intensity projections of confocal immunofluorescence images generated from z-stacks of $Plec^{+/+}$, $Plec^{-/-}$ and ACTIF-expressing $Plec^{-/-}$ cells. (B) Zoomed-in images of (A), showing the nucleus (dark blue), vimentin (cyan), and 1 µm equidistantly spaced contours used to calculate the radial variance of the vimentin signal around the nucleus. (C) Representative examples of polar histogram plots for the moving average of fluorescence intensity at 1 µm intervals around the nucleus, generated from the images shown in (B). Distance from the origin indicates averaged fluorescence intensity and the angle of the intensity is shown in degrees. (D) Boxplot showing the distribution of circular variance in $Plec^{+/+}$ cells ($N = 15$), $Plec^{-/-}$ cells ($N = 15$), and $Plec^{-/-}$ + ACTIF cells ($N = 13$). The perinuclear vimentin signal is more uniform in $Plec^{+/+}$ cells than in $Plec^{-/-}$ cells, and this distribution is not rescued by ACTIF.

circular variance from the radial fluorescence intensity pattern within a 1 µm perimeter of the nucleus. The circular variance was normalized so that its value ranges from 0 (indicating a highly directed distribution) to 1 (indicating a perfectly uniform distribution). As shown in Figure 4.5C, the median circular variance within 1 µm of the nucleus was somewhat larger for wild type cells (0.88 ± 0.02) as compared to $Plec^{-/-}$ cells (0.78 ± 0.02) as well as ACTIF-expressing $Plec^{-/-}$ cells (0.74 ± 0.03), consistent with a more uniform vimentin cage around the nucleus in wild-type cells.

4.2.5. PLECTIN SPEEDS UP 2D CELL MIGRATION

Our traction force measurements and focal adhesion size quantification indicate that the anchoring role of plectin is important for effective force transmission. Since force transmission influences cell migration dynamics, we decided to compare the effects of full

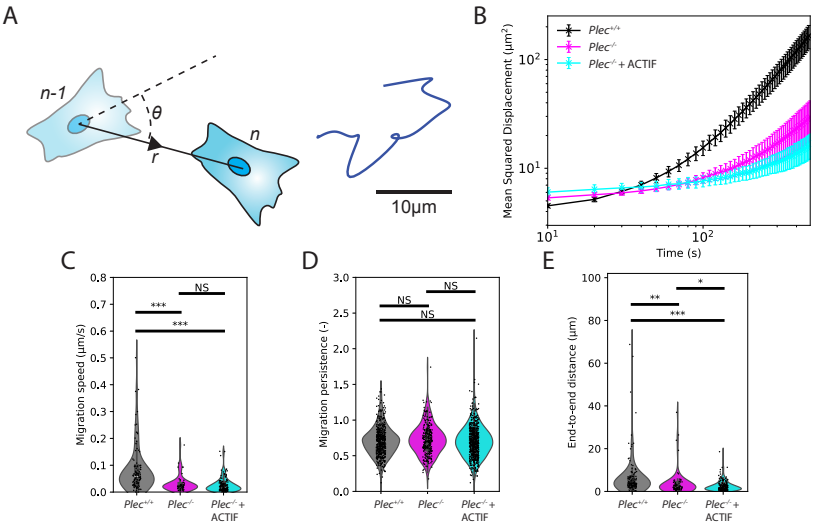

Figure 4.6: 2D migration of $Plec^{+/+}$, $Plec^{-/-}$ and ACTIF-expressing $Plec^{-/-}$ cells on fibronectin-coated glass. (A) Left schematic: We track the position of cell centroids through time-lapse epifluorescence imaging of the cellular cytoplasm (fluorescently labeled with CellTracker). Right: example cell trajectory. For all particle trajectories shown as Windrose plots, see Supplementary Figure 4.13 (B) Mean squared displacements of the cells on fibronectin-coated glass evaluated over an 500 s time period. (C) Mean migration speed. (D) Migration persistence defined as the direction autocorrelation from the displacement vectors of the migration tracks. (E) End-to-end distance of migration paths measured over a 500 s interval. * denotes P<0.05, ** denotes P<0.01, *** denotes P<0.01, NS denotes no significance.

length plectin versus ACTIF on the velocity and persistence of 2D cell migration. To this end, we seeded cells on fibronectin-coated glass, allowed them to adhere overnight, and examined their motility over a period of 1 hour using epifluorescence microscopy (Figure 4.6A and Supplementary Movie 1). To quantify the dynamics of cell movement, we computed the mean squared displacements (MSDs) from the tracked cell centroids (Figure 4.6B). Note that in case of the ACTIF-expressing $Plec^{-/-}$ cells, we analyzed only those cells for which a GFP signal was identified. When plotted on a log-log scale, the MSDs exhibited a biphasic profile, with trapped or constrained movement at short timescales, likely reflecting local probing, adhesion dynamics or cytoskeletal remodeling, and a transition to ballistic-like migration at longer timescales, consistent with the establishment of cell polarity and sustained directional movement. Interestingly, the MSDs for $Plec^{+/+}$ cells were notably higher than for $Plec^{-/-}$ cells, indicating that cells lacking plectin migrate slower. This interpretation was confirmed by our observations for $Plec^{-/-}$ cells expressing ACTIF, which also had lower mean squared displacements than $Plec^{+/+}$ cells.

Next, to quantify cell migration speed, we calculated the mean speed for each tracked cell by first computing the frame-to-frame displacement vectors from the migration tracks, and dividing by the corresponding time intervals to obtain instantaneous speeds, which were then averaged over each trajectory. The migration speeds calculated from the cell centroid displacements were somewhat lower on average for $Plec^{-/-}$ cells ($0.031 \pm 0.002\ \mu m s^{-1}$) than for $Plec^{+/+}$ cells ($0.081 \pm 0.003\ \mu m s^{-1}$) and ACTIF-expressing $Plec^{-/-}$ cells ($0.026 \pm 0.001\ \mu m s^{-1}$) (Figure 4.6C).

We then questioned whether the observed reduction in migration speed upon plectin depletion goes together with reduced directional persistence of the migration tracks. To assess this, we computed the direction autocorrelation from the displacement vectors of the migration tracks, providing a quantitative measure of how consistently cells maintained their direction over time. Specifically, we defined direction autocorrelation as the average cosine of the angle between successive displacement vectors along each track, such that higher values indicate more persistent, aligned movement [316]. As shown in Figure 4.6D, the persistence of the migration tracks did not differ significantly across the conditions, indicating that directional persistence remained unaltered.

Finally, we calculated the end-to-end migration distance over 500 seconds and found values of $6.5 \pm 0.8\ \mu m$ for $Plec^{+/+}$ cells, $3.6 \pm 0.6\ \mu m$ for $Plec^{-/-}$ cells, and $2.5 \pm 0.2\ \mu m$ for ACTIF-expressing $Plec^{-/-}$ cells (Figure 4.6 E). Taken together, our findings suggest that the actin-vimentin crosslinking function of plectin alone does not fully restore 2D cell migration efficiency.

4.3. DISCUSSION

The aim of this study was to untangle the distinct contributions of plectin's crosslinking and anchoring functions to cell mechanics and cytoskeletal organisation. To this end, we introduced a synthetic actin-vimentin crosslinker (ACTIF) into mouse embryonic fibroblasts, which is designed to mimic the crosslinking function of plectin while lacking its anchoring capabilities. We first combined atomic force microscopy, whole-cell compression, and two-particle microrheology to assess the impact of ACTIF-mediated

actin-vimentin crosslinking on both global and intracellular mechanical properties. We found that introducing ACTIF into plectin-deficient cells fully restored their mechanical stiffness and fluidity to the level of wild-type cells, indicating that plectin's crosslinking function is sufficient to maintain overall cell mechanics. We further conclude that plectin's anchoring role is not required for this aspect of cellular behaviour. We next performed 2D-traction force microscopy on cells seeded on polyacrylamide hydrogels to assess how actin-vimentin crosslinking influences the ability of cells to exert forces on their substrate. We found that, unlike cell stiffness, traction force generation was not rescued by ACTIF, indicating that restoring cytoskeletal crosslinking alone is not enough to support force transmission to the substrate. We then turned to nuclear morphology to test whether anchoring functions of plectin play a role in maintaining nuclear shape. While ACTIF-expressing cells showed highly deformed and irregularly shaped nuclei similar to plectin-deficient cells, expression of the truncated isoform-specific construct pEMF37 that is capable of nuclear anchoring restored the smooth nuclear shapes seen in wild type cells. Finally, we examined 2D cell migration to test whether cytoskeletal crosslinking influences cell motility. We found that plectin-deficient cells migrated faster than wild-type cells and ACTIF-expressing cells, indicating that actin-vimentin crosslinking slows down cell movement. Together, our results show that, while crosslinking is sufficient to restore bulk cell mechanics and 2D cell migration, anchoring is essential for traction force generation, and nuclear integrity.

Our results show that cytoskeletal crosslinking via ACTIF stiffens cells by reinforcing the mechanical coupling between actin and vimentin networks. This finding is consistent with measurements on biochemically reconstituted actin-vimentin networks crosslinked with ACTIF, where ACTIF likewise enhanced the network stiffness [250]. Although ACTIF expression increased cell stiffness, it also led to higher viscoelastic energy dissipation, suggesting that ACTIF (and plectin) form highly dynamic rather than permanent crosslinks. In other words, plectin adds elastic strength without reducing the cell's ability to dissipate stress. Together, these findings suggest that ACTIF, and by extension plectin, acts as a transient crosslinker that reinforces cytoskeletal stiffness while permitting network remodeling and stress relaxation [317, 228]. This interpretation is consistent with single-molecule measurements of ACTIF binding and unbinding rates in reconstituted actin and vimentin systems [250]. We propose that this balance between solid-like elasticity and fluid-like viscosity, governed by crosslinker dynamics, allows cells to remain both mechanically robust and adaptable.

While crosslinking restores the mechanical integrity of plectin-deficient cells, our results show that plectin's anchoring functions are essential for the full execution of cellular functions such as force transmission and nuclear shape regulation. Notably, our ACTIF crosslinker failed to restore traction force generation in plectin-deficient cells, indicating that actin–intermediate filament crosslinking alone is insufficient without proper intermediate filament anchorage at focal adhesions. This finding aligns with the established role of plectin isoform 1f (P1f) as a focal adhesion-anchoring link for vimentin filaments, which stabilises adhesions and enables efficient force transmission [318]. In the absence of P1f-mediated intermediate filament anchorage, contractile forces cannot be effectively relayed to the substrate – a deficit that an untargeted crosslinker like ACTIF cannot compensate. This is consistent with observations that traction stress alignment

depends on the proper anchorage and organisation of vimentin within the cytoskeletal network [319]. Likewise, ACTIF did not rescue the abnormal nuclear morphology of plectin-null cells, whereas a truncated version of plectin 1c (P1c), pEMF37, successfully restored normal nuclear shape. This highlights that plectin's nuclear anchoring function also requires more than generic actin–intermediate filament linkage. Consistent with this, specific plectin isoforms such as P1 and P1c localize to the nuclear envelope by binding the outer nuclear membrane protein nesprin-3 [320, 272], thereby tethering perinuclear intermediate filament networks to the nucleus. This connection is essential for the nucleus to withstand cytoskeletal tension, as loss of plectin–nesprin linkages (e.g. in cells that lack plectin due to mutations that cause a reduction of full length plectin expression [234]) leads to nuclei deforming due to acto-myosin contractility [242].

4.4. CONCLUSION

In conclusion, our results demonstrate that plectin's crosslinking and anchoring functions make distinct contributions to cellular mechanics, cytoskeletal organisation and nuclear shape regulation. While crosslinking alone is sufficient to restore cell stiffness and viscoelastic properties, anchoring is essential for traction force generation, nuclear integrity, and cytoskeletal architecture. These anchoring roles rely on isoform-specific targeting of plectin to structures such as focal adhesions and the nuclear envelope, where it tethers intermediate filaments to load-bearing interfaces. By separating these two functions, our study underscores how mechanical robustness and structural coordination in cells depend not only on filament connectivity but also on precise spatial anchoring of the cytoskeleton. Our work demonstrates that disentangling the mechanical roles of isoform-specific cytoskeletal crosslinkers is crucial for understanding how cells spatially organize force transmission and maintain structural integrity. Applying similar approaches based on engineered cytolinkers in mechanically specialised tissues such as muscle fibers could uncover how distinct crosslinker isoforms coordinate cytoskeletal networks to preserve contractile function and nuclear organization under mechanical load.

4.5. ACKNOWLEDGEMENTS

We thank I. Isturiz-Petitjean, S. Glastra and S. Heinen for helping to establish microrheology methods in our lab and A. Katan and F. Rico for valuable advice regarding AFM experiments and analysis. L.W. was funded by Austrian Science Fund (FWF) grants P31541-B27 (grant-DOI 10.55776/P31541) and I6049-B (grant-DOI 10.55776/I6049). G.H.K. gratefully acknowledges funding from the NWO Talent Programme which is financed by the Dutch Research Council (project number VI.C.182.004).

4.6. MATERIALS AND METHODS

4.6.1. CELL CULTURE

Immortalized murine fibroblasts were derived from plectin wild-type ($Plec^{+/+}$) and plectin-deficient ($Plec^{-/-}$) p53-deficient (p53-/-) mice as previously described (see [254, 255, 256]). Cells were cultured in Dulbecco's modified Eagle's medium with glutamax (DMEM, 10565018 Gibco) supplemented with 10% fetal bovine serum (FBS, 10270106 Gibco) and 5% penicillin-streptomycin (Pen-Strep antibiotic, 15070063 Gibco). Cells were maintained by subculturing twice a week and were screened for mycoplasma contamination every four months. Experiments were performed with cells up to passage number 20.

4.6.2. CELL TRANSFECTION

For plasmid transfection, we used FuGENE 4K (Promega) according to the manufacturer's instructions with minor modifications. Briefly, FuGENE and DMEM (without supplements) were equilibrated to room temperature prior to use. For each transfection, 2 µg of ACTIF plasmid DNA was mixed with 100 µl DMEM and vortexed briefly. Next, 4 µl of FuGENE was added directly into the center of the DNA-DMEM mixture (rather than pipetting against the tube wall to avoid reagent adherence to plastic), followed by a second brief vortex. This step was identified as critical for efficient complex formation. The transfection mixture was incubated for 15–20 minutes at room temperature to allow complex formation. Meanwhile, culture medium was aspirated from the cells and replaced with a minimal volume of fresh growth medium (300–500 µl per well of a 6-well plate). The transfection mixture was then added dropwise to the cells, followed by gentle swirling of the plate to ensure even distribution. Cells were incubated overnight at 37°C in a humidified incubator.

4.6.3. ATOMIC FORCE MICROSCOPY (AFM)

Two days prior to experiments, 35 mm glass-bottomed dishes (FD35-100, WPI) were prepared by incubating with bovine fibronectin (F1141, Sigma) at a concentration of 2 µg/mL in PBS for 40 minutes at 37°C. Cells were detached from their culture plate with Trypsin-EDTA (0.25%) (25200056, Thermo Fisher Scientific) and were counted using a Countess cell counter (Thermo Fisher Scientific). Subsequently, 10,000 cells were seeded in the coated dishes and allowed to adhere overnight. The next day, cells were transfected with ACTIF according to the protocol above. On the day of experiments, cells were washed with PBS and incubated in CO_2-independent medium (18045088, Thermo Fisher) containing 5% penicillin-streptomycin (Pen-Strep, 15070063). All experiments were conducted using a JPK Nanowizard IV (Bruker) mounted on a Thunder inverted optical microscope (Leica), equipped with a 200 mW solid state LED5 light source (Leica), a monochrome sCMOS camera (Leica), and a 10x dry objective (HC PL APO 0.45NA, Leica). Mechanical measurements on cells were made in force spectroscopy mode in the JPK control software (Bruker), with a set point force of 1 nN. Cells were indented in

the perinuclear region, as identified by bright field imaging. Cantilevers with a nominal spring constant of 0.25 N/m with a 23 μm cylinder and hemisphere with a 1 μm end radius (SAA-SPH-1UM, Brucker) were used for all measurements, chosen according to the manufacturer's recommendations. Cantilever spring constant and sensitivity were calibrated before each experiment using the thermal fluctuation method. To extract the apparent Young's modulus E_0 and cell fluidity β, we used the software PyFMLab[321], which simultaneously fits an analytical model [322] to the approach (Equation 4.1) and retract (Equation 4.2) segments of the indentation experiment assuming a power-law dependence $E(t) = E_0 (t/t_0)^{-\beta}$, no adhesion between the tip and cell surface, and treating the cell as a viscoelastic half-space:

$$F(t) = \frac{3}{4}\tilde{C} v_a^{3/2} E_0 t^{1-\beta} \frac{\pi\Gamma(\beta)}{\Gamma\left(\frac{5}{2}\right)\Gamma(1-\beta)}, \tag{4.1}$$

$$F(t) = \frac{3}{4}\tilde{C} v_r^{3/2} E_0 (t_1 - t)^{1-\beta} \frac{\pi\Gamma(\beta)}{\Gamma\left(\frac{5}{2}\right)\Gamma(1-\beta)}. \tag{4.2}$$

Here, v_a and v_r are the approach and retract velocities, t is time, t_1 is the time of viscoelastic relaxation, $\tilde{C} = 3(1-\nu^2)/(4R)$ is the geometry-dependent coefficient (specified here for a spherical indenter of radius R), ν is the Poisson ratio of the cell (which assume to be 0.5[323]), and Γ is the Gamma function.

4.6.4. SINGLE CELL COMPRESSION EXPERIMENTS AND DATA ANALYSIS

Single-cell compression experiments were conducted using a single-cell rheometer adapted from the commercially available Chiaro Nanoindenter (Optics11 Life). We modified the optical fiber-based tipless cantilevers (calibrated spring constant of 0.018 N/m) with a wedge made of UV-curable adhesive (NOA81, Norland) to correct for the 3°tilt of the cantilever tip and make the surface parallel with the bottom coverslip as described our previous work [253]. Two days prior to experiments, cells were trypsinized and 10,000 were seeded into plastic 6-well cell culture plates (83.3920.005, Sarstedt). The next day, cells were transfected with the GFP-ACTIF plasmid according to the protocol above. On the day of experiments, cells were washed with PBS, resuspended in CO_2 independent medium containing 5% penicillin-streptomycin, and then placed in 35mm glass-bottom dishes. To prevent cell adhesion, we incubated the cantilever and dishes with 1% w/v Pluronic (P2443, Sigma) in MilliQ for 30 minutes. Cells were confined between the wedged cantilever and glass bottom dish, where compression was applied at a controlled rate of 1 μm/s to a final distance of 6 μm. Upon reaching the target deformation, the cantilever was immediately retracted, also at a speed of 1 μm/s, to the initial starting position. To determine energy dissipation, we determined the area between the loading and retraction segments of the experiment using Python's Numpy library [212] with the trapezium rule.

4.6.5. LYSOSOME TRACKING EXPERIMENTS

For lysosome tracking experiments, dishes and cells were prepared identically as for AFM experiments. On the day of experiments, cell culture medium was aspirated from

the dishes and cells were incubated with medium containing 1 μM SiR-Lysosome (SC012, Tebu-bio) for 1 hour. Following labelling, cells were washed with PBS and incubated in CO_2-independent medium containing 5% penicillin-streptomycin. Lysosomes were imaged with a Leica Thunder Imager widefield microscope equipped with a 200 mW solid state LED5 light source (Leica). For imaging, we used a 63x 1.2 NA glycerol objective (Leica). During experiments, the 35mm cell culture dishes were placed in a stage top incubator heater (Tokai) at 37°C and imaged within 2 hours. Time lapse image series consisting of 2000 frames were captured at a frame rate of 25 frames per second by a monochrome sCMOS camera (Leica). To track the displacements of the centroid positions of lysosomes between frames, we used the Python library TrackPy [324], which is an implementation of the Crocker–Weeks tracking algorithm [325]. Using the TrackPy package, we drift-subtracted individual particle trajectories. We next reloaded the individual particle trajectories to quantify relative displacements between pairs of particles We calculated the two-point displacement correlation:

$$D_{rr}(R,t) = \langle \Delta r_1(t) \Delta r_2(t) \rangle, \tag{4.3}$$

where $\Delta r_1(t)$ and $\Delta r_2(t)$ are the displacements of the two particles along their line of centres during the lag time t, where we average over all particle pairs separated by a distance R, with a minimum separation of 2 μm and a maximum of 8 μm [310]. The two-particle mean squared displacement (2P-MSD) is then computed as:

$$\langle \Delta r^2(\tau) \rangle_{2P} = \frac{2R}{a} D_{rr}, \tag{4.4}$$

where a is the particle radius (estimated to be 500 nm[326]) and R is the separation distance [310]. The complex shear modulus of the material, comprising the storage modulus $G'(\omega)$ and the loss modulus $G''(\omega)$, was derived from the 2P-MSD using the generalized Stokes-Einstein relation (GSER):

$$|G^*(\omega)| \approx \frac{k_B T}{\pi a \langle \Delta r^2(t = 1/\omega) \rangle_{2P} \Gamma[1 + \alpha(t = 1/\omega)]}, \tag{4.5}$$

where k_B is Boltzmann's constant, T is the absolute temperature, and $\langle \Delta r^2(t) \rangle_{2P}$ is the 2P-MSD evaluated at the inverse of the frequency ω [310]. The function Γ represents the Gamma function, and $\alpha(t)$ is the logarithmic derivative of the 2P-MSD, defined as:

$$\alpha(t) = \frac{d \ln \langle \Delta r^2(t) \rangle_{2P}}{d \ln t}. \tag{4.6}$$

The modulus $G^*(\omega)$ is a complex quantity, where the real and imaginary components correspond to the storage modulus $G'(\omega)$ and the loss modulus $G''(\omega)$, respectively. These components were calculated as:

$$G'(\omega) = |G^*(\omega)| \cos \delta(\omega), \tag{4.7}$$

$$G''(\omega) = |G^*(\omega)| \sin \delta(\omega), \tag{4.8}$$

where $\delta(\omega)$ is the phase angle, defined as:

$$\delta(\omega) = \frac{\pi}{2} \frac{d \ln |G^*(\omega)|}{d \ln \omega}. \tag{4.9}$$

4.6.6. TRACTION FORCE MICROSCOPY (TFM)

For traction force microscopy (TFM), we prepared polyacrylamide hydrogels of 4.5 kPa stiffness[327]. First, we prepared a pre-gelation solution containing 5% (v/v in MQ) acrylamide solution (Sigma-Aldrich, A4058), 0.15% (v/v in MQ) bisacrylamide solution (Sigma-Aldrich, M1533) and sonicated 200 nm diameter carboxylate modified fluorescent microspheres (1:60 v:v in MQ) (F8807, Invitrogen), which we thoroughly mixed by repeated pipetting. Next, polymerization of the hydrogel was initiated using ammonium persulfate (4.4 µM) and catalyzed by 0.1% v/v) N,N,N',N'-tetramethylethylenediamine (TEMED, Sigma-Aldrich, T7024). A 15 µl aliquot of the hydrogel mixture was placed onto the glass bottom of a 6-well plate (Cellvis, P06-14-0-N) pre-treated with bind-silane (Serva, 28739.01). To achieve a uniform thickness, the droplet was gently flattened with a Sigmacote-treated glass coverslip and allowed to polymerize at room temperature for 30 minutes. Following polymerization, the hydrogel surface was functionalized by two sequential incubations with 0.67 µM Sulfo-SANPAH (Sigma-Aldrich, 803332), each activated under a UV light source (Bioforce, 254 nm wavelength) approximately 2 cm from the gel surface for 30 minutes. The gels were subsequently coated evenly by incubation with fibronectin (human plasma, Sigma-Aldrich, F0895) diluted to 10 µg/ml in 0.1% v/v acetic acid solution (pH 3.4) for 2 hours at 37 °C. Finally, 5000 cells were seeded onto each hydrogel and incubated overnight to allow cell attachment and spreading.

Live-cell imaging for traction force microscopy experiments was conducted using a Leica Stellaris confocal fluorescence microscope equipped with a supercontinuum white light laser. Images were acquired with a 40X 1.1 NA glycerol immersion objective at a zoom factor of 1.5 and 512x512 pixel resolution. Imaging was performed bidirectionally with phase correction at an Airy Unit (AU) of 1. Excitation wavelengths of 488 nm and 633 nm were employed for the green cell channel and the far-red fluorescent bead channel, respectively. Hybrid detectors were configured to detect fluorescence emission within 495-555 nm for the green channel and 640-800 nm for the far-red channel, minimizing channel crosstalk and enabling simultaneous dual-channel imaging. Images of cells in the stressed state were captured as z-stacks with a step size of 0.5 µm with a 10 µm total thickness. To obtain relaxed-state images, cells were removed by applying a droplet of 5% sodium dodecyl sulfate (SDS). After a 15-minute incubation period, allowing the hydrogel to relax and return to its stress-free state, confocal z-stacks of the beads were captured using identical imaging settings as described for the stressed-state images.

Traction force microscopy analysis was conducted using a computational pipeline implemented in MATLAB, as previously described [313]. Images of beads and cells were smoothed using Gaussian filtering to minimise noise interference. Cell masks were generated by applying a threshold to the cell fluorescence channel. To correct any spatial misalignment between stressed and relaxed image stacks, rigid image registration was performed using the findshift function from the DipImage library [328]. Cell-induced bead displacements were quantified via non-rigid, free-form deformation image registration utilizing the Elastix toolbox [311]. Traction forces were computed by treating the polyacrylamide hydrogel as a homogeneous, isotropic, linearly elastic half-space, employing a modified Tikhonov-regularized Fourier transform traction cytometry algorithm [313]. Considering consistent noise levels in displacement data across the dataset, the Tikhonov regularization parameter lambda was fixed at a value of 10. Finally, quan-

titative metrics for mean traction forces and contractility were limited to regions defined by the cell masks.

4.6.7. IMMUNOFLUORESCENCE IMAGING

Cells were fixed in 4% formaldehyde (Thermo Fisher) in PBS for 15 minutes at room temperature, followed by three PBS washes. Permeabilisation was carried out using 0.5% Triton X-100 (Sigma Aldrich) in PBS for 3 minutes. Samples were blocked in 3% BSA in PBS overnight at 4°C. For cytoskeletal imaging, cells were then incubated with chicken anti-vimentin primary antibody (ab24525, Abcam, 1:200 dilution) in 1.5% BSA/PBST (PBS containing Tween-20 detergent at 0.05% v/v) at 4°C overnight. The following day, cells were washed three times with PBST and incubated for 6 hours at room temperature in PBST containing goat anti-chicken Alexa Fluor 647 secondary antibody (ab150171, Abcam, 1:1000), Phalloidin 568 (10135092, Thermo Fisher Scientific, 1:1000) and Hoechst 33342 (Thermo Fisher, 1:1000) for nuclear staining. After a final set of washes in PBST, samples were imaged using a Leica Stellaris 8 confocal microscope equipped with a supercontinuum white light laser, 405 nm laser, and hybrid detectors. For cell images, we used a 40X 1.1 NA glycerol immersion objective to capture z stacks with 0.33 µm spacing, with a total height defined to circumscribe an entire single cell. Excitation wavelengths of 488 nm (ACTIF), 587 nm (actin) and 633 nm (vimentin) were employed. Hybrid detectors were configured to detect fluorescence emission within 495-555 nm for the ACTIF channel, 590-620 for the actin channel and 640-800 nm for the vimentin channel. For nucleus images, z-stacks with 0.33µm spacing were acquired using the 405 nm laser lines with a 63x glycerol (HC PL APO, WD 0.3 mm, NA 1.2) immersion objective.

For vinculin focal adhesion imaging, cells were first incubated with rabbit anti-vinculin primary antibody (ab91459, Abcam, 1:1000 dilution) in 1.5% BSA/PBST at 4°C overnight. The following day, cells were washed three times with PBST and incubated for 6 hours at room temperature in PBST containing goat anti-rabbit Alexa Fluor 647 secondary antibody (ab27040, Abcam, 1:500). Vinculin focal adhesions were also imaged with the Leica Stellaris 8 confocal microscope using a 40X 1.1 NA glycerol immersion objective, with an excitation wavelength of 633 and the hybrid detector configured to detect fluorescence emission within 640-800 nm.

4.6.8. ANALYSIS OF VIMENTIN DISTRIBUTION

Multi-channel TIF images were batch-processed using custom Python scripts to quantify the spatial distribution of vimentin intensity relative to the nucleus. For each TIF file containing confocal z-stacks of the nucleus and vimentin, maximum intensity projections were computed along the z-axis for both the nucleus and vimentin channels. The nucleus channel was thresholded using Otsu's method, and the largest connected region was selected to generate a binary nucleus mask. The centroid of the nucleus was then determined from this mask, and polar coordinates (i.e., angles in degrees) were calculated relative to the centroid. The vimentin intensity was then analyzed in multiple 1-µm radial bands (e.g., 1–2 µm, 2–3 µm, etc. from the nucleus). For each band, a 53-sample angular intensity profile was generated by weighting pixel intensities with a Gaussian kernel (standard deviation = 7°). The circular variance, S, was calculated as

$S = 1 - R$, where the resultant vector lengths were based on the 53 angular samples [286].

4.6.9. SINGLE CELL MIGRATION TRACKING

Two days before experiments, cells were seeded onto fibronectin-coated 35 mm glass-bottom dishes (FD35-100, WPI) at a density of 10,000 cells per dish and allowed to adhere overnight. The next day, plectin knockout cells were transfected with the ACTIF plasmid according to the protocol described above. After overnight incubation, cells were labelled with cell tracker orange and Hoechst. Live-cell imaging was performed using a Leica Thunder widefield microscope equipped with a stage-top incubator (Tokai) maintained at 37°C in CO_2-independent medium (18045088, Thermo Fisher) supplemented with 5% penicillin-streptomycin. Time-lapse image series were acquired using a 20x air objective at a frame rate of 6 frames per minute for a duration of 1 hour.

To quantify migration, we tracked the centroid positions of individual cells over time based on the Cytotracker images using the Python package TrackPy [324], an implementation of the Crocker–Weeks algorithm [325]. The centroid of each cell was determined by calculating the intensity-weighted center of mass within the mask. Tracks were filtered based on duration to exclude short or incomplete trajectories (less than 5 consecutive frames). From the resulting cell tracks, we computed the time-averaged mean-squared displacement (MSD) and averaged instantaneous speed.

To calculate the migration persistence, we computed the direction autocorrelation from the displacement vectors of individual cell tracks. For each trajectory, frame-to-frame displacement vectors were calculated from the centroid positions and normalized to unit length to remove the influence of speed. Directional autocorrelation was then defined as the average cosine of the angle between successive displacement vectors, such that values near 1 indicate highly persistent, aligned movement, and values closer to 0 indicate more frequent turning or random motion. Autocorrelation values were computed for each trajectory and averaged per condition to compare overall migration persistence. Additionally, we calculated the end-to-end displacement for each cell over a period of 500 s, as we chose this time window to ensure that all cells remained within the imaging frame, thereby avoiding biased or incomplete statistics due to partial tracks.

4.7. SUPPLEMENTARY INFORMATION

4.7.1. SUPPLEMENTARY METHODS

ANALYSIS OF SINGLE-CELL COMPRESSION DATA

All data analysis was performed using custom-written Python code available upon request. The load measured by the Nanoindenter was converted to compressive engineering stress based on the initial contact area between the cell and the cantilever. The contact area was determined from automated analysis of epifluorescence images of the cytosol by thresholding the images using Otsu's method in the Python library scikit-image [209] and multiplying the number of pixels by the pixel size in the thresholded image. The uniaxial strain was calculated by approximating cells as a sphere and dividing the amount of compression by the cell diameter. We note that the measurements and all analyses were previously benchmarked using cell-sized polyacrylamide microgel particles of known stiffness [253]. Curve fitting was done using the curve fit function from Python's SciPy library.

4.7.2. SUPPLEMENTARY FIGURES

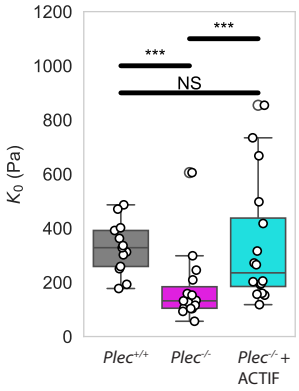

Figure 4.7: Small amplitude stiffness, K_0, of $Plec^{+/+}$, $Plec^{-/-}$, and ACTIF-expressing $Plec^{-/-}$ calculated from single cell compression curves, shown in the main text. We take the differential of the stress-strain curve, K, and take K_0 as the linear region of K plotted against stress. We found no significant difference in K_0 between $Plec^{+/+}$ (N=16), $Plec^{-/-}$ (N=16) and ACTIF-expressing $Plec^{-/-}$ cells (N=16). NS indicates P>0.05, *** indicates P<0.001.

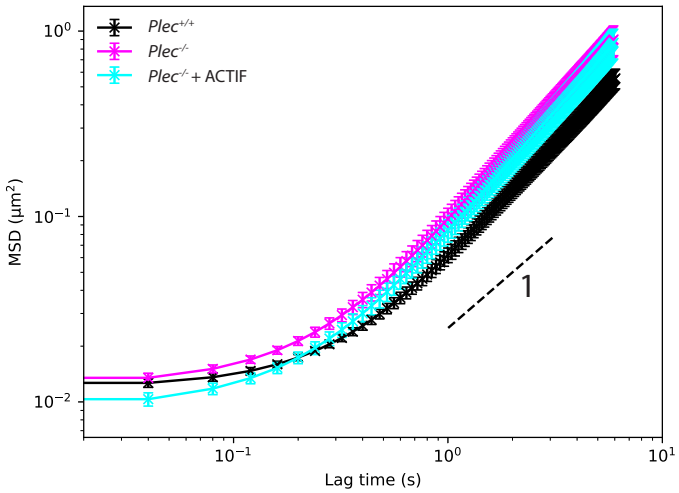

Figure 4.8: Ensemble averaged mean squared displacements (MSDs) for the motion of lysosomes in wild type fibroblasts ($Plec^{+/+}$), plectin knockout cells ($Plec^{-/-}$) and ACTIF-expressing $Plec^{-/-}$ cells ($Plec^{-/-}$ + ACTIF) seeded on fibronectin-coated glass. The motion is subdiffusive (due to particle caging) at short timescales and superdiffusive (due to active transport) at longer timescales. A power-law exponent of 1 (dotted line in the figure) indicates normal diffusive behaviour.

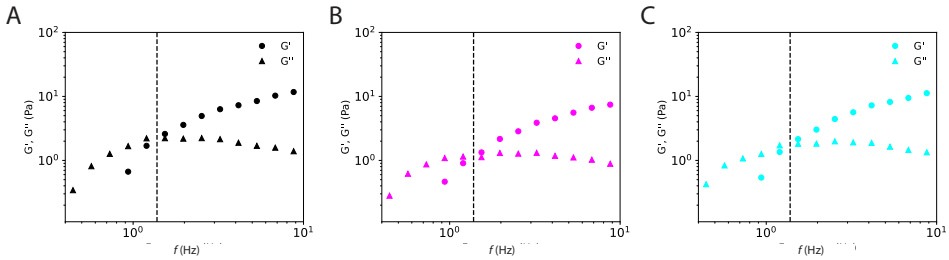

Figure 4.9: The storage (G') and loss (G'') shear moduli for (A) $Plec^{+/+}$, (B) $Plec^{-/-}$ and (C) $Plec^{-/-}$ ACTIF cells measured by particle tracking microrheology (based on fluorescence imaging of lysosomes). Vertical dashed lines indicate the crossover frequency where G' and G'' are equal. The crossover frequencies are 1.37 Hz for $Plec^{+/+}$ cells (N=11), 1.38 Hz for $Plec^{-/-}$ cells (N=11) and 1.38 Hz for ACTIF-expressing $Plec^{-/-}$ cells. Experiments were repeated on two separate days.

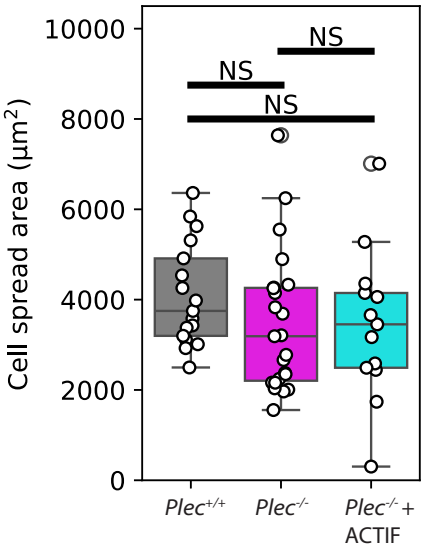

Figure 4.10: Spread area of *Plec*$^{+/+}$, *Plec*$^{-/-}$, and ACTIF-expressing *Plec*$^{-/-}$ cells seeded on fibronectin-coated glass. We found no significant difference in cell area between *Plec*$^{+/+}$ (N=17), *Plec*$^{-/-}$ (N=23) and ACTIF-expressing *Plec*$^{-/-}$ cells (N=13). NS indicates P>0.05. This experiment supports the idea that the increase in focal adhesion size seen by confocal imaging of vinculin (see main text) does not arise from changes in cell sizes.

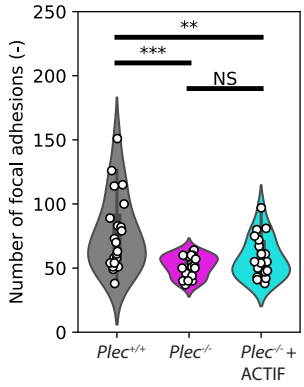

Figure 4.11: Number of focal adhesions per cell, quantified by immunofluorescence imaging of vinculin. $Plec^{+/+}$ (N=17) cells had a significantly larger number of focal adhesions per cell compared to $Plec^{-/-}$ (N=23) and ACTIF-expressing $Plec^{-/-}$ cells (N=11).

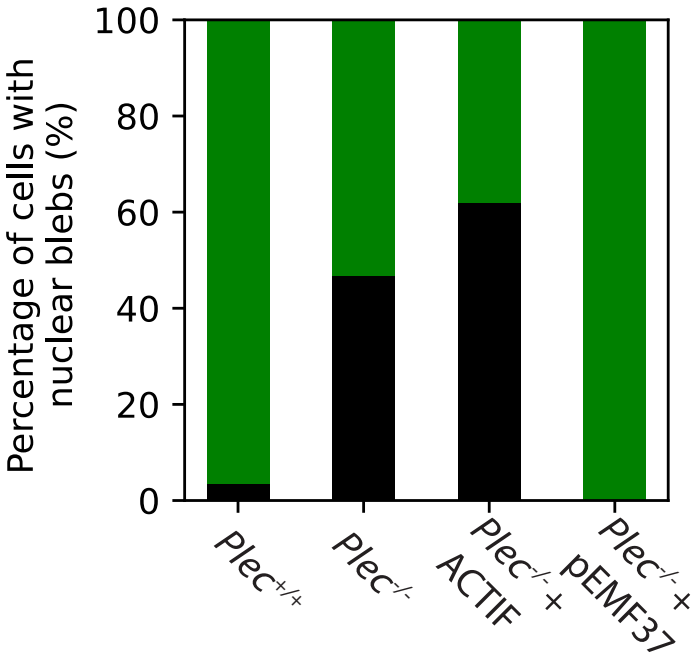

Figure 4.12: Percentage of cells which show nuclear blebbing, a sign that the nucleus is mechanically stressed because blebs form when a gap occurs in the nuclear lamina that becomes a site of membrane blebbing. We observe only a low frequency of nuclear blebbing in $Plec^{+/+}$ cells (3%, N=29) whereas $Plec^{-/-}$ cells show frequent blebbing (47%, N=32). We observe an even higher frequency of blebbing in ACTIF-expressing $Plec^{-/-}$ cells (62%, N=30). However, upon expressing pEMF37 in $Plec^{-/-}$, a truncated version of plectin 1c, we no longer observe any nuclear blebbing (0%, N = 16).

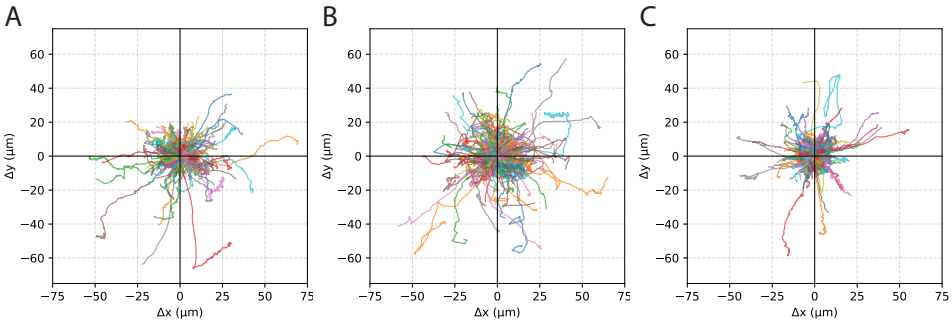

Figure 4.13: Windrose plots showing the trajectories of (A) $Plec^{+/+}$ cells (N=429), (B) $Plec^{-/-}$ cells (N=451) and (c) ACTIF-expressing $Plec^{-/-}$ fibroblasts (N=994) obtained in single-cell migration experiments over a time period of 1 hour.

4.7.3. SUPPLEMENTARY TABLES

f (Hz)	WT G' (Pa)	KO G' (Pa)	ACTIF G' (Pa)	WT G'/KO G' (–)	WT G'/ACTIF G' (–)
8.751959	11.712036	7.440386	11.239109	1.574117	1.042079
6.826695	10.279348	6.648499	9.454885	1.546116	1.087209
5.324953	8.469923	5.574895	8.195892	1.519297	1.033345
4.153565	7.257224	4.547740	7.237214	1.599744	1.002551
3.239861	6.311251	3.877685	5.647073	1.627844	1.117615
2.562514	5.694485	3.287985	4.318332	1.732493	1.318917
1.972238	5.388225	2.164678	3.092070	2.497562	1.744794
1.537596	2.593202	1.334268	2.152656	1.943939	1.204652
1.399345	1.960930	0.904612	1.352457	2.168190	1.250600
0.935119	0.666699	0.465250	0.539229	1.432991	1.236494
0.729723	0.030934	0.055103	0.067584	0.561376	0.457707

Table 4.1: Overview of the cytoplasmic storage (G') modulus of $Plec^{+/+}$ (N=11), $Plec^{-/-}$ (N=11) and ACTIF-expressing $Plec^{-/-}$ (N=11) cells obtained from two-particle microrheology of lysosomes.

f (Hz)	WT G'' (Pa)	KO G'' (Pa)	ACTIF G'' (Pa)	WT G''/KO G'' (–)	WT G''/ACTIF G'' (–)
8.751959	1.391434	0.886532	1.239399	1.569526	1.084361
6.826695	1.582105	1.082604	1.435958	1.462219	1.102726
5.324953	1.689349	1.129734	1.637427	1.517870	1.031518
4.153655	1.888109	1.314353	1.918100	1.436337	0.984366
2.939861	2.148662	1.374138	1.851810	1.564397	1.160226
2.527153	2.298822	1.266893	1.745657	1.814020	1.317118
1.987564	2.294929	1.364278	1.604628	1.681756	1.430161
1.537596	2.243547	1.124732	1.811645	1.994776	1.238705
1.199354	2.213389	1.148990	1.719464	1.926435	1.287298
0.993451	1.677088	1.088456	1.263465	1.540882	1.326148
0.729723	1.266295	0.867451	1.074728	1.459789	1.178248

Table 4.2: Overview of the cytoplasmic loss modulus (G'') of $Plec^{+/+}$ (N=11), $Plec^{-/-}$ (N=11) and ACTIF-expressing $Plec^{-/-}$ (N=11) cells obtained from two-particle microrheology of lysosomes.

5

ACTIN AND VIMENTIN EXHIBIT COMPLEMENTARY MECHANICAL RESPONSES IN SINGLE CELLS UNDER SHEAR

The mechanical properties of mammalian cells are governed by the cytoskeleton, a dynamic biopolymer network consisting of actin filaments, intermediate filaments, and microtubules. There is long-standing interest in measuring the contribution of each cytoskeletal component to cell stiffness, typically under compressive loading conditions. However, cells in the body experience varying mechanical conditions that often include shear deformation. It is unclear to what extent the mechanical response of cells and the contributions of the different cytoskeletal components may differ between shear and compressive loading. Here we employ a new custom-built single-cell shear rheometer to disentangle the contributions of actin and vimentin intermediate filaments to the overall mechanical behaviour of cells under shear. We utilise mouse embryonic fibroblasts from wild-type (WT) and vimentin-knockout (vim-/-) mice, combined with chemical treatments that inhibit actin polymerisation. Using strain ramp tests, we demonstrate that the actin network shear-softens, whereas the vimentin network shear-stiffens. Together this generates a biphasic response to shear, with shear-softening followed by stiffening at large strain. The shear-softening response contrasts with the compression-stiffening of the same cells observed previously. We reconcile this apparent contradiction by considering that shear exposes the cytoskeleton to much larger tensile strains than compression. We propose that large tensile strains cause softening by actin network disruption, leaving the vimentin cytoskeleton intact to allow the cell to recover. Our findings show that the combined properties of actin and vimentin networks as a composite material are important to

mechanically protect cells against large mechanical deformations.

5.1. INTRODUCTION

In multicellular organisms, cells are constantly subjected to physical forces whose nature varies with anatomical location. Cells in the heart, lungs and skin, for instance experience primarily compression and stretching, whereas shear forces are dominant in the brain and in blood vessels [155]. In mammalian cells, the primary structure responsible for both producing and responding to mechanical stress is the cytoskeleton [216]. The cytoskeleton is a biopolymer network consisting of three main components: actin filaments, microtubules, and intermediate filaments. Each component performs distinct biological functions that are related to its distinct structural, mechanical and dynamic characteristics [217].

Filamentous actin is predominantly found in the cortical layer beneath the plasma membrane and in stress fibers, which are bundled actin filaments extending across adherent cells [159]. Together with nonmuscle myosin 2 motor proteins, both the actin cortex and stress fibers generate contractile forces. In adherent cells, contractility causes cellular prestress, which influences cell stiffness [20]. Intermediate filaments, a diverse protein family expressed in a tissue-specific manner, include well-studied members such as keratin in non-motile epithelial cells and vimentin in motile mesenchymal cells [160]. In mesenchymal cells like fibroblasts, vimentin filaments form a structural cage around the nucleus, extending outward to the cell membrane [161, 162]. Vimentin has been described as a 'cellular safety belt' that protects the cell against substantial mechanical deformations [103]. Mechanical measurements on cells have shown that vimentin filaments form a hyperelastic, strain-stiffening network that enhances cytoplasmic strength, stretchability, and toughness by dispersing local stresses, thus preserving cell integrity under extreme deformations [193]. The slow (minutes-hours) turnover rate of intermediate filaments as compared to the fast (tens of seconds) turnover rate of actin filaments further contributes to their stabilizing role [217]. While microtubules also create an extensive intracellular network [163], their relatively low abundance and tendency to exist as individual filaments mean they contribute minimally to overall cell stiffness [37].

Investigations of cellular stiffness have significantly advanced our understanding of how the three different cytoskeletal networks contribute to cellular mechanics [158, 6, 216]. It is less well understood how the three networks modulate the time- and amplitude-dependent mechanical response of cells. Cells exhibit complex viscoelastic behaviour due to cytoskeletal (de)polymerization and the presence of a multitude of cross-linking proteins each having their own turnover dynamics. This molecular complexity causes dissipative mechanical responses evolving over different characteristic timescales [329, 187, 330, 198]. Moreover, the force-dependence of crosslinker unbinding together with the intrinsic strain-stiffening behavior of semiflexible cytoskeletal filaments make the elastic and viscous behaviours of the cell dependent on the rate,

This chapter is in preparation for publication. The paper is co-authored by **J. P. Conboy**, N. van Vliet, P. E. Boukany, F. C. MacKintosh and G. H. Koenderink.

duration and amplitude of deformation [331, 166]. Cell stiffness is typically evaluated under compressive loading conditions, such as those employed in atomic force microscopy (AFM) [332]. Under compressive loading, cells exhibit strain-stiffening behaviour [253, 176, 166]. It is often assumed that the compressive modulus can be directly converted into a shear modulus, implicitly treating cells as homogeneous elastic materials and assuming equivalent mechanical responses [333]. However, there is no inherent reason to assume that cells exhibit identical mechanical responses under shear and compression. At the tissue level, it is well-established that compressive and shear moduli are not equivalent, since tissues shear-soften but compression-stiffen [334, 335, 336]. Furthermore, recent theoretical models support the notion that shear-softening fibrous networks can exhibit compression-stiffening when they contain stiff inclusions [337], raising the intriguing question whether individual cells also display such contrasting mechanical behaviours and if these behaviours are time-dependent.

Here we investigate the specific roles of the actin and vimentin cytoskeletal networks in shaping the nonlinear and time-dependent mechanical behaviour of individual fibroblasts to large shear deformation. We developed a custom-built single-shear rheometer to perform shear rheology experiments on single fibroblasts confined between two parallel plates and identified the separate contributions of actin and vimentin by using mouse embryonic fibroblasts isolated from wild-type (WT) and vimentin-knockout (vim-/-) mice, combined with the actin-targeting drug cytochalasin D. We show that unlike in compression, where fibroblasts stiffen, the cells soften under large, but still physiological, shear deformations in a strain rate-dependent manner. We demonstrate that this softening response originates from the nonlinear response of the actin network, which is stiffer than the vimentin network at small strain, but shear-softens with increasing strain. Upon repeated shearing, the cells become as soft as cells where actin is depolymerised by cytochalasin D, leaving only the response of the shear-stiffening vimentin network. Our study reveals that cells exhibit distinct responses to compression versus shear, advancing our understanding of how the different cytoskeletal networks jointly shape cellular mechanics under different modes of deformation.

5.2. RESULTS

5.2.1. SINGLE-CELL SHEAR RHEOLOGY MEASUREMENTS

To quantify the nonlinear viscoelastic response of cells to shear deformation, we established a single cell shear rheometer assay (Figure 5.1 A). The rheometer consists of a flexible cantilever with a polymer plate glued to the bottom (Figure 5.1 B). The device is mounted on an inverted epifluorescence microscope to make it possible to find single cells and observe their morphology and cytoskeletal organization *in situ* by bright field and epifluorescence imaging. The force required to shear the cell is determined from the deflection of the cantilever measured with an optical fibre (Figure 5.1C). The force is converted to shear stress based on the cell area measured from the bright field images. To prevent cell slip during measurements while avoiding integrin-mediated signalling, we coated both plates with poly-L-lysine which enhances cell adhesion through electro-

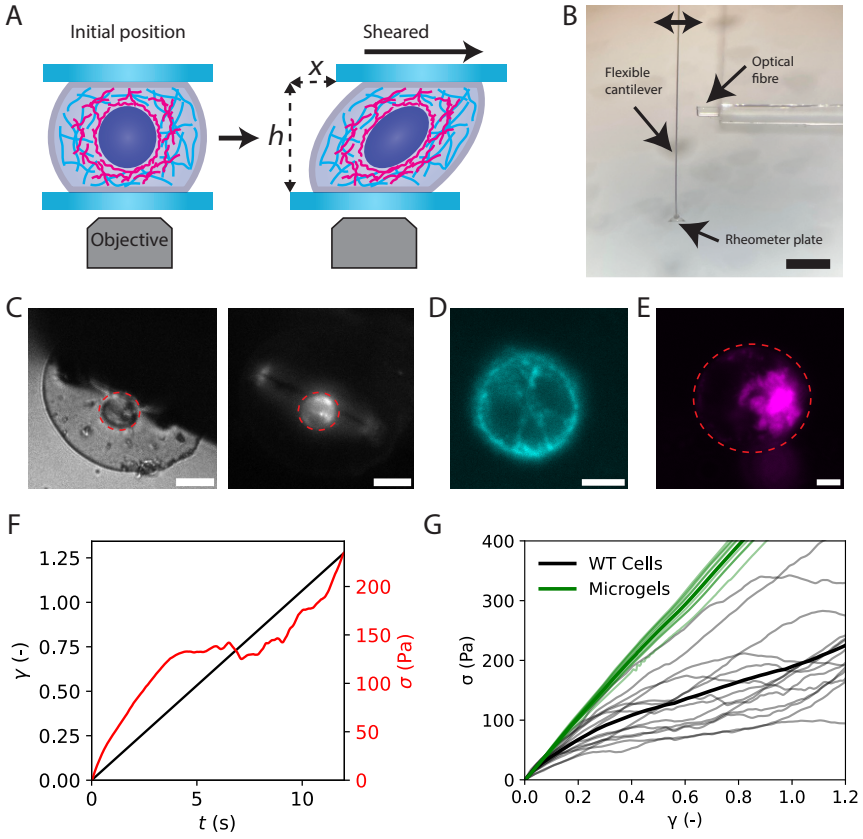

Figure 5.1: Single cell shear rheology measurements of the nonlinear viscoelastic properties of mouse embryonic fibroblasts. (A) Schematic showing a cell sandwiched between two parallel plates, allowing us to apply a simple shear deformation by moving the top plate. We focus on the mechanical contributions of the actin (cyan) and vimentin (magenta) cytoskeletons. The device is mounted on an inverted microscope. (B) Micrograph showing the top plate (~ 100 µm in diameter) glued to the bottom of a flexible cantilever. The force required to shear the cell confined underneath the plate is determined from the cantilever deflection measured with the optical fibre. Scale bar is 200 µm. (C) Left: Bright field image of a wild type fibroblast confined between the poly-L-lysine-coated rheometer plates. Right: epifluorescence image of the cytoplasm (labelled with CellTracker™) of the same cell. The dashed red circle indicates the cell outline. Scale bars are 25 µm. (D) Epifluorescence image of the actin cytoskeleton (cyan, labelled with SiR actin) of a wild type cell confined between the rheometer plates. Scale bar is 5 µm. (E) Epifluorescence image of the vimentin network (magenta, labelled with GFP-vimentin) of another wild type cell. The red dashed line indicates the outline of the cell. Scale bar is 5 µm. (F) Representative strain ramp measurement showing the applied time-dependent shear strain (black, left y-axis) and measured shear stress response (red, right y-axis). (G) Stress-strain response curves are nonlinear for wild type cells (N=18, black lines) and linear for polyacrylamide microgels (N=8, green lines). Thin lines show individual stress-strain curves and thicker lines show averages.

static interactions [338]. Bright field imaging of the cell and fluorescence imaging of its cytoplasm labeled with CellTracker™ dye shows that mouse embryonic fibroblasts confined between the plates have a circular cross-section (Figure 5.1 C). Fluorescence imaging furthermore shows that actin is largely localized near the cell membrane (Figure 5.1 D) whereas vimentin is concentrated around the nucleus (Figure 5.1 E). To measure the nonlinear viscoelastic response, we increase the shear strain at a fixed rate (1.25% s^{-1}) and measure the concomitant stress (Figure 5.1 F). We limited the shear strain to a maximal value of 1.2, to ensure that the cell remained clearly visible under the microscope while also preventing cell slip or rheometer tilting (see Supplementary Movie 1).

Before conducting experiments on cells, we first validated the setup using polyacrylamide microgels, a convenient cell-sized proxy with well-characterised rheological properties [168]. As shown in Figure 5.1G (green lines), the stress upon shearing the microgels increased linearly with the applied strain, consistent with the known linearly elastic behaviour of polyacrylamide in bulk rheology [339]. In stark contrast, the cells displayed a complex nonlinear response (Figure 5.1G black lines): they shear-softened until the strain reached ~0.7 and shear-stiffened beyond this point.

5.2.2. ACTIN SHEAR-SOFTENS WHILE VIMENTIN SHEAR-STIFFENS

To investigate the origins of this intriguing biphasic stress-strain response of cells under shear, we decided to determine the separate contributions of the actin and vimentin cytoskeleton (Figure 5.2A). To expose the contribution of vimentin, we performed shear ramp tests on cells genetically depleted of vimentin (vim-/-). Western Blot analysis confirmed the absence of vimentin while the expression level of actin was unchanged (Supplementary Figure 5.6). To expose the contribution of actin, we performed shear ramp tests on WT cells where we disrupted the actin network with cytochalasin D. The stress-strain curves revealed that WT cells (black line in Figure 5.2A) on average were significantly stiffer than cytochalasin D-treated cells (cyan) as well as vim-/- cells (magenta).

Since the stress response in all three cases was nonlinear in strain, we calculated the shear modulus as the differential (or tangent) modulus K, defined as the derivative of the stress with respect to strain. This quantity provides a more accurate quantification of nonlinear elastic responses than the ratio of stress-to-strain, as shown in previous shear rheology studies of reconstituted actin and vimentin networks [89, 96]. As shown in Figure 5.2B, wild type cells have an average shear modulus of $K_0 = 580 \pm 50$ Pa at small strains. They start to shear-soften when the shear stress reaches values between ~5 to 10 Pa (corresponding to a shear strain of ~0.02). However, once the shear stress exceeds ~ 130 Pa (corresponding to a shear strain of ~0.6), most (~ 2/3) of the wild type cells start to strain-stiffen. Vimentin knockout cells were on average about 3-fold softer at small strains than the wild type cells ($K_0 = 180 \pm 40$ Pa, Figure 5.2B and E). Strikingly, the vimentin knockout cells all strain-softened with increasing shear stress and lost the strain-stiffening response of wild type cells at high strain (Figure 5.2C). This observation suggests that actin is responsible for the strain-softening response of wild type cells, whereas vimentin is responsible for the strain-stiffening response. To test this idea, we depolymerized actin in the wild type cells, rendering the cells even softer than vim-/- cells ($K_0 = 60 \pm 10$ Pa, Figure 5.2E). Apparently actin plays a more prominent role than vimentin in determining cellular stiffness at low strain levels. However, with increas-

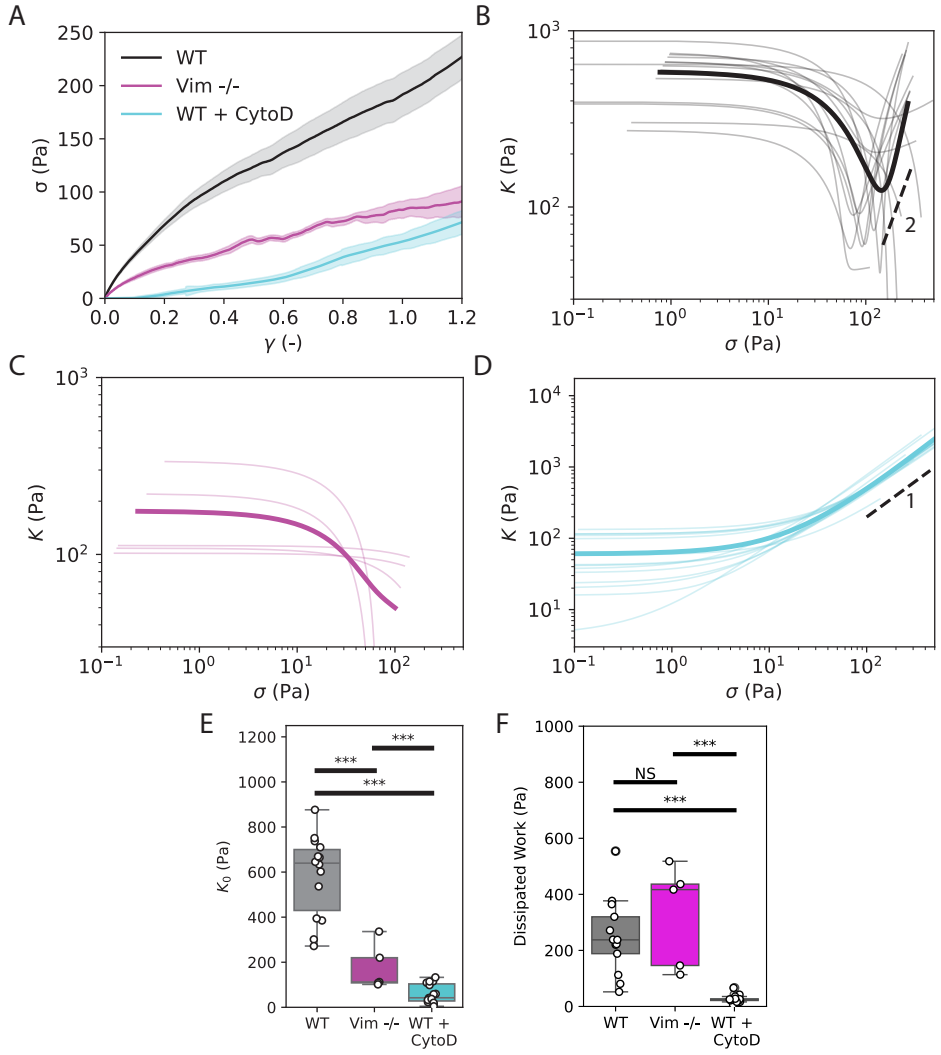

Figure 5.2: Actin and vimentin contribute opposite responses to the overall nonlinear viscoelastic response of mouse embryonic fibroblasts to shear deformation. (A) Average stress-strain curves for WT cells (black lines, N = 14), vim-/- cells (magenta, N = 5) and WT cells treated with the actin depolymerizing drug cytochalasin D (cyan, N = 15). The error bands show the SEM. (B-D) Differential modulus K calculated as the derivative of the stress-strain curves like the ones shown in (A). The shear strain dependence of K measured on individual cells (thin lines) are plotted along with the ensemble-averaged response (thicker lines). The data reveal initial softening, followed by stiffening for the majority of WT cells (B), softening-only for vim-/- cells (C), and stiffening-only for WT cells treated with cytochalasin D (D). (E) Comparison of the linear (small strain) modulus K_0 showing that vim-/- cells are significantly softer than WT cells, while cytochalasin D-treated WT cells are even softer. (F) Comparison of the dissipated work, defined as the area between the loading and unloading curves. Cytochalasin D-treated WT cells dissipate significantly less work than WT and vim-/- cells.

ing shear stress, the actin-depolymerised cells strongly shear-stiffened with no observed softening (Figure 5.2D). At the highest applied strain of 1.2, the actin-depolymerised cells were 10-100-fold stiffer than at small strain and on average reached the same stiffness as vim-/- cells. This observation strongly suggests that the vimentin cytoskeleton plays a more prominent role than actin in determining cellular stiffness at high strain levels and is responsible for strain-stiffening.

We next analysed the unloading curves, and by taking the area between the loading and unloading segments, we quantified the energy dissipated during shear deformation. We found no significant difference in energy dissipation between WT cells (250 ± 30 Pa) and vim-/- cells (330 ± 70 Pa), but the actin-depolymerised cells dissipated significantly less energy (27 ± 3 Pa). This observation indicates that energy dissipation during shear deformation is primarily governed by the actin cytoskeleton.

5.2.3. REPEATED SHEARING SOFTENS CELLS

To investigate the mechanism of shear-softening observed for wild type cells, we subjected them to cyclic loading and unloading tests. We increased the shear strain at a constant rate of 1.25% s^{-1} until a maximum strain of 1.2, moved back to zero strain at the same rate, and then repeated this cycle another 19 times without intervening waiting steps (Figure 5.3A). Upon repeated shear cycles, the cells gradually soften (Figure 5.3B). We note that plasticity begins to manifest at strains in the range of 25-30% (Supplementary Figure 5.9). After a total of 20 loading and unloading cycles, the cells have become 10-fold softer compared to 'virgin' cells, although they still display shear-stiffening behaviour at high strain. By cycle 5, the cells no longer show any initial shear-softening phase. Strikingly, the mechanical response after 20 cycles of loading was identical to that of 'virgin' wild type cells treated with cytochalasin D after actin depolymerization (Fig 5.3C). Specifically, the "worked cells" and cytochalasin-D-treated cells had an identical (low) modulus at small strain and did not shear-soften but only shear-stiffened. This resemblance suggests that repeated shear cycles gradually damage the actin network enough that it no longer measurably contributes to the shear modulus. To assess whether this plastic deformation of the actin cytoskeleton was permanent, we waited 10 minutes after the 20th cycle before applying an additional strain ramp (Fig 5.3D). We observed a recovery of the linear modulus back to the modulus of virgin cells and a partial recovery of the nonlinear response, with the cell once again exhibiting strain-softening.

To test whether the vimentin cytoskeleton also sustains damage under large shears, we repeated the cyclic loading and unloading tests on wild type cells drugged with cytochalasin D, allowing us to observe the resilience of the vimentin network in absence of actin. Strikingly, the loading curves obtained for the actin-depolymerised cells remained entirely unchanged over the 20 cycles of repeated loading (Fig 5.3E). These findings indicate that, while the actin cytoskeleton undergoes progressive and partially reversible softening under cyclic shear, the vimentin network remains largely unaffected.

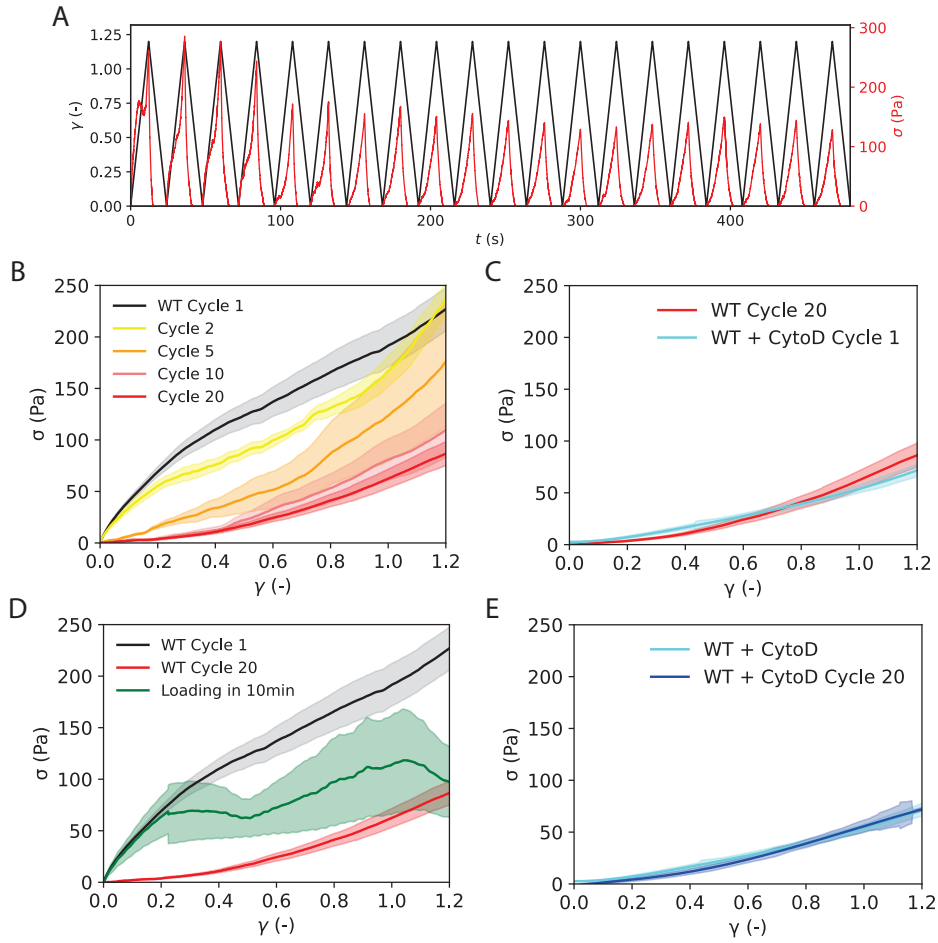

Figure 5.3: Repeated shearing softens wild type mouse embryonic fibroblasts, but also disrupts their shear-softening response. (A) We apply 20 shear cycles where we alternately increase the shear strain to 1.2 and return to zero at a constant strain rate (1.25% s^{-1}) without waiting steps. We measure the concomitant stress (shown in red in the figure), and observe softening behaviour. (B) Average stress-strain curves for wild type (WT) cells during the loading phase shown for cycles 1, 2, 5, 10 and 20. The error bands show the SEM. The cells gradually soften in each cycle and have lost their shear-softening response by cycle 5, while retaining the shear-stiffening response at large shears. (C) WT cells subjected to 20 cycles of repeated deformation have become as soft as WT cells treated with cytochalasin D and exhibit an identical shear-stiffening response. (D) After a waiting time of 10 minutes (green), the stress-strain response of WT cells with a history of 20 shear cycles (red) partially recovered the response of virgin WT cells (black). (D) Average stress-strain curves for WT cells treated with cytochalasin D to depolymerize actin during the loading phase shown for cycles 1 and 20. The curves from the 1st and 20th loading cycle show identical strain-stiffening behaviour across the entire strain range.

5.2.4. RATE DEPENDENCE OF THE NONLINEAR SHEAR RESPONSE OF SINGLE CELLS

We have seen that wild type cells exhibit shear-softening as well as inelastic behaviour, whereas both of these behaviours are lost upon actin depolymerization with cytochalasin D. These findings strongly suggest that shear deformations disrupt the actin cytoskeleton. To test this idea, we performed shear ramp tests at five different shear loading rates, ranging from 0.025 s^{-1} to 0.5 s^{-1}. These loading rates were selected to approximate timescales similar to the typical actin turnover rate, which we previously found by fluorescence photobleaching recovery experiments to be approximately 0.25 s^{-1} in fibroblasts [198]. As shown in Figure 5.4A, the stress-strain response indeed strongly depended on shear rate. Across all loading rates, the cells displayed an initial shear-softening regime followed by a shear-stiffening regime. This pattern was consistently seen in the majority of individual cells (Supplementary Figure 5.7). However, cells sheared at higher rates appeared stiffer, as indicated by an upward shift in their stress-strain curves compared to those deformed more slowly. Furthermore, the stress-strain responses appeared to group into two distinct sets, with the lower rates (0.025, 0.0625, 0.125 s^{-1}) forming a softer group, and the higher rates (0.375, 0.5 s^{-1}) forming a stiffer group.

A lower stiffness at a slower rate of deformation is indeed expected since slower deformation rates allow for more cytoskeletal remodelling. To quantify the rate dependence further, we first calculated the peak stress reached at the maximum applied strain of 1.2 (Figure 5.4B). The peak stress values indeed fell into two distinct groups, as confirmed by statistical analysis (see Supplementary Table 3). We additionally calculated the work done during the strain ramp by integrating the area under the stress-strain curves for individual cells, providing a measure of the total mechanical energy absorbed by the cell during deformation. Again, we observed that cells clustered into the same two groups identified by the peak stress analysis (Figure 5.4C and statistical analysis in Supplementary Table 4). We performed the same analysis for the dissipated work by calculating the area between the loading and unloading curves, which provides a measure of the energy lost due to inelastic deformation, and again observed that cells clustered into the same two groups (Figure 5.4D and statistical analysis in Supplementary Table 5). Thus, both the peak stress, extensional work and dissipated work distinguish two discrete shear-rate-dependent groups of cellular behaviour.

5.3. DISCUSSION

In this study, we aimed to characterise the nonlinear and time-dependent mechanical properties of single mouse embryonic fibroblasts in response to shear deformation, focusing on the roles played by the actin and vimentin cytoskeletal networks. To achieve this, we developed a single cell shear rheometer and subjected fibroblasts to strain ramps with careful control over strain amplitude and rate. We found that fibroblasts exhibit a complex biphasic dependence of shear stress on strain, with an initial softening regime followed by shear-stiffening (Figure 5.5A). Genetic depletion of vimentin resulted in a

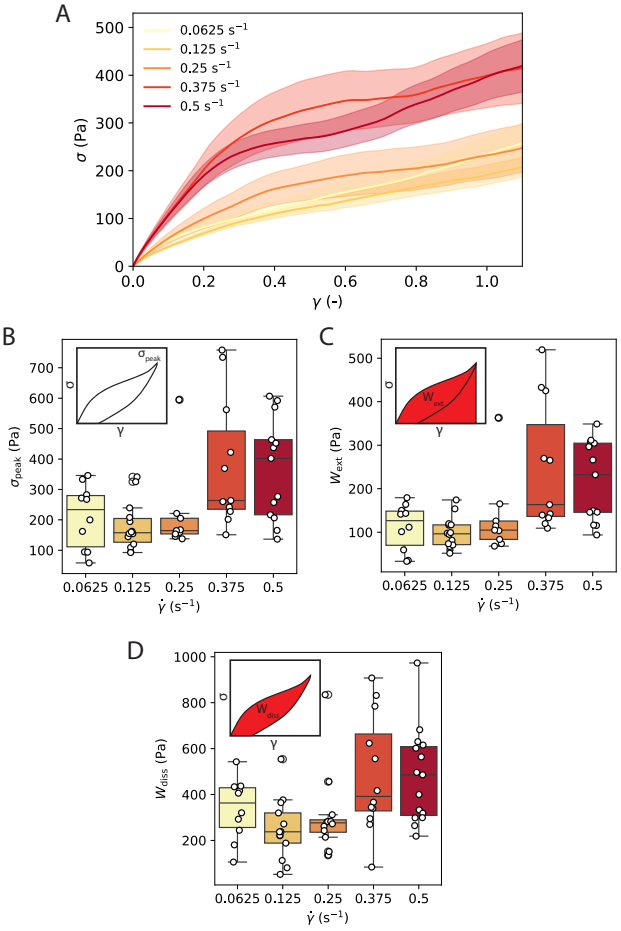

Figure 5.4: The nonlinear viscoelastic response of single mouse embryonic fibroblasts is dependent on shear rate. (A) Average stress-strain curves for wild type cells at five different strain rates: $0.025s^{-1}$ (N=10), $0.125s^{-1}$ (N=14), $0.25s^{-1}$ (N=9), $0.375s^{-1}$ (N=11) and $0.5s^{-1}$ (N=13). Error bars represent the SEM. Individual cell curves are shown in Supplementary Figure 5.9. (B) The peak stress, defined as the stress reached at the maximum strain (of 1.2) is rate-dependent: cells sheared at the two higher strain rates appear stiffer than those measured at the three lower strain rates ($p = 3.2 \times 10^{-5}$). (C) The extensional work, calculated as the area under the stress-strain curves of the individual cells, is also significantly higher at the two higher strain rates as compared to the three lower rates ($p = 6.8 \times 10^{-6}$). (D) The dissipated work (the area between the loading and unloading curves) shows the same behaviour as in (B) and (C).

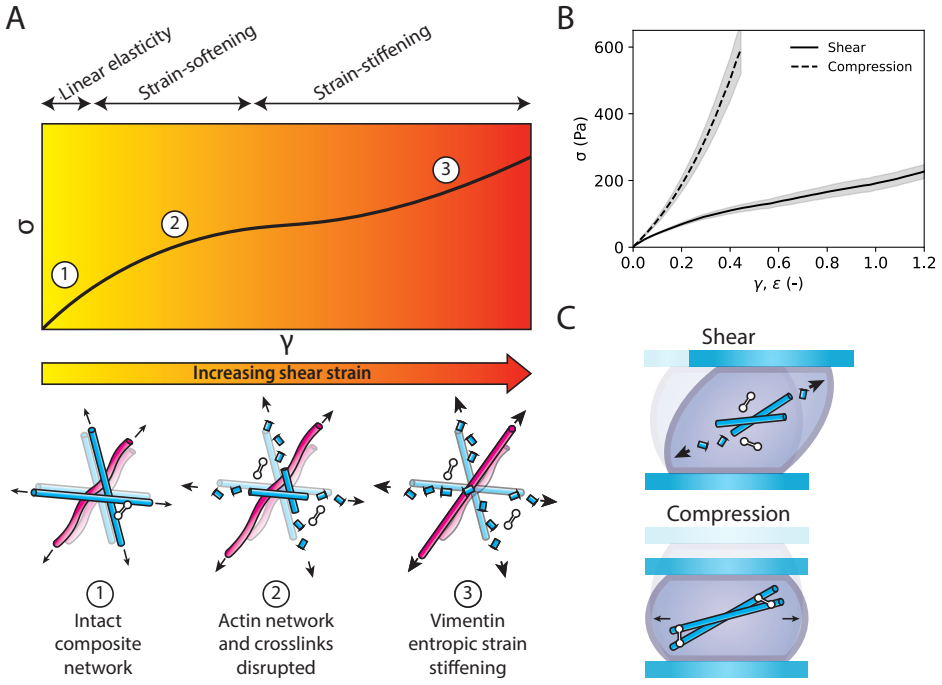

Figure 5.5: Conceptual model explaining why cells shear-soften but compression-stiffen and how these behaviours are related to the actin and vimentin cytoskeleton. (A) When a cell undergoes shear deformation, the change in cell geometry results in cytoskeletal stretching. Initially, the cytoskeleton comprises an interconnected network of actin and vimentin filaments. Shear causes disruption of the actin network, leaving only the structurally more robust and strain-stiffening vimentin network to withstand mechanical stress. (B) Direct comparison of stress-strain curves from wild type fibroblasts under shear (solid black lines, N=14) and compression (dashed black lines, N=18). The cells stiffen upon applying compressive strain, ϵ (data taken from Conboy et al. [253]), but exhibit a biphasic behaviour upon applying a shear strain, γ, with softening followed by stiffening. (C) We reconcile this contrasting behaviour by considering the different geometries of deformation. Compression causes tensile strain on the cytoskeleton mostly by causing cell bulging at the cell equator, since cells are incompressible. The associated increase in equatorial circumference is very small (see Supplementary Figure 5.8). Therefore, at the same bulk strain level, tensile strain on the filaments is much higher under shear than under compression. Note that, in addition, the cells tolerate much larger shear strains (at least 120%) than compressive strains (at most 50%).

notable decrease in cell stiffness as well as the removal of the shear-stiffening regime. Pharmacological disruption of actin polymerization also resulted in a decrease in cell stiffness, but removed the shear-softening regime observed in wild type cells. These contrasting effects of actin versus vimentin removal reveal that actin and vimentin exhibit opposite responses to an applied shear load, with actin shear-softening but vimentin shear-stiffening. At small strain, actin contributes more strongly to the shear modulus than vimentin. This could be due to its greater abundance (with mass spectrometry showing levels of 2563.6 for actin versus 1439.8 for vimentin, in normalised mass spectrometry intensity units [340]). With increasing shear strain, however, the actin cytoskeleton appears to be progressively disrupted, whereas the vimentin cytoskeleton remains intact and shear-stiffens. Rheological measurements on reconstituted cytoskeletal networks have indeed shown vimentin to be much more mechanically resilient than actin. Vimentin networks can tolerate shear strains of 200-300% [271, 341, 167], whereas transiently crosslinked actin networks tend to rupture at shear strains that are an order of magnitude lower [162]. Our findings also align well with recent whole-cell stretching and localised micromechanical measurements for wild type and vim-/- mouse embryonic fibroblasts [193]. This work showed that the vimentin network protects cells from large tensile deformations by forming a stretchable, hyperelastic network, while the actin cytoskeleton yields or disassembles under moderate strains. This work furthermore showed that the vimentin network is rate-insensitive while the actin network (and potentially microtubules) provides energy dissipation. This finding is consistent with our observation that energy dissipation during shear deformation is significantly larger when actin is present. Our rate-dependent shear experiments revealed an intriguing non-monotonic dependence of peak stress and energy dissipation on rate. It will be interesting to investigate the underlying molecular basis for this in future. Recent studies showed that actin-binding crosslinkers can exhibit different force-sensitive unbinding kinetics ranging from slip bond to catch bond behaviour[228, 342]. Experiments on cells with targeted genetic depletions of specific crosslinkers combined with computational modelling could test whether this behaviour can account for the nonlinear shear response of fibroblasts.

Previously, cell stiffness has typically been evaluated under compressive loading conditions (reviewed in Refs. [343, 216]). Under compressive loading, cells exhibit strain-stiffening behaviour [253, 176, 166], in contrast to the shear-softening we observe under shear (Figure 5.5B). The most likely explanation for this apparent discrepancy lies in the differing degree of stretching of individual cytoskeletal filaments that occurs in shear and compressive deformations (Figure 5.5C). When a nonadherent quasi-spherical cell is sheared between two parallel plates, we expect that filaments oriented along the principal direction of strain experience an extensional strain that is of the same order as the shear strain [344, 345]. Under compression, since the cell is volume-preserving, cytoskeletal filaments still experience shear and extension, perpendicular to the axis of compressive strain. The actual degree of strain caused by the expansion of the cell equator, however, is expected to be much smaller than the applied compressive strain for an initially spherical cell. Assuming a volume-conserving elastic shell model to account for the peripheral actin cortex observed in cells confined between two plates, we compute that the circumferential expansion is tiny. Specifically, a symmetric axial (polar)

compression of 15% results in only a 2% increase in the equatorial circumference, calculated for minimum elastic energy based on axisymmetric spherical harmonic expansion of a volume-preserving linear elastic shell with 2D Poisson ratio of 1/4 and shell thickness equal to 10% of the cell radius (see Supplementary Figure 5.8). In our experiments, the degree of extensional strain appears critical in controlling actin network disruption. Single-molecule experiments have shown that actin filaments rupture at tensile strains of order 10% [346, 347] while actin-binding crosslinkers tends to unbind at forces of order 4 pN [228]. Thus, cell shearing causes forces and deformations that should be large enough to cause rupture events, either within the actin filaments themselves or at filament junctions.

5.4. CONCLUSION

In this study, we showed that actin and vimentin cytoskeletal networks have complementary roles in shaping the mechanical behaviour of mouse embryonic fibroblasts to shear deformation. By employing a novel single-cell shear rheometer, we measured the elastic and time-dependent properties of suspended cells, uncovering complex mechanical responses. Both cytoskeletal components contribute to overall cellular stiffness. However, the actin cytoskeleton dominates the mechanical response at small shear strains and shear-softens at large strain, whereas the vimentin cytoskeleton shear-stiffens and dominates the response at large strains. These findings underscore the cooperative mechanical functions of the actin and vimentin networks in fibroblast mechanics, with the actin network being capable of remodelling while the vimentin network provides mechanical resilience.

5.5. ACKNOWLEDGEMENTS

We thank J. Eriksson (University of Turku) for kindly providing the cells utilized in this research and R. Rodriguez and T. Schmidt (Leiden University) for kindly supplying the hydrogel beads. Additionally, we acknowledge M. Mavrakis (Institut Fresnel) for providing the vimentin-GFP plasmid for our live-cell imaging experiments. G.H.K. gratefully acknowledges funding from the NWO Talent Programme, which is financed by the Dutch Research Council (project number VI.C.182.004). P.E.B. gratefully acknowledges funding from the European Research Council (ERC) under the European Union's Horizon 2020 research and innovation program (grant agreement no. 819424). F.C.M. was supported in part by the National Science Foundation Division of Materials Research (Grant No. DMR-2224030) and the Center for Theoretical Biological Physics (Grant No. PHY-2019745).

5.6. MATERIALS AND METHODS

5.6.1. CELL CULTURE

Wild-type (WT) and vimentin-deficient (vim-/-) mouse embryonic fibroblasts were kindly provided by prof. Eriksson (Åbo Akademi University, Turku). These cells were originally isolated from WT and vim-/- mouse embryos as described previously [206]. The cells were cultured in Dulbecco's modified Eagle medium containing GlutaMAX (DMEM, Gibco 10565018), supplemented with 10% fetal bovine serum (FBS, Gibco 10270106) and 5% penicillin-streptomycin solution (Pen-Strep, Gibco 15070063). Cells were maintained in a humidified environment at 37°C with 5% CO_2, and passaged when ~80% confluency was reached, typically twice weekly. Regular testing for mycoplasma contamination was conducted every four months.

5.6.2. SINGLE-CELL RHEOMETER PLATE MANUFACTURE

For plate fabrication, a small amount of NOA81 adhesive was carefully applied, using the back of a needle, onto the Surfasil-coated coverslip using a needle tip under a stereomicroscope. This approach allows us to precisely control the amount of polymer dispensed, enabling the fabrication of plates with diameters between 100 and 200µm. Next, a flexible cantilever, oriented perpendicular to the horizontal glass surface (see Supplementary Figure 5.10) was carefully positioned above the drop of curing polymer, and gently lowered into the liquid. Subsequently, we applied UV light to cure the drop for two hours under a UV (395 nm) LED (11504255 Leica) at about 5 cm distance. After curing, the modified cantilever was cautiously detached by lightly tapping the microscope stage to encourage separation, followed by incremental upward movement in 2 µm steps controlled by the motorised stage of the Chiaro nanoidenter system (Optics11 Life). By polymerising the drop *in situ*, we ensure that the plate is parallel with the glass coverslip for single cell measurements. Finally, cantilevers were cleaned using 2-Propanol, rinsed thoroughly with MilliQ water, and gently dried using Kimtech tissues.

5.6.3. SINGLE CELL SHEAR RHEOLOGY

One day before mechanical testing, cells were detached with 0.25% Trypsin-EDTA (Thermo Fisher Scientific, 25200056) and counted using a Countess cell counter (Thermo Fisher Scientific). Approximately 10,000 cells per well were seeded into 6-well plastic culture plates (Sarstedt 83.3920.005) in culture medium and left to adhere overnight. On the day of mechanical testing, cells were stained by replacing the medium with medium containing CellTracker™ Orange (10082742 Thermo Fisher Scientific, 1:1,000 dilution) for 30 minutes. Next, the cells were once again detached using Trypsin-EDTA and resuspended in CO_2-independent medium (Gibco 18045088) containing 10% FBS. For actin depolymerization experiments, Cytochalasin D (Sigma C8273) was added to the CO_2-independent medium at a concentration of 1 µµM, selected based on established protocols [188]. Cells were incubated in the supplemented media for at least 15 minutes prior to conducting the experiments.

The single cell shear rheometer was based on an optical fiber-based nanoindenter system (Optics11 Life) mounted on a Leica Thunder Imager widefield microscope, which was equipped with a 200 mW solid-state LED5 illumination source (Leica) and a monochrome sCMOS camera (Leica). Concurent imaging of the cells was performed using a 10x dry objective lens (HC PL APO 0.45NA, Leica). All measurements were performed at 37°C using a microscope stage heater (Tokai Hit). Calibration of the cantilever modified with a rheometer plate as explained above was conducted at the start of each measurement session using the stiff-surface contact calibration method recommended by the manufacturer. Since the cantilever is oriented perpendicularly to the dish surface (unlike in the compression experiments we recently reported with the same setup [253]), we had to develop a special calibration dish for shear experiments by glueing a glass microscope slide inside a 6 cm plastic petri dish with Norland NOA81 optical adhesive (see Supplementary Figure 5.11).

To prevent slip between the cell and the rheometer plates, culture dishes were cleaned prior to experiments with isopropanol followed by deep UV treatment using a ProCleaner UV ozone cleaner (Bioforce Nanosciences), incubation for one hour in a 0.01% solution of poly-l-lysine (Sigma), rinsing with MilliQ water, and air-drying. These poly-l-lysine-coated dishes were used within one week after preparation. Following each experimental session, cantilevers were cleaned with 2-Propanol, rinsed with MilliQ water, and dried using Kimtech tissues to remove any organic residues.

To shear the cells, we used the displacement mode within the Piuma control software (Optics11 Life) to control the applied strain rate. Measurements of elapsed time, piezo displacement, and force were collected at a frequency of 1000 Hz throughout experiments. The cell-to-plate contact area, necessary for converting measured force values to shear stress, was determined from epifluorescence microscopy images of the cytoplasm labelled with CellTracker Orange (Fisher Scientific). To accurately find the distance between the glass coverslip and the rheometer top plate, necessary to convert applied deformation to shear strain, the top plate was incrementally lowered towards the glass surface next to a cell in 1 μm steps until a noticeable deflection detected by the interferometer to indicate contact. Next, the cantilever was moved up above the glass surface by 1 μm, and the same procedure was repeated in steps of 0.1 μm to determine the surface position with a higher precision.

Following the surface position determination, the plate was moved up by 30 μm, moved above a cell, and gradually moved down in steps of 1 μm until the gap height between the top plate and glass coverslip was 15 μm (just smaller than the average cell size). We chose to keep the gap height constant in all our experiments, as this allowed us to maintain a constant strain rate without changing the ramp speed. Following contact, the cell was allowed to equilibrate for 1 minute before initiating the strain ramp measurement. This waiting step after initial point of contact was selected deliberately to prevent slippage during the strain ramp experiment. Subsequently, the cantilever was steadily moved to shear the cell at a controlled speed, typically set at 1 μm/s unless otherwise noted. Shear continued until achieving approximately 120% strain, confirmed via concurrent imaging to verify that cell deformation was reversible (Supplementary Video 1). We limited the shear strain to a maximal value of 120% strain as beyond this deformation we could no longer observe the cell on the optical microscope and were therefore no

longer able to confirm non-slip conditions or check for tilting of the top plate. Following the strain ramp, the cantilever was retracted at the identical speed, with the force exerted upon the cantilever continuously recorded throughout the loading and unloading phases.

We verified that the live-to-dead ratio of fibroblasts remained constant over two hours—the maximum duration of experiments [253]. Furthermore, we detected no gross shape changes such as cell blebbing, indicating that cells remained intact after shear experiments. For benchmarking the setup, polyacrylamide (PAA) microgels with radii ranging from 5 μm to 50 μm [210] were immersed in MilliQ water, selecting beads with diameters approximately matching those of cells (~ 18 μm). These microgels underwent identical measurement protocols as the cells.

5.6.4. IMAGING OF CELLS CONFINED BETWEEN THE RHEOMETER PLATES

Bright field imaging of the cells confined between the rheometer plates and fluorescence imaging of their actin and vimentin cytoskeletal networks was done using a 100x oil immersion objective (HC PL APO, numerical aperture 1.2, working distance 0.3 mm). For labelling of vimentin, cells were transfected four days prior to imaging using a vimentin-GFP plasmid [213] via the Neon Transfection System (Thermo Fisher Scientific). The transfection parameters followed the manufacturer's guidelines, employing a single pulse with a voltage of 1350 V and pulse width of 30 ms. Actin labelling was performed on the day of the experiment by substituting the cell culture medium with fresh medium supplemented with SiR actin dye (Tebu Bio, SC001, dilution 1:1000) and the efflux pump inhibitor verapamil (part of the SiR actin kit, dilution 1:1000). Cells were incubated for one hour with this staining solution, after which the solution was replaced with fresh medium.

5.6.5. DATA PROCESSING

To quantify the tangent shear modulus (K), shear stress-strain data were first interpolated using cubic splines using Python's SciPy library [211]. Interpolated curves were numerically differentiated using the gradient function from Python's numpy library [212]. Images were processed using Otsu's thresholding method implemented in the Python library scikit-image [209], and the pixel count of thresholded regions defined the contact area. Stress was subsequently computed by dividing the measured force by this calculated contact area. To determine the dissipated energy, we calculated the area under the curve of each stress-strain curve using the trapezium rule with Python's numpy library.

5.6.6. STATISTICS

P-values shown to determine statistical significance were calculated using the unpaired Student's t-test. Measured values in the main text are stated as the mean ± the standard error on the mean.

5.7. SUPPLEMENTARY INFORMATION

5.7.1. SUPPLEMENTARY FIGURES

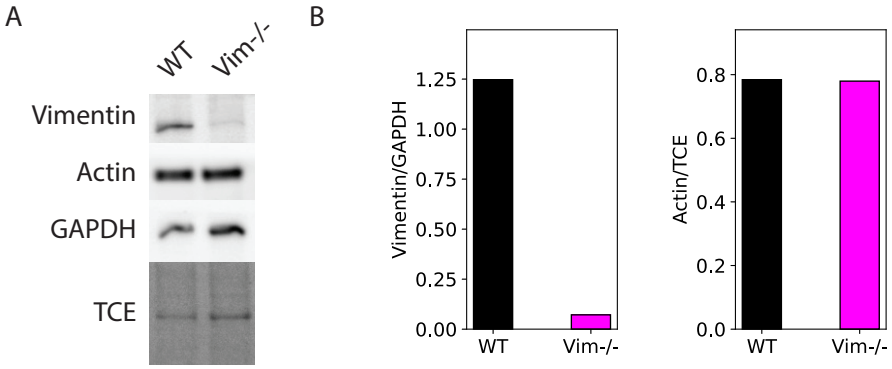

Figure 5.6: A) Cropped Western Blots analyzing the expression levels of vimentin and actin in mouse embryonic fibroblasts, comparing wild type (WT) and vimentin-deficient (vim-/-) cells. We used GAPDH as loading control for vimentin and TCE as loading control for actin. B) Quantification of the protein levels from the Western Blot shown in panel A. The blots confirm the absence of vimentin in vim-/- cells while demonstrating comparable levels of actin expression in WT and vim-/- cells. Data is shown for n=1 sample.

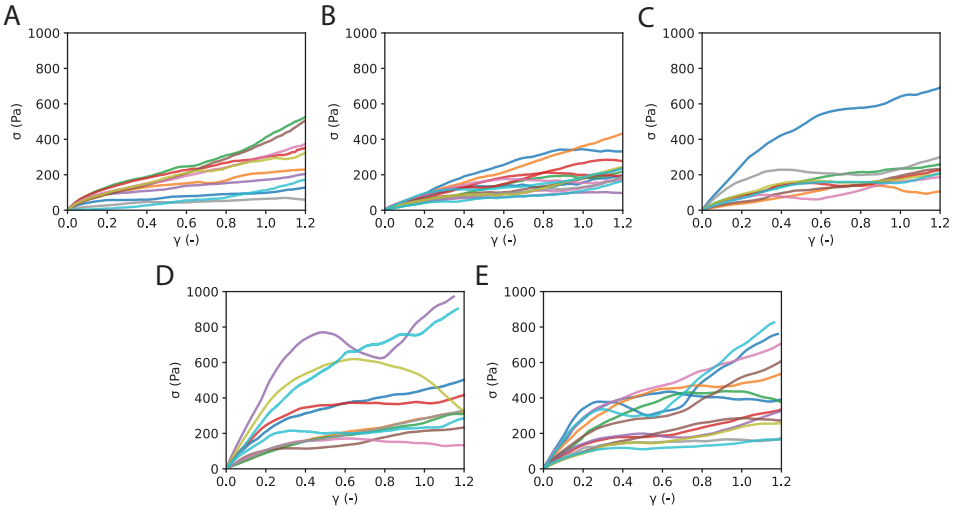

Figure 5.7: Rate dependence of the nonlinear response of single cells to an applied shear deformation. The curves show stress-strain measurements for the individual cells. The corresponding averaged stress-strain data are shown in the main text. The data were obtained at five different strain rates, namely: (A) $0.025s^{-1}$ (N=10), (B) $0.125s^{-1}$ (N=14), (C) $0.25s^{-1}$ (N=9), (D) $0.375s^{-1}$ (N=11) and (E) $0.5s^{-1}$ (N=13). Each colour indicates an individual cell.

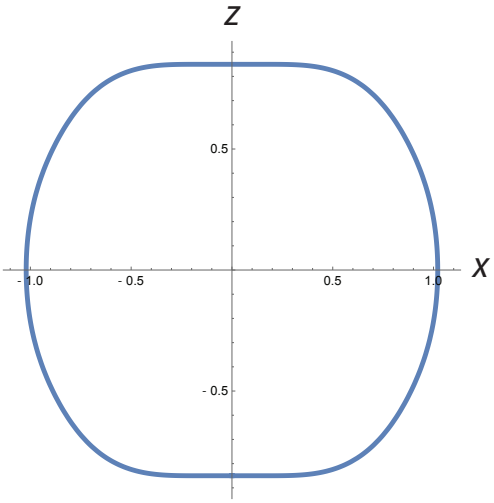

Figure 5.8: Analytical calculation of the increase in equatorial circumference of a cell modeled as an elastic shell under compressive defomation at 15% compressive strain. We find that compression by 15% results in only a 2% increase in the equatorial circumference. Calculated for minimum elastic energy based on axisymmetric spherical harmonic expansion of a volume-preserving linear elastic shell with 2D Poisson ratio of 1/4 and shell thickness set to 10% of the cell radius.

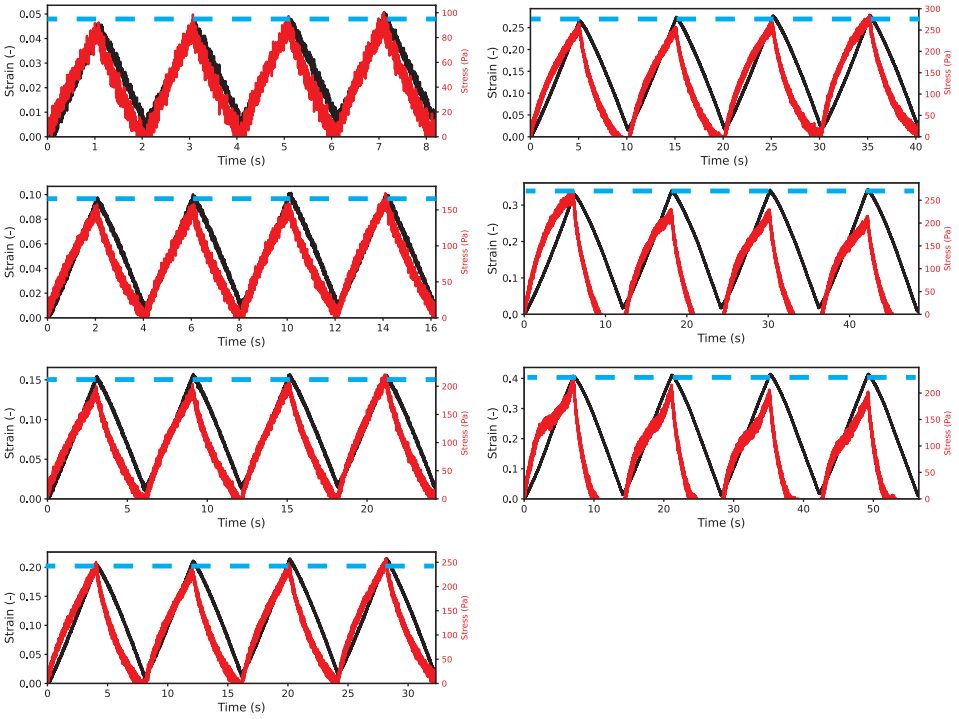

Figure 5.9: Representative shear loading measurements on a single wild type mouse embryonic fibroblast to determine the onset point of plastic deformation. We apply repeated repeated strains ramps with an increasing large amplitude from maximum strains of 5% up to 40% (top to bottom, left to right). We determine the point of onset of plastic deformation when the peak load drops between cycles of strain ramps. We find that plasticity sets in at shear strains within the range of 25-30%. The blue dashed lines are to aid the eye in assessing whether the maximum strain drops between cycles.

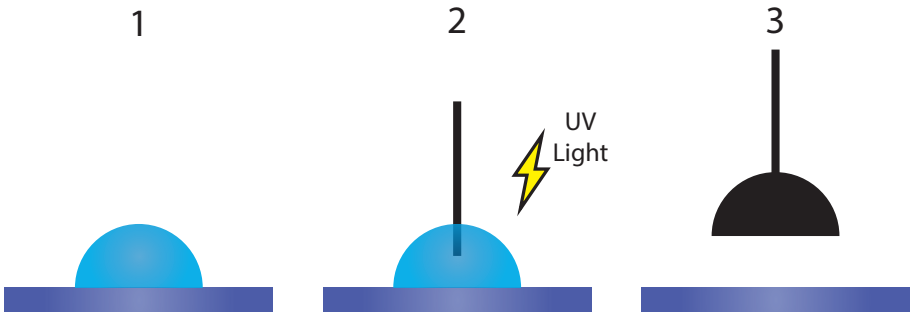

Figure 5.10: Schematic explanation of the procedure for fabricating the top rheometer plate for single cell shear measurements based on *in situ* polymerisation of a UV-curable polymer material to ensure that the plate is parallel with the bottom rheometer plate. 1) Using a needle, we place a small drop of UV curing glue on a glass coverslip coated with Surfasil to prevent adhesion of the glue. 2) We position a flexible cantilever in the middle of the polymer drop. Once in place, we cure the polymer drop by placing it for 2 hours under a UV LED light source placed at a distance of ~ 5 cm. 3) Finally we carefully remove the cured drop, leaving a flat plate that is parallel with the Surfasil-coated coverslip.

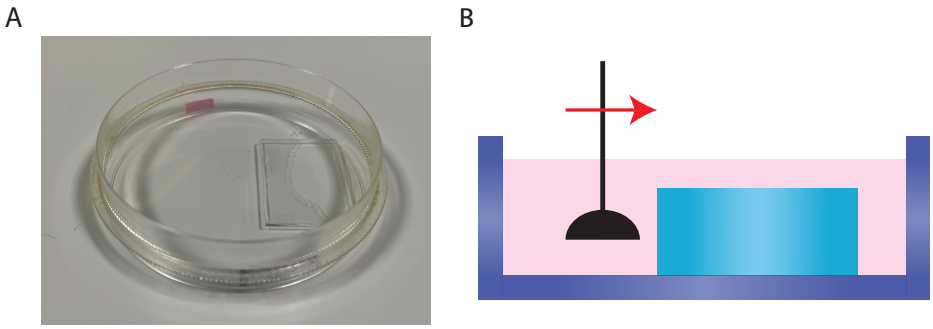

Figure 5.11: Custom-made calibration dish used for calibrating the single cell rheometer using the stiff-surface method. (A) Photograph of the calibration dish, which consists of a glass microscope slide cut to ≈ 2 cm in width glued inside a 6 cm plastic petri dish with Norland NOA81 optical adhesive. (B) Schematic explanation of the calibration procedure. We push the cantilever against the glued microscope slide (light blue block) with the entire system immersed in cell culture medium (shown in pink).

5.7.2. SUPPLEMENTARY TABLES

Primary antibody	Dilution	Manufacturer	Catalogue number
Mouse α-Actin IgG	1:500	Millipore	MAB1501 Clone C4
Mouse α-Vimentin IgG1	1:2000	Abcam	AB8978
Rabbit α-GAPDH IgG	1:5000	Cell signal/Bioke	2118s

Table 5.1: Primary antibodies used for western blot analysis of vimentin and actin expression levels of mouse embryonic fibroblasts.

Secondary antibody	Dilution	Manufacturer	Catalogue number
Rabbit α-mouse IgG (HRP)	1:5000	Abcam	AB6728
Goat α-rabbit IgG (HRP)	1:5000	Abcam	AB97051

Table 5.2: Secondary antibodies used for western blot analysis of vimentin and actin expression levels of mouse embryonic fibroblasts.

	0.0625	**0.125**	**0.25**	**0.375**	**0.5**
0.0625	-	3.94×10^{-1}	9.23×10^{-1}	3.46×10^{-2}*	1.67×10^{-2}*
0.125	3.94×10^{-1}	-	4.21×10^{-1}	3.21×10^{-3}*	7.78×10^{-4}*
0.25	9.23×10^{-1}	4.21×10^{-1}	-	6.51×10^{-2}	3.93×10^{-2}*
0.375	3.46×10^{-2}*	3.21×10^{-3}*	6.51×10^{-2}	-	8.68×10^{-1}
0.5	1.67×10^{-2}*	7.78×10^{-4}*	3.93×10^{-2}*	8.68×10^{-1}	-

Table 5.3: Statistical comparison of student's t-test results between loading rate conditions for the peak shear stress measured for wild type mouse embryonic fibroblasts (see Figure 4 of the main text). The strain rates (bold) are shown in units of s^{-1}. Asterisks indicate statistically significant differences ($p < 0.05$).

	0.0625	**0.125**	**0.25**	**0.375**	**0.5**
0.0625	-	4.47×10^{-1}	6.83×10^{-1}	1.05×10^{-1}	3.50×10^{-2}*
0.125	4.47×10^{-1}	-	4.88×10^{-1}	2.60×10^{-3}*	1.61×10^{-3}*
0.25	6.83×10^{-1}	4.88×10^{-1}	-	1.35×10^{-2}*	2.53×10^{-2}*
0.375	1.05×10^{-1}	2.60×10^{-3}*	1.35×10^{-2}*	-	9.31×10^{-1}
0.5	3.50×10^{-2}*	1.61×10^{-3}*	2.53×10^{-2}*	9.31×10^{-1}	-

Table 5.4: Statistical comparison of student's t-test results between loading rate conditions for the extensional work measured for wild type mouse embryonic fibroblasts (see Figure 4 of the main text). The strain rates (bold) are shown in units of s^{-1}. Asterisks indicate a statistically significant difference ($p < 0.05$).

	0.0625	**0.125**	**0.25**	**0.375**	**0.5**
0.0625	-	4.60×10^{-1}	5.29×10^{-1}	1.33×10^{-2}*	3.86×10^{-3}*
0.125	4.60×10^{-1}	-	2.02×10^{-1}	1.32×10^{-3}*	1.26×10^{-4}*
0.25	5.29×10^{-1}	2.02×10^{-1}	-	5.97×10^{-2}	4.59×10^{-2}*
0.375	1.33×10^{-2}*	1.32×10^{-3}*	5.97×10^{-2}	-	5.61×10^{-1}
0.5	3.86×10^{-3}*	1.26×10^{-4}*	4.59×10^{-2}*	5.61×10^{-1}	-

Table 5.5: Statistical comparison of student's t-test results between loading rate conditions for the dissipated work (the area between the loading and unloading curves) measured for wild type mouse embryonic fibroblasts (see Figure 4 of the main text). The strain rates (bold) are shown in units of s^{-1}. Asterisks indicate a statistically significant difference ($p < 0.05$).

5.7.3. SUPPLEMENTARY METHODS

WESTERN BLOT ANALYSIS OF ACTIN AND VIMENTIN EXPRESSION LEVELS

Mouse embryonic fibroblasts were seeded in 6-well culture plates (Thermo Fisher Scientific, NC2029375) in cell culture medium (Dulbecco's modified Eagle medium containing GlutaMAX (DMEM, Gibco 10565018), supplemented with 10% fetal bovine serum (FBS, Gibco 10270106) and 5% penicillin-streptomycin solution (Pen-Strep, Gibco 15070063)) and allowed to attach for 48 hours. Cells were scraped in phosphate buffer saline (PBS, Thermo Fisher Scientific, 10010023) and lysed in equal volumes of 2x Laemmli buffer (4% SDS, 20% glycerol, 120 mM Tris buffer pH 6.8). Lysates were cleared of large DNA by passing through a 25G needle and then heated to 65°C for 10 minutes. Protein concentrations were measured with the Lowry protein assay [278]. Equal amounts of protein were size-separated by SDS-PAGE with with Mini-PROTEAN TGX gels (Bio-rad) containing 2,2,2-trichloroethanol (TCE). Depending on the protein of interest, HDAC1, GAPDH or TCE were used as a loading control. After running the gel, it was exposed to a 300 nm transilluminator (Bio-Rad ChemiDoc Imaging System) for 5 min for band visualisation. The separated proteins were then transferred to a polyvinylidene fluoride (PVDF) membrane (Bio-Rad, 1704156) using the Bio-Rad Trans-Blot Turbo Transfer System and imaged on the transilluminator, providing a picture of the total protein content. The membranes were blocked for 1 hour at room temperature by 5% Bovine Serum Albumin (BSA) in PBS supplemented with 0.1% Tween-20. Membranes were incubated overnight at 4° C with primary antibody (see Table 5.1). Next, the membranes were washed 5 times with 0.1% Tween-20 in PBS and incubated with horseradish peroxidase-conjugated secondary antibodies (see Table 5.2) for 1 hour at room temperature. After adding Enhanced Chemiluminescence (ECL) substrate (ThermoScientific, 32106), the blots were imaged with the Bio-Rad ChemiDoc Imaging System. Band intensities were quantified using the default gel analysis tools of Fiji [214].

6

BEYOND BELL CURVES: THE ORIGIN OF NON-GAUSSIAN DISTRIBUTIONS IN ATOMIC FORCE MICROSCOPY ELASTICITY MEASUREMENTS

Atomic force microscopy (AFM) is a widely used tool for probing the local mechanical properties of soft materials, including mammalian cells. While the Young's modulus of cells is often reported to follow a log-normal distribution, the origin of this apparent non-normality has remained unclear. Here, we show that this distribution can arise from the nonlinear force-indentation relationship described by Hertzian contact mechanics, rather than reflecting any intrinsic material property. By analysing both the underlying distribution of sample indentation depths and the distribution of calculated elastic moduli, we can distinguish contributions from true material heterogeneity from those arising from the measurement geometry itself. We propose that examining both indentation depth and modulus distributions provides a rapid test to discern true material heterogeneity from artifacts of nonlinear analysis, with implications for the accurate interpretation of AFM-based mechanical measurements in soft materials.

This chapter is in preparation for publication. The paper is co-authored by **J. P. Conboy**, F. Rico and G. H. Koenderink.

6.1. INTRODUCTION

The mechanical properties of tissues and their cell and extracellular matrix constituents play a vital role in physiological and pathological processes like cell differentiation and tissue regeneration [348, 155]. These properties are not merely descriptive, but active regulators of biological function, guiding behaviours such as cell migration and proliferation [349, 217]. Disruptions to the normal mechanical properties of cells have been linked to a wide range of diseases, including cancer and fibrosis, where alterations in tissue stiffness directly impact cellular behaviour and progression of disease [350, 351, 352, 353].

Accurately measuring these mechanical properties, however, is technically challenging. Biological materials are generally soft and structurally complex at the nanoscale, with Young's moduli ranging from hundreds of pascals to a few megapascals [354, 355, 356]. Their heterogeneity and viscoelastic nature make them difficult to characterise using bulk mechanical testing techniques, which often lack the resolution or sensitivity to capture microscale variations. For example, single-cell methods like micropipette aspiration or optical stretching can measure deformability, but provide only coarse average values and are limited in spatial resolution [36, 35]. Atomic force microscopy (AFM) has therefore emerged as a powerful tool for probing the mechanical properties of soft biological materials at high spatial and force resolution [357, 358]. Operating in physiological environments and capable of nanoscale indentation, AFM has become widely adopted for investigating the mechanical properties of cells, tissues, and hydrogels [359]. Its ability to simultaneously map topography and elasticity in cell culture conditions makes it particularly well-suited to biological applications [360].

From the plethora of AFM experiments performed on cells over the past 4 decades, it has been consistently shown that elasticity values do not follow a normal, or Gaussian, distribution [361, 362, 363]. Instead, the data are characteristically skewed, often better described by a log-normal distribution [364]. This skew has been observed across various mammalian cell types and has also been observed in tissue-derived hydrogels [365, 366]. In the absence of an analytic distribution function, it has become best practice to transform measured Young's modulus values into logarithmic space and take the geometric mean of the transformed data as the average cell elasticity [207]. This transformation improves statistical robustness and reduces the influence of extreme values, which can distort the arithmetic mean. However, this approach remains rather unsatisfactory, as it is based purely on the phenomenological observation that the data appear more normal in log space. Interestingly, it has been found that the elasticity of much simpler, homogeneous soft samples, such as hydrogels, also follows a skewed distribution [367]. This raises the question whether this skew may not solely reflect biological heterogeneity but could also arise from methodological choices during AFM analysis.

In this chapter, we demonstrate that the nonlinear force–distance relationship described by the Hertzian contact mechanics model can contribute to a skewed distribution of measured Young's moduli. For polyacrylamide hydrogels, we find that the skewed distribution can be fully attributed to this effect, whereas for both single cells and cell populations, the observed skew reflects true underlying mechanical heterogeneity.

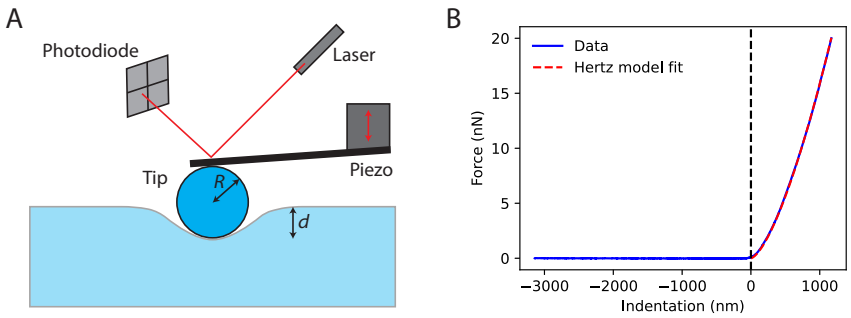

Figure 6.1: The fundamentals of atomic force microscopy. (A) Schematic of an AFM experiment. The z-position of the AFM tip is controlled by a piezo micromotor. When the tip is moved down and makes contact with the soft sample, this interaction causes the microcantilever to bend. The microcantilever deflection is monitored via the reflection of a laser beam onto a photodiode. During the experiment, the force is recorded as the tip is pushed into the surface by a distance relative to the contact point, d. (B) Example force-indentation curve obtained from a polyacrylamide hydrogel (expected Young's modulus ~ 2.5 kPa) with an AFM cantilever with a nominal spring constant of 2.5 N/m and a spherical colloidal bead tip of radius $R = 10\,\mu$m. No force is exerted on the probe until contact with the surface of the polyacrylamide gel (indicated with the dashed vertical line). Thereafter, force increases with indentation in a nonlinear fashion. To extract the Young's modulus, E, we fit the Hertz model to the contact region of the force-distance curve for a spherical indenter (Equation 6.1).

These findings highlight that the nonlinear measurement relationship can substantially influence the interpretation and statistical analysis of AFM-based mechanical data. This discovery opens the way to properly characterising heterogeneities inherent to cells and tissues and separating these from analysis artefacts.

6.2. RESULTS

6.2.1. MEASURING ELASTICITY USING ATOMIC FORCE MICROSCOPY

Atomic force microscopy (AFM) measures surface interactions between a probe, typically either a sharp tip or a colloidal bead, and the sample, using a flexible microcantilever as a sensitive force detector (Figure 6.1A). The deflection of the microcantilever upon contact with the sample is monitored by reflecting a laser beam off its surface onto a quadrant photodiode. Precise movements of the probe relative to the sample are controlled using piezoelectric actuators, which enable both lateral scanning across the sample surface and vertical displacements for indentation measurements. Sharp tips are preferred when high spatial resolution is required, while spherical colloidal probes are better suited for indentation experiments, as their shape enables deeper interaction with the sample for quantitative mechanical characterisation [368].

In a typical AFM indentation protocol, the piezo actuator drives the cantilever base towards the sample at a constant vertical velocity. Initially, the probe does not interact with the sample, but upon reaching the surface, called the contact point, the tip begins to

indent the sample. The indentation continues until a predefined maximum interaction force, also known as the set point force or the trigger force, is attained. After reaching this set point, the cantilever is retracted. The force exerted on the sample is derived from the cantilever's deflection (q), following Hooke's law ($F = k \times q$, where k is the cantilever's spring constant). The raw data collected during this procedure is the force–distance curve, which plots the measured force against the piezo displacement. After determining the contact point, the force-distance curve is converted to a force–indentation curve, accounting for the actual indentation of the probe into the sample. To illustrate this, we show an example curve measured on a polyacrylamide hydrogel in Figure 6.1B.

Typically, the analysis of these force-indentation curves employs Hertzian contact mechanics models, which describe how force varies with indentation depth depending on the geometry of the AFM probe tip [369]. Commonly, the classical Hertz model is used to fit to force-indentation curves, providing a straightforward mathematical description for interpreting indentation data, with the assumption that the sample is uniform in composition, behaves the same in all directions (isotropic), follows linear elastic behaviour, and is large enough to be treated as an infinite half-space, with no adhesion or attractive interactions present between the probe and the sample. The Hertzian force-indentation relation for a spherical indenter is given by

$$F(d) = \frac{4}{3} \cdot \frac{E}{1-\nu^2} \cdot \sqrt{R} \cdot d^{3/2}, \tag{6.1}$$

where d is the indentation depth, R is the radius of the spherical tip, E is the elastic modulus of the sample and ν is the Poisson ratio of the material, generally assumed to be 0.5 for soft, incompressible samples [369]. This force-distance relationship allows us to extract the Young's modulus E of a material by fitting force-distance measurements. Furthermore, Equation 6.1 can be generalised to differently shaped indenters as

$$F(d) = C \cdot \frac{E}{1-\nu^2} \cdot d^n, \tag{6.2}$$

where C and n are constants specific to the geometry of the AFM tip [358]. For example, in the case of a pyramidal indenter, $C = 1.4906 \cdot \tan(\alpha)/2$, where α is the angle between the faces of the pyramid and $n = 2$ [358]. Importantly, the force–indentation relationship is inherently nonlinear and strongly dependent on the geometry of the AFM probe, with different tip shapes yielding distinct mathematical forms of the contact mechanics model.

6.2.2. THE ELASTIC MODULI OF POLYACRYLAMIDE HYDROGELS DISPLAY A SKEWED DISTRIBUTION

While single-point indentation provides local mechanical information, generating a force map enables spatially resolved measurements across a defined area, allowing us to visualise heterogeneity in the sample's mechanical properties. To illustrate this, we performed a nanoindentation force map of a polyacrylamide (PAA) hydrogel. We chose this test material due to its linear elastic properties, as measured with bulk rheometry [370]. We indented the PAA gel in a 10×10 matrix of indentation points arranged in a

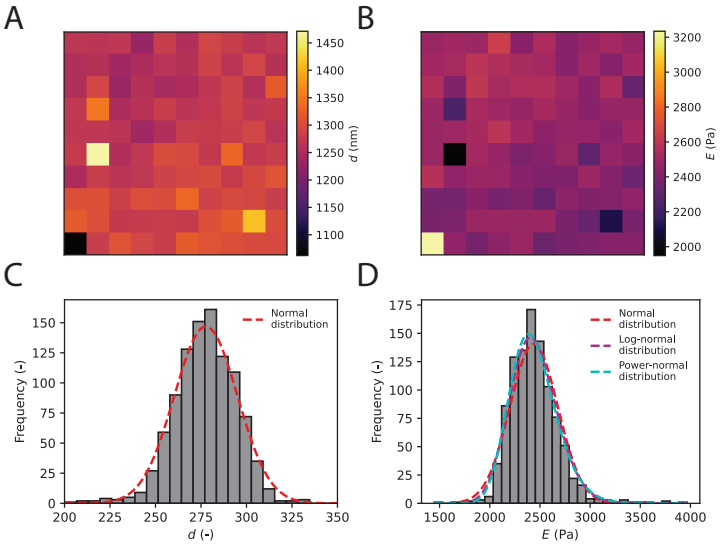

Figure 6.2: The distribution of indentation depths, d, and Young's moduli, E, from AFM measurements on a polyacrylamide gel, with expected stiffness ~ 2 kPa. (A) Map of indentation depths, d, over a 10 x 10 grid, with each pixel spaced by 5 µm. We indent each point of grid to a set point force of 10 nN with a 10 µm radius spherical tip. (B) Map of Young's moduli, E, calculated using the indentation depths in (A). (C) The distribution of measured indentation depths (N=1000) follows a normal distribution (shown by the dashed red line). (D) The distribution of Young's moduli does not follow a normal distribution (dashed red line) but displays skewness, with a tail on the right of the distribution, which originates from the nonlinear force-indentation relationship described by the Hertz model (Equation 6.2). Both the log-normal (dashed magenta line) and power-normal (dashed cyan line) distributions pass the Kolmogorov–Smirnov test and provide a reasonable fit to the data, but Bayesian analysis indicates that the power-normal distribution offers a superior fit.

grid pattern, with each point spaced 5 μm apart, using a 10 μm radius spherical probe. At each indentation location, the user will choose a maximum force to indent to, which depends on the stiffness of the sample and the geometry of the indenter chosen for the experiment. We chose a set point force of 10 nN to ensure sufficient indentation depth for modulus estimation while remaining within the small-strain regime of the material. We repeated this mapping at 10 randomly selected locations across the gel surface. A representative map of indentation depths is shown in Figure 6.2A. The corresponding distribution of indentation depths, pooled over all 10 maps, followed a normal distribution (confirmed by a Kolmogorov–Smirnov test [371], p>0.05), with a mean indentation depth of 280 μm (Figure 6.2C).

At each indentation point, a force–indentation curve was acquired and fitted to the Hertz contact model, allowing the elastic modulus to be calculated and assembled into a spatial map of mechanical properties (Figure 6.2B). Instead of fitting the overall force–indentation curves, we next directly converted each individual indentation depth into a pointwise elastic modulus [372] value using the Hertz model for a spherical indenter (Equation 6.1), enabling a detailed spatial analysis of the sample's mechanical properties. The resulting distribution of elastic modulus values appeared noticeably right-skewed, with a pronounced tail extending toward higher values, in contrast to the symmetric, normally distributed indentation depths (Figure 6.2D).

We hypothesise that this skew arises because the measured indentation depth, d, is normally distributed, and in the Hertz model, the elastic modulus is calculated by raising d to the power of 3/2, which nonlinearly transforms the distribution and amplifies variation in the upper tail. To test this hypothesis, we started with the normal distribution of indentation depths, with a probability density function given by

$$f(d) = \frac{1}{\sqrt{2\pi\sigma^2}} \exp\left(-\frac{(d-\mu)^2}{2\sigma^2}\right), \tag{6.3}$$

where μ is the mean depth and σ^2 is the variance. We then applied a change of variables based on the Hertz model, in which the elastic modulus is proportional to $d^{3/2}$ (see supplementary information for details of the calculation). This transformation yielded a closed-form expression for the probability distribution of the elastic modulus, given by

$$f(d) = \frac{2}{3\sqrt{2\pi}\,\sigma}\, d^{-1/3} \left[\exp\left(-\frac{(d^{2/3}-\mu)^2}{2\sigma^2}\right) + \exp\left(-\frac{(d^{2/3}+\mu)^2}{2\sigma^2}\right)\right], \quad d > 0, \tag{6.4}$$

which we then fit to the distribution of elastic moduli (cyan dashed line in Figure 6.2D). We confirmed that the transformed distribution provided a good fit to the measured elastic modulus values using a Kolmogorov–Smirnov test, which yielded a p-value greater than 0.05 (p=0.30), indicating no significant difference between the theoretical and measured E distribution. In contrast, fitting a normal distribution to the modulus values failed the Kolmogorov–Smirnov test, with p<0.05, reflecting the skewed nature of the data (red line in Figure 6.2D). Because elastic modulus distributions are frequently modelled empirically using a log-normal distribution [361, 362, 363], we also fitted a log-normal curve to our data for comparison (magenta line in Figure 6.2D). This fit yielded a Kolmogorov–Smirnov p-value of 0.05, indicating that the log-normal distribution was

at the threshold of statistical significance and did not describe the data as well as the power-transformed distribution.

As the Kolmogorov–Smirnov test is non-parametric and evaluates only the agreement between the observed and theoretical cumulative distributions, we also performed a Bayesian model comparison using the Bayesian Information Criterion. The Bayesian Information Criterion (BIC) is a parametric model selection metric that evaluates how well a probability distribution fits the data while penalising models with more free parameters, thereby favouring simpler models that still explain the observed variation effectively [373]. This analysis showed that the transformed distribution had a lower Bayesian Information Criterion value (BIC=13728) compared to the log-normal model (BIC=13744), indicating that it achieved a better balance between goodness of fit and model complexity. The corresponding Bayes factor of 2.29×10^3 provides strong evidence in favour of the transformed distribution over the log-normal alternative. Therefore, our data demonstrate that the observed distribution of elastic moduli in polyacrylamide gels can be accurately predicted from the underlying distribution of indentation depths using a theoretically grounded variable transformation, offering a robust alternative to empirical fitting approaches.

6.2.3. THE ELASTIC MODULUS DISTRIBUTION OF SINGLE MAMMALIAN CELLS

Having established and validated our approach using polyacrylamide, a well-characterised linear elastic material, we next applied the same analysis to force maps acquired on living cells, where mechanical properties are expected to be more heterogeneous. We first performed force–indentation measurements on a single mouse embryonic fibroblast (Figure 6.3A) and recorded the resulting indentation depths at each point in the force map (Figure 6.3B). Unlike the polyacrylamide gels, the distribution of indentation depths did not follow a normal distribution, as confirmed by a Kolmogorov–Smirnov test ($p<0.05$), indicating substantial heterogeneity in the cell's mechanical response. As with the polyacrylamide gels, we then applied the Hertz model (Equation 6.1) to convert the measured indentation depths into pointwise elastic modulus values. This nonlinear transformation once again amplified the asymmetry in the indentation depth data, producing an even more pronounced right-skew in the distribution of elastic modulus values (Figure 6.3C). To compare the log-normal and power-transformed distributions, we used the Bayesian Information Criterion, finding BIC values of 50053 for the log-normal model and 50328 for the transformed distribution (with a corresponding Bayes factor of $\approx 10^{59}$), indicating that the log-normal model provided a significantly better fit to the measured cell moduli. Therefore, the observed skew in the elastic modulus distribution could not be explained solely by the nonlinear transformation inherent to the Hertz model.

Next, we cropped the force map to include only the nuclear region of the cell to assess whether the mechanical heterogeneity persisted within this defined subcellular compartment (Figure 6.3D). Unlike the distribution obtained from the whole cell, the indentation depths within the nuclear region followed a normal distribution, as confirmed by a Kolmogorov–Smirnov test ($p>0.05$), indicating a good fit (Figure 6.3E). When we cal-

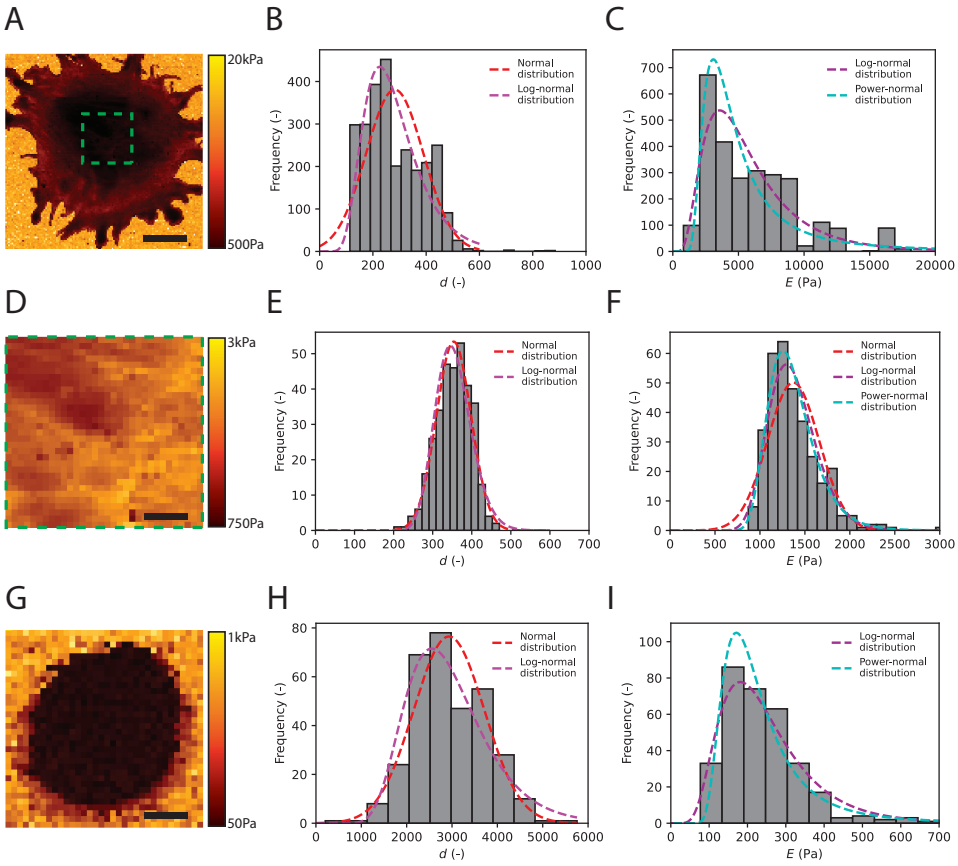

Figure 6.3: The distribution of indentation depths, d, and Young's moduli, E, from AFM measurements on mammalian cells. (A) Young's modulus map of a single mouse embryonic fibroblast over a 50 x 50 grid, with each pixel spaced by 1 µm. We indented each point of the grid to a set point force of 1 nN with a 1 µm radius spherical tip. Scale bar 20 µm. (B) The distribution of measured indentation depths (N=3321) does not follow a normal distribution (shown by the dashed red line), but is better captured by a log-normal distribution (dashed magenta line). (C) Due to the skewed nature of the underlying distribution of indentation depths, a log-normal distribution (magenta line) better captures the distribution of calculated Young's moduli than the power-transformed distribution (cyan line). (D) To see if the heterogeneity in indentation depths persists within subcellular regions, we zoom-in on the cell shown in (A), cropping only its nuclear region, indicated by the dashed green lines. Scale bar 5 µm. (E) The distribution of indentation depths in the nuclear region of the cell conforms to a normal distribution (red dashed line), which translated into the power-transformed distribution shown in (F). (G) To test for cell-type specificity, we performed force mapping on a single monocyte. The panel shows a 64 × 64 pixel Young's modulus map of a single monocyte in a 30 µm square area (468 nm pixel^{-1}). We indented each point of the grid to a set point force of 0.8 nN with a 70 µnm radius spherical tip. Scale bar 5 µm. (H) The monocyte displays a skewed distribution of indentation depths. (I) The corresponding distribution of Young's moduli is better captured by a log-normal distribution (magenta line) than by the power-transformed distribution (cyan line).

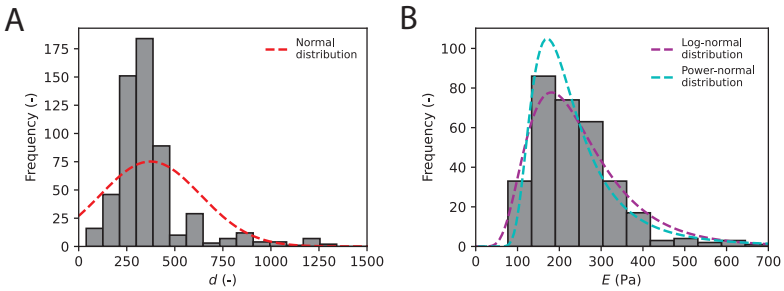

Figure 6.4: The distribution of indentation depths, d, and Young's moduli, E, from single-point AFM indentations in the perinuclear region of sparsely seeded fibroblasts. Each data point corresponds to an individual cell (N=500). (A) The distribution of measured indentation depths does not follow a normal distribution (red dashed line). (B) Accordingly, a log-normal distribution (magenta line) better captures the distribution of calculated Young's moduli than the power-transformed distribution (cyan line).

culated the elastic modulus values within the nuclear region, the Bayesian Information Criterion values were 4622 for the log-normal fit and 4603 for the power-transformed distribution, indicating that the transformed model provided a better fit in this subcellular region. Therefore, in contrast to the whole-cell analysis, the mechanical response within the nuclear region could be well explained by a normally distributed indentation depth and its nonlinear transformation via the Hertz model.

Finally, to test whether the observed skew in indentation depth and elastic modulus distributions was specific to cell type, we performed force mapping on monocytes (Figure 6.3G). Specifically, we performed a force map on a single monocyte adhered to glass via a poly-L-lysine coating and measured the resulting indentation depths (Figure 6.3H). Again the indentation depths did not follow a normal distribution (Figure 6.3H), as confirmed by a Kolmogorov–Smirnov test, similar to what we observed in single fibroblast cells. ($p<0.05$). We then used the Hertz model to calculate the point-wise elastic modulus from the measured force–indentation curves. Since the underlying indentation depth distribution was already skewed, we found that a log-normal distribution provided a better fit to the resulting elastic modulus values than the power-transformed normal model (Figure 6.3I). We conclude that the skewed distributions of elastic modulus measurements are influenced by the intrinsic skew in indentation depth distributions, regardless of cell type.

6.2.4. THE ELASTIC MODULUS DISTRIBUTION OF A CELL POPULATION

To assess whether the mechanical heterogeneity observed in individual force maps was representative at the population level, we measured 500 mouse embryonic fibroblasts, performing a single-point indentation in the perinuclear region of each cell. Across the cell population, we observed a right-skewed distribution of indentation depths that could not be described by a normal distribution, as confirmed by a Kolmogorov–Smirnov test ($p<0.05$; Figure 6.4A). Therefore, when we calculated the elastic moduli, we found that a log-normal distribution provided a better fit to the data, as indicated by a lower BIC

value (BIC = 9772) compared to the transformed distribution (BIC = 9858) (Figure 6.4B). This finding suggests that, at the population level, the mechanical variability among fibroblasts reflects underlying biological heterogeneity that cannot be explained solely by the nonlinear indentation-to-modulus relationship defined by the Hertz model.

6.2.5. DEVIATIONS FROM THE HERTZ MODEL LEAD TO A SKEWED DISTRIBUTION OF YOUNG'S MODULI

In practice, rather than extracting pointwise modulus values from individual indentation depths, as we have done thus far, it is common to estimate the Young's modulus by performing a least-squares fit to the entire force–indentation curve. When we fit the entire force–indentation curves of polyacrylamide, for which we have shown the indentation depths follow a normal distribution, the extracted modulus values still exhibit a skewed distribution (Figure 6.5A). However, because the modulus is obtained by fitting the full force–indentation curve rather than transforming individual indentation depths, the resulting distribution cannot be derived analytically from the known distribution of indentation values. We hypothesize that this skew arises because we cannot measure the indentation to infinite precision (Figure 6.5B), and the resulting uncertainty in the contact point propagates through the fitting procedure, leading to a skewed distribution of the extracted elastic moduli.

To demonstrate how uncertainty in contact point determination leads to a skewed distribution of elastic moduli, we simulated 100,000 force–indentation curves for a material that ideally follows the Hertz model, using an elastic modulus of 1 kPa and indenting to a maximum force of 1 nN. We then added a small offset to the contact point, drawn from a normal distribution, and fitted the Hertz model to each individual simulated curve. By doing this, we observed a normal distribution of maximum indentation depths used in the analysis, consistent with our experimental observations on polyacrylamide (Figure 6.5C). Furthermore, we observed a skewed distribution of elastic moduli, where both the width and the skew of the distribution increased as the contact point uncertainty σ_{contact} was increased from 20 nm to 50 nm to 80 nm (Figure 6.5D-F). To quantify the shape of the distributions, we measured the skew, γ, which describes the asymmetry of the distribution around its mean for σ_{contact} values ranging from 1-80 nm (Figure 6.5G). We found that the skew, γ, increased with increasing contact point uncertainty, showing that greater uncertainty in contact point determination leads to greater asymmetry in the extracted modulus distribution. We then calculated the excess kurtosis, $\beta - 3$, which measures the 'tailedness' of the distribution relative to a normal distribution (Figure 6.5H). The excess kurtosis likewise increased with increasing contact point uncertainty, indicating that greater uncertainty leads not only to more asymmetry but also to heavier tails in the distribution of extracted modulus values.

Returning to our polyacrylamide measurements, we can now use the measured skew and kurtosis of the extracted Young's modulus distribution, together with simulations calibrated to match the mean modulus, to estimate the width of the indentation-depth distribution that would be expected if contact-point uncertainty were the only source of variability. Using the calculated skew and kurtosis of 0.2 and 0.01, respectively, from the distribution shown in Figure 6.5A, we estimate that this corresponds to a contact-

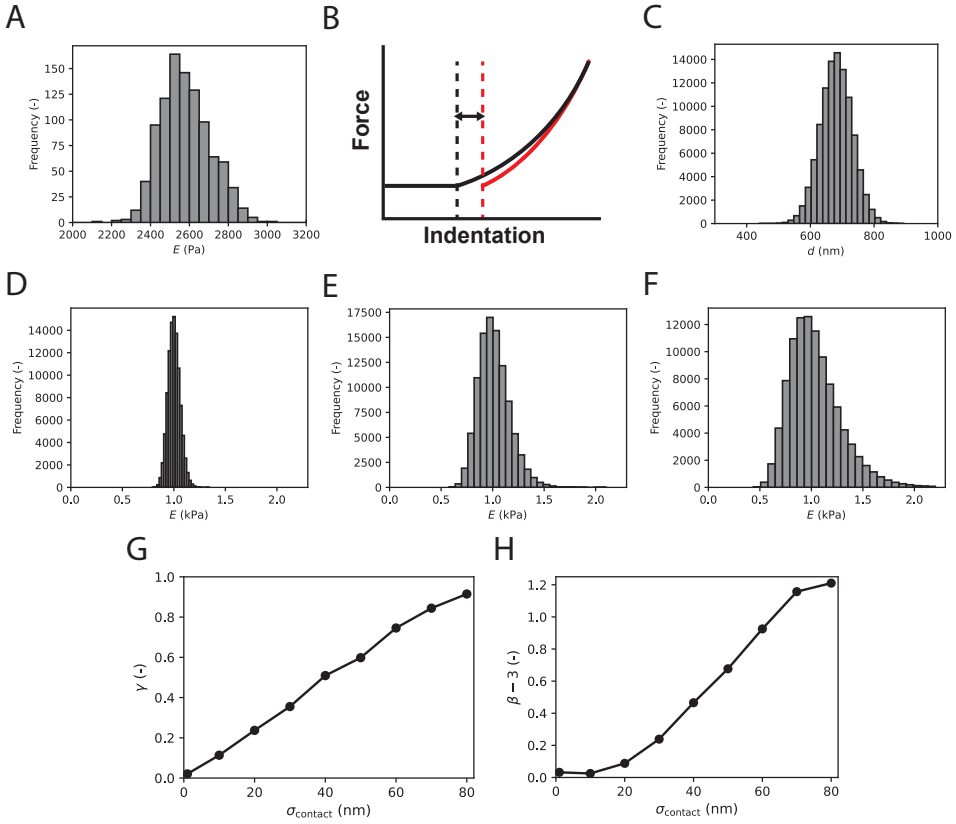

Figure 6.5: Monte Carlo simulations demonstrate how a small uncertainty in contact point determination leads to a skewed elastic modulus distribution. (A) Histogram showing the distribution of elastic moduli inferred from an AFM force map of the same polyacrylamide gel analysed in Figure 6.2. Fitting the force–distance curves, rather than calculating the pointwise modulus, still yields a skewed distribution. (B) We hypothesize that, since there is always an uncertainty on the contact point determination, as we cannot measure indentation depth to an infinite precision, one will always obtain a skewed distribution of elastic moduli. (C) To demonstrate this, we generate 100,000 force curves using the Hertz model for a material with an elastic modulus of 1 kPa, indented to a set point force of 1 nN, and to each of these force curves, add a small offset drawn from a normal distribution (σ_{contact} = 50 nm) to simulate the uncertainty on the contact point. The panel shows the normal distribution of indentation depths obtained from the simulations, similar to the distributions we experimentally observe for polyacrylamide gels. (D-F) We then fit the Hertz model to each of these simulated force-distance curves with a σ_{contact} of 20 nm, 50 nm and 80 nm, respectively, to obtain the histograms of elastic moduli. As σ_{contact} increases, the width and the skew of the E distribution also increases. (G) The skewness, γ, of the E distributions for simulated σ_{contact} values from 1-80 nm increases with increasing contact point uncertainty. (H) We further analyse the shape of the E distribution by calculating the excess kurtosis, $\beta - 1$, which quantifies how 'heavy' the tails of the distributions are. We find that the kurtosis also increases with increasing σ_{contact}.

point uncertainty of approximately 20 nm. Strikingly, this estimated contact-point uncertainty corresponds to the same standard deviation measured directly from the indentation depths (20 nm) in our experiments on polyacrylamide (Figure 6.2C). Therefore, the width of the indentation-depth distribution observed experimentally can be fully accounted for by uncertainty in contact-point determination during force–indentation measurements. Together, these results show that finite uncertainty in contact point determination leads to extracted modulus distributions that are both skewed and heavy-tailed, even when the underlying indentation depths are normally distributed.

6.3. DISCUSSION

We have demonstrated that the frequently observed skewness in elastic modulus distributions from AFM indentation experiments can originate from the nonlinear Hertzian force–indentation relationship rather than intrinsic sample heterogeneity alone. For homogeneous polyacrylamide hydrogels, we showed that an initially normal distribution of indentation depths translates directly into a skewed modulus distribution, accurately captured by a power-transformed theoretical model. In contrast, mammalian cells exhibited intrinsic heterogeneity, reflected in skewed distributions of indentation depths themselves, which were best described by a log-normal model. However, subcellular regions such as the nucleus displayed homogeneous indentation depths and consequently matched the predictions from the nonlinear transformation of a normal distribution. Population-level measurements on fibroblasts further supported the presence of intrinsic mechanical heterogeneity, emphasising that observed skewness in cellular elasticity data arises both from true biological variability and from measurement nonlinearities.

Our findings have important implications for interpreting AFM-derived elasticity measurements in soft materials and biological systems. The observation that a normally distributed set of indentation depths can yield a skewed distribution of extracted moduli highlights that the nonlinearity of the Hertz model alone can introduce apparent non-normality into AFM data. Furthermore, we demonstrate that finite uncertainty in contact point determination systematically increases both the skewness and kurtosis of the modulus distribution, even in otherwise homogeneous materials. This suggests that the commonly observed log-normal-like distributions of cell stiffness may, in part, reflect methodological artefacts arising from measurement geometry and fitting procedures, rather than exclusively indicating true biological heterogeneity. Therefore, careful examination of the underlying indentation depth distributions prior to modulus calculation can help researchers discern whether observed mechanical variability is intrinsic to the sample or arises from the nonlinearities inherent to the measurement process.

While our study provides a clear framework for interpreting the origins of skewed modulus distributions in AFM measurements, several limitations should be acknowledged. First, our analysis is predicated on the validity of the Hertz model, which assumes purely elastic, isotropic, and homogeneous materials in the absence of adhesion, conditions that may not fully capture the complex viscoelastic or poroelastic behaviours of living cells and tissues [374, 253]. Additionally, uncertainties in cantilever calibration, tip geometry, and variations in experimental conditions may introduce further variabil-

ity in the measured indentation depths and extracted moduli, beyond the contact point uncertainty considered in our simulations [375]. All these factors will accentuate the skew in the measured modulus distributions, further complicating the interpretation of AFM elasticity data in soft biological systems.

Taken together, our findings provide a practical framework for the interpretation of AFM-based elasticity measurements in soft materials and biological systems. By examining the distribution of indentation depths prior to the calculation of elastic moduli, researchers can discern whether the observed variability arises from true mechanical heterogeneity or from the nonlinearities inherent to the measurement and analysis process. This approach will enable more accurate interpretation of AFM data, facilitating the reliable use of cell and tissue mechanics as quantitative biomarkers in mechanobiology and soft matter research.

6.4. CONCLUSION

In conclusion, our findings demonstrate that AFM measurements inherently introduce skewness into elastic modulus distributions due to the nonlinear force–indentation relationship and uncertainties in contact point determination. By systematically comparing indentation depth distributions and the resulting modulus distributions, we provide a framework for distinguishing measurement artefacts from true biological variability in AFM elasticity studies. This has practical implications for interpreting cell stiffness data, particularly in studies linking mechanical properties to disease states, where careful separation of technical artefacts from genuine biological signals is critical.

6.5. ACKNOWLEDGEMENTS

The authors thank C. Valotteau and L. Redondo-Morata for their help with AFM experiments in the Rico lab in Marseille and Mar Eroles for providing the AFM measurement on monocytes. We gratefully thank A. Katan for technical assistance with AFM experiments in Delft. J.P.C. acknowledges funding from the Casimir Research School. We gratefully acknowledge funding from the NWO Talent Programme, which is financed by the Dutch Research Council (project number VI.C.182.004).

6.6. MATERIALS AND METHODS

6.6.1. ATOMIC FORCE MICROSCOPY

All experiments were conducted using a Nanowizard IV (Bruker, USA) mounted on an inverted optical microscope (Nikon, Japan). For polyacrylamide gels, cantilevers with a nominal spring constant of 0.25 N/m and a hemisphere with a 10 μm radius colloidal sphere at the tip (SAA-SPH-1UM, Brucker, USA) were used. For mouse embryonic fibroblast measurements, cantilevers with a nominal spring constant of 0.25 N/m and a

hemisphere with a 1µm end radius (SAA-SPH-1UM, Brucker, USA) were used. For monocyte measurements, we used PFQNM-LC-cal cantilevers (Bruker) with a spring constant of 0.1 N/m and a paraboloid with a 70 nm radius. Cantilever spring constant and sensitivity were calibrated before each experiment using the thermal fluctuation method [376].

6.6.2. DATA AND STATISTICAL ANALYSIS

Force-indentation curves were analysed using a custom-written Python script. Text files containing force displacement data were exported using the JPK data analysis software, which were read into the custom Python script using the Numpy Python library [212]. Contact points were identified using the ratio of variances (RoV) method [377]. For each trial point, the variance of the deflection signal was calculated in two adjacent windows before and after the point. The RoV was defined as:

$$\mathrm{RoV}_i = \frac{\mathrm{var}(z_{i+1:i+N})}{\mathrm{var}(z_{i-N:i-1})}, \tag{6.5}$$

where z is the cantilever deflection signal, i is the trial contact point index, and N is the window size in number of data points. The contact point was assigned to the trial point with the maximum RoV value within the defined search region. Curve fitting was performed using the curve fit function from the SciPy library [211].

Each distribution (normal, log-normal, and power-transformed) was fitted using the maximum likelihood estimation (MLE) method implemented in the SciPy statistics module [211]. To assess the goodness of fit between the empirical and theoretical distributions, a Kolmogorov–Smirnov (KS) test was then performed with SciPy. To compare model fits, the Bayesian Information Criterion (BIC) was calculated for each distribution. The BIC was defined as:

$$\mathrm{BIC} = k \cdot \ln(n) - 2 \cdot \ln(\hat{L}), \tag{6.6}$$

where k is the number of parameters in the model, n is the number of observations, and $\hat{L}$ is the maximum value of the likelihood function. To compare model evidence, the Bayes Factor was then approximated using the BIC values. The Bayes Factor indicates how strongly the data support one model over another. It was calculated using:

$$\mathrm{BF}_{12} = \exp\left(\frac{\mathrm{BIC}_2 - \mathrm{BIC}_1}{2}\right), \tag{6.7}$$

where BIC_1 and BIC_2 are the BIC values of the models being compared. A Bayes Factor greater than 1 indicates evidence in favour of the first model, while a Bayes Factor less than 1 indicates evidence in favour of the second model.

6.6.3. POLYACRYLAMIDE GEL PREPARATION

Polyacrylamide hydrogels were prepared inside 35 mm glass bottomed dishes (FD35-100, WPI) according to a previously established protocol [378]. The dishes were first functionalised by incubation with 0.1 N NaOH for 5 minutes, then 3-APTMS (281778, Sigma) for 2 minutes and then 10%/v glutaraldehyde (49629, Sigma) in MilliQ for 20 minutes, each time adding enough liquid to cover the surface of the dish. Furthermore,

16 mm coverslips (Thermo Fisher Scientific, 12323148) were cleaned with absolute ethanol and then coated with Sigma Coat (SL2-25ML, Sigma), in order to prevent adhesion between the coverslip and gel surface, and allowed to dry overnight. In a 1 mL Eppendorf tube, 5% (v/v in MQ) acrylamide solution (Sigma-Aldrich, A4058), 0.15% (v/v in MQ) bisacrylamide solution (Sigma-Aldrich, M1533) were combined to a total volume of 45μL, which was pipetted into the middle of the dish. Next, polymerization of the hydrogel was initiated using ammonium persulfate (4.4 μM) and catalyzed by 0.1% v/v) N,N,N',N'-tetramethylethylenediamine (TEMED, Sigma-Aldrich, T7024). One of the Sigma Coat-coated coverslips was then carefully added on top of the gel mixture. After 30 minutes of polymerization, the coverslip was carefully peeled off the gel. To prevent drying, 2 mL of phosphate-buffered saline (PBS) (10010023, Thermo Fisher Scientific) was then added to the dish. The gel was stored overnight at 4 °C and used in experiments the next day.

6.6.4. CELL CULTURE

MOUSE EMBRYONIC FIBROBLASTS

Mouse embryonic fibroblast cells obtained from mouse embryos [206], were cultured in Dulbecco's modified Eagle's medium with glutamax (DMEM, 10565018 Gibco) supplemented with 10% fetal bovine serum (FBS, 10270106 Gibco) and 5% penicillin-streptomycin (Pen-Step, 15070063 Gibco). Cells were cultured in a humidified incubator maintained at 37°C and 5% CO_2, and subcultured when they reached approximately 80% confluency. Cells were subcultured twice per week and were tested for mycoplasma contamination every four months. The day prior to experiments, 35 mm glass-bottomed dishes (FD35-100, WPI) were prepared by incubating with bovine fibronectin (F1141, Sigma) at a concentration of 2 μg/mL in MilliQ for 40 minutes. Subsequently, cells were detached with Trypsin-EDTA (0.25%) (25200056 Thermo Fisher Scientific) and resuspended in cell culture medium. From the resuspended cell solution, 10,000 cells counted with a Countess cell counter (Thermo Fisher Scientific) were seeded in the fibronectin-coated dishes and allowed to adhere overnight. On the day of experiments, cells were washed with PBS and incubated in CO_2-independent medium (18045088, Thermo Fisher) containing 5% penicillin-streptomycin (Pen-Strep, 15070063).

MONOCYTES

The THP-1 cell line (ATCC TIB-202) was sourced from the American Type Culture Collection and cultured in RPMI-1640 medium (Gibco, Thermo Fisher Scientific, 11875093). The medium was supplemented with 1% sodium pyruvate (Gibco, Thermo Fisher Scientifc, 11360070), 1% MEM Non-Essential Amino Acids (NEAA; Gibco, Thermo Fisher Scientific, 10370047), 1% penicillin-streptomycin (Gibco, Thermo Fisher Scientific, 15140148), 10 mM HEPES (Gibco, Thermo Fisher Scientific, 15630080), and 10% fetal bovine serum (FBS). Cells were incubated at 37°C in humidified conditions containing 5% CO_2. Cultures were were subcultured every 2–3 days. To maintain phenotype consistency, cells were not used beyond 20 passages. Glass bottomed for AFM experiments were incubated with a poly-L-lysine 0.01% solution, to promote non-specific adhesion of the cells. On the day of experiments, cells were trypsinized and seeded with fresh culture media in the glass-bottomed dishes, immediately followed by mechanical testing.

6.6.5. MONTE CARLO FORCE-CURVE SIMULATIONS

Force–indentation curves were generated in silico using a custom Python script employing the Hertz contact model for a spherical indenter:

$$F(\delta) = \frac{4}{3}\frac{E}{1-\nu^2}\sqrt{R}\delta^{3/2}, \tag{6.8}$$

where $E = 1$ kPa is the true elastic modulus, $\nu = 0.5$ the Poisson ratio, and $R = 1$ µm the tip radius. A linear array of 50 indentation values δ_i was calculated to span forces up to $F_{\max} = 1$ nN. To mimic uncertainty in contact-point determination, each simulated curve was shifted by a single random offset $\delta_0 \sim \mathcal{N}(0, \sigma_{\text{cp}}^2)$ (e.g., $\sigma_{\text{contact}} = 50$ nm). For each of $N = 100,000$ Monte Carlo runs, the elastic modulus was recovered by non-linear least-squares fitting of the above Hertz model using the curve fit function from the SciPy library [211]. The fitted modulus values and the maximum measured indentation depth were recorded for each run.

6.6.6. SKEWNESS AND KURTOSIS CALCULATION

Skewness (γ) and kurtosis (β) of the fitted modulus distributions were calculated to quantify the asymmetry and tail heaviness introduced by contact-point uncertainty. Skewness was defined as:

$$\gamma = \frac{\mathbb{E}[(X-\mu)^3]}{\sigma^3}, \tag{6.9}$$

where $\mathbb{E}[\cdot]$ denotes the expectation over the distribution of fitted Young's moduli (X), μ is the mean, and σ is the standard deviation of the distribution. Kurtosis was defined as:

$$\beta = \frac{\mathbb{E}[(X-\mu)^4]}{\sigma^4}, \tag{6.10}$$

and the *excess kurtosis* was calculated as $\beta - 3$ to normalise against a Gaussian distribution, which has excess kurtosis of zero. Both metrics were computed using the SciPy skew and kurtosis functions on the distributions.

6.7. SUPPLEMENTARY INFORMATION

6.7.1. THEORY

MATHEMATICAL BACKGROUND

In AFM Young's modulus measurements, an underlying normal distribution of indentation depths is transformed by nonlinear force-indentation relationships, resulting in skewed distributions of the derived moduli. In this section, we derive the probability distributions that result from applying these nonlinear transformations to a normally distributed set of indentation depths. This allows us to understand the shape and properties of the resulting distributions of elastic moduli observed in AFM measurements. To derive the distribution of a transformed random variable, we begin with a general result from probability theory, where X is a continuous random variable with a probability density function $f_X(\cdot)$ [379]. Set $A = \{x : f_X(x) > 0\}$. We shall assume that:

1. y = g(x) defines a one-to-one transformation of set A onto a second set, set B
2. The derivative of $x = g^{-1}(y)$ with respect to y is continuous and non-zero for $y \in B$.

Then $Y = g(X)$ is a continuous random variable with density

$$f_Y(y) = \left| \frac{d}{dy} g^{-1}(y) \right| f_X(g^{-1}(y)) I_B(y). \tag{6.11}$$

THE FOLDED NORMAL DISTRIBUTION

Using a standard normal distribution for X would cause problems when applying transformations such as $Y = X^2$, since negative values of X would map to the same value of Y as their positive counterparts, making the transformation non one-to-one. To remedy this, we can use a *folded normal distribution* [380]. This is largely a technical choice: by defining X as the absolute value of a normally distributed variable Z (i.e. $X = |Z|$ with $Z \sim N(\mu, \sigma^2)$), we automatically restrict X to nonnegative values. This is not only mathematically convenient for ensuring a one-to-one transformation, but also physically justified in our context, as Young's moduli measurements from AFM experiments are inherently positive. The probability density function of a folded-normal distribution for X is given by

$$f_X(x) = \frac{1}{\sqrt{2\pi}\sigma} \left[\exp\left(-\frac{(x-\mu)^2}{2\sigma^2} \right) + \exp\left(-\frac{(x+\mu)^2}{2\sigma^2} \right) \right] I_{[0,\infty)}(x), \tag{6.12}$$

where μ is the mean of the original normal distribution, σ its standard deviation, and $I_{[0,\infty)}(x)$ is the indicator function that ensures the density is defined only for nonnegative values of x.

THE TRANSFORMATION $Y = X^n$

Now we consider the special cases where we transform a normal distribution to the power n. We consider the special cases where $n = 2$ (i.e. for a pyramidal AFM tip) and $n = 3/2$ (i.e. for a spherical AFM tip) [369].

THE TRANSFORMATION $Y = X^2$

Assume X follows the folded normal density in Equation (2) and consider the transformation $Y = g(x) = x^2$. Since $X \geq 0$, this mapping is one-to-one. We have

$$x = g^{-1}(y) = \sqrt{y},$$

with

$$\frac{d}{dy} g^{-1}(y) = \frac{1}{2\sqrt{y}}.$$

By Equation (1), the density of Y is

$$f_Y(y) = \frac{1}{2\sqrt{y}} f_X\left(\sqrt{y}\right) I_{(0,\infty)}(y). \tag{6.13}$$

Substituting the folded normal density from Equation (2) into Equation (3) gives

$$f_Y(y) = \frac{1}{2\sqrt{y}} \cdot \frac{1}{\sqrt{2\pi}\sigma} \left[\exp\left(-\frac{(\sqrt{y}-\mu)^2}{2\sigma^2} \right) + \exp\left(-\frac{(\sqrt{y}+\mu)^2}{2\sigma^2} \right) \right] I_{(0,\infty)}(y). \tag{6.14}$$

THE TRANSFORMATION $Y = X^{3/2}$

Similarly, for $Y = g(x) = x^{3/2}$ we have:

$$x = g^{-1}(y) = y^{2/3},$$

and

$$\frac{d}{dy} g^{-1}(y) = \frac{2}{3} y^{-1/3}.$$

Then, by Equation (1),

$$f_Y(y) = \frac{2}{3} y^{-1/3} f_X\left(y^{2/3}\right) I_{(0,\infty)}(y). \tag{6.15}$$

Substituting the folded normal density from Equation (2) into Equation (5) yields

$$f_Y(y) = \frac{2}{3\sqrt{2\pi}\sigma} y^{-1/3} \left[\exp\left(-\frac{(y^{2/3}-\mu)^2}{2\sigma^2} \right) + \exp\left(-\frac{(y^{2/3}+\mu)^2}{2\sigma^2} \right) \right] I_{(0,\infty)}(y). \tag{6.16}$$

7

OUTLOOK

In this chapter, we summarise the key findings of this thesis and reflect on how insights from the sort of cell-based experiments described in this thesis can be integrated with in vitro reconstitution experiments to address open questions about how the cytoskeleton and its internal crosstalk contribute to the remarkable mechanical properties of cells. We conclude by offering our perspective on the future directions and challenges in the study of cell mechanics.

Part of this chapter is based on the review paper *How cytoskeletal crosstalk makes cells move: Bridging cell-free and cell studies.* published in Biophysics Reviews (2024). The review paper was jointly written by **J. P. Conboy**, I. Istúriz Petitjean, A. van der Net and G. H. Koenderink.

7.1. WHERE ARE WE NOW?

In this thesis, we investigated the contributions of the actin and vimentin cytoskeletal networks to cell mechanics under compression and shear deformation using single-cell rheology. Under uniaxial compression, we demonstrated that actin and vimentin contribute equally to cell stiffness and compression-stiffening behaviour; however, actin predominantly governs energy dissipation. Using shear rheology, we showed that actin and vimentin exhibit complementary mechanical responses: actin filaments mediate shear-softening through network disruption, while vimentin intermediate filaments exhibit shear-stiffening, preserving structural integrity under high shear strains. Additionally, we identified that the cytoskeletal crosslinker plectin significantly influences cellular viscoelasticity at both small and large deformations, enhancing cell stiffness and slowing stress relaxation. Finally, by introducing an engineered actin-vimentin crosslinker (ACTIF) in plectin-deficient cells, we demonstrated that crosslinking alone restores normal cell stiffness, whereas anchoring functions of plectin are necessary for traction force generation and nuclear shape maintenance. Taken together, our results reveal how actin and vimentin networks synergistically determine cell viscoelasticity and highlight the importance of cytoskeletal crosslinking in regulating cell mechanical behaviour. So, where does this leave us? How do these findings fit into the broader context of cytoskeletal mechanics, and what are the next steps? In the rest of this Outlook chapter, I shall address these questions by considering how our findings contribute to the current understanding of cytoskeletal mechanics and by outlining potential directions for future research.

7.2. BRIDGING CELL AND CELL-FREE STUDIES

Cytoskeletal crosstalk is increasingly recognised as a major determinant of cell mechanics. Coupling between the actin, microtubule and intermediate filament cytoskeleton influences cell mechanics by regulating cell deformability and contractility. Coupling of filaments through physical entanglements as well as cytolinker-mediated crosslinking and bundling regulates a variety of mechanisms that mediate cellular mechanics and cytoskeletal dynamics (Figure 7.1). To complicate matters, there is growing evidence that a fourth cytoskeletal protein family, the septins, also strongly impacts cell mechanics and active mechanical behaviours such as cell migration and division. Septins are well-equipped to mediate cytoskeletal crosstalk since they can bind to the cell membrane, actin and microtubules [381]. For example, recent research demonstrated the role of septins in the regulation of endothelial and epithelial cell-cell adhesion [382, 383].

Elucidating the biophysical mechanisms by which cytoskeletal crosstalk regulates cell mechanics is challenging due to the enormous molecular complexity of the cell and feedback between mechanical forces and biochemical signalling. Cell-free reconstitution provides a valuable complement to live-cell studies because it simplifies the challenge of separating biochemical and physical contributions to cytoskeletal crosstalk. Using cell-based studies, one can then test how these findings carry over to the cellular en-

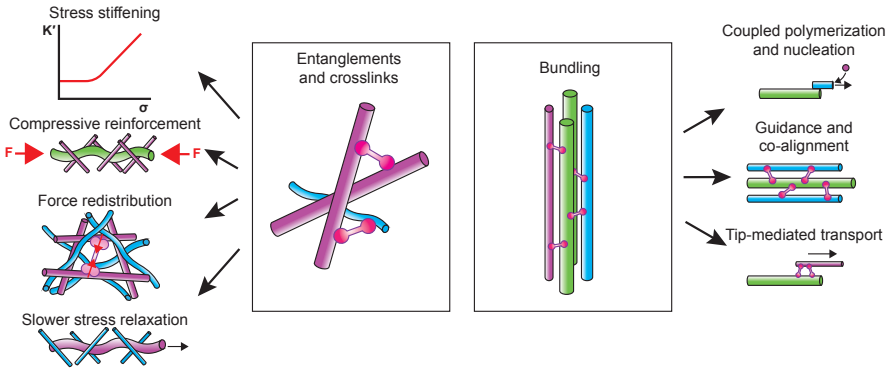

Figure 7.1: Schematic of the two general types of physical interactions that contribute to cytoskeletal crosstalk, and their effect on cytoskeletal biophysics. *Entanglements* and *crosslinks* regulate cytoskeletal stress stiffening, compressive reinforcement, force distribution and stress relaxation. *Bundling* regulates coupled polymerization and nucleation, guidance and co-alignment, and tip-mediated transport of filaments. Actin (magenta), microtubules (green), intermediate filaments (cyan) and crosslinkers (pink).

vironment. Clearly there still remains an enormous gap between the complexity of cells and the simplicity of reconstituted systems. How can this gap be bridged?

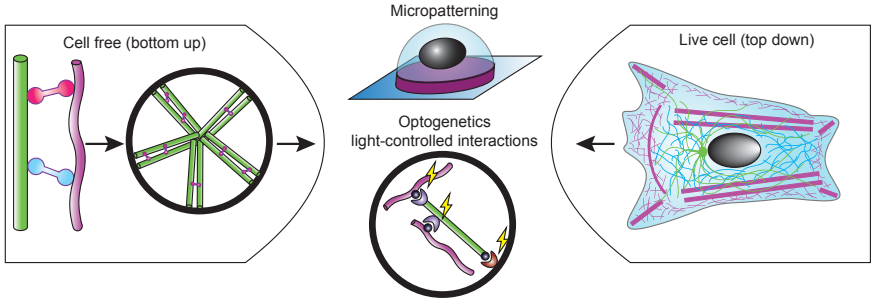

Figure 7.2: New experimental approaches to bridge the gap between live-cell (top down) and cell-free (bottom up) approaches in the research of cytoskeletal crosstalk in cell mechanics. *Micropatterning* and *optogenetic tools* can be used to manipulate cytoskeletal interactions. In cell-free systems, these tools make it possible to generate more complex cytoskeletal geometries that mimic structures found in cells. In cells, they make it possible to control and standardize cytoskeletal geometry or locally induce interactions. Actin (magenta), microtubules (green), intermediate filaments (cyan) and crosslinkers (pink).

We propose different routes to bridge this gap (Figure 7.2). One obvious route is to enhance the complexity of cell-free assays. Simple assays combining cytoskeletal filaments without any accessory proteins showed that steric interactions alone suffice to give rise to nonlinear stiffening and enhanced compressive strength. There is some evidence that intermediate filaments additionally interact with actin filaments and microtubules via electrostatic interactions [111, 112], although this could be an artefact of *in*

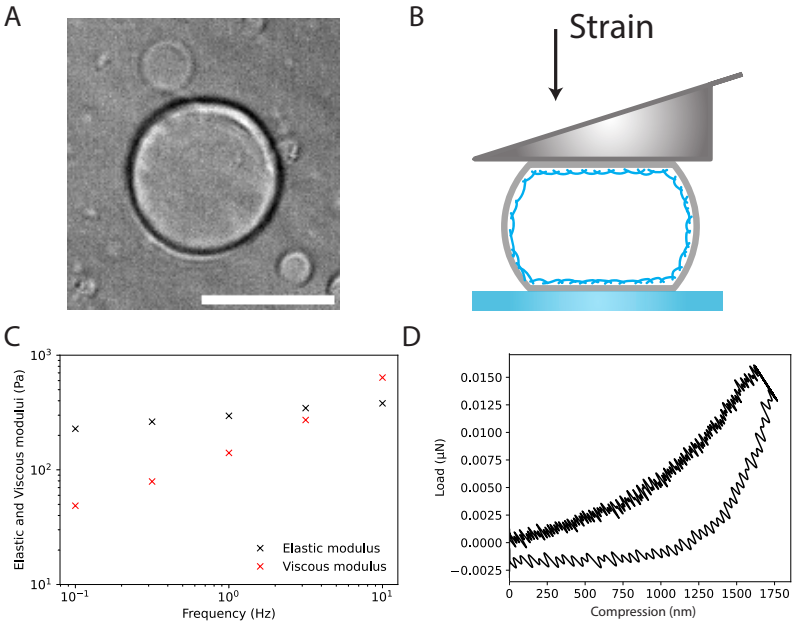

Figure 7.3: Uniaxial compression measurements on cell-sized giant unilamellar vesicles (GUVs) with encapsulated cytoskeletal proteins could help to bridge the gap between our mechanical understanding of cells and cell-free reconstitution systems. (A) Brightfield image showing a GUV with an actin cortex. (B) We perform uniaxial compression experiments on the GUVs, analogous to the experiments on mammalian cells shown in Chapters 2, 3 and 4. (C) Frequency-dependent elastic and viscous moduli at five logarithmically spaced frequencies between 0.1 and 10 Hz. $N = 1$. (D) Strain ramp experiment on a GUV showing compression-stiffening behaviour, similar to the response of single cells. $N = 1$. The GUVs used in these measurements were prepared by **Marcos Arribas Perez**.

vitro conditions. Single-molecule measurements of filament interactions within cells or cell lysates could shed light on this issue. An important next step to bridge the gap to the cell is to incorporate accessory proteins that mediate cytoskeletal coupling. Several studies have shown that crosslinking via cytolinkers is sufficient to give rise to cytoskeletal filament co-alignment and mechanical synergy (e.g. [119, 120]). More detailed investigations of the effects of cytolinkers, both *in vitro* and in cells, will be important to delineate their roles in cytoskeletal co-organization, mechanical synergy, and mechanotransduction. In the cell, cytoskeletal crosstalk is guided by geometrical constraints provided by the cell membrane. The membrane organizes the cytoskeleton through spatial confinement and by providing adhesion sites where cytoskeletal filaments are nucleated or anchored. Reconstitution experiments have begun to recapitulate these constraints by encapsulating cytoskeletal proteins inside cell-sized emulsion droplets or lipid vesicles, including actin/microtubule and actin/keratin composites [107, 384].

To begin bridging this gap, we performed uniaxial compression on giant unilamellar vesicles (GUVs) encapsulating an actin cortex (Figure 7.3A,B), in analogy to the cellular experiments described in Chapters 2, 3, and 4 (Figure 7.3) [1]. In GUVs which contain an actin cortex, we observe a clear rigidification of the lipid membrane, visible under the microscope as a suppression of membrane fluctuations We first performed a frequency sweep on a single GUV under uniaxial compression to probe its mechanical response across a range of timescales, allowing us to assess the viscoelastic properties imparted by the encapsulated actin network (Figure 7.3C). We found that GUVs with an actin network exhibit frequency-dependent rheology, displaying mechanical behaviour that closely resembles the power law viscoelastic response observed in single cells, as described in the preceding chapters of this thesis. When we performed a strain ramp to test the nonlinear mechanical response, we observed compression-stiffening behaviour of the GUV (Figure 7.3D), further reflecting the mechanical responses characteristic of single cells discussed in earlier chapters. This reductionist system provides a platform to isolate the mechanical contributions of actin under controlled confinement, and could be extended to composite networks to further explore cytoskeletal crosstalk in a minimal, yet increasingly complex, context.

The opposite direction to bridge the gap between live-cell and cell-free studies is to tame the complexity of living cells. Some of the same techniques that can provide more control over cell-free systems can also provide control over the behaviour of living cells. A good example is surface micropatterning to confine cells to adhesive islands with precisely controlled geometries, forcing the cells to adopt prescribed shape and corresponding cytoskeletal organisations [386]. An additional benefit of this method is that imaging many cells adhered on the same pattern greatly facilitates quantification of cytoskeletal

[1] Methods: briefly, we prepare actin encapsulated giant unilamellar vesicles (GUVs) according to the emulsion droplet interface crossing encapsulation (eDICE) method [385]. The lipid mixture (94.985% DOPC, 5% DGS-NTA(Ni), 0.01% DOPE-PEG2000, and 0.005% DOPE-Cy5 (mol/mol)) dissolved in chloroform was dried and resuspended in a 5.3:1.2 mixture of silicone oil and mineral oil. The inner aqueous solution (IAS) contained 20 mM Tris-HCl (pH 7.4), 50 mM KCl, 2 mM $MgCl_2$, 1 mM DTT, 0.5 mM MgATP, 0.5 mM PCD, 10 mM PCA, and 6.5% Optiprep. Proteins included rabbit skeletal muscle G-actin (12 μM), 10xHis-tagged VCA (6.5 μM), and 50 nM Arp2/3 complex. Emulsion droplets were formed by manual emulsification of IAS in the lipid-in-oil phase and injected into a spinning chamber pre-filled with 700 μL of 190 mM glucose outer aqueous solution (OAS). Centrifugation at 2000 rpm for 3 minutes facilitated vesicle formation. Post-formation, 233 μL of buffer (40 mM Tris-HCl, 90 mM glucose) was added to stabilize the pH, and GUVs were harvested

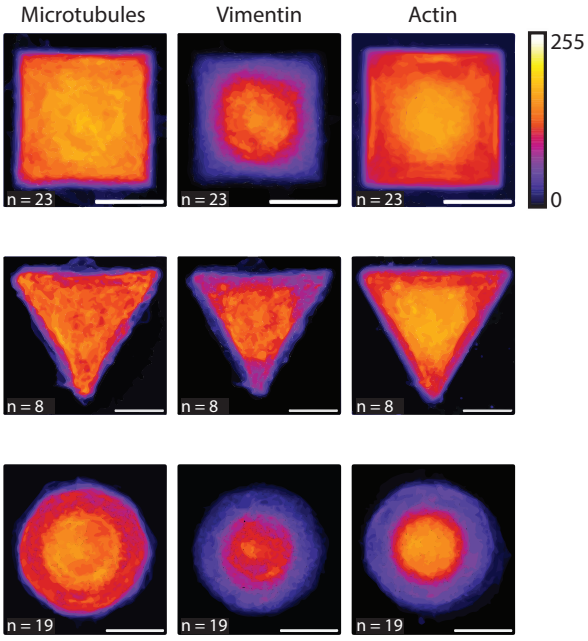

Figure 7.4: Wild-type mouse embryonic fibroblasts were confined to square, triangular, and circular fibronectin-coated micropatterns, each with an area of 900μm^2. (A) Heat maps of the fluorescence intensities of microtubules, vimentin, and actin in square patterns reveal that actin responds to the geometry of the pattern, whereas vimentin does not. Microtubules display a uniform distribution throughout the cell. Heat maps are generated from maximum intensity confocal projections, averaged over multiple cells. (B) A similar pattern is observed in triangular cells, with actin aligning to shape-specific features while vimentin remains unaffected. (C) In circular patterns, both actin and microtubules show increased perinuclear concentration compared to their distribution in square and triangular geometries. The three panels on the left display representative images of microtubules (green), vimentin (red), and the nucleus (blue) for each pattern type. Scale bars represent 15 μm. The colour scale indicates pixel intensity values in the heat maps, with n denoting the number of cells analysed. Data for square and circular patterns were collected from one experiment, while triangular data originate from a separate experiment. Confocal imaging was performed by **Dani Feldmann**.

crosstalk [387, 388]. To illustrate the power of this approach, we cultured mouse embryonic fibroblasts on fibronectin-coated patterns made by photolithography-based micropatterning and imaged the three cytoskeletal networks by confocal fluorescence microscopy (Figure 7.4) [2]. When we compared square, triangular and circular patterns, we observed that vimentin localisation responded to the global shape of their confinement whereas actin localisation was dependent on the curvature of the micropattern. On symmetric circles and squares, the spatial distribution of vimentin was similar, whereas the actin distribution differed due to the contrasting curvature of the shapes (Figure 7.4A,C). On asymmetric triangles, vimentin averted the sharp edges where actin was concentrated (Figure 7.4B). In future it will be interesing to spatially map the viscoelastic properties of the micropatterned cells to probe the mechanical crosstalk between the cytoskeletal networks, using the methods demonstrated in Chapters 4 and 6. By correlating the local viscoelastic properties obtained from AFM indentation with the spatial distribution of cytoskeletal components visualised by confocal microscopy, we can directly assess how micropattern-induced reorganisation of actin, microtubules, and vimentin contributes to the mechanical crosstalk between these networks.

A new method to bridge between cell-free and cell-based assays that we did not yet attempt is light-induced dimerisation to manipulate cytoskeletal interactions with high spatial and temporal control. Light-inducible dimers (LIDs) come from photoactivatable systems naturally occurring in plants and allow for reversible photoactivation [389]. For example, recently it was shown that microtubule-interacting proteins fused to optochemical dimerisation domains can be used to drive symmetry breaking of microtubule networks inside emulsion droplets [390]. In cells, it was shown that F-actin can be crosslinked to microtubule plus ends by transfecting cells with an iLID-tagged EB-binding SxIP peptide and SspB-tagged actin-binding domains [391]. This could be an interesting tool to systematically study the crosstalk of microtubules with actin and intermediate filaments that takes place near cell adhesions. Finally, molecular tension

[2] Methods: To prepare PLL-g-PEG coated surfaces with micropatterns, glass coverslips (Merck Sigma, 341631) were first ultrasonically cleaned in isopropanol (98%) using a bath sonicator (Emerson, Branson 2510) for 5 minutes to remove dust. Residual isopropanol was removed by sonicating the coverslips in MilliQ water for another 5 minutes. After drying with a nitrogen flow gun, the coverslips were placed on a petri dish (Sarstedt, 83.3902) covered with Parafilm M and exposed to UV-ozone treatment for 5 minutes. Meanwhile, 50 µL droplets of a solution of PLL-g-PEG (SuSoS AG, 0.1 mg/mL in 10 mM HEPES buffer, pH 7.4) were pipetted onto fresh Parafilm. Each coverslip was placed with its UV-exposed side down on a PLL-g-PEG droplet and incubated for 1 hour. Unbound PLL-g-PEG was washed offin MilliQ and the coverslips were dried with nitrogen. A chrome photomask with micropattern designs (Delta Mask BV) was cleaned in a UV ozone cleaner for 5 minutes with the dark side facing the UV source. On each grid of the photomask, 1.5 µL of MilliQ was pipetted (i.e. 1 drop per coverlsip), and the PLL-g-PEG coated side of each coverslip was placed onto these droplets. The photomask, with coverslips beneath, was then UV-ozone treated for 10 minutes, selectively removing PLL-g-PEG from transparent regions. The coverslips were transferred to a 6-well plate (FisherScientific, 40675). Inside a laminar flowhood, 100 µL of a solution of fibronectin (Merck Sigma, 0.05 mg/mL in sodium carbonate, 341631) was mixed with 2.5 µL of fluorescently labelled fibrinogen (Alexa Fluor 546, Thermo Fisher Scientific, stock: 3 mg/mL, F13192). This mixture (100 µL) was pipetted onto Parafilm and the coverslips were placed PLL-g-PEG side down on the droplets and incubated for 30 minutes at room temperature. Finally, the coverslips were washed once with sodium bicarbonate (Thermo Fisher Scientific, 5080094) and twice with PBS (Thermo Fisher Scientific, 10010023). Cells were trypsinizing and 100,000 cells, counted with a Countess cell counter (Thermo Fisher Scientific), were seeded onto the patterns and allowed to adhere overnight. Cells were fixed with 4% paraformaldehyde (Thermo Fisher Scientific, J19943.K2) the following day.

sensors provide a very interesting tool to selectively interrogate mechanical interactions between cytoskeletal networks. Tension sensors consist of two fluorescent proteins separated by a peptide with a calibrated mechanical compliance. Under strain, the fluorescent proteins are separated, decreasing fluorescence energy transfer (FRET) between them. By embedding a tension sensor in the actin crosslinker filamin A, it was recently shown that molecular tension can be measured within the actin cytoskeleton [392]. It will be interesting to use a similar approach to measure tension within the intermediate filament cytoskeleton and test force transmission between the actin and intermediate filament cytoskeleton.

7.3. THE FUTURE IS 3D

Finally, in this last section, I would like to address some of the limitations of this thesis, and how I believe these limitations point towards (part of) the future of cell mechanics research. A common criticism I have encountered is the challenge of interpreting what our findings mean for understanding cellular mechanics in biological contexts, particularly the part of this work focused on either compression or shear of suspended single cells trapped between two plates. I believe this is a very fair concern, and one that is worth careful consideration and discussion. In the reality of the human body, a cell is unlikely to encounter a completely non-adherent environment like the one we used in our uniaxial compression and shear experiments. We know from the actin literature that the organisation of the actin cytoskeleton, which is crucial for determining the mechanical behaviour of the network, is highly sensitive to the adhesion conditions of the cell [393]. Once a cell adheres to its extracellular environment, the actin network, and quite possibly the intermediate filament network as well, begins to remodel, resulting in a structure that is no longer isotropic [394, 395]. Therefore, there is no guarantee that the results presented here will apply *in vivo*, or even in conditions where the cell is adhered to a surface.

Nevertheless, we think that measuring the mechanical properties under adhesion-free conditions offers a clearer understanding of the intrinsic mechanical properties of the cytoskeletal components. Specifically, we find that even in the absence of adhesion, cells exhibit complex and distinct mechanical behaviours that are shaped by the interplay of their cytoskeletal components, offering a new perspective on how cells might respond to less conventionally studied physical environments. Our setup naturally offers the possibility to introduce controlled adhesion as a next step by coating the parallel plates with extracellular matrix proteins such as fibronectin (as used in Chapter 4 of this thesis), or with collagen or laminin, and I hope that future experimentalists will take the opportunity to explore how adhesion changes cytoskeletal mechanics.

The fact that a cell suspended between parallel plates behaves quite differently from cells adhered to a two-dimensional surface, as is typical in classical cell biology experiments, opens up a whole range of exciting scientific questions about how cellular mechanics are influenced by the physical context in which cells are studied. I am by no means the first to suggest this, as many researchers have placed cells on two-dimensional hydrogels to mimic the stiffness of the extracellular environment [396, 397],

and more recently, there has been a growing interest in studying cells within three-dimensional hydrogels, motivated from a biological perspective to better capture the complexity of *in vivo* conditions [398]. I believe that this is interesting from a physics perspective as well, because it raises fundamental questions about how forces are transmitted within cells in different geometries and boundary conditions, and how the cytoskeleton adapts to maintain structural integrity and function under such varying mechanical constraints. For example, how do entropic effects, shaped by a three-dimensional geometry and changes in cellular volume, alter the organisation of the cytoskeleton, and do they lead to changes in its mechanical behaviour? I propose that we begin to test this by varying the osmotic pressure on the cell, using our single-cell rheometer assay as described in Chapters 2 through 5. For this purpose, we can introduce PEG molecules in the extracellular medium under non-adherent conditions to induce controlled changes in cell volume [399, 400], thereby modulating macromolecular crowding. We anticipate that these volume perturbations will influence cytoskeletal bundle formation [401], which I suspect will change the mechanical response of the cells. I further propose that we also explore confining single cells in microfabricated 3D wells to precisely define the confinement geometry [402], allowing us to investigate how spatial constraints influence cellular mechanics and cytoskeletal organisation, which we could test using two-point microrheology as explored in Chapter 4.

Moreover, to liberally paraphrase the English poet John Donne, no cell is an island. Cells, including the fibroblasts studied in this thesis, rarely function in isolation but are typically embedded within multicellular systems, where mechanical interactions with neighbouring cells further complicate their mechanical responses. One approach to study such collective behaviours in a controlled setting is to use a three-dimensional collection of cells known as spheroids, which reproduce key aspects of the physical and mechanical environment found in tissues, including cell-cell interactions, force transmission, and spatial confinement [403]. In particular, it would be interesting to create spheroids in which actin–vimentin organisation can be tuned through either native plectin or our engineered ACTIF crosslinker, allowing us to probe how their coordinated crosstalk governs emergent mechanical behaviour at the multicellular scale. Our single cell rheometer could be modified to accommodate spheroids and enable direct measurements of their viscoelastic response under controlled compression and shear conditions.

7.4. ACKNOWLEDGEMENTS

We thank Marcos Arribas Perez for preparing actin-encapsulated GUVs and assisting with uniaxial compression measurements. We thank Alara Kiris and Sterre Schouten for early experiments that formed the basis for establishing the micropatterning method and to Dani Feldmann for further developing the micropatterning method and acquiring confocal images of micropatterned cells. We thank Mohammad Amin Eskandari for useful suggestions regarding micropatterning printing efficiency and labelling. We gratefully acknowledge funding from the VICI project *How cytoskeletal teamwork makes cells strong* (project number VI.C.182.004) and from the OCENW.GROOT.20t9.O22 project

The Active Matter Physics of Collective Metastasis, both financed by the Dutch Research Council (NWO).

REFERENCES

[1] Antoni Van Leeuwenhoek. Observations, communicated to the publisher by Mr. Antony van Leewenhoeck, in a dutch letter of the 9th Octob. 1676. here English'd: concerning little animals by him observed in rain-well-sea- and snow water; as also in water wherein pepper had lain infus. *Philosophical Transactions of the Royal Society of London*, 12(133):821–831, 1677.

[2] Nick Lane. The unseen world: reflections on Leeuwenhoek (1677) 'Concerning little animals'. *Philosophical Transactions of the Royal Society B: Biological Sciences*, 370(1666):20140344, 2015.

[3] Hooke Robert, Allestry James, and Martyn John. *Micrographia, or, Some physiological descriptions of minute bodies made by magnifying glasses: with observations and inquiries thereupon*. London, Printed by Jo. Martyn and Ja. Allestry, printers to the Royal Society, 1665, 1665.

[4] Frederic Català-Castro, Erik Schäffer, and Michael Krieg. Exploring cell and tissue mechanics with optical tweezers. *Journal of Cell Science*, 135(15):jcs259355, 2023.

[5] Daisuke Mizuno, Rommel Bacabac, Catherine Tardin, David Head, and Christoph F. Schmidt. High-resolution probing of cellular force transmission. *Physical Review Letters*, 102(16):1–4, 2009.

[6] Kristina Haase and Andrew E Pelling. Investigating cell mechanics with atomic force microscopy. *Journal of the Royal Society Interface*, 12(104):20140970, aug 2015.

[7] Yuejin Zhang, Fuxiang Wei, Yeh-Chuin Poh, Qiong Jia, Junjian Chen, Junwei Chen, Junyu Luo, Wenting Yao, Wenwen Zhou, Wei Huang, Fang Yang, Yao Zhang, and Ning Wang. Interfacing 3D magnetic twisting cytometry with confocal fluorescence microscopy to image force responses in living cells. *Nature Protocols*, 12(7):1437–1450, 2017.

[8] Denis Wirtz. Particle-Tracking Microrheology of Living Cells: Principles and Applications. *Annual Review of Biophysics*, 38(1):301–326, 2009.

[9] Jun Guo, Yuexiu Wang, Frederick Sachs, and Fanjie Meng. Actin stress in cell reprogramming. *Proceedings of the National Academy of Sciences of the United States of America*, 111(49):5252–5261, 2014.

[10] Nikta Fakhri, Alok D. Wessel, Charlotte Willms, Matteo Pasquali, Dieter R. Klopfenstein, Frederick C. MacKintosh, and Christoph F. Schmidt. High-resolution mapping of intracellular fluctuations using carbon nanotubes. *Science*, 344(6187):1031–1035, 2014.

[11] N Desprat, A Guiroy, and A Asnacios. Microplates-based rheometer for a single living cell. *Review of Scientific Instruments*, 77(5):55111, 2006.

[12] Pablo Fernández, Pramod A. Pullarkat, and Albrecht Ott. A master relation defines the nonlinear viscoelasticity of single fibroblasts. *Biophysical Journal*, 90(10):3796–3805, may 2006.

[13] Elisabeth Fischer-Friedrich, Yusuke Toyoda, Cedric J. Cattin, Daniel J. Müller, Anthony A. Hyman, and Frank Jülicher. Rheology of the Active Cell Cortex in Mitosis. *Biophysical Journal*, 111(3):589–600, 2016.

[14] Serge Mostowy and Pascale Cossart. Septins: the fourth component of the cytoskeleton. *Nature Reviews Molecular Cell Biology*, 13(3):183–194, 2012.

[15] Vitold E. Galkin, Albina Orlova, Matthijn R. Vos, Gunnar F. Schröder, and Edward H. Egelman. Near-Atomic Resolution for One State of F-Actin. *Structure*, 23(1), 2015.

[16] Hyeran Kang, Michael J. Bradley, Brannon R. McCullough, Anaëlle Pierre, Elena E. Grintsevich, Emil Reisler, and Enrique M. De La Cruz. Identification of cation-binding sites on actin that drive polymerization and modulate bending stiffness. *Proceedings of the National Academy of Sciences of the United States of America*, 109(42), 2012.

[17] Peter J. Carman, Kyle R. Barrie, Grzegorz Rebowski, and Roberto Dominguez. Structures of the free and capped ends of the actin filament. *Science*, 380(6651), 2023.

[18] Naoki Watanabe and Timothy J. Mitchison. Single-molecule speckle analysis of actin filament turnover in lamellipodia. *Science*, 295(5557):1083–1086, 2002.

[19] Marco Fritzsche, Alexandre Lewalle, Tom Duke, Karsten Kruse, and Guillaume Charras. Analysis of turnover dynamics of the submembranous actin cortex. *Mol. Biol. Cell*, 24(6):757, 2013.

[20] Michael Murrell, Patrick W. Oakes, Martin Lenz, and Margaret L. Gardel. Forcing cells into shape: The mechanics of actomyosin contractility. *Nature Reviews Molecular Cell Biology*, 16(8):486–498, jul 2015.

[21] Yuejin Zhang, Fuxiang Wei, Yeh-chuin Poh, Qiong Jia, Junjian Chen, Junyu Luo, Wenting Yao, Wenwen Zhou, Wei Huang, Fang Yang, Yao Zhang, and Ning Wang. HHS Public Access. 12(7):1437–1450, 2018.

[22] Katja M. Taute, Francesco Pampaloni, Erwin Frey, and Ernst Ludwig Florin. Microtubule dynamics depart from the wormlike chain model. *Physical Review Letters*, 100(2), 2008.

[23] Gary J. Brouhard. Dynamic instability 30 years later: Complexities in microtubule growth and catastrophe, 2015.

[24] Ulrike Rölleke, Pallavi Kumari, Ruth Meyer, and Sarah Köster. The unique biomechanics of intermediate filaments - From single filaments to cells and tissues. *Curr. Opin. Cell Biol.*, 85(102263):102263, 2023.

[25] Hyeran Kang, Michael J Bradley, Wenxiang Cao, Kaifeng Zhou, Elena E Grintsevich, Alphée Michelot, Charles V Sindelar, Mark Hochstrasser, and Enrique M De La Cruz. Site-specific cation release drives actin filament severing by vertebrate cofilin. *Proc. Natl. Acad. Sci. U. S. A.*, 111(50):17821–17826, 2014.

[26] Roy Beck, Joanna Deek, Myung Chul Choi, Taiji Ikawa, Osamu Watanabe, Erwin Frey, Philip Pincus, and Cyrus R. Safinya. Unconventional salt trend from soft to stiff in single neurofilament biopolymers. *Langmuir*, 26(24), 2010.

[27] Bernd Nöding and Sarah Köster. Intermediate filaments in small configuration spaces. *Phys. Rev. Lett.*, 108(8):88101, 2012.

[28] Paul Pawelzyk, Norbert Mücke, Harald Herrmann, and Norbert Willenbacher. Attractive interactions among intermediate filaments determine network mechanics in vitro. *PLoS ONE*, 9(4), 2014.

[29] Michael Schopferer, Harald Bär, Bernhard Hochstein, Sarika Sharma, Norbert Mücke, Harald Herrmann, and Norbert Willenbacher. Desmin and Vimentin Intermediate Filament Networks: Their Viscoelastic Properties Investigated by Mechanical Rheometry. *Journal of Molecular Biology*, 388(1), 2009.

[30] N. Mücke, L. Kreplak, R. Kirmse, T. Wedig, H. Herrmann, U. Aebi, and J. Langowski. Assessing the Flexibility of Intermediate Filaments by Atomic Force Microscopy. *Journal of Molecular Biology*, 335(5):1241–1250, 2004.

[31] Bernd Nöding, Harald Herrmann, and Sarah Köster. Direct observation of subunit exchange along mature vimentin intermediate filaments. *Biophys. J.*, 107(12):2923–2931, 2014.

[32] Quang D Tran, Valerio Sorichetti, Gerard Pehau-Arnaudet, Martin Lenz, and Cécile Leduc. Fragmentation and Entanglement Limit Vimentin Intermediate Filament Assembly. *Phys. Rev. X*, 13(1):11014, 2023.

[33] Amélie Robert, Molly J. Rossow, Caroline Hookway, Stephen A. Adam, and Vladimir I. Gelfand. Vimentin filament precursors exchange subunits in an ATP-dependent manner. *Proceedings of the National Academy of Sciences of the United States of America*, 112(27):E3505–E3514, 2015.

[34] Caroline Hookway, Liya Ding, Michael W. Davidson, Joshua Z. Rappoport, Gaudenz Danuser, and Vladimir I. Gelfand. Microtubule-dependent transport and dynamics of vimentin intermediate filaments. *Molecular Biology of the Cell*, 26(9), 2015.

[35] Blanca González-Bermúdez, Gustavo V. Guinea, and Gustavo R. Plaza. Advances in Micropipette Aspiration: Applications in Cell Biomechanics, Models, and Extended Studies. *Biophysical Journal*, 116(4):587–594, 2019.

[36] Jochen Guck, Revathi Ananthakrishnan, Hamid Mahmood, Tess J. Moon, C. Casey Cunningham, and Josef Käs. The optical stretcher: A novel laser tool to micromanipulate cells. *Biophysical Journal*, 81(2):767 – 784, 2001.

[37] Olivier Thoumine and Albrecht Ott. Time scale dependent viscoelastic and contractile regimes in fibroblasts probed by microplate manipulation. *Journal of Cell Science*, 110(17):2109–2116, sep 1997.

[38] Marta Urbanska, Hector E. Muñoz, Josephine Shaw Bagnall, Oliver Otto, Scott R. Manalis, Dino Di Carlo, and Jochen Guck. A comparison of microfluidic methods for high-throughput cell deformability measurements. 17(6):587–593, apr 2020.

[39] P Fernandez, L Heymann, A Ott, N Aksel, and P A Pullarkat. Shear rheology of a cell monolayer. *New J. Phys.*, 9:419, 2007.

[40] Amy A. Sutton, Clayton W. Molter, Ali Amini, Johanan Idicula, Max Furman, Pouria Tirgar, Yuanyuan Tao, Ajinkya Ghagre, Newsha Koushki, Adele Khavari, and Allen J. Ehrlicher. Cell monolayer deformation microscopy reveals mechanical fragility of cell monolayers following EMT. *Biophysical Journal*, 121(4), 2022.

[41] Khawaja Muhammad Imran Bashir, Suhyang Lee, Dong Hee Jung, Santanu Kumar Basu, Man Gi Cho, and Andreas Wierschem. Narrow-gap Rheometry: A Novel Method for Measuring Cell Mechanics, 2022.

[42] Kellie Beicker, E. Timothy O'Brien, Michael R. Falvo, and Richard Superfine. Vertical Light Sheet Enhanced Side-View Imaging for AFM Cell Mechanics Studies. *Scientific Reports*, 8(1), 2018.

[43] Katarzyna Pogoda, Fitzroy Byfield, Piotr Deptuła, Mateusz Cieśluk, Łukasz Suprewicz, Karol Skłodowski, Jordan L. Shivers, Anne Van Oosten, Katrina Cruz, Ekaterina Tarasovetc, Ekaterina L. Grishchuk, Fred C. MacKintosh, Robert Bucki, Alison E. Patteson, and Paul A. Janmey. Unique Role of Vimentin Networks in Compression Stiffening of Cells and Protection of Nuclei from Compressive Stress. *Nano Letters*, 22(12):4725–4732, jun 2022.

[44] B Fabry, G N Maksym, J P Butler, M Glogauer, D Navajas, and J J Fredberg. Scaling the microrheology of living cells. *Phys. Rev. Lett.*, 87(14):148102, 2001.

[45] Sajedeh Kerdegari, Paolo Canepa, Davide Odino, Reinier Oropesa-Nuñez, Annalisa Relini, Ornella Cavalleri, and Claudio Canale. Insights in Cell Biomechanics through Atomic Force Microscopy, 2023.

[46] Frederic Català-Castro, Erik Schäffer, and Michael Krieg. Exploring cell and tissue mechanics with optical tweezers. *J. Cell Sci.*, 135(15):259–355, 2022.

[47] Andreas R. Bausch, Florian Ziemann, Alexei A. Boulbitch, Ken Jacobson, and Erich Sackmann. Local measurements of viscoelastic parameters of adherent cell surfaces by magnetic bead microrheometry. *Biophysical Journal*, 75(4), 1998.

[48] A. W.C. Lau, B. D. Hoffman, A. Davies, J. C. Crocker, and T. C. Lubensky. Microrheology, stress fluctuations, and active behavior of living cells. *Physical Review Letters*, 91(19), 2003.

[49] Franziska Lautenschläger, Stephan Paschke, Stefan Schinkinger, Arlette Bruel, Michael Beil, and Jochen Guck. The regulatory role of cell mechanics for migration of differentiating myeloid cells. *Proceedings of the National Academy of Sciences of the United States of America*, 106(37), 2009.

[50] C Rotsch and M Radmacher. Drug-induced changes of cytoskeletal structure and mechanics in fibroblasts: an atomic force microscopy study. *Biophys. J.*, 78(1):520–535, 2000.

[51] Jan Christian Martens and Manfred Radmacher. Softening of the actin cytoskeleton by inhibition of myosin II. *Pflugers Archiv European Journal of Physiology*, 456(1), 2008.

[52] Elisabeth Fischer-Friedrich, Yusuke Toyoda, Cedric J Cattin, Daniel J Müller, Anthony A Hyman, and Frank Jülicher. Rheology of the active cell cortex in mitosis. *Biophys. J.*, 111(3):589–600, 2016.

[53] Ming Guo, Allen J. Ehrlicher, Saleemulla Mahammad, Hilary Fabich, Mikkel H. Jensen, Jeffrey R. Moore, Jeffrey J. Fredberg, Robert D. Goldman, and David A. Weitz. The role of vimentin intermediate filaments in cortical and cytoplasmic mechanics. *Biophysical Journal*, 105(7):1562–1568, oct 2013.

[54] Martin J. Brown, John A. Hallam, Emma Colucci-Guyon, and Stephen Shaw. Rigidity of Circulating Lymphocytes Is Primarily Conferred by Vimentin Intermediate Filaments. *The Journal of Immunology*, 166(11), 2001.

[55] Kristin Seltmann, Anatol W Fritsch, Josef A Käs, and Thomas M Magin. Keratins significantly contribute to cell stiffness and impact invasive behavior. *Proc. Natl. Acad. Sci. U. S. A.*, 110(46):18507–18512, 2013.

[56] Alison E Patteson, Katarzyna Pogoda, Fitzroy J Byfield, Kalpana Mandal, Zofia Ostrowska-Podhorodecka, Elisabeth E Charrier, Peter A Galie, Piotr Deptuła, Robert Bucki, Christopher A McCulloch, and Paul A Janmey. Loss of vimentin enhances cell motility through small confining spaces. *Small.*, 15(50):e1903180, 2019.

[57] Sandrine B. Lavenus, Sara M. Tudor, Maria F. Ullo, Karl W. Vosatka, Jeremy S. Logue, Enrique M De, and La Cruz. A flexible network of vimentin intermediate filaments promotes migration of amoeboid cancer cells through confined environments. *Journal of Biological Chemistry*, 295(19):6700–6709, may 2020.

[58] Ning Wang. Mechanical interactions among cytoskeletal filaments. In *Hypertension*, volume 32, 1998.

[59] Yuhui Li, Ondřej Kučera, Damien Cuvelier, David M. Rutkowski, Mathieu Deygas, Dipti Rai, Tonja Pavlovič, Filipe Nunes Vicente, Matthieu Piel, Grégory Giannone, Dimitrios Vavylonis, Anna Akhmanova, Laurent Blanchoin, Manuel Théry, Filipe Nunes Vicente, Matthieu Piel, Grégory Giannone, Dimitrios Vavylonis, Anna Akhmanova, Laurent Blanchoin, and Manuel Théry. Compressive forces stabilize microtubules in living cells. 22(7):913–924, 2023.

[60] Benjamin P. Bouchet, Rosemarie E. Gough, York Christoph Ammon, Dieudonnée van de Willige, Harm Post, Guillaume Jacquemet, A. F. Maarten Altelaar, Albert J.R. Heck, Benjamin T. Goult, and Anna Akhmanova. Talin-KANK1 interaction controls the recruitment of cortical microtubule stabilizing complexes to focal adhesions. *eLife*, 5(JULY), 2016.

[61] Jan Maarten Van Doorn, Luuk Lageschaar, Joris Sprakel, and Jasper Van Der Gucht. Criticality and mechanical enhancement in composite fiber networks. *Physical Review E*, 95(4):042503, 2017.

[62] Sihan Chen, Tomer Markovich, and Fred C. Mackintosh. Nonaffine Deformation of Semiflexible Polymer and Fiber Networks. *Physical Review Letters*, 130(8), 2023.

[63] Yuan-Chen Chang, Perihan Nalbant, Jörg Birkenfeld, Zee-Fen Chang, and Gary M Bokoch. {GEF-H1} couples nocodazole-induced microtubule disassembly to cell contractility via {RhoA}. *Mol. Biol. Cell*, 19(5):2147–2153, 2008.

[64] Ernest Latorre, Sohan Kale, Laura Casares, Manuel Gómez-González, Marina Uroz, Léo Valon, Roshna V. Nair, Elena Garreta, Nuria Montserrat, Aránzazu del Campo, Benoit Ladoux, Marino Arroyo, and Xavier Trepat. Active superelasticity in three-dimensional epithelia of controlled shape. *Nature*, 563(7730), 2018.

[65] Magdalena Prechova, Zuzana Adamova, Anna Lena Schweizer, Miloslava Maninova, Andreas Bauer, Delf Kah, Samuel M Meier-Menches, Gerhard Wiche, Ben Fabry, and Martin Gregor. Plectin-mediated cytoskeletal crosstalk controls cell tension and cohesion in epithelial sheets. *Journal of Cell Biology*, 221(3):e202105146, 2022.

[66] Moumita Das and F. C. MacKintosh. Poisson's ratio in composite elastic media with rigid rods. *Physical Review Letters*, 105(13), 2010.

[67] Marileen Dogterom and Bernard Yurke. Measurement of the force-velocity relation for growing microtubules. *Science*, 278(5339), 1997.

[68] Clifford P. Brangwynne, Frederick C. MacKintosh, Sanjay Kumar, Nicholas A. Geisse, Jennifer Talbot, L. Mahadevan, Kevin K. Parker, Donald E. Ingber, and David A. Weitz. Microtubules can bear enhanced compressive loads in living cells because of lateral reinforcement. *Journal of Cell Biology*, 173(5):733–741, 2006.

[69] Patrick Robison, Matthew A. Caporizzo, Hossein Ahmadzadeh, Alexey I. Bogush, Christina Yingxian Chen, Kenneth B. Margulies, Vivek B. Shenoy, and Benjamin L. Prosser. Detyrosinated microtubules buckle and bear load in contracting cardiomyocytes. *Science*, 352(6284), 2016.

[70] Ning Wang, Keiji Naruse, Dimitrije Stamenović, Jeffrey J. Fredberg, Srboljub M. Mijailovich, Iva Marija Tolić-Nørrelykke, Thomas Polte, Robert Mannix, and Donald E. Ingber. Mechanical behavior in living cells consistent with the tensegrity model. *Proceedings of the National Academy of Sciences of the United States of America*, 98(14), 2001.

[71] Pei-Hsun Wu, Dikla Raz-Ben Aroush, Atef Asnacios, Wei-Chiang Chen, Maxim E Dokukin, Bryant L Doss, Pauline Durand-Smet, Andrew Ekpenyong, Jochen Guck, Nataliia V Guz, Paul A Janmey, Jerry S H Lee, Nicole M Moore, Albrecht Ott, Yeh-Chuin Poh, Robert Ros, Mathias Sander, Igor Sokolov, Jack R Staunton, Ning Wang, Graeme Whyte, and Denis Wirtz. A comparison of methods to assess cell mechanical properties. *Nature Methods*, 15(7):491–498, 2018.

[72] Johanna Block, Hannes Witt, Andrea Candelli, Jordi Cabanas Danes, Erwin J G Peterman, Gijs J L Wuite, Andreas Janshoff, and Sarah Köster. Viscoelastic properties of vimentin originate from nonequilibrium conformational changes. *Sci. Adv.*, 4(6):aat1161, 2018.

[73] Joost Van Mameren, Karen C. Vermeulen, Fred Gittes, and Christoph F. Schmidt. Leveraging single protein polymers to measure flexural rigidity. 113(12):3837–3844, mar 2009.

[74] Ryohei Yasuda, Hidetake Miyata, and Kazuhiko Kinosita. Direct measurement of the torsional rigidity of single actin filaments. *Journal of Molecular Biology*, 263(2), 1996.

[75] Jeffrey P. Bibeau, Nandan G. Pandit, Shawn Gray, Nooshin Shatery Nejad, Charles V. Sindelar, Wenxiang Cao, and Enrique M. De La Cruz. Twist response of actin filaments. *Proceedings of the National Academy of Sciences of the United States of America*, 120(4), 2023.

[76] L. Kreplak, H. Bär, J. F. Leterrier, H. Herrmann, and U. Aebi. Exploring the mechanical behavior of single intermediate filaments. *Journal of molecular biology*, 354(3):569–577, dec 2005.

[77] A. Kis, S. Kasas, B. Babić, A. J. Kulik, W. Benoît, G. A.D. Briggs, C. Schönenberger, S. Catsicas, and L. Forró. Nanomechanics of Microtubules. *Physical Review Letters*, 89(24), 2002.

[78] Laura Schaedel, Karin John, Jeremie Gaillard, Maxence V. Nachury, Laurent Blanchoin, and Manuel Thery. Microtubules self-repair in response to mechanical stress. *Nature Materials*, 14(11), 2015.

[79] Yuri Tsuda, Hironori Yasutake, Akihiko Ishuima, and Toshio Yanaogida. Torsional rigidity of single actin filaments and actin-actin bond breaking force under torsion measured directly by in vitro micromanipulation. *Proceedings of the National Academy of Sciences of the United States of America*, 93(23), 1996.

[80] Sharyn A. Endow and Piotr E. Marszalek. An estimate to the first approximation of microtubule rupture force. *European Biophysics Journal*, 48(6), 2019.

[81] Charlotta Lorenz, Johanna Forsting, Robert W. Style, Stefan Klumpp, and Sarah Köster. Keratin filament mechanics and energy dissipation are determined by metal-like plasticity. *Matter*, 6(6), 2023.

[82] Filipe Nunes Vicente, Mickael Lelek, Jean-Yves Tinevez, Quang D Tran, Gerard Pehau-Arnaudet, Christophe Zimmer, Sandrine Etienne-Manneville, Gregory Giannone, and Cécile Leduc. Molecular organization and mechanics of single vimentin filaments revealed by super-resolution imaging. *Sci. Adv.*, 8(8):eabm2696, 2022.

[83] Margaret L. Gardel, Karen E. Kasza, Clifford P. Brangwynne, Jiayu Liu, and David A. Weitz. Chapter 19 Mechanical Response of Cytoskeletal Networks, 2008.

[84] Daphne Weihs, Thomas G. Mason, and Michael A. Teitell. Bio-microrheology: A frontier in microrheology. *Biophysical Journal*, 91(11), 2006.

[85] Yali Yang, Mo Bai, William S. Klug, Alex J. Levine, and Megan T. Valentine. Microrheology of highly crosslinked microtubule networks is dominated by force-induced crosslinker unbinding. *Soft Matter*, 9(2), 2013.

[86] Yi Chia Lin, Gijsje H. Koenderink, Frederick C. MacKintosh, and David A. Weitz. Viscoelastic properties of microtubule networks. *Macromolecules*, 40(21):7714–7720, oct 2007.

[87] Yali Yang, Jun Lin, Bugra Kaytanli, Omar A. Saleh, and Megan T. Valentine. Direct correlation between creep compliance and deformation in entangled and sparsely crosslinked microtubule networks. *Soft Matter*, 8(6):1776–1784, jan 2012.

[88] Inka Kirchenbuechler, Donald Guu, Nicholas A. Kurniawan, Gijsje H. Koenderink, and M. Paul Lettinga. Direct visualization of flow-induced conformational transitions of single actin filaments in entangled solutions. *Nature Communications*, 5, 2014.

[89] M. L. Gardel, J. H. Shin, F. C. MacKintosh, L. Mahadevan, P. Matsudaira, and D. A. Weitz. Elastic behavior of cross-linked and bundled actin networks. *Science*, 304(5675):1301–1305, 2004.

[90] F. C. MacKintosh, J. Käs, and P. A. Janmey. Elasticity of semiflexible biopolymer networks. *Physical Review Letters*, 75(24):4425, 1995.

[91] K E Kasza, C P Broedersz, G H Koenderink, Y C Lin, W Messner, E A Millman, F Nakamura, T P Stossel, F C MacKintosh, and D A Weitz. Actin filament length tunes elasticity of flexibly cross-linked actin networks. *Biophys. J.*, 99(4):1091–1100, 2010.

[92] Chase P. Broedersz, Karen E. Kasza, Louise M. Jawerth, Stefan Münster, David A. Weitz, and Frederick C. MacKintosh. Measurement of nonlinear rheology of cross-linked biopolymer gels. *Soft Matter*, 6(17):4120–4127, aug 2010.

[93] Jan Wilhelm and Erwin Frey. Elasticity of stiff polymer networks. *Phys. Rev. Lett.*, 91(10):108103, 2003.

[94] David A. Head, Alex J. Levine, and F. C. MacKintosh. Deformation of Cross-Linked Semiflexible Polymer Networks. *Physical Review Letters*, 91(10), 2003.

[95] Ovijit Chaudhuri, Sapun H. Parekh, and Daniel A. Fletcher. Reversible stress softening of actin networks. *Nature*, 445(7125), 2007.

[96] Yi Chia Lin, Norman Y Yao, Chase P Broedersz, Harald Herrmann, Fred C MacKintosh, and David A Weitz. Origins of elasticity in intermediate filament networks. *Phys. Rev. Lett.*, 104(5):58101, 2010.

[97] Norman Y Yao, Chase P Braedersz, Yi Chia Lin, Karen E Kasza, Frederick C MacKintosh, and David A Weitz. Elasticity in lonically cross-linked neurofilament networks. *Biophys. J.*, 98(10):2147–2153, 2010.

[98] Yi Chia Lin, Chase P Broedersz, Amy C Rowat, Tatjana Wedig, Harald Herrmann, Frederick C MacKintosh, and David A Weitz. Divalent cations crosslink vimentin intermediate filament tail domains to regulate network mechanics. *J. Mol. Bio*, 399(4):637–644, 2010.

[99] Anders Aufderhorst-Roberts and Gijsje H. Koenderink. Stiffening and inelastic fluidization in vimentin intermediate filament networks. *Soft Matter*, 15(36):7127–7136, 2019.

[100] Harald Bär, Michael Schopferer, Sarika Sharma, Bernhard Hochstein, Norbert Mücke, Harald Herrmann, and Norbert Willenbacher. Mutations in desmin's carboxy-terminal "tail" domain severely modify filament and network mechanics. *Journal of Molecular Biology*, 397(5), 2010.

[101] Huayin Wu, Yinan Shen, Dianzhuo Wang, Harald Herrmann, Robert D. Goldman, David A. Weitz, and John A Paulson. Effect of Divalent Cations on the Structure and Mechanics of Vimentin Intermediate Filaments. *Biophysical Journal*, 119(1):55, jul 2020.

[102] Kimie Fukuyama, Takashi Murozuka, Russell Caldwell, and William L Epstein. Divalent cation stimulation of in vitro fibre assembly from epidermal keratin protein. *J. Cell Sci*, 33:255–263, 1978.

[103] Anna V Schepers, Charlotta Lorenz, Peter Nietmann, Andreas Janshoff, Stefan Klumpp, and Sarah Köster. Multiscale mechanics and temporal evolution of vimentin intermediate filament networks. *Proc. Natl. Acad. Sci. U. S. A.*, 118(27):2102026118, 2021.

[104] Oliver I Wagner, Sebastian Rammensee, Neha Korde, Qi Wen, Jean Francois Leterrier, and Paul A Janmey. Softness, strength and self-repair in intermediate filament networks. *Exp. Cell Res.*, 313(10):2228, 2007.

[105] Manuela Denz, Manuel Marschall, Harald Herrmann, and Sarah Köster. Ion type and valency differentially drive vimentin tetramers into intermediate filaments or higher order assemblies. *Soft Matter*, 17(4), 2021.

[106] Tom Golde, Constantin Huster, Martin Glaser, Tina Händler, Harald Herrmann, Josef A Käs, and Jörg Schnauß. Glassy dynamics in composite biopolymer networks. *Soft Matter.*, 14(39):7970–7978, 2018.

[107] J. Deek, R. Maan, E. Loiseau, and A. R. Bausch. Reconstitution of composite actin and keratin networks in vesicles. *Soft Matter*, 14(10), 2018.

[108] Iman Elbalasy, Paul Mollenkopf, Cary Tutmarc, Harald Herrmann, and Jörg Schnauß. Keratins determine network stress responsiveness in reconstituted actin-keratin filament systems. *Soft Matter*, 17(14), 2021.

[109] Vincent Pelletier, Naama Gal, Paul Fournier, and Maria L. Kilfoil. Microrheology of microtubule solutions and actin-microtubule composite networks. *Physical Review Letters*, 102(18), 2009.

[110] I K Piechocka. Biopolymers: from structural hierarchy to nonlinear rheology. 2011.

[111] Osigwe Esue, Ashley A Carson, Yiider Tseng, and Denis Wirtz. A direct interaction between actin and vimentin filaments mediated by the tail domain of vimentin. *J. Biol. Chem.*, 281(41):30393–30399, 2006.

[112] Laura Schaedel, Charlotta Lorenz, Anna V Schepers, Stefan Klumpp, and Sarah Köster. Vimentin intermediate filaments stabilize dynamic microtubules by direct interactions. *Nat. Commun.*, 12(1):1–12, 2021.

[113] Mikkel H. Jensen, Eliza J. Morris, Robert D. Goldman, and David A. Weitz. Emergent properties of composite semiflexible biopolymer networks. *Bioarchitecture*, 4(4-5), 2014.

[114] Yi Chia Lin, Gijsje H. Koenderink, Frederick C. MacKintosh, and David A. Weitz. Control of non-linear elasticity in F-actin networks with microtubules. *Soft Matter*, 7(3), 2011.

[115] Shea N. Ricketts, Jennifer L. Ross, and Rae M. Robertson-Anderson. Co-Entangled Actin-Microtubule Composites Exhibit Tunable Stiffness and Power-Law Stress Relaxation. *Biophysical Journal*, 115(6), 2018.

[116] Shea N. Ricketts, Madison L. Francis, Leila Farhadi, Michael J. Rust, Moumita Das, Jennifer L. Ross, and Rae M. Robertson-Anderson. Varying crosslinking motifs drive the mesoscale mechanics of actin-microtubule composites. *Scientific Reports*, 9(1), 2019.

[117] Yinan Shen, Huayin Wu, Peter J. Lu, Dianzhuo Wang, Marjan Shayegan, Hui Li, Weichao Shi, Zizhao Wang, Li Heng Cai, Jing Xia, Meng Zhang, Ruihua Ding, Harald Herrmann, Robert Goldman, Fred C. Mackintosh, Arturo Moncho-Jordá, and David A. Weitz. Effects of Vimentin Intermediate Filaments on the Structure and Dynamics of in Vitro Multicomponent Interpenetrating Cytoskeletal Networks. *Physical Review Letters*, 127(10), sep 2021.

[118] Huayin Wu, Yinan Shen, Suganya Sivagurunathan, Miriam Sarah Weber, Stephen A Adam, Jennifer H Shin, Jeffrey J Fredberg, Ohad Medalia, Robert Goldman, David A Weitz, and Jennifer Lippincott-Schwartz. Vimentin intermediate filaments and filamentous actin form unexpected interpenetrating networks that redefine the cell cortex.

[119] Magdalena Preciado López, Florian Huber, Ilya Grigoriev, Michel O Steinmetz, Anna Akhmanova, Gijsje H Koenderink, and Marileen Dogterom. Actin-microtubule coordination at growing microtubule ends. *Nat. Commun.*, 5(1):4778, 2014.

[120] Irene Istúriz Petitjean, Quang D. Tran, Angeliki Goutou, Zima Kabir, Gerhard Wiche, Cécile Leduc, and Gijsje H. Koenderink. Reconstitution of cytolinker-mediated crosstalk between actin and vimentin. *European Journal of Cell Biology*, 103(2):151403, 2024.

[121] Shuvasree SenGupta, Carole A. Parent, and James E. Bear. The principles of directed cell migration, 2021.

[122] Ryan J. Petrie and Kenneth M. Yamada. Multiple mechanisms of 3D migration: The origins of plasticity, 2016.

[123] Sean P. Palecek, Anna Huttenlocher, Alan F. Horwitz, and Douglas A. Lauffenburger. Physical and biochemical regulation of integrin release during rear detachment of migrating cells. *Journal of Cell Science*, 111(7), 1998.

[124] Robert W. Style, Rostislav Boltyanskiy, Guy K. German, Callen Hyland, Christopher W. Macminn, Aaron F. Mertz, Larry A. Wilen, Ye Xu, and Eric R. Dufresne. Traction force microscopy in physics and biology. *Soft Matter*, 10(23):4047–4055, 2014.

[125] Ryan J. Petrie, Hyun Koo, and Kenneth M. Yamada. Generation of compartmentalized pressure by a nuclear piston governs cell motility in a 3D matrix. *Science*, 345(6200):1062–1065, aug 2014.

[126] Ewa K. Paluch and Erez Raz. The role and regulation of blebs in cell migration, 2013.

[127] Ching Yi Liu, Hsi Hui Lin, Ming Jer Tang, and Yang Kao Wang. Vimentin contributes to epithelial-mesenchymal transition cancer cell mechanics by mediating cytoskeletal organization and focal adhesion maturation. *Oncotarget*, 6(18):15966, 2015.

[128] Kimberly M. Stroka, Hongyuan Jiang, Shih Hsun Chen, Ziqiu Tong, Denis Wirtz, Sean X. Sun, and Konstantinos Konstantopoulos. Water permeation drives tumor cell migration in confined microenvironments. *Cell*, 157(3), 2014.

[129] Mira Krendel, Frank T. Zenke, and Gary M. Bokoch. Nucleotide exchange factor GEF-H1 mediates cross-talk between microtubules and the actin cytoskeleton. *Nature Cell Biology*, 4(4), 2002.

[130] Andrew Rape, Wei Hui Guo, and Yu Li Wang. Microtubule depolymerization induces traction force increase through two distinct pathways. *Journal of Cell Science*, 124(24):4233–4240, dec 2011.

[131] Mihai L Azoitei, Jungsik Noh, Daniel J Marston, Philippe Roudot, Christopher B Marshall, Timothy A Daugird, Sidney L Lisanza, Mar\'\ia-José Sand\'\i, Mitsu Ikura, John Sondek, Robert Rottapel, Klaus M Hahn, and Gaudenz Danuser. Spatiotemporal dynamics of {GEF-H1} activation controlled by microtubule- and Src-mediated pathways. *J. Cell Biol.*, 218(9):3077–3097, 2019.

[132] Jessica N. Heck, Suzanne M. Ponik, Maria G. Garcia-Mendoza, Carolyn A. Pehlke, David R. Inman, Kevin W. Eliceiri, and Patricia J. Keely. Microtubules regulate GEF-H1 in response to extracellular matrix stiffness. *Molecular Biology of the Cell*, 23(13), 2012.

[133] Aglaja Kopf, Jörg Renkawitz, Robert Hauschild, Irute Girkontaite, Kerry Tedford, Jack Merrin, Oliver Thorn-Seshold, Dirk Trauner, Hans Häcker, Klaus Dieter Fischer, Eva Kiermaier, and Michael Sixt. Microtubules control cellular shape and coherence in amoeboid migrating cells. *Journal of Cell Biology*, 219(6), 2020.

[134] Yaming Jiu, Johan Peränen, Niccole Schaible, Fang Cheng, John E Eriksson, Ramaswamy Krishnan, and Pekka Lappalainen. Vimentin intermediate filaments control actin stress fiber assembly through GEF-H1 and RhoA. *Journal of Cell Science*, 130(5):892–902, 2017.

[135] Zhuo Gan, Liya Ding, Christoph J. Burckhardt, Jason Lowery, Assaf Zaritsky, Karlyndsay Sitterley, Andressa Mota, Nancy Costigliola, Colby G. Starker, Daniel F. Voytas, Jessica Tytell, Robert D. Goldman, and Gaudenz Danuser. Vimentin Intermediate Filaments Template Microtubule Networks to Enhance Persistence in Cell Polarity and Directed Migration. *Cell Systems*, 3(3):252–263.e8, sep 2016.

[136] Shailaja Seetharaman, Benoit Vianay, Vanessa Roca, Aaron J Farrugia, Chiara De Pascalis, Batiste Boëda, Florent Dingli, Damarys Loew, Stéphane Vassilopoulos, Alexander Bershadsky, Manuel Théry, and Sandrine Etienne-Manneville. Microtubules tune mechanosensitive cell responses. *Nat. Mat.*, 21(3):366–377, 2022.

[137] Yaming Jiu, Jaakko Lehtimäki, Sari Tojkander, Fang Cheng, Harri Jäälinoja, Xiaonan Liu, Markku Varjosalo, John E. Eriksson, and Pekka Lappalainen. Bidirectional Interplay between Vimentin Intermediate Filaments and Contractile Actin Stress Fibers. *Cell Reports*, 11(10):1511–1518, jun 2015.

[138] Pragati C Marks, Breanne R Hewitt, Michelle A Baird, Gerhard Wiche, and Ryan J Petrie. Plectin linkages are mechanosensitive and required for the nuclear piston mechanism of three-dimensional cell migration. *Molecular Biology of the Cell*, 33(12):E21–08–0414, aug 2022.

[139] Csaba Daday, Katra Kolšek, and Frauke Gräter. The mechano-sensing role of the unique SH3 insertion in plakin domains revealed by Molecular Dynamics simulations. *Sci. Rep.*, 7(1):11669, 2017.

[140] Michael Murrell, Patrick W Oakes, Martin Lenz, and Margaret L Gardel. Forcing cells into shape: the mechanics of actomyosin contractility. *Nat. Rev. Mol. Cell Biol.*, 16(8):486–498, 2015.

[141] Michael P. Murrell and Margaret L. Gardel. F-actin buckling coordinates contractility and severing in a biomimetic actomyosin cortex. *Proceedings of the National Academy of Sciences of the United States of America*, 109(51), 2012.

[142] Viktoria Wollrab, Julio M Belmonte, Lucia Baldauf, Maria Leptin, François Nédeléc, and Gijsje H Koenderink. Polarity sorting drives remodeling of actin-myosin networks. *J. Cell Sci.*, 132(4):jcs219717, 2018.

[143] José Alvarado, Michael Sheinman, Abhinav Sharma, Fred C. MacKintosh, and Gijsje H. Koenderink. Force percolation of contractile active gels. *Soft Matter*, 13(34):5624–5644, aug 2017.

[144] Poul M. Bendix, Gijsje H. Koenderink, Damien Cuvelier, Zvonimir Dogic, Bernard N. Koeleman, William M. Brieher, Christine M. Field, L. Mahadevan, and David A. Weitz. A quantitative analysis of contractility in active cytoskeletal protein networks. *Biophysical Journal*, 94(8), 2008.

[145] Kevin Carvalho, Feng C. Tsai, Edouard Lees, Raphaël Voituriez, Gijsje H. Koenderink, and Cecile Sykes. Cell-sized liposomes reveal how actomyosin cortical tension drives shape change. *Proceedings of the National Academy of Sciences of the United States of America*, 110(41):16456–16461, oct 2013.

[146] Etienne Loiseau, Jochen A.M. Schneider, Felix C. Keber, Carina Pelzl, Gladys Massiera, Guillaume Salbreux, and Andreas R. Bausch. Shape remodeling and blebbing of active cytoskeletal vesicles. *Science Advances*, 2(4), 2016.

[147] William M. McFadden, Patrick M. McCall, Margaret L. Gardel, and Edwin M. Munro. Filament turnover tunes both force generation and dissipation to control long-range flows in a model actomyosin cortex. *PLoS Computational Biology*, 13(12), 2017.

[148] Sven K. Vogel, Christian Wölfer, Diego A. Ramirez-Diaz, Robert J. Flassig, Kai Sundmacher, and Petra Schwille. Symmetry Breaking and Emergence of Directional Flows in Minimal Actomyosin Cortices. *Cells*, 9(6), 2020.

[149] Sonal, Kristina A. Ganzinger, Sven K. Vogel, Jonas Mücksch, Philipp Blumhardt, and Petra Schwille. Myosin-II activity generates a dynamic steady state with continuous actin turnover in a minimal actin cortex. *Journal of Cell Science*, 132(4), feb 2019.

[150] Tzer Han Tan, Maya Malik-Garbi, Enas Abu-Shah, Junang Li, Abhinav Sharma, Fred C MacKintosh, Kinneret Keren, Christoph F Schmidt, and Nikta Fakhri. Self-organized stress patterns drive state transitions in actin cortices. *Science Advances*, 4(6):eaar2847, 2018.

[151] Mathieu Pinot, Villier Steiner, Benoit Dehapiot, Byung Kuk Yoo, Franck Chesnel, Laurent Blanchoin, Charles Kervrann, and Zoher Gueroui. Confinement induces actin flow in a meiotic cytoplasm. *Proceedings of the National Academy of Sciences of the United States of America*, 109(29), 2012.

[152] Maya Malik-Garbi, Niv Ierushalmi, Silvia Jansen, Enas Abu-Shah, Bruce L. Goode, Alex Mogilner, and Kinneret Keren. Scaling behaviour in steady-state contracting actomyosin networks. *Nature Physics*, 15(5), 2019.

[153] Ryota Sakamoto, Ziane Izri, Yuta Shimamoto, Makito Miyazaki, and Yusuke T. Maeda. Geometric trade-off between contractile force and viscous drag determines the actomyosin-based motility of a cell-sized droplet. *Proceedings of the National Academy of Sciences of the United States of America*, 119(30), 2022.

[154] Gloria Lee, Gregor Leech, Michael J Rust, Moumita Das, Ryan J Mcgorty, Jennifer L Ross, and Rae M Robertson-Anderson. Myosin-driven actin-microtubule networks exhibit self-organized contractile dynamics. Technical report, 2021.

[155] Alison E. Patteson, Merrill E. Asp, and Paul A. Janmey. Materials science and mechanosensitivity of living matter. *Applied Physics Reviews*, 9(1):011320, 2022.

[156] James P. Conboy, Irene Istúriz Petitjean, Anouk van der Net, and Gijsje H. Koenderink. How cytoskeletal crosstalk makes cells move: Bridging cell-free and cell studies. *Biophysics Reviews*, 5(2):021307, 2024.

[157] Yohalie Kalukula, Andrew D. Stephens, Jan Lammerding, and Sylvain Gabriele. Mechanics and functional consequences of nuclear deformations. *Nature Reviews Molecular Cell Biology*, 23(9):583–602, 2022.

[158] Daniel A. Fletcher and R. Dyche Mullins. Cell mechanics and the cytoskeleton. *Nature*, 463(7280):485–492, 2010.

[159] Timothée Vignaud, Calina Copos, Christophe Leterrier, Mauricio Toro-Nahuelpan, Qingzong Tseng, Julia Mahamid, Laurent Blanchoin, Alex Mogilner, Manuel Théry, and Laetitia Kurzawa. Stress fibres are embedded in a contractile cortical network. *Nature Materials*, 20(3):410–420, 2021.

[160] Sandrine Etienne-Manneville. Cytoplasmic Intermediate Filaments in Cell Biology. *Annual Review of Cell and Developmental Biology*, 34:1–28, 2018.

[161] Alison E Patteson, Robert J Carroll, Daniel V Iwamoto, and Paul A Janmey. The vimentin cytoskeleton: when polymer physics meets cell biology. *Physical Biology*, 18(1):11001, nov 2020.

[162] P. A. Janmey, U. Euteneuer, P. Traub, and M. Schliwa. Viscoelastic properties of vimentin compared with other filamentous biopolymer networks. *The Journal of Cell Biology*, 113(1):155, apr 1991.

[163] Ariana D. Sanchez and Jessica L. Feldman. Microtubule-organizing centers: from the centrosome to non-centrosomal sites. *Current Opinion in Cell Biology*, 44:93–101, 2017.

[164] Alicia Calzado-Martín, Mario Encinar, Javier Tamayo, Montserrat Calleja, and Alvaro San Paulo. Effect of Actin Organization on the Stiffness of Living Breast Cancer Cells Revealed by Peak-Force Modulation Atomic Force Microscopy. *ACS Nano*, 10(3):3365–3374, 2016.

[165] Ben Fabry, Geoffrey N. Maksym, James P. Butler, Michael Glogauer, Daniel Navajas, Nathan A. Taback, Emil J. Millet, and Jeffrey J. Fredberg. Time scale and other invariants of integrative mechanical behavior in living cells. *Physical Review E - Statistical Physics, Plasmas, Fluids, and Related Interdisciplinary Topics*, 68(4):1–18, 2003.

[166] Katarzyna Pogoda, Fitzroy Byfield, Piotr Deptuła, Mateusz Cieśluk, Łukasz Suprewicz, Karol Skłodowski, Jordan L. Shivers, Anne Van Oosten, Katrina Cruz, Ekaterina Tarasovetc, Ekaterina L. Grishchuk, Fred C. MacKintosh, Robert Bucki, Alison E. Patteson, and Paul A. Janmey. Unique Role of Vimentin Networks in Compression Stiffening of Cells and Protection of Nuclei from Compressive Stress. *Nano Letters*, 22(12):4725–4732, 2022.

[167] Yi Chia Lin, Chase P. Broedersz, Amy C. Rowat, Tatjana Wedig, Harald Herrmann, Frederick C. MacKintosh, and David A. Weitz. Divalent cations crosslink vimentin intermediate filament tail domains to regulate network mechanics. *Journal of molecular biology*, 399(4):637–644, 2010.

[168] Yara Abidine, Valérie M. Laurent, Richard Michel, Alain Duperray, Liviu Iulian Palade, and Claude Verdier. Physical properties of polyacrylamide gels probed by AFM and rheology. *Epl*, 109(3):38003, 2015.

[169] Philip Kollmannsberger and Ben Fabry. Linear and Nonlinear Rheology of Living Cells. *Annual Review of Materials Research*, 41(Volume 41, 2011):75–97, 2011.

[170] Manfred Schliwa. Action of Cytochalasin D on Cytoskeletal Networks High-voltage Electron Microscopy Cytochalasin D Applied to Intact Cells. *Journal of Cell Biology1*, 92(1):79–91, 1982.

[171] Fang Cheng, Yue Shen, Ponnuswamy Mohanasundaram, Michelle Lindström, Johanna Ivaska, Tor Ny, and John E. Erikss. Vimentin coordinates fibroblast proliferation and keratinocyte differentiation in wound healing via TGF-β-Slug signaling.

Proceedings of the National Academy of Sciences of the United States of America, 113(30):E4320–E4327, 2016.

[172] Ben Fabry, Geoffrey N. Maksym, James P. Butler, Michael Glogauer, Daniel Navajas, and Jeffrey J. Fredberg. Scaling the microrheology of living cells. *Physical Review Letters*, 87(14):148102, 2001.

[173] Sebastian Hurst, Bart E. Vos, Matthias Brandt, and Timo Betz. Intracellular softening and increased viscoelastic fluidity during division. *Nature Physics*, 17(11):1270–1276, 2021.

[174] A. Bonfanti, J. L. Kaplan, G. Charras, and A. Kabla. Fractional viscoelastic models for power-law materials. *Soft Matter*, 16(26):6002–6020, 2020.

[175] Aleksandra K. Denisin and Beth L. Pruitt. Tuning the Range of Polyacrylamide Gel Stiffness for Mechanobiology Applications. *ACS Applied Materials and Interfaces*, 8(34):21893–21902, 2016.

[176] M. C. Gandikota, Katarzyna Pogoda, Anne Van Oosten, T. A. Engstrom, A. E. Patteson, P. A. Janmey, and J. M. Schwarz. Loops: Versus lines and the compression stiffening of cells. *Soft Matter*, 16(18):4389–4406, 2020.

[177] Gijsje H. Koenderink, Zvonimir Dogic, Fumihiko Nakamura, Poul M. Bendix, Frederick C. MacKintosh, John H. Hartwig, Thomas P. Stossel, and David A. Weitz. An active biopolymer network controlled by molecular motors. *Proceedings of the National Academy of Sciences of the United States of America*, 106(36):15192–15197, sep 2009.

[178] C. P. Broedersz and F. C. MacKintosh. Molecular motors stiffen non-affine semiflexible polymer networks. *Soft Matter*, 7(7):3186–3191, 2011.

[179] M. Wyart, H. Liang, A. Kabla, and L. Mahadevan. Elasticity of floppy and stiff random networks. *Physical Review Letters*, 101(21):1–4, 2008.

[180] C. P. Broedersz and F. C. Mackintosh. Modeling semiflexible polymer networks. *Reviews of Modern Physics*, 86(3):995–1036, 2014.

[181] Jing Xia, Li Heng Cai, Huayin Wu, Frederick C. MacKintosh, and David A. Weitz. Anomalous mechanics of Zn2+-modified fibrin networks. *Proceedings of the National Academy of Sciences of the United States of America*, 118(10), 2021.

[182] Jan Lammerding. *Mechanics of the Nucleus*, pages 783–807. John Wiley & Sons, Ltd, 2011.

[183] Noel H. Reynolds, W. Ronan, Enda P. Dowling, P. Owens, Robert M. McMeeking, and J. Patrick McGarry. On the role of the actin cytoskeleton and nucleus in the biomechanical response of spread cells. *Biomaterials*, 35(13):4015–4025, 2014.

[184] H. Kubitschke, J. Schnauss, K. D. Nnetu, E. Warmt, R. Stange, and J. Kaes. Actin and microtubule networks contribute differently to cell response for small and large strains. *New Journal of Physics*, 19(9):093003, 2017.

[185] Fitzroy J Byfield, Behnaz Eftekhari, Kaeli Kaymak-Loveless, Kalpana Mandal, David Li, Rebecca G Wells, Wenjun Chen, Jasna Brujic, Guilia Bergamaschi, Gijs J L Wuite, Alison E Patteson, and Paul A Janmey. Metabolically intact nuclei are fluidized by the activity of the chromatin remodeling motor BRG1. *Biophysical Journal*, 2024.

[186] R. D. Goldman, R. Pollack, and N. H. Hopkins. Preservation of normal behavior by enucleated cells in culture. *Proceedings of the National Academy of Sciences of the United States of America*, 70(3):750–754, 1973.

[187] M G Mendez, D Restle, and P A Janmey. Vimentin enhances cell elastic behavior and protects against compressive stress. *Biophysical Journal*, 107(2):314–323, aug 2014.

[188] Richard Gerum, Elham Mirzahossein, Mar Eroles, Jennifer Elsterer, Astrid Mainka, Andreas Bauer, Selina Sonntag, Alexander Winterl, Johannes Bartl, Lena Fischer, Shada Abuhattum, Ruchi Goswami, Salvatore Girardo, Jochen Guck, Stefan Schrüfer, Nadine Ströhlein, Mojtaba Nosratlo, Harald Herrmann, Dorothea Schultheis, Felix Rico, Sebastian Johannes Müller, Stephan Gekle, and Ben Fabry. Viscoelastic properties of suspended cells measured with shear flow deformation cytometry. *eLife*, 11:1–26, 2022.

[189] Dennis E. Discher, Paul Janmey, and Yu Li Wang. Tissue cells feel and respond to the stiffness of their substrate. *Science*, 310(5751):1139–1143, 2005.

[190] M Reza Shaebani, Luiza Stankevicins, Doriane Vesperini, Marta Urbanska, Daniel A D Flormann, Emmanuel Terriac, Annica K B Gad, Fang Cheng, John E Eriksson, and Franziska Lautenschläger. Effects of vimentin on the migration, search efficiency, and mechanical resilience of dendritic cells. *Biophysical Journal*, 121(20):3950–3961, oct 2022.

[191] Takumi Saito, Daiki Matsunaga, and Shinji Deguchi. Long-term molecular turnover of actin stress fibers revealed by advection-reaction analysis in fluorescence recovery after photobleaching. *PLoS ONE*, 17(11 November):1–17, 2022.

[192] Marco Fritzsche, Alexandre Lewalle, Tom Duke, Karsten Kruse, and Guillaume Charras. Analysis of turnover dynamics of the submembranous actin cortex. *Molecular Biology of the Cell*, 24(6):757–767, 2013.

[193] Jiliang Hu, Yiwei Li, Yukun Hao, Tianqi Zheng, Satish K. Gupta, German Alberto Parada, Huayin Wu, Shaoting Lin, Shida Wang, Xuanhe Zhao, Robert D. Goldman, Shengqiang Cai, and Ming Guo. High stretchability, strength, and toughness of living cells enabled by hyperelastic vimentin intermediate filaments. *Proceedings of the National Academy of Sciences of the United States of America*, 116(35):17175–17180, 2019.

[194] Grace E Peng, Sarah R Wilson, and Orion D Weiner. A pharmacological cocktail for arresting actin dynamics in living cells. *Molecular biology of the cell*, 22(21):3986–3994, nov 2011.

[195] Ang Li, John C Dawson, Manuel Forero-Vargas, Heather J Spence, Xinzi Yu, Ireen König, Kurt Anderson, and Laura M Machesky. The Actin-Bundling Protein Fascin Stabilizes Actin in Invadopodia and Potentiates Protrusive Invasion. *Current Biology*, 20(4):339–345, feb 2010.

[196] Loïc Chaubet, Abdullah R. Chaudhary, Hossein K. Heris, Allen J. Ehrlicher, and Adam G. Hendricks. Dynamic actin cross-linking governs the cytoplasm's transition to fluid-like behavior. *Molecular Biology of the Cell*, 31(16):1744–1752, 2020.

[197] Svetlana Mukhina, Yu-li Wang, and Maki Murata-Hori. α-Actinin Is Required for Tightly Regulated Remodeling of the Actin Cortical Network during Cytokinesis. *Developmental Cell*, 13(4):554–565, oct 2007.

[198] James P Conboy, Mathilde G Lettinga, Nicole Van Vliet, Lilli Winter, Gerhard Wiche, and C Frederick. Plectin affects cell viscoelasticity at small and large deformations. *bioRxiv*, 1(1):1–24, 2025.

[199] Haijiao Liu, Jun Wen, Yun Xiao, Jun Liu, Sevan Hopyan, Milica Radisic, Craig A. Simmons, and Yu Sun. In situ mechanical characterization of the cell nucleus by atomic force microscopy. *ACS Nano*, 8(4):3821–3828, 2014.

[200] A. F. Huxley. Muscle structure and theories of contraction. *Progress in biophysics and biophysical chemistry*, 7:255–318, 1957.

[201] Murielle P. Serres, Matthias Samwer, Binh An Truong Quang, Geneviève Lavoie, Upamali Perera, Dirk Görlich, Guillaume Charras, Mark Petronczki, Philippe P. Roux, and Ewa K. Paluch. F-Actin Interactome Reveals Vimentin as a Key Regulator of Actin Organization and Cell Mechanics in Mitosis. *Developmental Cell*, 52(2):210–222.e7, 2020.

[202] Huayin Wu, Yinan Shen, Suganya Sivagurunathan, Miriam Sarah, and Stephen A Adam. Vimentin intermediate filaments and filamentous actin form unexpected interpenetrating networks that redefine the cell cortex. *Proceedings of the National Academy of Sciences of the United States of America*, 119(10):1–10, 2022.

[203] Alison E. Patteson, Katarzyna Pogoda, Fitzroy J. Byfield, Kalpana Mandal, Zofia Ostrowska-Podhorodecka, Elisabeth E. Charrier, Peter A. Galie, Piotr Deptuła, Robert Bucki, Christopher A. McCulloch, and Paul A. Janmey. Loss of Vimentin Enhances Cell Motility through Small Confining Spaces. *Small*, 15(50):1903180, dec 2019.

[204] Gerhard Wiche. Role of plectin in cytoskeleton organization and dynamics. *Journal of cell science*, 111(9):2477–2486, 1998.

[205] Sabine M. Volkmer Ward, Astrid Weins, Martin R. Pollak, and David A. Weitz. Dynamic viscoelasticity of actin cross-linked with wild-type and disease-causing mutant α-actinin-4. *Biophysical Journal*, 95(10):4915–4923, 2008.

[206] Reetta Virtakoivu, Anja Mai, Elina Mattila, Nicola De Franceschi, Susumu Y Imanishi, Garry Corthals, Riina Kaukonen, Markku Saari, Fang Cheng, Elin Torvaldson, Veli Matti Kosma, Arto Mannermaa, Ghaffar Muharram, Christine Gilles, John Eriksson, Ylermi Soini, James B Lorens, and Johanna Ivaska. Vimentin-ERK signaling uncouples slug gene regulatory function. *Cancer Research*, 75(11):2349–2362, aug 2015.

[207] Annafrancesca Rigato, Atsushi Miyagi, Simon Scheuring, and Felix Rico. High-frequency microrheology reveals cytoskeleton dynamics in living cells. *Nature Physics*, 13(8):771–775, aug 2017.

[208] Hedde Van Hoorn, Nicholas A. Kurniawan, Gijsje H. Koenderink, and Davide Iannuzzi. Local dynamic mechanical analysis for heterogeneous soft matter using ferrule-top indentation. *Soft Matter*, 12(12):3066–3073, mar 2016.

[209] Stéfan Van Der Walt, Johannes L. Schönberger, Juan Nunez-Iglesias, François Boulogne, Joshua D. Warner, Neil Yager, Emmanuelle Gouillart, and Tony Yu. Scikit-image: Image processing in python. *PeerJ*, 2014(1):1–18, 2014.

[210] Rick Rodrigues De Mercado, Klara Beslmüller, Daan Vorselen, Erik H J Danen, and Thomas Schmidt. Single-Cell Local Stress Analysis in Tumoroids. *BiorXiv*, 2024.

[211] Pauli Virtanen, Ralf Gommers, Travis E. Oliphant, Matt Haberland, Tyler Reddy, David Cournapeau, Evgeni Burovski, Pearu Peterson, Warren Weckesser, Jonathan Bright, Stéfan J. van der Walt, Matthew Brett, Joshua Wilson, K. Jarrod Millman, Nikolay Mayorov, Andrew R.J. Nelson, Eric Jones, Robert Kern, Eric Larson, C. J. Carey, İlhan Polat, Yu Feng, Eric W. Moore, Jake VanderPlas, Denis Laxalde, Josef Perktold, Robert Cimrman, Ian Henriksen, E. A. Quintero, Charles R. Harris, Anne M. Archibald, Antônio H. Ribeiro, Fabian Pedregosa, Paul van Mulbregt, Aditya Vijaykumar, Alessandro Pietro Bardelli, Alex Rothberg, Andreas Hilboll, Andreas Kloeckner, Anthony Scopatz, Antony Lee, Ariel Rokem, C. Nathan Woods, Chad Fulton, Charles Masson, Christian Häggström, Clark Fitzgerald, David A. Nicholson, David R. Hagen, Dmitrii V. Pasechnik, Emanuele Olivetti, Eric Martin, Eric Wieser, Fabrice Silva, Felix Lenders, Florian Wilhelm, G. Young, Gavin A. Price, Gert Ludwig Ingold, Gregory E. Allen, Gregory R. Lee, Hervé Audren, Irvin Probst, Jörg P. Dietrich, Jacob Silterra, James T. Webber, Janko Slavič, Joel Nothman, Johannes Buchner, Johannes Kulick, Johannes L. Schönberger, José Vinícius de Miranda Cardoso, Joscha Reimer, Joseph Harrington, Juan Luis Cano Rodríguez, Juan Nunez-Iglesias, Justin Kuczynski, Kevin Tritz, Martin Thoma, Matthew Newville, Matthias Kümmerer, Maximilian Bolingbroke, Michael Tartre, Mikhail Pak, Nathaniel J. Smith, Nikolai Nowaczyk, Nikolay Shebanov, Oleksandr Pavlyk, Per A. Brodtkorb, Perry Lee, Robert T. McGibbon, Roman Feldbauer, Sam Lewis, Sam Tygier, Scott Sievert, Sebastiano Vigna, Stefan Peterson, Surhud More, Tadeusz Pudlik, Takuya Oshima, Thomas J. Pingel, Thomas P. Robitaille, Thomas Spura, Thouis R. Jones, Tim Cera, Tim Leslie, Tiziano Zito, Tom Krauss, Utkarsh Upadhyay, Yaroslav O. Halchenko, and Yoshiki Vázquez-Baeza. SciPy 1.0: fundamental algorithms for scientific computing in Python. *Nature Methods*, 17(3):261–272, 2020.

[212] Charles R. Harris, K. Jarrod Millman, Stéfan J. van der Walt, Ralf Gommers, Pauli Virtanen, David Cournapeau, Eric Wieser, Julian Taylor, Sebastian Berg, Nathaniel J. Smith, Robert Kern, Matti Picus, Stephan Hoyer, Marten H. van Kerkwijk, Matthew Brett, Allan Haldane, Jaime Fernández del Río, Mark Wiebe, Pearu Peterson, Pierre Gérard-Marchant, Kevin Sheppard, Tyler Reddy, Warren Weckesser, Hameer Abbasi, Christoph Gohlke, and Travis E. Oliphant. Array programming with NumPy. *Nature*, 585(7825):357–362, 2020.

[213] Cécile Leduc and Sandrine Etienne-Manneville. Regulation of microtubule-associated motors drives intermediate filament network polarization. *Journal of Cell Biology*, 216(6):1689–1703, aug 2017.

[214] Johannes Schindelin, Ignacio Arganda-Carreras, Erwin Frise, Verena Kaynig, Mark Longair, Tobias Pietzsch, Stephan Preibisch, Curtis Rueden, Stephan Saalfeld, Benjamin Schmid, Jean Yves Tinevez, Daniel James White, Volker Hartenstein, Kevin Eliceiri, Pavel Tomancak, and Albert Cardona. Fiji: An open-source platform for biological-image analysis. *Nature Methods*, 9(7):676–682, 2012.

[215] Ved P. Sharma, Binwu Tang, Yarong Wang, Camille L. Duran, George S. Karagiannis, Emily A. Xue, David Entenberg, Lucia Borriello, Anouchka Coste, Robert J. Eddy, Gina Kim, Xianjun Ye, Joan G. Jones, Eli Grunblatt, Nathan Agi, Sweta Roy, Gargi Bandyopadhyaya, Esther Adler, Chinmay R. Surve, Dominic Esposito, Sumanta Goswami, Jeffrey E. Segall, Wenjun Guo, John S. Condeelis, Lalage M. Wakefield, and Maja H. Oktay. Live tumor imaging shows macrophage induction and TMEM-mediated enrichment of cancer stem cells during metastatic dissemination. *Nature Communications*, 12(1):1–24, 2021.

[216] Marta Urbanska and Jochen Guck. Single-Cell Mechanics: Structural Determinants and Functional Relevance. *Annual Review of Biophysics*, 53(1):367–395, 2024.

[217] James P. Conboy, Irene Istúriz Petitjean, Anouk van der Net, and Gijsje H. Koenderink. How cytoskeletal crosstalk makes cells move: Bridging cell-free and cell studies. *Biophysics Reviews*, 5(2):021307, 2024.

[218] Bernd Nöding and Sarah Köster. Intermediate filaments in small configuration spaces. *Physical Review Letters*, 108(8):1–4, 2012.

[219] Andrew A Bridges, Huaiying Zhang, Shalin B Mehta, Patricia Occhipinti, Tomomi Tani, and Amy S Gladfelter. Septin assemblies form by diffusion-driven annealing on membranes. *Proceedings of the National Academy of Sciences*, 111(6):2146–2151, 2014.

[220] F. Gittes, B. Mickey, J. Nettleton, and J. Howard. Flexural rigidity of microtubules and actin filaments measured from thermal fluctuations in shape. *Journal of Cell Biology*, 120(4):923–934, 1993.

[221] Pekka Lappalainen, Tommi Kotila, Antoine Jégou, and Guillaume Romet-Lemonne. Biochemical and mechanical regulation of actin dynamics. *Nature reviews. Molecular cell biology*, 23(12):836–852, dec 2022.

[222] Anna Akhmanova and Lukas C. Kapitein. Mechanisms of microtubule organization in differentiated animal cells. *Nature Reviews Molecular Cell Biology*, 23(8):541–558, 2022.

[223] Leila S Coelho-Rato, Sepideh Parvanian, Sarka Andrs Salajkova, Ohad Medalia, and John E Eriksson. Intermediate filaments at a glance. *Journal of cell science*, 137(16):4345–4347, aug 2024.

[224] Janik N Schampera and Carsten Schwan. Septin dynamics and organization in mammalian cells. *Current Opinion in Cell Biology*, 91:102442, 2024.

[225] Oliver Lieleg, Mireille M.A.E. Claessens, and Andreas R. Bausch. Structure and dynamics of cross-linked actin networks. *Soft Matter*, 6(2):218–225, 2010.

[226] Kei W. Müller, Robijn F. Bruinsma, Oliver Lieleg, Andreas R. Bausch, Wolfgang A. Wall, and Alex J. Levine. Rheology of semiflexible bundle networks with transient linkers. *Physical Review Letters*, 112(23):1–5, 2014.

[227] Chase P. Broedersz, Martin Depken, Norman Y. Yao, Martin R. Pollak, David A. Weitz, and Frederick C. MacKintosh. Cross-link-governed dynamics of biopolymer networks. *Physical Review Letters*, 105(23):1–4, 2010.

[228] Yuval Mulla, Mario J Avellaneda, Antoine Roland, Lucia Baldauf, Wonyeong Jung, Taeyoon Kim, Sander J Tans, and Gijsje H Koenderink. Weak catch bonds make strong networks. *Nature Materials 2022 21:9*, 21(9):1019–1023, 2022.

[229] Kathleen C Suozzi, Xiaoyang Wu, and Elaine Fuchs. Spectraplakins: Master orchestrators of cytoskeletal dynamics. *Journal of Cell Biology*, 197(4):465–475, may 2012.

[230] Jamie Zhang, Jiping Yue, and Xiaoyang Wu. Spectraplakin family proteins - Cytoskeletal crosslinkers with versatile roles. *Journal of Cell Science*, 130(15):2447–2457, 2017.

[231] R Pytela and G Wiche. High molecular weight polypeptides (270,000-340,000) from cultured cells are related to hog brain microtubule-associated proteins but copurify with intermediate filaments. *Proceedings of the National Academy of Sciences of the United States of America*, 77(8):4808–4812, aug 1980.

[232] R Foisner, F E Leichtfried, H Herrmann, J V Small, D Lawson, and G Wiche. Cytoskeleton-associated plectin: in situ localization, in vitro reconstitution, and binding to immobilized intermediate filament proteins. *The Journal of cell biology*, 106(3):723–733, mar 1988.

[233] Chang Gong Liu, Christian Maercker, Maria J. Castañon, Rudolf Hauptmann, and Gerhard Wiche. Human plectin: Organization of the gene, sequence analysis, and chromosome localization (8q24). *Proceedings of the National Academy of Sciences of the United States of America*, 93(9):4278–4283, 1996.

[234] Gerhard Wiche. Plectin-Mediated Intermediate Filament Functions: Why Isoforms Matter. *Cells*, 10(8):2154, aug 2021.

[235] Tatyana M. Svitkina, Alexander B. Verkhovsky, and Gary B. Borisy. Plectin sidearms mediate interactions of intermediate filaments with microtubules and other components of the cytoskeleton. *Journal of Cell Biology*, 194(3):409–410, 1998.

[236] Wily G Ruiz, Dennis R Clayton, Tanmay Parakala-Jain, Marianela G Dalghi, Jonathan Franks, and Gerard Apodaca. The rat bladder umbrella cell keratin network: Organization, dependence on the plectin cytolinker, and responses to bladder filling. *Molecular Biology of the Cell*, 35(11):ar139, 2024.

[237] Selma Osmanagic-Myers, Stefanie Rus, Michael Wolfram, Daniela Brunner, Wolfgang H. Goldmann, Navid Bonakdar, Irmgard Fischer, Siegfried Reipert, Aurora Zuzuarregui, Gernot Walko, and Gerhard Wiche. Plectin reinforces vascular integrity by mediating crosstalk between the vimentin and the actin networks. *Journal of Cell Science*, 128(22):4138–4150, 2015.

[238] Marketa Jirouskova, Katerina Nepomucka, Gizem Oyman-Eyrilmez, Alzbeta Kalendova, Helena Havelkova, Lenka Sarnova, Karel Chalupsky, Bjoern Schuster, Oldrich Benada, Petra Miksatkova, Martin Kuchar, Ondrej Fabian, Radislav Sedlacek, Gerhard Wiche, and Martin Gregor. Plectin controls biliary tree architecture and stability in cholestasis. *Journal of Hepatology*, 68(5):1006–1017, 2018.

[239] Lilli Winter and Gerhard Wiche. The many faces of plectin and plectinopathies: pathology and mechanisms. *Acta Neuropathologica*, 125(1):77–93, 2013.

[240] Dimitra Kiritsi, Leonidas Tsakiris, and Franziska Schauer. Plectin in Skin Fragility Disorders. *Cells*, 10(10):2738, oct 2021.

[241] Michaela M Zrelski, Monika Kustermann, and Lilli Winter. Muscle-Related Plectinopathies. *Cells*, 10(9):2480, 2021.

[242] Michaela M Zrelski, Sabrina Hösele, Monika Kustermann, Petra Fichtinger, Delf Kah, Ioannis Athanasiou, Philipp R Esser, Anja Wagner, Rebecca Herzog, Klaus Kratochwill, Wolfgang H Goldmann, Dimitra Kiritsi, and Lilli Winter. Plectin Deficiency in Fibroblasts Deranges Intermediate Filament and Organelle Morphology, Migration, and Adhesion. *Journal of Investigative Dermatology*, 144(3):547–562.e9, 2024.

[243] Selma Osmanagic-Myers, Martin Gregor, Gernot Walko, Gerald Burgstaller, Siegfried Reipert, and Gerhard Wiche. Plectin-controlled keratin cytoarchitecture affects MAP kinases involved in cellular stress response and migration. *Journal of Cell Biology*, 174(4):557–568, 2006.

[244] Murielle P Serres, Matthias Samwer, Binh An Truong Quang, Geneviève Lavoie, Upamali Perera, Dirk Görlich, Guillaume Charras, Mark Petronczki, Philippe P Roux, and Ewa K Paluch. F-Actin Interactome Reveals Vimentin as a Key Regulator of Actin Organization and Cell Mechanics in Mitosis. *Developmental Cell TA - TT -*, 52(2):210–222.e7, 2020.

[245] Sofia Duarte, Álvaro Viedma-Poyatos, Elena Navarro-Carrasco, Alma E Martínez, María A Pajares, and Dolores Pérez-Sala. Vimentin filaments interact with the actin cortex in mitosis allowing normal cell division. *Nature communications*, 10(1):4200, sep 2019.

[246] Mihoko Sutoh Yoneyama, Shingo Hatakeyama, Tomonori Habuchi, Takamitsu Inoue, Toshiya Nakamura, Tomihisa Funyu, Gerhard Wiche, Chikara Ohyama, and Shigeru Tsuboi. Vimentin intermediate filament and plectin provide a scaffold for invadopodia, facilitating cancer cell invasion and extravasation for metastasis. *European Journal of Cell Biology*, 93(4):157–169, 2014.

[247] Yaming Jiu, Jaakko Lehtimäki, Sari Tojkander, Fang Cheng, Harri Jäälinoja, Xiaonan Liu, Markku Varjosalo, John E. Eriksson, and Pekka Lappalainen. Bidirectional Interplay between Vimentin Intermediate Filaments and Contractile Actin Stress Fibers. *Cell Reports*, 11(10):1511–1518, 2015.

[248] Pragati C. Marks, Breanne R. Hewitt, Michelle A. Baird, Gerhard Wiche, and Ryan J. Petrie. Plectin linkages are mechanosensitive and required for the nuclear piston mechanism of three-dimensional cell migration. *Molecular Biology of the Cell*, 33(12):E21–08–0414, oct 2022.

[249] Sungsoo Na, Farhan Chowdhury, Bernard Tay, Mingxing Ouyang, Martin Gregor, Yingxiao Wang, Gerhard Wiche, and Ning Wang. Plectin contributes to mechanical properties of living cells. *American Journal of Physiology - Cell Physiology*, 296(4):868–877, 2009.

[250] Irene Istúriz Petitjean, Quang D. Tran, Angeliki Goutou, Zima Kabir, Gerhard Wiche, Cécile Leduc, and Gijsje H. Koenderink. Reconstitution of cytolinker-mediated crosstalk between actin and vimentin. *European Journal of Cell Biology*, 103(2):151403, 2024.

[251] Navid Bonakdar, Achim Schilling, Marina Spörrer, Pablo Lennert, Astrid Mainka, Lilli Winter, Gernot Walko, Gerhard Wiche, Ben Fabry, and Wolfgang H. Goldmann. Determining the mechanical properties of plectin in mouse myoblasts and keratinocytes. *Experimental Cell Research*, 331(2):331–337, 2015.

[252] Marcin Moch, Reinhard Windoffer, Nicole Schwarz, Raphaela Pohl, Andreas Omenzetter, Uwe Schnakenberg, Fabian Herb, Kraisorn Chaisaowong, Dorit Merhof, Lena Ramms, and Others. Effects of plectin depletion on keratin network dynamics and organization. *PLOS One*, 11(3):e0149106, 2016.

[253] James P Conboy, Mathilde G Lettinga, Pouyan E Boukany, Fred C MacKintosh, and Gijsje H Koenderink. Actin and vimentin jointly control cell viscoelasticity and compression stiffening. *bioRxiv*, 1:1–36, 2025.

[254] Kerstin Andrä, Hans Lassmann, Reginald Bittner, Sigrid Shorny, Reinhard Fässler, Friedrich Propst, and Gerhard Wiche. Targeted inactivation of plectin reveals essential function in maintaining the integrity of skin, muscle, and heart cytoarchitecture. *Genes and Development*, 11(23):3143–3156, 1997.

[255] Kerstin Andrä, Iris Kornacker, Almut Jörgl, Michael Zörer, Daniel Spazierer, Peter Fuchs, Irmgard Fischer, and Gerhard Wiche. Plectin-isoform-specific rescue of hemidesmosomal defects in plectin (-/-) keratinocytes. *The Journal of investigative dermatology*, 120(2):189–197, feb 2003.

[256] Gerald Burgstaller, Martin Gregor, Lilli Winter, and Gerhard Wiche. Keeping the vimentin network under control: cell-matrix adhesion-associated plectin 1f affects cell shape and polarity of fibroblasts. *Molecular biology of the cell*, 21(19):3362–3375, oct 2010.

[257] Selma Osmanagic-Myers, Martin Gregor, Gernot Walko, Gerald Burgstaller, Siegfried Reipert, and Gerhard Wiche. Plectin-controlled keratin cytoarchitecture affects MAP kinases involved in cellular stress response and migration. *The Journal of cell biology*, 174(4):557–568, 2006.

[258] Gerald Burgstaller, Martin Gregor, Lilli Winter, and Gerhard Wiche. Keeping the Vimentin Network under Control: Cell-Matrix Adhesion-associated Plectin 1f Affects Cell Shape and Polarity of Fibroblasts. *Molecular Biology of the Cell*, 21:3362–3375, 2010.

[259] A. Bonfanti, J. L. Kaplan, G. Charras, and A. Kabla. Fractional viscoelastic models for power-law materials. *Soft Matter*, 16(26):6002–6020, 2020.

[260] A. Bonfanti, J. Fouchard, N. Khalilgharibi, G. Charras, and A. Kabla. A unified rheological model for cells and cellularised materials. *Royal Society Open Science*, 7(1):190920, 2020.

[261] Atsuo Kondo and Jacques G Susset. Physical properties of the urinary detrusor muscle: A mechanical model based upon the analysis of stress relaxation curve. *Journal of Biomechanics*, 6(2):141–151, 1973.

[262] Ramin Oftadeh, Brianne K Connizzo, Hadi Tavakoli Nia, Christine Ortiz, and Alan J Grodzinsky. Biological connective tissues exhibit viscoelastic and poroelastic behavior at different frequency regimes: Application to tendon and skin biophysics. *Acta Biomaterialia*, 70:249–259, 2018.

[263] Emad Moeendarbary, Léo Valon, Marco Fritzsche, Andrew R. Harris, Dale A. Moulding, Adrian J. Thrasher, Eleanor Stride, L. Mahadevan, and Guillaume T. Charras. The cytoplasm of living cells behaves as a poroelastic material. *Nature Materials*, 12(3):253–261, 2013.

[264] T G Mason and D A Weitz. Optical Measurements of Frequency-Dependent Linear Viscoelastic Moduli of Complex Fluids. *Phys. Rev. Lett.*, 74(7):1250–1253, feb 1995.

[265] C R Cantor and P R Schimmel. *Biophysical Chemistry. Pt. 1. The conformation of biological macromolecules*. Freeman, San Francisco, 1980.

[266] Nargess Khalilgharibi, Jonathan Fouchard, Nina Asadipour, Ricardo Barrientos, Maria Duda, Alessandra Bonfanti, Amina Yonis, Andrew Harris, Payman Mosaffa,

Yasuyuki Fujita, Alexandre Kabla, Yanlan Mao, Buzz Baum, José J. Muñoz, Mark Miodownik, and Guillaume Charras. Stress relaxation in epithelial monolayers is controlled by the actomyosin cortex. *Nature Physics*, 15(8):839–847, 2019.

[267] Amélie Robert, Molly J Rossow, Caroline Hookway, Stephen A Adam, and Vladimir I Gelfand. Vimentin filament precursors exchange subunits in an ATP-dependent manner. *Proceedings of the National Academy of Sciences*, 112(27):E3505–E3514, 2015.

[268] M. L. Gardel, F. Nakamura, J. H. Hartwig, J. C. Crocker, T. P. Stossel, and D. A. Weitz. Prestressed F-actin networks cross-linked by hinged filamins replicate mechanical properties of cells. *Proceedings of the National Academy of Sciences of the United States of America*, 103(6):1762–1767, 2006.

[269] Branislav Nikolic, Elisabeth Mac Nulty, Birgit Mir, and Gerhard Wiche. Basic amino acid residue cluster within nuclear targeting sequence motif is essential for cytoplasmic plectin-vimentin network junctions. *The Journal of cell biology*, 134(6):1455–1467, 1996.

[270] Kerstin Andrä, Branislav Nikolic, Markus Stöcher, Detlev Drenckhahn, and Gerhard Wiche. Not just scaffolding: plectin regulates actin dynamics in cultured cells. *Genes & Development*, 12(21):3442–3451, 1998.

[271] Anders Aufderhorst-Roberts and Gijsje H. Koenderink. Stiffening and inelastic fluidization in vimentin intermediate filament networks. *Soft Matter*, 15(36):7127–7136, 2019.

[272] Kevin Wilhelmsen, Sandy H.M. Litjens, Ingrid Kuikman, Ntambua Tshimbalanga, Hans Janssen, Iman Den Van Bout, Karine Raymond, and Arnoud Sonnenberg. Nesprin-3, a novel outer nuclear membrane protein, associates with the cytoskeletal linker protein plectin. *Journal of Cell Biology*, 171(5):799–810, 2005.

[273] Ilona Staszewska, Irmgard Fischer, and Gerhard Wiche. Plectin isoform 1-dependent nuclear docking of desmin networks affects myonuclear architecture and expression of mechanotransducers. *Human Molecular Genetics*, 24(25):7373–7389, 2015.

[274] Jonathan Kaplan, Alessandra Bonfanti, and Alexandre Kabla. RHEOS.jl – A Julia Package for Rheology Data Analysis. *Journal of Open Source Software*, 4(41):1700, 2019.

[275] Edwin P. Chan, Blessing Deeyaa, Peter M. Johnson, and Christopher M. Stafford. Poroelastic relaxation of polymer-loaded hydrogels. *Soft Matter*, 8(31):8234–8240, 2012.

[276] Minchul Kang, Charles A. Day, Kimberly Drake, Anne K. Kenworthy, and Emmanuele DiBenedetto. A generalization of theory for two-dimensional fluorescence recovery after photobleaching applicable to confocal laser scanning microscopes. *Biophysical Journal*, 97(5):1501–1511, 2009.

[277] Héctor Vázquez-Meza, María Magdalena Vilchis-Landeros, Melissa Vázquez-Carrada, Daniel Uribe-Ramírez, and Deyamira Matuz-Mares. Cellular Compartmentalization, Glutathione Transport and Its Relevance in Some Pathologies. *Antioxidants*, 12(4):834, 2023.

[278] O H Lowry, N J Rosebrough, A L Farr, and R J Randall. Protein measurement with the Folin phenol reagent. 193:265–275, 1951.

[279] Serge Mostowy, Sébastien Janel, Claire Forestier, Charles Roduit, Sandor Kasas, Javier Pizarro-Cerdá, Pascale Cossart, and Frank Lafont. A Role for Septins in the Interaction between the Listeria monocytogenes Invasion Protein InlB and the Met Receptor. *Biophysical Journal*, 100(8):1949–1959, 2011.

[280] Carla Silva Martins, Cyntia Taveneau, Gerard Castro-Linares, Mikhail Baibakov, Nicolas Buzhinsky, Mar Eroles, Violeta Milanović, Shizue Omi, Jean-Denis Pedelacq, Francois Iv, Léa Bouillard, Alexander Llewellyn, Maxime Gomes, Mayssa Belhabib, Mira Kuzmić, Pascal Verdier-Pinard, Stacey Lee, Ali Badache, Sanjay Kumar, Cristel Chandre, Sophie Brasselet, Felix Rico, Olivier Rossier, Gijsje H Koenderink, Jerome Wenger, Stéphanie Cabantous, and Manos Mavrakis. Human septins organize as octamer-based filaments and mediate actin-membrane anchoring in cells. *Journal of Cell Biology*, 222(3):e202203016, 2022.

[281] Brittany MacTaggart and Anna Kashina. Posttranslational modifications of the cytoskeleton. *Cytoskeleton*, 78(4):142–173, 2021.

[282] Allen J Ehrlicher, Ramaswamy Krishnan, Ming Guo, Cécile M Bidan, David A Weitz, and Martin R Pollak. Alpha-actinin binding kinetics modulate cellular dynamics and force generation. *Proceedings of the National Academy of Sciences*, 112(21):6619–6624, 2015.

[283] Ning Wang, Jessica D Tytell, and Donald E Ingber. Mechanotransduction at a distance: mechanically coupling the extracellular matrix with the nucleus. *Nature Reviews Molecular Cell Biology*, 10(1):75–82, 2009.

[284] Shyam B. Khatau, Christopher M. Hale, P. J. Stewart-Hutchinson, Meet S. Patel, Colin L. Stewart, Peter C. Searson, Didier Hodzic, and Denis Wirtz. A perinuclear actin cap regulates nuclear shape. *Proceedings of the National Academy of Sciences of the United States of America*, 106(45):19017–19022, 2009.

[285] Mai Pho, Yasmin Berrada, Aachal Gunda, Anya Lavallee, Katherine Chiu, Arimita Padam, Marilena L Currey, and Andrew D Stephens. Actin contraction controls nuclear blebbing and rupture independent of actin confinement. *Molecular biology of the cell*, 35(2):ar19, feb 2024.

[286] Alison E Patteson, Amir Vahabikashi, Katarzyna Pogoda, Stephen A Adam, Kalpana Mandal, Mark Kittisopikul, Suganya Sivagurunathan, Anne Goldman, Robert D Goldman, and Paul A Janmey. Vimentin protects cells against nuclear rupture and DNA damage during migration. *The Journal of cell biology*, 218(12):4079–4092, dec 2019.

[287] Alfonso J Sarria, Jonathan G Lieber, Steven K Nordeen, and Robert M Evans. The presence or absence of a vimentin-type intermediate filament network affects the shape of the nucleus in human SW-13 cells. *Journal of Cell Science*, 107(6):1593–1607, 1994.

[288] Oscar M Lancaster and Buzz Baum. Shaping up to divide: coordinating actin and microtubule cytoskeletal remodelling during mitosis. *Seminars in cell & developmental biology*, 34:109–115, oct 2014.

[289] F A Steinböck and G Wiche. Plectin: A Cytolinker by Design. *Journal of Cell Science*, 380(2):151–158, 1999.

[290] T M Svitkina, A B Verkhovsky, and G G Borisy. Plectin sidearms mediate interaction of intermediate filaments with microtubules and other components of the cytoskeleton. *Journal of Cell Biology*, 135(4):991–1007, 1996.

[291] Gerhard Wiche and Lilli Winter. Plectin isoforms as organizers of intermediate filament cytoarchitecture. *BioArchitecture*, 1(1):14–20, 2011.

[292] Maria J. Castañón, Gernot Walko, Lilli Winter, and Gerhard Wiche. Plectin-intermediate filament partnership in skin, skeletal muscle, and peripheral nerve. *Histochemistry and Cell Biology*, 140(1):33–53, 2013.

[293] Arnoud Sonnenberg and Ronald K.H. Liem. Plakins in development and disease. *Experimental Cell Research*, 313(10):2189–2203, 2007.

[294] Günther A Rezniczek, Christina Abrahamsberg, Peter Fuchs, Daniel Spazierer, and Gerhard Wiche. Plectin 5-transcript diversity: short alternative sequences determine stability of gene products, initiation of translation and subcellular localization of isoforms. *Human Molecular Genetics*, 12(23):3181–3194, 2003.

[295] Jae-Geun Song, Julius Kostan, Friedel Drepper, Bettina Knapp, Euripedes de Almeida Ribeiro Jr., Petr V. Konarev, Irina Grishkovskaya, Gerhard Wiche, Martin Gregor, Dmitri I. Svergun, Bettina Warscheid, and Kristina Djinović-Carugo. Structural Insights into Ca2+ -Calmodulin Regulation of Plectin 1a-Integrin β4 Interaction in Hemidesmosomes. *Structure*, 23(3):558–570, mar 2015.

[296] Konieczny Patryk, Fuchs Peter, Reipert Siegfried, Kunz Wolfram S., Zeold Aniko, Fischer Irmgard, Paulin Denise, Schroder Rolf, and Wiche Gerhard. Myofiber integrity depends on desmin network targeting to Z-disks and costameres via distinct plectin isoforms. *Journal of Cell Biology*, 181(4):667–681, 2008.

[297] Eva Mihailovskaa, Marianne Raitha, Rocio G. Valenciaa, Irmgard Fischera, Mumna Al Banchaabouchib, Ruth Herbstc, and Gerhard Wiche. Neuromuscular synapse integrity requires linkage of acetylcholine receptors to postsynaptic intermediate filament networks via rapsyn-plectin 1f complexes. *Molecular Biology of the Cell*, 25(25):4130–4149, 2014.

[298] Winter Lilli, Abrahamsberg Christina, and Wiche Gerhard. Plectin isoform 1b mediates mitochondrion–intermediate filament network linkage and controls organelle shape. *Journal of Cell Biology*, 181(6):903–911, 2008.

[299] Lilli Winter, Andrey V Kuznetsov, Michael Grimm, Anikó Zeöld, Irmgard Fischer, and Gerhard Wiche. Plectin isoform P1b and P1d deficiencies differentially affect mitochondrial morphology and function in skeletal muscle. *Human Molecular Genetics*, 24(16):4530–4544, 2015.

[300] Rocio G. Valencia, Gernot Walko, Lubomir Janda, Jirka Novacek, Eva Mihailovska, Siegfried Reipert, Kerstin Andrä-Marobela, and Gerhard Wiche. Intermediate filament-associated cytolinker plectin 1c destabilizes microtubules in keratinocytes. *Molecular Biology of the Cell*, 24(6):768–784, 2013.

[301] R G Valencia, E Mihailovska, L Winter, K Bauer, I Fischer, G Walko, J Jorgacevski, M Potokar, R Zorec, and G Wiche. Plectin dysfunction in neurons leads to tau accumulation on microtubules affecting neuritogenesis, organelle trafficking, pain sensitivity and memory. *Neuropathology and Applied Neurobiology*, 47(1):73–95, 2021.

[302] Michelle G Palmisano, Shannon N Bremner, Troy A Hornberger, Gretchen A Meyer, Andrea A Domenighetti, Sameer B Shah, Balázs Kiss, Miklos Kellermayer, Allen F Ryan, and Richard L Lieber. Skeletal muscle intermediate filaments form a stress-transmitting and stress-signaling network. *Journal of Cell Science*, 128(2):219–224, 2015.

[303] Arnoud Sonnenberg, Ana M Rojas, and José M de Pereda. The Structure of a Tandem Pair of Spectrin Repeats of Plectin Reveals a Modular Organization of the Plakin Domain. *Journal of Molecular Biology*, 368(5):1379–1391, 2007.

[304] Caezar Al-Jassar, Pau Bernad, Martyn Chidgey, and Michael Overduin. Hinged Plakin Domains Provide Specialized Degrees of Articulation in Envoplakin, Periplakin and Desmoplakin. *PLOS ONE*, 8(7):1–11, 2013.

[305] Esther Ortega, José A Manso, Rubén M Buey, Ana M Carballido, Arturo Carabias, Arnoud Sonnenberg, and José M de Pereda. The Structure of the Plakin Domain of Plectin Reveals an Extended Rod-like Shape *. *Journal of Biological Chemistry*, 291(36):18643–18662, sep 2016.

[306] Jamal-Eddine Bouameur, Bertrand Favre, Lionel Fontao, Prakash Lingasamy, Nadja Begré, and Luca Borradori. Interaction of Plectin with Keratins 5 and 14: Dependence on Several Plectin Domains and Keratin Quaternary Structure. *Journal of Investigative Dermatology*, 134(11):2776–2783, 2014.

[307] Magdalena Preciado López, Florian Huber, Ilya Grigoriev, Michel O Steinmetz, Anna Akhmanova, Gijsje H Koenderink, and Marileen Dogterom. Actin–microtubule coordination at growing microtubule ends. *Nature Communications*, 5(1):1–9, 2014.

[308] Yuri M. Efremov, Wen Horng Wang, Shana D. Hardy, Robert L. Geahlen, and Arvind Raman. Measuring nanoscale viscoelastic parameters of cells directly from AFM force-displacement curves. *Scientific Reports*, 7(1):1–14, 2017.

[309] Debjyoti Bandyopadhyay, Austin Cyphersmith, Jairo A. Zapata, Y. Joseph Kim, and Christine K. Payne. Lysosome transport as a function of lysosome diameter. *PLoS ONE*, 9(1):18–23, 2014.

[310] John C. Crocker and Brenton D. Hoffman. Multiple-Particle Tracking and Two-Point Microrheology in Cells. *Methods in Cell Biology*, 83:141–178, 2007.

[311] Jessica L Eisenberg, Kristin G Beaumont, Desire Takawira, Susan B Hopkinson, Milan Mrksich, G R Scott Budinger, and Jonathan C R Jones. Plectin-containing, centrally localized focal adhesions exert traction forces in primary lung epithelial cells. *Journal of Cell Science*, 126(16):3746–3755, 2013.

[312] Samet Aytekin, Laurens Kimps, Quinten Coucke, Débora Linhares, and Swaraj Deodhar. Linking Molecular Tension and Cellular Tractions : A Muliscale Approach to Focal Adhesion Mechanics. *bioRxiv*, pages 1–24, 2025.

[313] Diego A Vargas, Inês G Gonçalves, Tommy Heck, Bart Smeets, Laura Lafuente-Gracia, Herman Ramon, and Hans Van Oosterwyck. Modeling of Mechanosensing Mechanisms Reveals Distinct Cell Migration Modes to Emerge From Combinations of Substrate Stiffness and Adhesion Receptor-Ligand Affinity. *Frontiers in bioengineering and biotechnology*, 8:459, 2020.

[314] Humphries Jonathan D., Wang Pengbo, Streuli Charles, Geiger Benny, Humphries Martin J., and Ballestrem Christoph. Vinculin controls focal adhesion formation by direct interactions with talin and actin. *Journal of Cell Biology*, 179(5):1043–1057, 2007.

[315] Filipe V. Almeida, Gernot Walko, James R. McMillan, John A. McGrath, Gerhard Wiche, Asa H. Barber, and John T. Connelly. The cytolinker plectin regulates nuclear mechanotransduction in keratinocytes. *Journal of Cell Science*, 128(24):4475–4486, 2015.

[316] Roman Gorelik and Alexis Gautreau. Quantitative and unbiased analysis of directional persistence in cell migration. *Nature Protocols*, 9(8):1931–1943, 2014.

[317] O. Lieleg, J. Kayser, G. Brambilla, L. Cipelletti, and A. R. Bausch. Slow dynamics and internal stress relaxation in bundled cytoskeletal networks. *Nature Materials*, 10(3):236–242, 2011.

[318] Gerald Burgstaller, Martin Gregor, Lilli Winter, and Gerhard Wiche. Keeping the Vimentin Network under Control: Cell-Matrix Adhesion-associated Plectin 1f Affects Cell Shape and Polarity of Fibroblasts. *Molecular Biology of the Cell*, 21:3362–3375, 2010.

[319] Nancy Costigliola, Liya Ding, Christoph J. Burckhardt, Sangyoon J. Han, Edgar Gutierrez, Andressa Mota, Alex Groisman, Timothy J. Mitchison, and Gaudenz Danuser. Vimentin fibers orient traction stress. *Proceedings of the National Academy of Sciences of the United States of America*, 114(20):5195–5200, may 2017.

[320] Mirjam Ketema, Maaike Kreft, Pablo Secades, Hans Janssen, and Arnoud Sonnenberg. Nesprin-3 connects plectin and vimentin to the nuclear envelope of Sertoli cells but is not required for Sertoli cell function in spermatogenesis. *Molecular Biology of the Cell*, 24(15):2454–2466, 2013.

[321] Javier López-Alonso, Mar Eroles, Sébastien Janel, Massimiliano Berardi, Jean Luc Pellequer, Vincent Dupres, Frank Lafont, and Felix Rico. PyFMLab: Open-source software for atomic force microscopy microrheology data analysis. *Open Research Europe*, 3, 2024.

[322] Bastian Rouven Brückner, Helen Nöding, and Andreas Janshoff. Viscoelastic Properties of Confluent MDCK II Cells Obtained from Force Cycle Experiments. *Biophysical Journal*, 112(4):724–735, 2017.

[323] Manfred Radmacher. Measuring the Elastic Properties of Living Cells by the Atomic Force Microscope. In Bhanu P Jena and J K Heinrich Hörber, editors, *Atomic Force Microscopy in Cell Biology*, volume 68 of *Methods in Cell Biology*, pages 67–90. Academic Press, 2002.

[324] Daniel B Allan, Thomas Caswell, Nathan C Keim, Casper M van der Wel, and Ruben W Verweij. soft-matter/trackpy: v0.6.2, feb 2024.

[325] John Crocker and David Grier. Methods of Digital Video Microscopy for Colloidal Studies | Elsevier Enhanced Reader. *Journal of Colloid and Interface Science*, 179(179):298–310, 1995.

[326] Duarte C Barral, Clare E Futter, Antony Galione, Dan F Cutler, Emily R Eden, Diego Luis Medina, Gennaro Napolitano, Johannes M F G Aerts, Carmine Settembre, Otília V Vieira, Peace Atakpa-adaji Gemma, Bruno Antonella, Rita O Teodoro, Alessandra Esposito, Paolo Grumati, Michael J Hall, J Paul Luzio, Susana S Lopes, Sandro Montefusco, Frances M Platt, Jlenia Monfregola, and Irene Sambri. Current methods to analyze lysosome morphology , positioning , motility and function. 23(5):238–269, 2022.

[327] Samet Aytekin, Laurens Kimps, Quinten Coucke, Débora Linhares, and Swaraj Deodhar. Linking Molecular Tension and Cellular Trac3ons : A Mul3scale Approach to Focal Adhesion Mechanics Introduc3on. pages 1–24, 2025.

[328] C L Luengo Hendriks and L J van Vliet. *DiPimage user manual: a scientific image processing toolbox*. s.n., 2001.

[329] Xavier Trepat, Guillaume Lenormand, and Jeffrey J. Fredberg. Universality in cell mechanics, aug 2008.

[330] Jiu-Tao Hang, Huajian Gao, and Guang-Kui Xu. Characteristic frequencies of localized stress relaxation in scaling-law rheology of living cells. *Biophysical journal*, 124(1):125–133, jan 2025.

[331] Gladys Massiera, Kathleen M. Van Citters, Paul L. Biancaniello, and John C. Crocker. Mechanics of single cells: Rheology, time dependence, and fluctuations. *Biophysical Journal*, 93(10):3703–3713, 2007.

[332] Valentin Lulevich, Tiffany Zink, Huan Yuan Chen, Fu Tong Liu, and Gang Yu Liu. Cell mechanics using atomic force microscopy-based single-cell compression. *Langmuir*, 22(19):8151–8155, 2006.

[333] Nataliia Guz, Maxim Dokukin, Vivekanand Kalaparthi, and Igor Sokolov. If Cell Mechanics Can Be Described by Elastic Modulus: Study of Different Models and Probes Used in Indentation Experiments. *Biophysical Journal*, 107(3):564–575, 2014.

[334] Kristy Tan, Shaokoon Cheng, Lauriane Jugé, and Lynne E Bilston. Characterising soft tissues under large amplitude oscillatory shear and combined loading. *Journal of Biomechanics*, 46(6):1060–1066, 2013.

[335] Maryna Perepelyuk, Likang Chin, Xuan Cao, Anne Van Oosten, Vivek B. Shenoy, Paul A. Janmey, and Rebecca G. Wells. Normal and fibrotic rat livers demonstrate shear strain softening and compression stiffening: A model for soft tissue mechanics. *PLoS ONE*, 11(1):1–18, 2016.

[336] Jake Song, Elad Deiss-Yehiely, Serra Yesilata, and Gareth H Mckinley. Strain stiffening universality in composite hydrogels and tissues. 2025.

[337] Jordan L. Shivers, Jingchen Feng, Anne S.G. Van Oosten, Herbert Levine, Paul A. Janmey, and Fred C. MacKintosh. Compression stiffening of fibrous networks with stiff inclusions. *Proceedings of the National Academy of Sciences of the United States of America*, 117(35):21037–21044, 2020.

[338] D Mazia, G Schatten, and W Sale. Adhesion of cells to surfaces coated with polylysine. Applications to electron microscopy. *Journal of Cell Biology*, 66(1):198–200, 1975.

[339] Mamdouh T. Ghannam and M. Nabil Esmail. Rheological properties of aqueous polyacrylamide solutions. *Journal of Applied Polymer Science*, 69(8):1587–1597, 1998.

[340] Yanfang Chen, Severine Roselli, Nikita Panicker, Joshua S Brzozowski, David A Skerrett-Byrne, Heather C Murray, and Nicole M Verrills. Proteomic and phosphoproteomic characterisation of primary mouse embryonic fibroblasts. *PROTEOMICS*, 24(7):2300267, 2024.

[341] Michael Schopferer, Harald Bär, Bernhard Hochstein, Sarika Sharma, Norbert Mücke, Harald Herrmann, and Norbert Willenbacher. Desmin and Vimentin Intermediate Filament Networks: Their Viscoelastic Properties Investigated by Mechanical Rheometry. *Journal of Molecular Biology*, 388(1):133–143, 2009.

[342] Valentin Ruffine, Andreas Hartmann, Annika Frenzel, Michael Schlierf, and Elisabeth Fischer-Friedrich. Twofold Mechanosensitivity Ensures Actin Cortex Reinforcement upon Peaks in Mechanical Tension. *Advanced Physics Research*, 2(12):2300046, 2023.

[343] Laura M Faure, Valeria Venturini, and Pere Roca-Cusachs. Cell compression - relevance, mechanotransduction mechanisms and tools. *Journal of cell science*, 138(6):jcs263704, mar 2025.

[344] Z Zhang, H T Davis, and D M Kroll. Scaling behavior of self-avoiding tethered vesicles. *Phys. Rev. E*, 48(2):R651—-R654, aug 1993.

[345] I L Ivanovska, P J de Pablo, B Ibarra, G Sgalari, F C MacKintosh, J L Carrascosa, C F Schmidt, and G J L Wuite. Bacteriophage capsids: Tough nanoshells with complex elastic properties. *Proceedings of the National Academy of Sciences*, 101(20):7600–7605, 2004.

[346] Yuri Tsuda, Hironori Yasutake, Akihiko Ishijima, and Toshio Yanagida. Torsional rigidity of single actin filaments and actin-actin bond breaking force under torsion measured directly by in vitro micromanipulation. *Proceedings of the National Academy of Sciences*, 93(23):12937–12942, 1996.

[347] Johanna Block, Hannes Witt, Andrea Candelli, Erwin J G Peterman, Gijs J L Wuite, Andreas Janshoff, and Sarah Köster. Nonlinear Loading-Rate-Dependent Force Response of Individual Vimentin Intermediate Filaments to Applied Strain. *Phys. Rev. Lett.*, 118(4):48101, 2017.

[348] Diana E Jaalouk and Jan Lammerding. Mechanotransduction gone awry. *Nature Reviews Molecular Cell Biology*, 10(1):63–73, 2009.

[349] Darci T. Butcher, Tamara Alliston, and Valerie M. Weaver. A tense situation: forcing tumour progression. *Nature Reviews Cancer 2009 9:2*, 9(2):108–122, feb 2009.

[350] Mar Eroles and Felix Rico. Advances in mechanical biomarkers. *Journal of Molecular Recognition*, 36(8):e3022, 2023.

[351] Hamid Mohammadi and Erik Sahai. Mechanisms and impact of altered tumour mechanics. *Nature Cell Biology*, 20(7):766–774, 2018.

[352] Shamik Mascharak, Jason L. Guo, Michelle Griffin, Charlotte E. Berry, Derrick C. Wan, and Michael T. Longaker. Modelling and targeting mechanical forces in organ fibrosis. *Nature Reviews Bioengineering*, 2(4):305–323, 2024.

[353] Marija Plodinec, Marko Loparic, Christophe A. Monnier, Ellen C. Obermann, Rosanna Zanetti-Dallenbach, Philipp Oertle, Janne T. Hyotyla, Ueli Aebi, Mohamed Bentires-Alj, Roderick Y.H. Lim, and Cora Ann Schoenenberger. The nanomechanical signature of breast cancer. *Nature Nanotechnology*, 7(11):757–765, 2012.

[354] Yi Deng, Mingzhai Sun, and Joshua W Shaevitz. Direct Measurement of Cell Wall Stress Stiffening and Turgor Pressure in Live Bacterial Cells. *Phys. Rev. Lett.*, 107(15):158101, oct 2011.

[355] Nicolas Bouchonville, Mikaël Meyer, Christophe Gaude, Emmanuel Gay, David Ratel, and Alice Nicolas. AFM mapping of the elastic properties of brain tissue reveals kPa μm-1 gradients of rigidity. *Soft Matter*, 12(29):6232–6239, 2016.

[356] Elise Spedden, James D. White, Elena N. Naumova, David L. Kaplan, and Cristian Staii. Elasticity maps of living neurons measured by combined fluorescence and atomic force microscopy. *Biophysical Journal*, 103(5):868–877, 2012.

[357] M. Radmacher, R. W. Tillmann, M. Fritz, and H. E. Gaub. From molecules to cells: Imaging soft samples with the atomic force microscope. *Science*, 257(5078):1900–1905, 1992.

[358] Yuri M. Efremov, Takaharu Okajima, and Arvind Raman. Measuring viscoelasticity of soft biological samples using atomic force microscopy. *Soft Matter*, 16(1):64–81, 2019.

[359] Ricardo Garcia. Nanomechanical mapping of soft materials with the atomic force microscope: Methods, theory and applications. *Chemical Society Reviews*, 49(16):5850–5884, 2020.

[360] Yuri M Efremov, Alexander X Cartagena-Rivera, Ahmad I M Athamneh, Daniel M Suter, and Arvind Raman. Mapping heterogeneity of cellular mechanics by multi-harmonic atomic force microscopy. *Nature Protocols*, 13(10):2200–2216, 2018.

[361] Annafrancesca Rigato, Atsushi Miyagi, Simon Scheuring, and Felix Rico. High-frequency microrheology reveals cytoskeleton dynamics in living cells. *Nature Physics*, 13(8):771–775, aug 2017.

[362] Fabian M Hecht, Johannes Rheinlaender, Nicolas Schierbaum, Wolfgang H Goldmann, Ben Fabry, and Tilman E Schäffer. Imaging viscoelastic properties of live cells by AFM: Power-law rheology on the nanoscale. *Soft Matter*, 11(23):4584–4591, aug 2015.

[363] Pinggen Cai, Yusuke Mizutani, Masahiro Tsuchiya, John M Maloney, Ben Fabry, Krystyn J Van Vliet, and Takaharu Okajima. Quantifying cell-to-cell variation in power-law rheology. *Biophysical Journal*, 105(5):1093–1102, aug 2013.

[364] J H Gaddum. Lognormal Distributions. *Nature*, 156(3964):463–466, 1945.

[365] J. K. Wenderott, Carmen G. Flesher, Nicki A. Baker, Christopher K. Neeley, Oliver A. Varban, Carey N. Lumeng, Lutfiyya N. Muhammad, Chen Yeh, Peter F. Green, and Robert W. O'Rourke. Elucidating nanoscale mechanical properties of diabetic human adipose tissue using atomic force microscopy. *Scientific Reports*, 10(1):1–9, 2020.

[366] Mar Eroles, Javier Lopez-Alonso, Alexandre Ortega, Thomas Boudier, Khaldoun Gharzeddine, Frank Lafont, Clemens M. Franz, Arnaud Millet, Claire Valotteau, and Felix Rico. Coupled mechanical mapping and interference contrast microscopy reveal viscoelastic and adhesion hallmarks of monocyte differentiation into macrophages. *Nanoscale*, 15(29):12255–12269, 2023.

[367] Arnaud Millet. A Universal Model for the Log-Normal Distribution of Elasticity in Polymeric Gels and Its Relevance to Mechanical Signature of Biological Tissues. *Biology*, 10(1):64, 2021.

[368] R. Vargas-Pinto, H. Gong, A. Vahabikashi, and M. Johnson. The effect of the endothelial cell cortex on atomic force microscopy measurements. *Biophysical Journal*, 105(2):300–309, 2013.

[369] Leda Lacaria, Alessandro Podestà, Manfred Radmacher, and Felix Rico. *2.2 Contact Mechanics*, pages 21–64. De Gruyter, Berlin, Boston, 2023.

[370] Yara Abidine, Valérie M. Laurent, Richard Michel, Alain Duperray, Liviu Iulian Palade, and Claude Verdier. Physical properties of polyacrylamide gels probed by AFM and rheology. *Epl*, 109(3):11–17, 2015.

[371] Frank J Massey Jr. The Kolmogorov-Smirnov Test for Goodness of Fit. *Journal of the American Statistical Association*, 46(253):68–78, 1951.

[372] Jia Jye Lee, Satish Rao, Gaurav Kaushik, Evren U. Azeloglu, and Kevin D. Costa. Dehomogenized Elastic Properties of Heterogeneous Layered Materials in AFM Indentation Experiments. *Biophysical Journal*, 114(11):2717–2731, 2018.

[373] D S Sivia. *Data analysis: a Bayesian tutorial*. Oxford University Press, 1996.

[374] Guillaume Charras. Stress fibres and the cortex work in tandem. *Nature Materials*, 20(3):281–283, 2021.

[375] John E Sader, Riccardo Borgani, Christopher T Gibson, David B Haviland, Michael J Higgins, Jason I Kilpatrick, Jianing Lu, Paul Mulvaney, Cameron J Shearer, Ashley D Slattery, Per-Anders Thorén, Jim Tran, Heyou Zhang, Hongrui Zhang, and Tian Zheng. A virtual instrument to standardise the calibration of atomic force microscope cantilevers. *Review of Scientific Instruments*, 87(9):93711, sep 2016.

[376] Jeffrey L Hutter and John Bechhoefer. Calibration of atomic-force microscope tips. *Review of Scientific Instruments*, 64(7):1868–1873, 1993.

[377] Núria Gavara. Combined strategies for optimal detection of the contact point in AFM force-indentation curves obtained on thin samples and adherent cells. *Scientific Reports*, 6(February):1–13, 2016.

[378] Tony Yeung, Penelope C Georges, Lisa A Flanagan, Beatrice Marg, Miguelina Ortiz, Makoto Funaki, Nastaran Zahir, Wenyu Ming, Valerie Weaver, and Paul A Janmey. Effects of substrate stiffness on cell morphology, cytoskeletal structure, and adhesion. *Cell Motility and the Cytoskeleton*, 60(1):24–34, aug 2005.

[379] Alexander M Mood, Franklin A Graybill, and Duane C Boes. *Introduction to the theory of statistics*. McGraw-Hill, 3d ed edition, 1974.

[380] F. C. Leone, L. S. Nelson, and R. B. Nottingham. The Folded Normal Distribution. *Technometrics*, 3(4):543–550, 1961.

[381] Elias T. Spiliotis and Michael A. McMurray. Masters of asymmetry-lessons and perspectives from 50 years of septins, 2020.

[382] Joanna Kim, Olivia L. Mooren, Michael D. Onken, and John A. Cooper. Septin and actin contributions to endothelial cell–cell junctions and monolayer integrity. *Cytoskeleton*, 2022.

[383] Xueying Wang, Wenwen Wang, Xiwei Wang, Ming Wang, Lijuan Zhu, Fatima Garba, Chuanhai Fu, Barbara Zieger, Xu Liu, Xing Liu, and Xuebiao Yao. The septin complex links the catenin complex to the actin cytoskeleton for establishing epithelial cell polarity. *J. Mol. Cell Biol.*, 13(6):395, 2021.

[384] Kim J.A. Vendel, Celine Alkemade, Nemo Andrea, Gijsje H. Koenderink, and Marileen Dogterom. In vitro reconstitution of dynamic co-organization of microtubules and actin filaments in emulsion droplets. In *Methods in Molecular Biology*, volume 2101. 2020.

[385] Lucia Baldauf, Felix Frey, Marcos Arribas Perez, Timon Idema, and Gijsje H. Koenderink. Branched actin cortices reconstituted in vesicles sense membrane curvature. *Biophysical Journal*, 122(11):2311–2324, 2023.

[386] Andreas Fink, Charlotte R. Doll, Ana Yagüe Relimpio, Yannik Dreher, Joachim P. Spatz, Kerstin Göpfrich, and Elisabetta Ada Cavalcanti-Adam. Extracellular Cues Govern Shape and Cytoskeletal Organization in Giant Unilamellar Lipid Vesicles. *ACS Synthetic Biology*, 12(2), 2023.

[387] Shagufta H. Shabbir, Megan M. Cleland, Robert D. Goldman, and Milan Mrksich. Geometric control of vimentin intermediate filaments. *Biomaterials*, 35(5):1359–1366, feb 2014.

[388] Shagufta H. Shabbir, Megan M. Cleland, Robert D. Goldman, and Milan Mrksich. Geometric control of vimentin intermediate filaments. *Biomaterials*, 35(5):1359–1366, feb 2014.

[389] Torsten Wittmann, Alessandro Dema, and Jeffrey van Haren. Lights, cytoskeleton, action: Optogenetic control of cell dynamics, 2020.

[390] Jessica G. Bermudez, Alexander Deiters, and Matthew C. Good. Patterning Microtubule Network Organization Reshapes Cell-Like Compartments. *ACS Synthetic Biology*, 10(6), 2021.

[391] Rebecca C. Adikes, Ryan A. Hallett, Brian F. Saway, Brian Kuhlman, and Kevin C. Slep. Control of microtubule dynamics using an optogenetic microtubule plus end-F-actin cross-linker. *Journal of Cell Biology*, 217(2), 2018.

[392] Sorosh Amiri, Camelia Muresan, Xingbo Shang, Clotilde Huet-Calderwood, Martin A Schwartz, David A Calderwood, and Michael Murrell. Intracellular tension sensor reveals mechanical anisotropy of the actin cytoskeleton. *Nat. Commun.*, 14(1):8011, 2023.

[393] Margaret L Gardel, Ian C Schneider, Yvonne Aratyn-Schaus, and Clare M Waterman. Mechanical Integration of Actin and Adhesion Dynamics in Cell Migration. *Annu. Rev. Cell Dev. Biol.*, 26:315, 2010.

[394] Mukund Gupta, Bibhu Ranjan Sarangi, Joran Deschamps, Yasaman Nematbakhsh, Andrew Callan-Jones, Felix Margadant, René Marc Mège, Chwee Teck Lim, Raphaël Voituriez, and Benoît Ladoux. Adaptive rheology and ordering of cell cytoskeleton govern matrix rigidity sensing. *Nature Communications*, 6(7525), 2015.

[395] Maxx Swoger, Sarthak Gupta, Elisabeth E. Charrier, Michael Bates, Heidi Hehnly, and Alison E. Patteson. Vimentin Intermediate Filaments Mediate Cell Morphology on Viscoelastic Substrates. *ACS Applied Bio Materials*, 5(2):552–561, feb 2022.

[396] Jérôme Solon, Ilya Levental, Kheya Sengupta, Penelope C. Georges, and Paul A. Janmey. Fibroblast adaptation and stiffness matching to soft elastic substrates. *Biophysical Journal*, 93(12):4453–4461, 2007.

[397] Johannes Rheinlaender, Andrea Dimitracopoulos, Bernhard Wallmeyer, Nils M. Kronenberg, Kevin J. Chalut, Malte C. Gather, Timo Betz, Guillaume Charras, and Kristian Franze. Cortical cell stiffness is independent of substrate mechanics. *Nature Materials*, 19(9):1019–1025, sep 2020.

[398] Caleb Jensen and Yong Teng. Is It Time to Start Transitioning From 2D to 3D Cell Culture? *Frontiers in Molecular Biosciences*, 7(March):1–15, 2020.

[399] Dan Deviri and Samuel A Safran. Balance of osmotic pressures determines the nuclear-to-cytoplasmic volume ratio of the cell. *Proceedings of the National Academy of Sciences*, 119(21):e2118301119, 2022.

[400] Ming Guo, Adrian F Pegoraro, Angelo Mao, Enhua H Zhou, Praveen R Arany, Yulong Han, Dylan T Burnette, Mikkel H Jensen, Karen E Kasza, Jeffrey R Moore, Frederick C Mackintosh, Jeffrey J Fredberg, David J Mooney, Jennifer Lippincott-Schwartz, and David A Weitz. Cell volume change through water efflux impacts cell stiffness and stem cell fate. *Proceedings of the National Academy of Sciences*, 114(41):E8618–E8627, 2017.

[401] T L Madden and J Herzfeld. Crowding-induced organization of cytoskeletal elements: I. Spontaneous demixing of cytosolic proteins and model filaments to form filament bundles. *Biophysical Journal*, 65(3):1147–1154, sep 1993.

[402] Soares E Silva M., Alvarado J., Nguyen J., Georgoulia N., Mulder B.M., and Koenderink G.H. Self-organized patterns of actin filaments in cell-sized confinement. *Soft Matter*, 7(22):10631–10641, 2011.

[403] Ruben C Boot, Gijsje H Koenderink, and Pouyan E Boukany. Spheroid mechanics and implications for cell invasion. *Advances in Physics: X*, 6(1):1978316, 2021.

PUBLICATIONS

PUBLICATIONS INCLUDED IN THIS THESIS

J. P. Conboy, M.G. Lettinga, P. E. Boukany, F. C. MacKintosh & G. H. Koenderink (2026). Actin and vimentin jointly control cell visoelasticity and compression stiffening. Molecular Biology of the Cell, mbcE24120584.

J. P. Conboy*, M.G. Lettinga*, N. van Vliet, L. Winter, G. Wiche, F. C. MacKintosh & G. H. Koenderink (2026). Plectin affects cell viscoelasticity at small and large deformations. Biophysical Journal, 125 (1) 125(1), 35–53.

J. P. Conboy*, I. Istúriz Petitjean* , A. van der Net*, & G. H. Koenderink* (2024). How cytoskeletal crosstalk makes cells move: Bridging cell-free and cell studies. Biophysics Reviews, 5(2), 021307

J. P. Conboy, N. Vaes, J. Barrasa-Fano, L. Winter, H. van Oosterwyck, G. Wiche & G. H. Koenderink. Untangling the cytoskeletal crosslinking and anchoring functions of plectin in cells. *In preparation*

J. P. Conboy, N. van Vliet, P. E. Boukany, F. C. MacKintosh & G. H. Koenderink. Actin and vimentin in single cells exhibit reciprocal mechanical responses under shear deformation. *In preparation*

J. P. Conboy, M. Eroles, F. Rico & G. H. Koenderink. Beyond bell curves: The origin of non-Gaussian distributions in atomic force microscopy elasticity measurements. *In preparation*

OTHER PUBLICATIONS

A. van der Net, R. C. Boot, I. van Dijk, **J. P. Conboy**, P. E. Boukany & G. H. Koenderink. Cancer cell deformability impacts the rate of confined migration but not decision making (2025). Biomicrofluidics, 19 (6): 064101.

M. Pasolli, J. C. M. Meiring, **J. P. Conboy**, G. H. Koenderink & A. Akhmanova (2025). Optogenetic and chemical genetic tools for rapid repositioning of vimentin intermediate filaments. Journal of Cell Biology, 224 (9): e202504004.

B. Meijlink, G. Collado-Lara, K. Bishard, **J. P. Conboy**, S. A. G. Langeveld, G. H. Koenderink, A. F. W. van der Steen, N. de Jong, I. Beekers, S. J. Trietsch & K. Kooiman (2025). Characterizing Microbubble-Mediated Permeabilization in a Vessel-on-a-Chip Model. Small 2025, 21, 2407550.

G.S. van Tienderen, M. E. A. van Beek, I. J. Schurink, O. Rosmark, H. P. Roest, J. Tieleman, J. Demmers, I. Muntz, **J. P. Conboy**, G. Westergren-Thorsson, G. H. Koenderink, L. J. W. van der Laan & M.M.A Verstegen (2023). Modelling metastatic colonization of cholangiocarcinoma organoids in decellularized lung and lymph nodes. Frontiers in oncology 12, 1101901.

G. S. van Tienderen, **J. P. Conboy**, I. Muntz, J. Willemse, J. Tieleman, K. Monfils, I. J. Schurink, J. A. A. Demmers, M. Doukas, G. H. Koenderink, L. J. W. Van der Laan & M. M. A. Verstegen (2023). Tumor decellularization reveals proteomic and mechanical characteristics of the extracellular matrix of primary liver cancer. Biomaterials Advances 146, 213289.

*Denotes equal contribution

CURRICULUM VITAE

James Peter Conboy

24/12/1997 Born in the United Kingdom

Education

2020-2025	PhD research *Delft University of Technology*
2020	Master of Physics (Honours) *University of Manchester*
2016	A levels *Beauchamp College*

ACKNOWLEDGEMENTS

So you have finished or, perhaps just as likely, just started reading this little book. Although my name may be on the front cover, the work bound in these pages is the result of years of support from many wonderful, intelligent and compassionate people. It is to you that I dedicate these final words.

I must begin, of course, with Gijsje. My sense of your warmth and the excitement for science you exuded in our first online meeting when the world was in its first Covid lockdown only grew during my time in Delft. In that selfsame pandemic, when I reached rock bottom, it was because of your perpetual support that I could piece myself back together again and make it to the finish line. Thank you for having belief in me when I did not, and for your boundless kindness and optimism when I was totally overwhelmed and out of action. Since then, I have become a lot more knowledgeable, organised and scientifically skilled thanks to your wise guidance. Thank you for giving me close to limitless freedom to shape my own project and explore my sometimes fruitful ideas with curious abandon, also with the knowledge that you would always have my back. I think you are an inspiration to us all.

Pouyan, I was delighted when you accepted the mantle of becoming my second promotor. I always appreciated your injections of enthusiasm into my projects during our meetings and your many ideas. Thank you for your support; you were always a pleasure to do science with. I would also like to warmly thank my thesis committee. Thank you to Anna, Timo, Chase, Guillaume, Chirlmin and Stephen for taking the time and effort to read my thesis. Thank you also for your words of encouragement, which I appreciate greatly.

My dear fellow Biosofties and Co., it has been my pleasure to spend these past years with you. Whilst I cannot put an order to this illustrious group, I do have to start with my fantastic paranymphs. Irène, you managed to bring so much brightness into the lab when you came to Delft. Thank you for your sense of fun, kindness and competence; my PhD would not have been the same without you. It was always enjoyable to spend time with you both inside and outside of the lab, where we could always rely on you to take a photo for a souvenir of the night. I greatly enjoyed our evenings in Delft, especially when things went in a more *Jamie* direction. Hidde, though not officially a Biosoftie, I think the fact that your office was sandwiched by our hordes qualifies you for honorary membership. Your contagious enthusiasm for all fun facts, especially those pertaining to trains, and your passion for music is always a pleasure to be around. I always felt more positive after talking with you. Thank you for your curiosity, openness and warmth, which I'm sure will get you far in whatever you choose to do next.

Iain, thank you for being a great pal, for all the fun, and for being someone with whom I could (sadly, regularly) bemoan the state of British politics. It was also because of your experiments that I started hatching a plan to find a new way of torturing cells by shearing them. Together with Amy, you were both there when I needed all the support I could get. Thank you for everything and I'm so happy for you that Little Marnie is now in Delft too. Rachel, thank you for being a great friend, your penchant for quoting Pride and Prejudice, and for being my confessor. Thank you for all the wonderful time together, bestowing upon me the honour of being your paranymph, and I hope you weren't too scarred by Star Wars. The best of luck with your Edinburgh adventure and I look forward to visiting you lots! Irene, thank you for your support and ever understanding kindness. I think you recognised how tough things would be for me in lockdown before even I did. You are always somebody whom I feel comfortable sharing with. Thank you for readily hosting me in Covid-deserted Amsterdam, for honest conversations, and great chats over our shared love of cinema and good food. It is because of your indefatigable work building your crosslinker library that the ACTIF project in this thesis was even possible. Luci, your infectious passion for science to dancing is an absolute pleasure to have around and it has been wonderful to visit you in London. Thank you for your kindness when I was trying to escape 'the box', your listening ear, and introducing me to the concept of a sugar cone on fire where one should never drink the rum under any circumstances. Anouk, thank you for being my fellow noob-ish PhD student as we tried to navigate the graduate school, start supervising students, and work out what I was actually trying to achieve in this PhD. You were also a great partner in crime as we attempted to illegally dispose of that rather large sack of expired media. Thank you for always being supportive, always willing to listen and just being great to talk to. You are extremely hard working, intelligent and a great scientist capable of doing anything super competently. Lennard, thank you for your great sense of humour and openness. After every time we had a coffee I always left feeling better and more optimistic, and I think the way you stayed level-headed in the face of bedevilled GUV aspirations was remarkable. I would like to say I learnt from your experience of doing graduate school courses last-minute but I am afraid I cannot. It was an honour to be your paranymph and thank you for all your support and kindness when I needed it the most. Gerard, thank you for your 'chaotic clown' energy, your musings on food, particularly with regard to the merits of potatoes and lemons, and your kindness. Despite your deep rooted cynicism for science (or more fairly academia), you are really, really good at it. Thank you for your compassion, wise advice and always being willing to help others. I hope you get your farm soon so I can come and visit. Marcos, thank you for your friendship, all the fun outside of the lab we had together, great advice, kindness, and always wanting to make the lab a better place to be in. I am sure the way you selflessly helped whomever needed it in the lab pulled many people out of a pit of despair. I wish we could have continued our GUV squishing project together as you're a great person to work with and you were such a positive presence in the lab. Bert, thank you for sharing your dry, acerbic sense of humour with us and for the fun times outside of the lab. In the face of a really tough project, the way you've pushed through your PhD via sheer competence has been something to behold. Jeff, you are a remarkably kind person and always looking out for all those around you. Thank you for organising board

game nights, initiating group activities, generally ensuring that everybody felt welcome in the lab and looking out for anyone who might be struggling. Also thank you for trying to get me to join tea breaks with decreasing success as I was trying to finish up. Let's grab a drink together but perhaps this time with no more 'announcements'. SaFyre, you brought a great deal to the group with your open and approachable personality. Thank you for encouraging me to take breaks, all the dark room shenanigans (poking around a roll of film in a bucket remains my most memorable development experience) and your photo book documenting my post-holiday demise was so touching. Fede, I apparently may have not left the best initial impression upon you but I hope that's changed at least a little. You were great to spend time with both in and out of the lab, and thanks for being even more of a labaholic than me so I didn't look so bad. Thank you for your curiosity, openness, fondness for Kapsalons, and always being there to help. Christine, thank you for bringing your warm personality to the lab. You make doing a PhD look remarkably linear and I'm sure you'll have a fantastic project. It was great to get to know you, spend time with you outside the lab, and thank you for your help with the rheometers. Charu, thank you for teaching me how to FRAP, and for being such a warm and nice person to chat with. I wish you all the best with the rest of your postdoc. Nicky, thank you for being a great lab mate, your tofu wisdom, the nice chats over beers, and showing us how to make a good summer roll. I hope you have a great time doing your postdoc in Delft. Ivy, thank you for being such a great co-supervisor on our shared project with Charlie. I hope you have a lot of fun with the rest of your project. Nicole, without your cell culture help, many of the experiments in this thesis would simply not have been possible. Thank you for being such a good technician to work with and for being such a competent cell culturer. Nikki, it was really nice to chat with you and to hear your dark sense of humour. I wish you the best in wrapping up your PhD. Sonam, thank you for relishing the organisation of our lab Christmas dinners, and teaching me that not everybody in the Netherlands likes to cycle. Good luck with the rest of your adventures in Delft. Sebastien, it was such a pleasure to have you in the group. Although you were in Delft for such a short time, you were always really energising to talk with and I think you're a great role model. Thank you for all your kind words and I wish you the best in growing your group in Eindhoven. Hande, it was always nice to chat with you and lament the art of nanoindentation when you sporadically popped up in Delft. Good luck finishing up! Marieke, it was always really nice to see you in Delft and I am really happy to have contributed to your AFM work. Risa, you are a very talented scientist. It was always a pleasure to chat with you, and I wish you the best of luck with your project. Joris, you only started your PhD as I was wrapping up but I wish you all the best with your project.

I also had the pleasure of supervising many talented students and I hope you are all as proud as I am of the work you contributed to this thesis. Stein, thank you for being my first student. In such a short period of time you helped me to set up our first microrheology experiments which led to really cool results later on. Alara, thank you for the fun summer we had live-cell imaging together with Anouk. Your experiments were the indispensable starting gun for all the live microscopy experiments in my projects. Sterre, thank you for being the first brave volunteer to really start up

micropatterning in the lab. From the results of your project, micropatterning came to be used as an essential tool in the lab by Ivy, Anouk and I. I hope your confidence has kept growing as you were a really great student. Danny, I was so lucky that I'd found such an independent and prolific student, especially when I could only provide remote supervision after I abandoned you for the south of France. Thank you for your amazing work and your bright presence. Charlie, thank you for all your work on our Fibrosis project with Ivy. It was really fun to supervise your project and although you may not be continuing down the physics path, it was really nice to see you enjoy the project and I think you wrote a beautiful report. It was always nice talking with you about cinema and I hope you have fun finishing up your philosophy master's. Stijn, you did such a great job at tackling the difficult project Irene and I dreamt up, combining pretty tricky reconstitution experiments with unreliable cell work. It was so rewarding to see you grow in confidence and you were always delightful to be around in the lab. Mathilde, I was so lucky that you chose to work on my project and you were the best cell squishing enthusiast I could have hoped for. Not only did we write two papers together, I could not have wished for a better collaborator both inside and outside of the lab (more on that later). You all made working in the lab so much more interesting.

A lot of people outside of Biosoft lab were also instrumental in getting me to the end. Cátia, thank you for all your cell culture support. It was thanks to you that we got our new cell culture facility and kept it running smoothly, without which my PhD would have been far more difficult. Thank you Martin for trying to breathe life back into the department after Covid. Thank you Sacha, Esengül, Ramon, Allard, Jan, Ilja and Dimitri for all your work in the department and for always being on hand when I needed knowledge or materials. Thank you to all of the management assistants, especially Tracey, for always being super efficient and for helping me out when things needed doing urgently. Marieke, Stefan, Nynke, Ireth, Ilina, George, Pietro, Daniel, Marijn, Vincent, Olivier, Felix, Moritz, Ran, Iris, Jos, Marianne, Beatriz and many more, thank you for making Delft so much better a place to do science.

Throughout my PhD, I had the privilege to work with many fantastic scientists. Fred, thank you for our collaborative projects. I always came out of our meetings with a renewed sense of enthusiasm and bouncing with ideas for new experiments and interpreting our data. My thesis would not be the same without you as you were a treasure trove of scientific input into my projects. Thank you for being that rare theorist with an appreciation of the challenges and unfortunate practicalities of experimental work. To Felix, even though almost anything that could go wrong indeed did go wrong during my visit to Marseille including Fedex disasters, riots, broken AFMs, a cyberattack and to top it all off, a stolen computer, I still greatly value the time I got to spend in your lab. Despite the aforementioned trials, we still managed to write a chapter that I'm very proud of. A further thank you to the rest of the AFMers: Claire and Lorena for letting me hold onto a half-working AFM for an extra couple of weeks, and to Mar, Natalia, Prithwidip, Ismahene, Alex, Yogesh and Lorenzo for making me feel welcome in Marseille. Staying in the south of France, thank you to Manos and Carla for taking the time and effort to teach me the tricks of electroporation and giving me my first foray into live cell imaging,

which became indispensable as my project developed. Gerhard, thank you for all of your plectin wisdom and for all of your insightful comments that greatly strengthened our manuscripts. Lilli, thank you for making our ACTIF construct expressible in cells, which kickstarted an entire chapter that became one of the highlights of this thesis. Nele and Jorge, thank you for facilitating my Marathon of TFM experiments and making me feel very welcome in Leuven. Thank you all for your supportive words and for being such great collaborators.

To Mum and Dad, thank you for helping me wherever you could every step of the way and supporting me through my studies. Thank you for letting me be my obsessed self, from safes and sea urchins to the pursuit of science.

Tilly, where to even begin. Thank you for always believing in me, keeping me in a semi-sane state and taking such good care of me as I attempted to put this book together. Above all else, meeting you has been the most wonderful and exciting thing to have happened to me during my time in Delft. You are such a brilliant partner, friend and scientist, and you made my PhD so much more rewarding and fun. I'm so looking forward to the life we'll build together in Dresden and beyond. To the future!

James
Dresden, December 2025

